Schriftenreihe des Energie-Forschungszentrums Niedersachsen (EFZN)

Band 64

Das EFZN ist ein gemeinsames wissenschaftliches Zentrum der Universitäten:

Technische Universität Braunschweig

TU Clausthal

GEORG-AUGUST-UNIVERSITÄT GÖTTINGEN

Leibniz Universität Hannover

CARL VON OSSIETZKY universität OLDENBURG

TU Clausthal
Clausthal University of Technology

Numerical study of the stimulation related thermo-hydro-mechanical processes in tight gas and deep geothermal reservoirs

Doctoral Thesis

(Dissertation)

to be awarded the degree

Doctor of Engineering (Dr.-Ing.)

submitted by

M.Sc. Wentao Feng

from Chongqing, P.R. China

approved by the Faculty of Energy and Economic Sciences,

Clausthal University of Technology,

Date of oral examination

12.12.2019

Bibliografische Information der Deutschen Nationalbibliothek

Die Deutsche Nationalbibliothek verzeichnet diese Publikation in der Deutschen Nationalbibliografie; detaillierte bibliografische Daten sind im Internet über http://dnb.d-nb.de abrufbar.

1. Aufl. Göttingen : Cuvillier, 2020

Zugl.: (TU) Clausthal, Univ., Diss., 2020

D104

Dean

Prof. Dr. rer. nat, habil. Bernd Lehmann

<in case: > Chairperson of the Board of Examiners

Supervising tutor

Prof. Dr.-Ing. habil. Michael Z. Hou

Reviewer

Prof. Dr.-Ing. habil. Olaf Kolditz

Nonnenstieg 8, 37075 Göttingen
Telefon: 0551-54724-0
Telefax: 0551-54724-21
www.cuvillier.de

1. Auflage, 2020

Gedruckt auf umweltfreundlichem, säurefreiem Papier aus nachhaltiger Forstwirtschaft

ISBN 978-3-7369-7170-7

eISBN 978-3-7369-6170-8

Acknowledgement

First, I would like to express my deepest gratitude and appreciation to my supervisor Prof. Dr.-Ing. habil. Michael Zhengmeng Hou for his consistent support, motivation and guidance. It would be impossible to finish this thesis without his helpful supervision. I also would like to thank Prof. Dr.-Ing. habil. Olaf Kolditz for his immense advice and expert evaluation of this dissertation.

I own special thanks to Mr. Muhammad Haris for his kind advice and professional corrections of this dissertation.

I would like to thank several professors, researchers as well as industrial partners in the DGMK-project 680-IV and BMWi-project MAGS2, who are happy to share their experiences with me and provide me valuable advice.

I owe many thanks to all my colleagues at Research Center Energy Storage Technologies (EST) and Clausthal University of Technology (TUC) for making my life here interesting and fun. Thank you all for your care and love.

Finally, I would like to thank my family, especially my wife, Can Zhang, for their support and encouragement through all these years.

Clausthal-Zellerfeld, Juni 2019 Wentao Feng

Abstract

In recent times, the efficient development of unconventional gas/oil reservoirs and deep geothermal resources has become a focal point of research in the field of energy. Since the inception of stimulation in the 1940s, the technique has been revolutionized especially by combining hydraulic fracturing with horizontal well technology. Hydraulic fracturing operation is a complicated operation owing to several important issues, such as fluid viscosity's influence on the stimulation results and the induced seismicity during the fracturing operation or even reactivation of the natural faults etc. In this thesis, targeted improvements have been achieved through the development of a series of mathematical/physical models, and their implementation into the existing numerical tools (FLAC3D^{plus} and TOUGH2MP-FLAC3D), including: (a) a new thermal module for FLAC3D^{plus} based entirely on the finite volume method (FVM), which is especially developed for the fracturing process and can also achieve the modeling of gel breaking; (b) a rock damage module of TOUGH2MP-FLAC3D, which also considers the impacts of rock damaging process on evolution of permeability; (c) an in-depth improved FLAC3D^{plus} simulator that obtains the ability to simulate a 3D fracture propagation with arbitrary orientation.

After the corresponding verifications of the improved tools, different case studies are conducted and analyzed. The following conclusions can be drawn from these case studies:

1) Systematic study of the fluid viscosity's impacts on shaping of a fracture in tight sandstone: a) the fracture's growth during stimulation is governed by two competing energy dissipation mechanisms (viscous flow and fracturation) and two competing storage mechanisms (in the fracture or in the porous formation). The system tends to be storage (in fracture)-dominated, when fracture's leak off ability is sufficiently low (depending on the combined effects of formation permeability and fluid viscosity); b) Change in horizontal stress (σ_h) and pore pressure (P_p) are actually two competing mechanisms. Change of the pore pressure is mainly driven by the leak off process but the minimum horizontal stress varies mainly due to the fracture pressure, i.e. σ_h alters more intensively when a system is hard to

leak off. Furthermore, the fluid viscosity also affects the final shape of fracture through its proppant-carrying ability. To make the simulation results closes to the practical situation, the function of simulating gel breaking was developed for the thermal module. Through conducting a real case study in tight gas reservoir Leer (considering the THM coupling effects and the gel breaking process), it was found that not only the leak off but also the proppant's settling would be accelerated by smoother fluid. A possible way to solve this problem is introducing gas-based fracturing such as supercritical CO_2, as in this method the fracture's close rate can be much faster than the settling.

2) Geothermal utilization induced microseismic in stimulation and production phase of Landau project: a) Core area within and around the natural faults is more susceptible to the stimulation work. Its plastic strain, therefore, increases further even after the propagation has stopped; b) Mechanic and hydraulic equilibrium cannot be achieved immediately. Thus in the post failure process, fracturing and seismicity occurred even after the injection is stopped; c) intense rise or fall in injection/production rates induces disturbance in the system. A huge difference between them possesses the same effect. The stronger the disturbance, the more intensive the fracturing and seismic would be. It can be concluded that, immoderate changes of injection/production rate or a huge difference between them lead to induced seismicity, while the reactivation trend of natural faults is impacted by the absolute value of injection/production rate, i.e. intensity of the operation. A reasonable response to reduce the risks is: reducing the injection and production rates immediately with a moderate and equal rate (injection/production) when critical seismicity magnitude (e.g. $M_L \geq 2.0$) occurs.

3) Advanced FLAC3D^{plus}: this powerful simulator has gained new features through several in-depth improvements. After implementing the triangle prism element and reprograming the mechanic and hydraulic codes, this simulator is verified to be able to model the fracture propagation with arbitrary orientation. More importantly, it overcomes the shortcoming of XFEM (extended finite element method) and can be employed in 3D situation.

Contents

List of figures

List of tables

1 Introduction

1.1 Motivations and Objectives

Energy demand of the world is undergoing a process of rapid growth. From 1991 to 2016, total world energy consumption had increased by about 60% [1]. Even in nowadays scenario, i.e. due to the improvement in the efficiency of the energy intensity by 2015 was more than 30% lower than that in 1992 [2], the total consumption will still expand by 30% until 2040, equivalent to add another China and India to today's global demand [3].

Since the beginning of the 21st century, many countries and organizations have proposed that human beings should vigorously develop the renewable energy. This is on one hand to ensure its own energy security, and on the other hand sustainable development can also be maintained. However, although countries have increased their investment in renewable energy, compared with the original plan, the nowadays' schedule has been greatly delayed. As a result, fossil energy will remain an important pillar of the world's energy system for the foreseeable future. In the projection of EIA in 2016 [4] (Fig. 1.1), fossil fuels will still account for 78% of the world's energy consumption until 2040 [5], especially in the non-OECD countries.

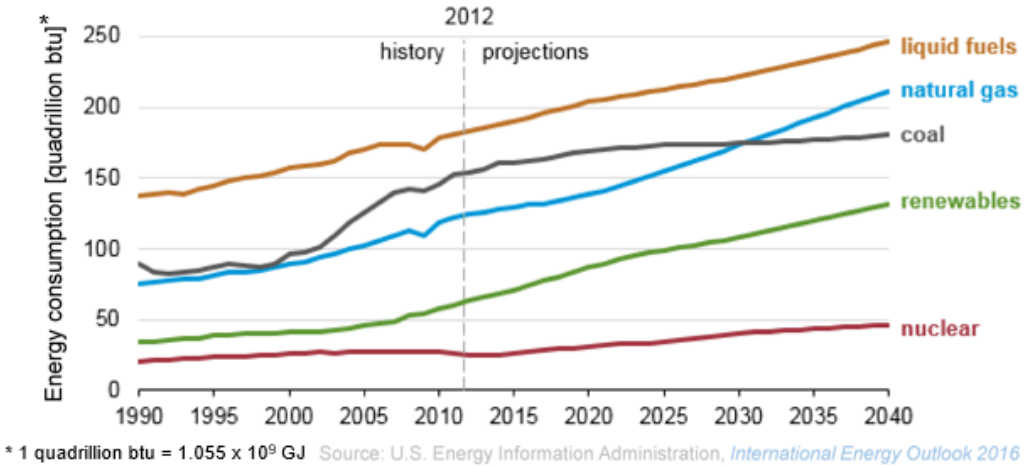

Figure 1.1 World energy consumption by source, 1990-2040 [4]

Based on this situation, reservoir stimulation once again becomes a very important operation not only in petroleum industry but also in geothermal exploitation. Since most of the new proven gas/oil reserves are unconventional reservoirs, i.e. tight and the deep geothermal reservoirs, they both have the characteristic that the involved permeability is too small to provide an economical production (the permeability of a tight gas reservoir is usually smaller than 0.1mD). In order to create artificial conductive channel or to enhance the conductivity of natural fracture, stimulation operations have become essential (Fig. 1.2). However, although the reservoir stimulation techniques represented by hydraulic fracturing has been developed since 1940s, the related scientific research is still only a matter of recent decades. Relying on the rapid development of computer science in the past 30 years, now it becomes possible to use numerical simulations to conduct detailed pre- or post-production studies on the fracturing process. As a result, a large number of numerical simulators have emerged in industrial and research fields.

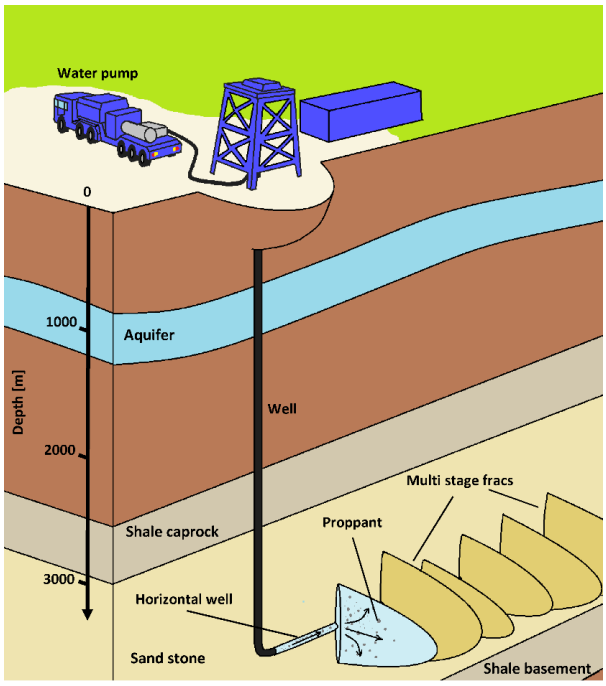

Figure 1.2 Demonstration of the stimulation operation in tight gas reservoir

Although commercial simulators such as FracPro and MFrac can generally provide a good reference to the fracturing's results, however, these simulators are still too simplistic for

researchers who want to achieve further improvements in the fracturing methods. For example, in MFrac of Baker Hughes, developers adopted several classical models such as PKG and KGD to perform the simulation. In this way, although these models can provide a fast semi-analytical solution, but the resulted fracture always possesses a fixed form. For this reason, some research groups have developed their own simulation codes.

1.2 Background

Prof. Hou's team believes that combining the most advantageous simulators in different fields (especially those simulators that can simulate physical processes at engineering scales.) with servo codes to obtain their capabilities in corresponding areas, will be the best solution for the above mentioned problems. Based on this idea, after several years of development, the team has developed two sets of simulation codes named FLAC3D^{plus} and TOUGH2MP-FLAC3D.

Among them, FLAC3D^{plus} mainly utilizes the features of FLAC3D in geo-mechanics. On this basis, by further developing the calculation program for fluid flow (within main fracture and porous rock formations) and proppant transport, the set of code has finally obtained complete ability to simulate hydraulic fracturing in the tight sandstone (dominated by tensile fracture perpendicular to the minimum principal stress). TOUGH2MP-FLAC3D provides the calculation of hydraulic and thermal fields to TOUGH2MP while transferring the geomechanical calculation to FLAC3D. The advantage of this coupling is that as the thermal and hydraulic calculations performed by TOUGH2MP can be more complex, FLAC3D can also perform its ability to simulate the mechanical behavior of rocks other than tight sandstone. However, this simulator cannot model the transport of solid proppant.

1.3 Thesis outline

In this thesis, several numerical studies focusing on reservoir stimulations in tight sandstone and deep geothermal reservoirs were carried out. Using FLAC3D^{plus} and TOUGH2MP-

FLAC3D, corresponding modeling involving hydro-mechanical (HM) or thermo-hydro-mechanical (THM) couplings have were performed.

In order to narrative the research work more clearly, the theoretical background or rather governing equations for describing the thermal, hydraulic and mechanical processes will firstly be introduced in Chapter 2.

Chapter 3 conducts a systematical study of the influences from fluid's viscosity on the fracturing results. Using the improved thermal module, which gains the ability to model thermal effects on fluid's properties, several important phenomena that reflect the interactions between fluid viscosity, development of fractures and rock formations have been analyzed. After considering the fluid's ability to carry solid proppant and depending on a real case study of the Leer, several recommendations to improve the results have been proposed.

Chapter 4 illustrates a research work for the EGS (Enhanced Geothermal System) project Landau. This study aims to analyze the relationship between reservoir stimulation and induced seismicity. In order to rationalize the granite's gradual loss of strength during the failure process, the concept of damage was also introduced. Relying on various modified treatment schedules, suggestions and countermeasures for dealing with induced seismicity have been explained at the end of study.

To further enhance the functionality of FLAC3D^{plus}, Chapter 5 proposes the improvement from the perspective of geometry. After implementing the modified codes into the simulator, two verifications and one 3D example have been presented in order to demonstrate the new features of this powerful simulator.

2 Fundamentals for describing the reservoir stimulation in a geosystem

2.1 Overview of a reservoir stimulation and the corresponding geo-processes

Reservoir stimulation is a very important activity of the production engineer in the modern petroleum and related industries (such as geothermal). Its main purpose is to obtain a faster delivery of the oil/gas [6] from the reservoir to the wellbore or an increased heat exchange area of the medium. Thus the working efficiency of the production system can be increased and consequently the ultimate economic recovery can be enhanced.

In recent years, by utilizing the application of reservoir stimulation in various unconventional oil/gas exploitation (tight oil/gas, shale oil/gas, etc.), through horizontal well-based multi-stage matrix stimulation and hydraulic fracturing, the connection of the wellbore with the reservoir has been greatly improved (Fig. 2.1). Such improvements, on the one hand, enable the oil/gas to be released from the tight reservoir and quickly reach towards wellbore, and on the other hand the need for another important activity, i.e. artificial lift, is delayed.

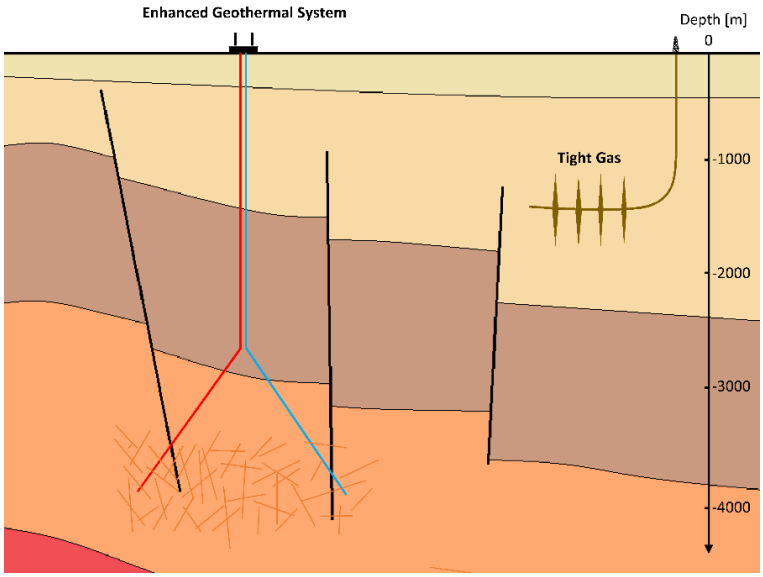

Figure 2.1 Reservoir stimulations in a subsurface geosystem

Another exploitation activity that possesses a high demand for the reservoir stimulation is the development of Hot Dry Rock (HDR) geothermal energy, which is also called the Enhanced Geothermal System (EGS) (Fig. 2.1). Since the high-temperature rock mass in an EGS is mainly located in the underground of several kilometers and is tight and impermeable, the pressurized water can not only make many hydraulic fractures perpendicular to the direction of the minimum principal stress, but can also enable some small natural joints in the rock mass to be expanded into larger ones. In this way, by increasing the contact area, the thermal energy contained in the underground hot rock can be extracted by the heat exchange medium more effectively.

Since all the main processes of reservoir stimulation occur in the underground, the various geo-processes in the subsurface geosystem during or after an operation have become focuses of the research. In the depth of the formations where reservoir stimulation carries out, solid rocks form the main support structure [5]. As the rocks are primarily porous media made of various mineral grains and cementations, after many tectogenesis, volcanic activities and weathering, natural cracks are generated in most rocks and in large scales even form several faults. Therefore, from the perspective of the integrity, the rocks can be classified into the intact rocks without fractures and fractured rock mass with fractures. In this large number of intact rock and fractured rock masses, the introduction of reservoir stimulation leads to many additional processes that are more dramatic than natural processes. Depending on their different principles, both natural and additional/induced processes can be classified into several different categories, such as thermal (T), hydraulic (H), mechanical (M) and chemical (C) processes. Although these processes are independent of each other in terms of principle, they will interact with each other during actual execution, e.g. the fluid flow in the fracture also causes the heat transport, and the contact of the low temperature fluid with the high temperature rock mass will lead to thermal contraction of the solid body. Such effects are referred to as mutual coupling as well, and Figure 2.2 is a schematic representation of such coupling effects. In order to better understand and describe these processes and

their coupling effects, in this chapter, the governing equations of the individual processes involved in a reservoir stimulation (except chemical processes) will be introduced.

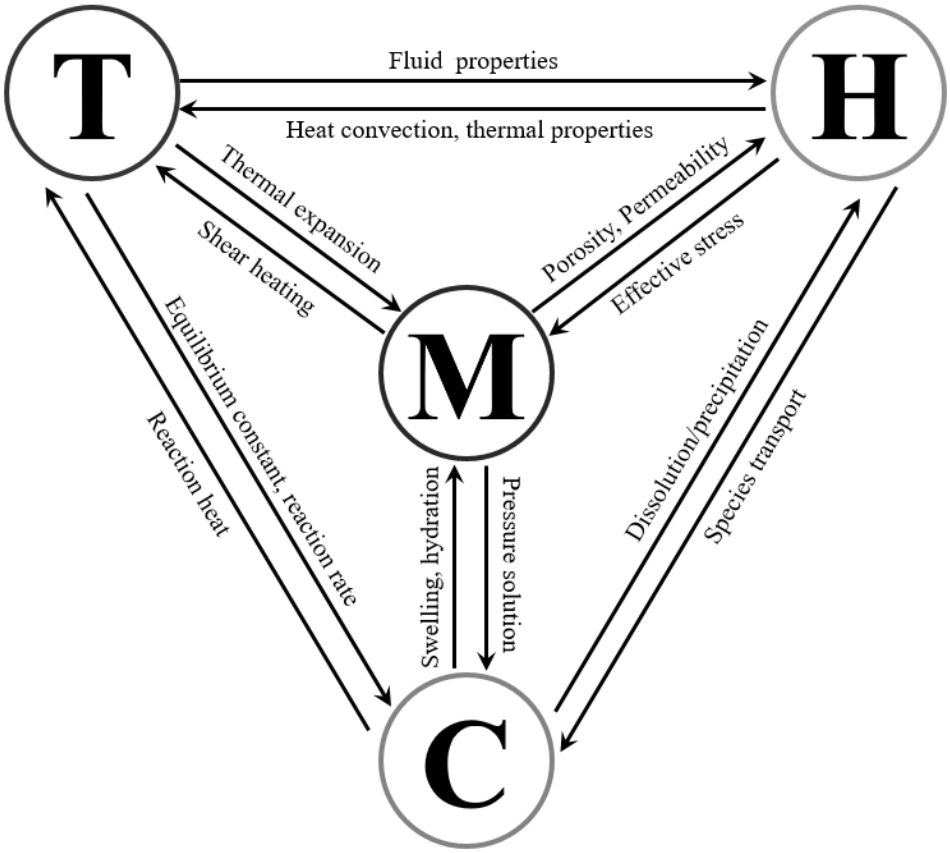

Figure 2.2 Overview of the coupled THM/C processes in a reservoir stimulation [5]

2.2 Geomechanics in the reservoir stimulation

Describing the geomechanics in a reservoir stimulation is actually very complicated. Since many different mechanical processes appear in an operation, the corresponding governing equations will be numerous. For example, the linear poro-elasticity theory can be used to describe the rock's deformation due to the change of fluid pressure but the fracture propagation can usually only be determined by using elastic or plastic fracture mechanics. Despite of this, analysis of the geomechnical problems is mainly considered by three conditions, namely the equilibrium, the continues and the physics [7].

2.2.1 Stresses and forces equilibrium

The study of the classical mechanics focuses on the position of a body and its two time derivatives, namely the velocity and the acceleration. In order to quantify the interaction of a given body with other objects, the forces that other objects apply on the body must be analyzed. These effects of forces applied on the body are described by Newton's law of motion. This law states that the sum of the forces acting on a body is equal to the mass of the body times its acceleration, i.e. when the sum of the external forces and moments acting on the body is null, the body will be in an equilibrium state.

The basic mechanical concepts given above can also be applied to the deformable bodies such as rock masses. However, in rock mechanics, the analysis methods must be slightly altered for various reasons: first, the force applied to a rock will, in general, vary from point to point, i.e. distribution of the force over the body must be taken into account; second, the idealization that forces act at localized points is not sufficiently general to apply to all problems encountered in rock mechanics [8]. Hence, Cauchy proposed the continuum mechanics and gave the definition of stress and strain in 19th century (Eq. (2.1)). The stress, which is also called traction, is defined as the force acting on an infinitesimal area (Fig. 2.3). Since the traction generally varies with the orientation of the surface on which it acts, the most convenient way for its representation is by means of an entity known as stress tensor.

$$\vec{\sigma} = \lim_{\Delta S \to 0} \frac{\Delta \vec{F}}{\Delta S} \tag{2.1}$$

Where $\vec{\sigma}$ is the stress vector [Pa], $\Delta \vec{F}$ is the vector of the internal force [N], ΔS is the corresponding area to the internal force [m^2].

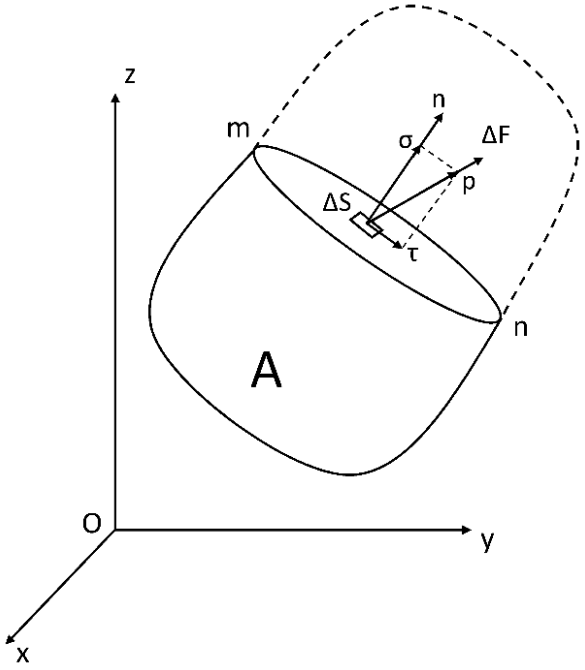

Figure 2.3 Schematics of the stress

2.2.1.1 Cauchy's stress tensor

In order to derive the Cauchy's stress tensor, first consider division of the internal force into one normal and two shear directions of a surface, therefore, one normal and two shear stresses are obtained (Fig. 2.4 (a)). Extending the same idea to the planes perpendicular to the three axes of a Cartesian coordinate system, yields three normal stresses (σ_{xx}, σ_{yy}, σ_{zz}) and six shear stresses (τ_{xy}, τ_{yz}, τ_{zx}, τ_{xz}, τ_{zy}, τ_{yx}). From this, the stress state of a point in a Cartesian coordinate system can be described through all these decomposed stresses (Fig. 2.4 (b)).

$$T_j^{(n)} = \alpha_{ni}\sigma_{ij} \tag{2.2}$$

Where $T_j^{(n)}$ is the component of the stress vector $\overrightarrow{T^{(n)}}$ on section ABC in j-direction [Pa], j = x, y, z, α_{ni} is the cosine between normal of the plane and three Cartesian coordinate axes [-], i = x, y, z, $\alpha_{n1} = \cos(n,x)$, $\alpha_{n2} = \cos(n,y)$, $\alpha_{n3} = \cos(n,z)$, σ_{ij} is the components of the stress vector above the section i (BOC, AOC, AOB) on three axes, i, j = x, y, z.

The oblique section introduced in above derivation process is used as a new coordinate plane to establish a new orthogonal coordinate system. At the same time, the normal vector of this section is taken as a new coordinate axis x. Thus the components of the stress vector along coordinate axis in the new coordinate system can be expressed as:

$$\sigma_{i'j'} = \alpha_{j'j} T_j^{(i')} = \alpha_{i'i}\alpha_{j'j}\sigma_{ij} \tag{2.3}$$

Where $\sigma_{i'j'}$ are the normal and shear stresses in the new coordinate system [Pa], i, j = x, y, z, $\alpha_{j'j}$ and $\alpha_{i'i}$ is the cosine between j or i-direction in the new coordinate system and j- or i-direction in the old coordinate system [-], i, j = x, y, z, $T_j^{(i')}$ is the component of the stress vector $\overrightarrow{T^{(i')}}$ in j-direction [Pa], σ_{ij} is the component of the stress vector above the section i on three axes, i, j = x, y, z.

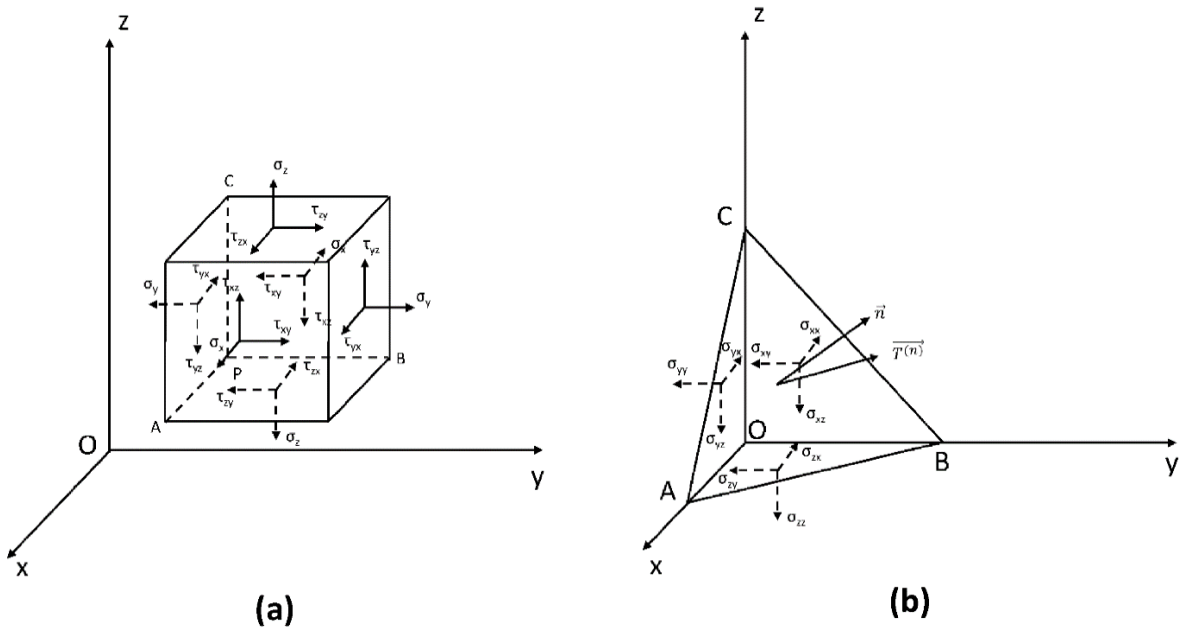

Figure 2.4 (a) Stresses in a Cartesian coordinate system and (b) schematics for derivation of Cauchy's stress tensor

2.2.1.2 Principal stress

Since Cauchy's stress tensor fulfilled the relation described in Eq. (2.3), it can be called a tensor with second order. Thus, this tensor can be represented in a 3 × 3 matrix and has three

principal values and the corresponding directions (Fig. 2.5). In order to estimate the principal stress, characteristic equation of a stress state (Eq. (2.4)) can be used [9].

$$\sigma^3 - I_1\sigma^2 - I_2\sigma - I_3 = 0 \tag{2.4}$$

Where σ is the stress [Pa], I_i is the invariants of the stress tensor [Pa], i = 1, 2, 3.

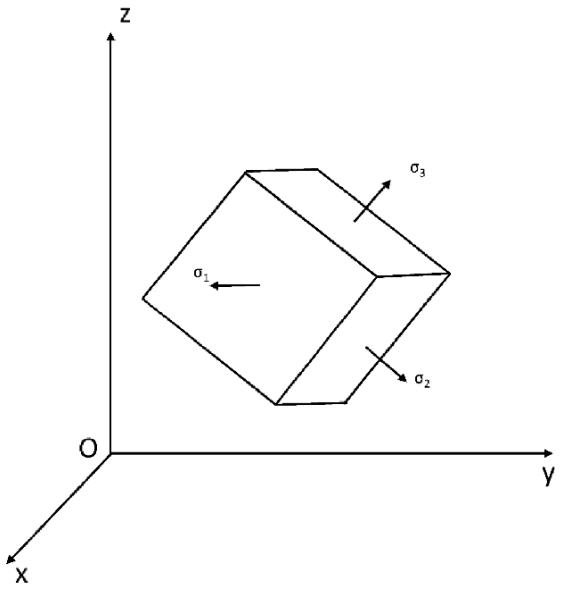

Figure 2.5 Schematics of principal stresses

Three coefficients (I_1, I_2, I_3) also arise in the derivation of the characteristic equation. Since these coefficients do not change with the variation of the coordinate system, they are called the first, second and third invariants of the stress tensor (Eq. 2.5).

$$\begin{aligned} I_1 &= \sigma_{ii} = \sigma_{xx} + \sigma_{yy} + \sigma_{zz} = \frac{\sigma_m}{3} \\ I_2 &= \begin{vmatrix} \sigma_{xx} & \tau_{xy} \\ \tau_{yx} & \sigma_{yy} \end{vmatrix} + \begin{vmatrix} \sigma_{yy} & \tau_{yz} \\ \tau_{zy} & \sigma_{zz} \end{vmatrix} + \begin{vmatrix} \sigma_{zz} & \tau_{zx} \\ \tau_{xz} & \sigma_{xx} \end{vmatrix} \\ &= \sigma_{xx}\sigma_{yy} + \sigma_{yy}\sigma_{zz} + \sigma_{xx}\sigma_{zz} - \tau_{xy}^2 - \tau_{yz}^2 - \tau_{zx}^2 \\ I_3 &= det(\sigma_{ij}) = \sigma_{xx}\sigma_{yy}\sigma_{zz} + 2\tau_{xy}\tau_{yz}\tau_{zx} - \tau_{xy}^2\sigma_{zz} - \tau_{yz}^2\sigma_{xx} - \tau_{xz}^2\sigma_{yy} \end{aligned} \tag{2.5}$$

Where I_i is the invariants of the stress tensor [Pa], i = 1, 2, 3, σ_{ii} is the normal component of the stress vector above the section i, i = x, y, z, τ_{ij} is the shear component of the stress vector above the section i on different axes, i, j = x, y, z and i ≠ j.

Then, the three principal stresses of a stress state can be computed through Eq. (2.6).

$$\begin{cases} \sigma_1 = \frac{1}{3} I_1 + \frac{2}{\sqrt{3}} \sqrt{J_2} \sin\left(\theta + \frac{2}{3}\pi\right) \\ \sigma_2 = \frac{1}{3} I_1 + \frac{2}{\sqrt{3}} \sqrt{J_2} \sin\theta \\ \sigma_3 = \frac{1}{3} I_1 + \frac{2}{\sqrt{3}} \sqrt{J_2} \sin\left(\theta - \frac{2}{3}\pi\right) \end{cases} \tag{2.6}$$

Where σ_i is the principal stress of a stress state [Pa], I_i is the invariants of the stress tensor [Pa], i = 1, 2, 3, J_i is the invariants of the stress deviator tensor [Pa], i = 1, 2, 3, θ is the Lode's angle [°].

In Eq. 2.6 there appears two new coefficients, namely J_2 and θ. Together with J_1 and J_3, J_2 are called the three invariants of stress deviator tensor (Eq. 2.7). Deviatoric stress is related to changes in distortion and plays an important role in the creep process.

$$\begin{aligned} J_1 &= S_{ii} = 0 \\ J_2 &= -\left[\begin{vmatrix} \sigma_{xx} & \tau_{xy} \\ \tau_{yx} & \sigma_{yy} \end{vmatrix} + \begin{vmatrix} \sigma_{yy} & \tau_{yz} \\ \tau_{zy} & \sigma_{zz} \end{vmatrix} + \begin{vmatrix} \sigma_{zz} & \tau_{zx} \\ \tau_{xz} & \sigma_{xx} \end{vmatrix}\right] \\ &= \frac{1}{6}\left[\left(\sigma_{xx} - \sigma_{yy}\right)^2 + \left(\sigma_{yy} - \sigma_{zz}\right)^2 + \left(\sigma_{zz} - \sigma_{xx}\right)^2\right] + \tau_{xy}^2 \\ J_3 &= det\left(S_{ij}\right) = \left(\sigma_{xx} - \sigma_m\right)\left(\sigma_{yy} - \sigma_m\right)\left(\sigma_{zz} - \sigma_m\right) \end{aligned} \tag{2.7}$$

Where J_i is the invariants of the stress deviator tensor [Pa], i = 1, 2, 3, S_{ij} is the component of the stress deviator tensor [Pa], i, i = x, y, z, σ_{ii} is the normal component of the stress vector above the section i, i = x, y, z, τ_{ij} is the shear component of the stress vector above the section i on different axes, i, j = x, y, z and i ≠ j.

θ is the Lode's angle, which is the angle between O'P and O'R in Fig. 2.6. In the principal stress space, P is the point that characterizes a certain stress state, while O'R is between the axes of $\sigma_{1'}$ and $\sigma_{2'}$ and at an angle of 90° to the positive direction of $\sigma_{2'}$.

$$\sin 3\theta = -\frac{3\sqrt{3} J_3}{2\sqrt{J_2^3}} \tag{2.8}$$

Where θ is the Lode's angle [°], J_2 and J_3 are the invariants of the stress deviator tensor [Pa].

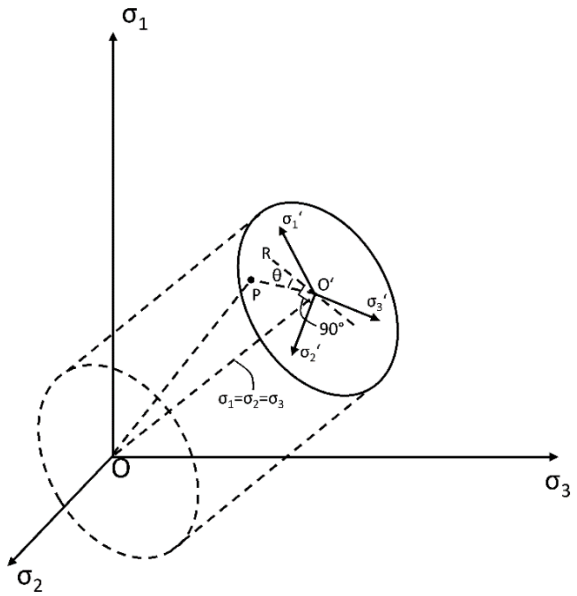

Figure 2.6 Principal stress space and the projection plane

2.2.1.3 Force equilibrium

In addition to the various basic concepts of stress, when solving practical problems, the equilibrium force of a unit body (with a dimension of dx × dy × dz) should need attention too. As described before, Newton's law of motion can be used to solve such a problem. Considering the existence of inertial forces such as the gravity and the acceleration forces, the general form of force equilibrium equations in a Cartesian coordinate is as shown in Eq. (2.9).

$$\begin{cases} \dfrac{\partial \sigma_{xx}}{\partial x} + \dfrac{\partial \tau_{xy}}{\partial y} + \dfrac{\partial \tau_{xz}}{\partial z} + F_x - \rho \dfrac{\partial^2 u}{\partial t^2} = 0 \\ \dfrac{\partial \sigma_{xx}}{\partial x} + \dfrac{\partial \tau_{xy}}{\partial y} + \dfrac{\partial \tau_{xz}}{\partial z} + F_y - \rho \dfrac{\partial^2 v}{\partial t^2} = 0 \\ \dfrac{\partial \sigma_{xx}}{\partial x} + \dfrac{\partial \tau_{xy}}{\partial y} + \dfrac{\partial \tau_{xz}}{\partial z} + F_z - \rho \dfrac{\partial^2 w}{\partial t^2} = 0 \end{cases} \tag{2.9}$$

Where σ_{ii} is the normal component of the stress vector above the section i [Pa], i = x, y, z, τ_{ij} is the shear component of the stress vector above the section i on different axes [Pa], i,

j = x, y, z and i ≠ j, F_i is the component of the force in i direction [N], i = x, y, z, ρ is the density of object [kg/m^3], u, v, w are the components of object's displacement on x, y and z axes [m], t is the time [s].

2.2.2 Strain and geometric equations

In the elasticity and plasticity theories of geomechanics, an intact rock mass is normally treated as continuum. Hence, the displacement (u, v, w) and deformation of the object in x-, y- and z-coordinate directions should be monotonous and derivable both in time and space. Based on this cognition, strain is defined as the relative displacement (deformation) and can be expressed through a strain tensor.

More precisely, in the mechanics there are two theories that concern the strain, one is the infinitesimal stain theory, and the other is the finite strain theory [8]. Since most problems in the geomechanics can be related to small deformation, the infinitesimal strain theory, which considers only the linear part of the displacement gradient (the first-order term of Taylor series), is often applied.

In the infinitesimal strain theory, the deformation of an object can be further divided into three different parts by considering the linear relationship between displacement gradient and the strain [5]. As in a rigid movement the displacements of all the points are constant, the derivative of the displacements should be zero. Thus in this part, the deformation is strain-free. In the second part, namely the stretching/distorting, the deformation is considered as the strain. Since the elongations (parallel to corresponding axis) and the change of angle of the object (Fig. 2.7) are represented by Eq. (2.10), the strain tensor can be defined through Eq. (2.11) and is the symmetric part of the displacement gradient.

$$\begin{cases} AB\colon \dfrac{\partial u}{\partial x}dx, & \dfrac{\partial v}{\partial x}dx, & \angle B'A'B''\colon \tan^{-1}\dfrac{\dfrac{\partial v}{\partial x}dx}{dx\left(1+\dfrac{\partial u}{\partial x}\right)} \\ AC\colon \dfrac{\partial u}{\partial y}dy, & \dfrac{\partial v}{\partial y}dy, & \angle C'A'C''\colon \tan^{-1}\dfrac{\dfrac{\partial u}{\partial y}dy}{dy\left(1+\dfrac{\partial v}{\partial y}\right)} \end{cases} \tag{2.10}$$

$$\varepsilon_{ij} = \begin{pmatrix} \dfrac{\partial u}{\partial x} & \dfrac{1}{2}\left(\dfrac{\partial u}{\partial y}+\dfrac{\partial v}{\partial x}\right) & \dfrac{1}{2}\left(\dfrac{\partial u}{\partial z}+\dfrac{\partial w}{\partial x}\right) \\ \dfrac{1}{2}\left(\dfrac{\partial u}{\partial y}+\dfrac{\partial v}{\partial x}\right) & \dfrac{\partial v}{\partial y} & \dfrac{1}{2}\left(\dfrac{\partial v}{\partial z}+\dfrac{\partial w}{\partial y}\right) \\ \dfrac{1}{2}\left(\dfrac{\partial u}{\partial z}+\dfrac{\partial w}{\partial x}\right) & \dfrac{1}{2}\left(\dfrac{\partial v}{\partial z}+\dfrac{\partial w}{\partial y}\right) & \dfrac{\partial w}{\partial z} \end{pmatrix} \tag{2.11}$$

Where u, v, w are the components of object's displacement on x, y and z axes [m], ε is the strain [-].

The third part is the infinitesimal rotation, which is also strain-free. Simultaneously it satisfies the equality $\omega_{ij} = -\omega_{ji}$. Thus, the infinitesimal rotation is the asymmetric part of the displacement gradient (Eq. 2.12).

$$\omega_{ij} = \begin{pmatrix} 0 & \dfrac{1}{2}\left(\dfrac{\partial u}{\partial y}-\dfrac{\partial v}{\partial x}\right) & \dfrac{1}{2}\left(\dfrac{\partial u}{\partial z}-\dfrac{\partial w}{\partial x}\right) \\ -\dfrac{1}{2}\left(\dfrac{\partial u}{\partial y}-\dfrac{\partial v}{\partial x}\right) & 0 & \dfrac{1}{2}\left(\dfrac{\partial v}{\partial z}-\dfrac{\partial w}{\partial y}\right) \\ -\dfrac{1}{2}\left(\dfrac{\partial u}{\partial z}-\dfrac{\partial w}{\partial x}\right) & -\dfrac{1}{2}\left(\dfrac{\partial v}{\partial z}-\dfrac{\partial w}{\partial y}\right) & 0 \end{pmatrix} \tag{2.12}$$

Where u, v, w are the components of object's displacement on x, y and z axes [m], ω is the rotation angle [-].

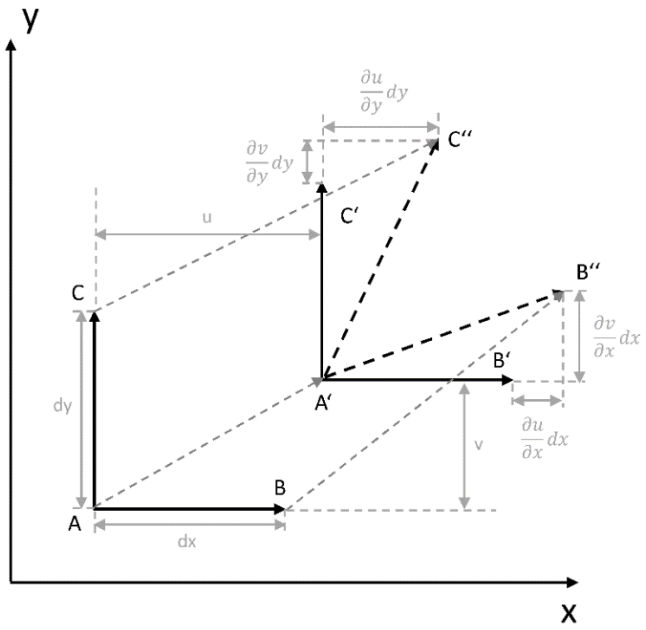

Figure 2.7 Schematics of the infinitesimal straines

2.2.3 Geomechanical constitutive models

Although the deformation in a rock mass is caused by the stress change, the force equilibrium equations and the geometric equations are not enough to obtain the stress, the strain and the displacement field. In other words, since the way that the stress induces the strain is different for different rocks, an additional relationship called constitutive model is essential for describing these behaviors.

At the same time, the induced strain can be reversible, irreversible and sometimes even time-dependent. For this reason, according to different mechanisms, a total strain increment can be divided into four parts, i.e. the elastic strain increment ε^{el}, the plastic strain increment ε^{pl}, the viscous strain increment ε^{v} and the thermal strain increment ε^{th} (Eq. 2.13 and Fig. 2.8).

$$\varepsilon = \varepsilon^{el} + \varepsilon^{pl} + \varepsilon^{v} + \varepsilon^{th} \tag{2.13}$$

Where ε is the total strain increment [-], ε^{el} is the total strain increment [-], ε^{pl} is the total strain increment [-], ε^{v} is the total strain increment [-], ε^{th} is the total strain increment [-].

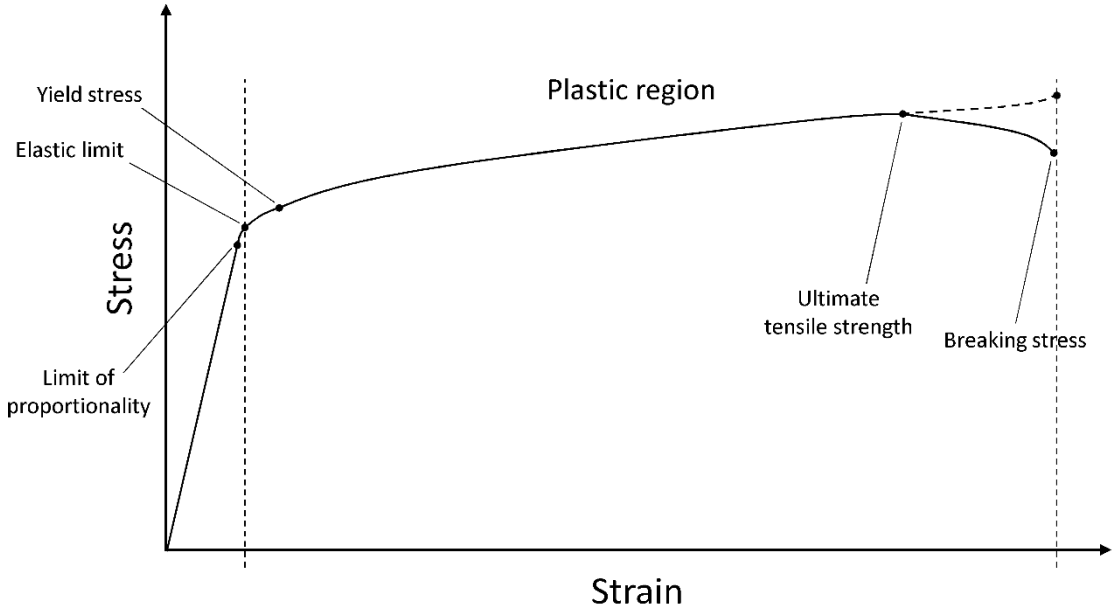

Figure 2.8 Principal stress space and the projection plane

The relationship of stress and strain can be derived from the stress-strain curves that are attained from the various mechanical tests.

2.2.3.1 Elastic models

As shown in Fig. 2.8, when the load of a rock mass is under its yield strength, the relationship between stress and strain can be described by the elastic theory. Since deformation in elasticity is reversible and happens instantaneously when the stress changes, Hooke's law was developed to characterize the behavior of an isotropic linear elastic material.

$$\begin{cases} \varepsilon_{xx} = \dfrac{1}{E}\left[\sigma_{xx} - \upsilon\left(\sigma_{yy} + \sigma_{zz}\right)\right], \;\; \varepsilon_{xy} = \dfrac{\tau_{xy}}{2G} \\ \varepsilon_{yy} = \dfrac{1}{E}\left[\sigma_{yy} - \upsilon(\sigma_{xx} + \sigma_{zz})\right], \;\; \varepsilon_{yz} = \dfrac{\tau_{yz}}{2G} \\ \varepsilon_{zz} = \dfrac{1}{E}\left[\sigma_{zz} - \upsilon\left(\sigma_{xx} + \sigma_{yy}\right)\right], \;\; \varepsilon_{zx} = \dfrac{\tau_{zx}}{2G} \end{cases} \tag{2.13}$$

Where ε_{ii} is the normal and shear component of the strain vector above the section i on different axes [-], i, j = x, y, z, σ_{ii} is the normal component of the stress vector above the section i [Pa], i = x, y, z, τ_{ij} is the shear component of the stress vector above the section

i on different axes [Pa], i, j = x, y, z and i ≠ j, E is the Young's modulus [Pa], ν is the Poisson's ratio [-], G is the shear modulus [Pa].

2.2.3.2 Plastic models

When the load conditions reach to the yield strength, permanent and path-dependent deformations that are caused by micro fractures etc. begin to appear in the object. These nonlinear parts of strain are also referred to as plastic strain. Different models in plasticity theory usually use two functions to describe the process of plastic strain, one is the yield function, and the other is the flow rule (Eq. 2.14 and Eq. 2.15).

$$f^s = \sigma_1 - \sigma_3 N_\phi + 2c\sqrt{N_\phi} \tag{2.14}$$

$$g^s = \sigma_1 - \sigma_3 N_\psi \tag{2.15}$$

Where f^s is the shear yield function based on the criterion of Mohr-Coulomb [Pa], σ_1 and σ_3 are the maximum and minimum principal stresses of a stress state [Pa] respectively, $N_\phi = (1 + \sin\phi)/(1 - \sin\phi)$ and ϕ is the friction angle [°], c is the cohesion [Pa], g^s is the potential function of shear flow in Mohr-Coulomb's theory [Pa], $N_\psi = (1 + \sin\psi)/(1 - \sin\psi)$ and ψ is the dilation angle [°].

Among them, the yield function defines the stress combination when plastic flow takes place. It can be represented by one or more limiting surfaces in a generalized stress space (Fig. 2.9), and the points below or above these surfaces are considered to characterize the stress state that initiates elastic or plastic deformation. The flow rule specifies that the direction of the plastic strain increment vector is normal to the potential surface. If its potential function is coincident with the yield function, the two functions are called associated, otherwise they are called non-associated.

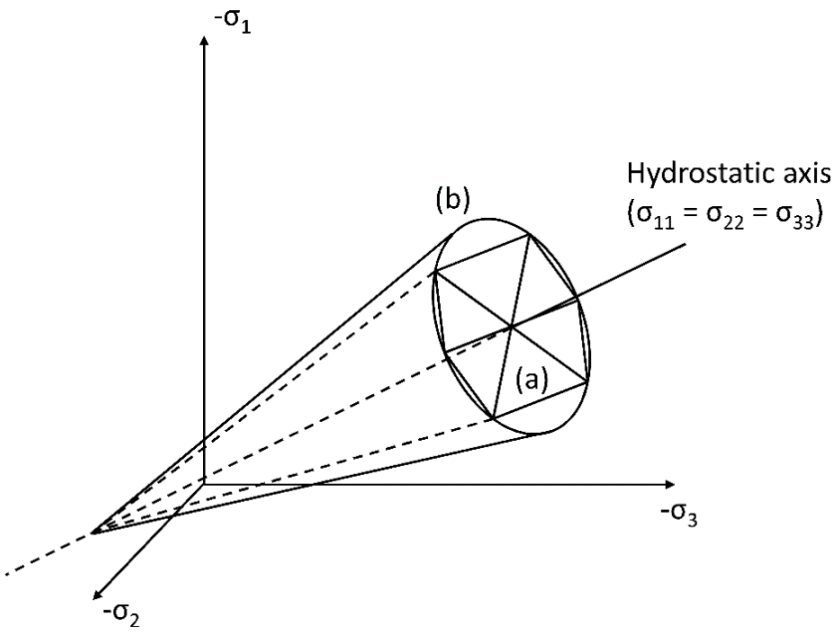

Figure 2.9 Limiting surfaces of the Yield functions of (a) the Mohr-Coulomb's criterion and (b) the Druck-Prager's criterion in a generalized stress space

2.2.4 Fracture mechanics

Fracture mechanics is a branch of solid mechanics. It was originally developed, in order to describe the material's destruction process in the area of engineering. Since the fracture processes also occur in the geological processes, corresponding mechanics is now often applied in the earth and geotechnical science. Like elasticity and plasticity theories, there have been various theories in the development to explain the mechanisms of fracture. The two most well-known ones are proposed by Griffith and Irwin.

2.2.4.1 Griffith's theory based on energy concept

Two important keywords in Griffith's theory are "release" and "absorption" of energy. In the work of 1921 [10], in order to evade the problem of stress' singularity at the fracture tip, Griffith proposed a theory (of fracture mechanics) based on the concept of energy. Through this theory, the influences of crack have been taken into account since the beginning of the fracture process.

To have a better understanding of this theory, the concept of deformation energy should firstly be grasped. The deformation energy means that when a system (e.g. an element in a model) undergoes deformation, part of the outer work will be converted into a form of energy and stored in the system, mathematically it can be calculated through Eq. 2.16 [11].

$$U_d = \int_{\Omega} U_0 d\Omega \tag{2.16}$$

Where U_d is the deformation energy [J], U_0 is the density of deformation energy [J/m^3], Ω is the boundary of the system.

In Griffith's theory, if the release rate of system's potential energy is larger than the increase rate of surface energy, fracture will be in an unstable state. In other words, fracture will continue to propagate. For this reason, it can be understood that generation of the fracture can lead to a reduction in the system's potential energy. When object achieves an equilibrium state, the release rate of potential energy becomes 0 and the system possesses a minimum potential energy.

To illustrate above issues, Zhou gave a more practical example in his dissertation of 2014 [12]. As shown in Fig. 2.10, an object obtains a fracture with the length of a, when it suffers a load of stress σ. Then, if the red area around the fracture is considered to be completely unloaded, the total energy released during this process is:

$$U = -\frac{\sigma^2}{2E} n a^2 \tag{2.18}$$

Where U is the release energy [J], σ is the stress due to load [Pa], E is the Young's modulus [Pa], n is the geometric constant [-], a is the fracture length [m].

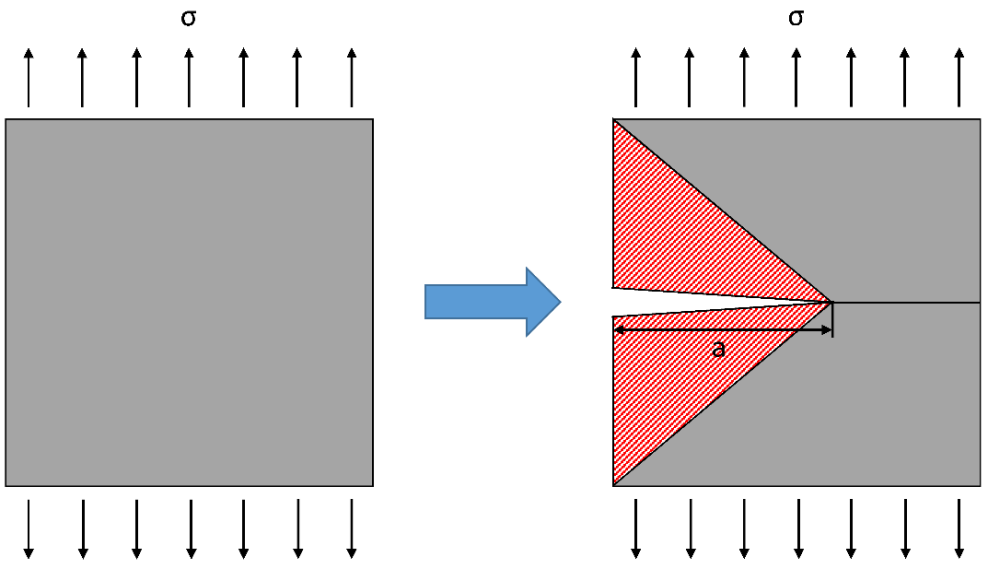

Figure 2.10 A plain under tensile stress to obtain a fracture

The essential energy to generate new fracture surface can be obtained by Eq. 2.19. Then the total energy change can be computed through Eq. 2.20. E would get a minimum value, when the system achieves an equilibrium state.

$$U_n = 2\gamma_0 a \tag{2.19}$$

$$\Delta E_{total} = 2\gamma_0 a - \frac{\sigma^2}{2E} n a^2 \tag{2.20}$$

Where U_n is the dissipated energy to yield new fracture surface [J], γ_0 is the density surface energy [J/m^2], a is the fracture length [m], ΔE_{total} is the change of total energy [J], σ is the stress due to load [Pa], E is the Young's modulus [Pa], n is the geometric constant [-].

2.2.4.2 Irwin's stress intensity factor

Griffith has introduced the energy concept to the analysis of fracture's propagation successfully. However, his work is entirely based on the elastic mechanics. Therefore its application is only limited to the so-called "ideal brittle materials", i.e. the stress-strain relationship of these materials remain elastic until the fracture occurs. For the more complex influences from the plasticity of the materials, in the work of Irwin [13], Irwin proposed stress intensity factor based on the different fracture types to deal with corresponding problems.

In Irwin's theory, it should be clear that the stress intensity factor is the only physical quantity that needs to be determined to characterize the stress field at the edge of the fracture. In other words, the stress field's distributions for each type of the fracture are the same. Its value depends entirely on the stress intensity factor K_i. Thus, to have a better understanding of K_i, the types of simple fractures must be introduced.

Irwin divided simple fractures into three different types (Fig. 2.11). The type I represents the case that, when the fracture surface suffers a tensile load perpendicular to itself, its movement will be in the same direction. For this reason, it is also called the open type.

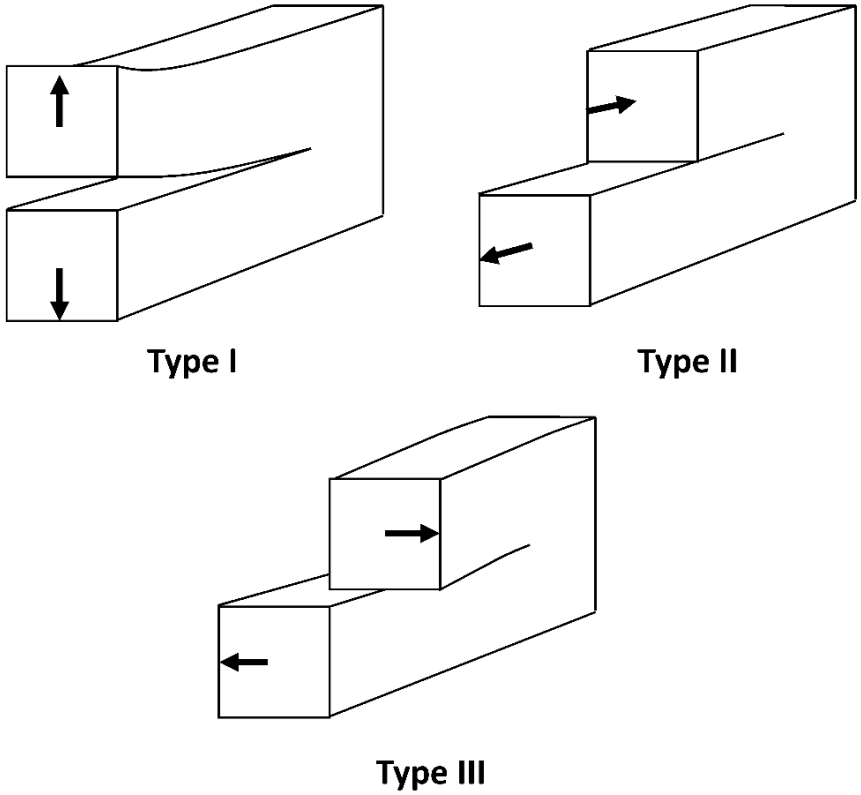

Figure 2.11 Three different types of simple fracture

Eq. 2.21 gives a solution to the stress field around the right edge of a pure Type I fracture (Fig. 2.12), which was illustrated in the work of Bertram in 2008 [14].

$$\begin{cases} \sigma_{xx} = \dfrac{K_I}{\sqrt{2\pi r}} \cos\dfrac{\varphi}{2}\left(1 - \sin\dfrac{\varphi}{2}\sin\dfrac{3\varphi}{2}\right) \\ \sigma_{yy} = \dfrac{K_I}{\sqrt{2\pi r}} \cos\dfrac{\varphi}{2}\left(1 + \sin\dfrac{\varphi}{2}\sin\dfrac{3\varphi}{2}\right) \\ \tau_{xy} = \dfrac{K_I}{\sqrt{2\pi r}} \cos\dfrac{\varphi}{2}\sin\dfrac{\varphi}{2}\cos\dfrac{3\varphi}{2} \end{cases} \quad (2.21)$$

Where σ_{xx} and σ_{yy} are the normal stress in x- and y-direction respectively [Pa], K_I is the stress intensity factor of fracture type I [Pa•m$^{1/2}$], r is the distance between studied element and edge of the fracture [m], φ is the angle between x-direction and direction of the studied element (from fracture edge) [°], τ_{xy} is the shear stress in xy-plane [Pa].

The resulted deformation in the x and y directions can be calculated through Eq. 2.22.

$$\begin{cases} u_d = \dfrac{K_I}{4G}\sqrt{\dfrac{r}{2\pi}}\left[(2k-1)\cos\dfrac{\varphi}{2} - \cos\dfrac{3\varphi}{2}\right] \\ v_d = \dfrac{K_I}{4G}\sqrt{\dfrac{r}{2\pi}}\left[(2k+1)\cos\dfrac{\varphi}{2} - \cos\dfrac{3\varphi}{2}\right] \end{cases} \quad (2.22)$$

Where u_d is the displacement of studied element in x-direction [m], K_I is the stress intensity factor of fracture type I [Pa•m$^{1/2}$], G is the shear modulus [Pa], r is the distance between studied element and edge of the fracture [m], φ is the angle between x-direction and direction of the studied element (from fracture edge) [°], v_d is the displacement of studied element in y-direction [m].

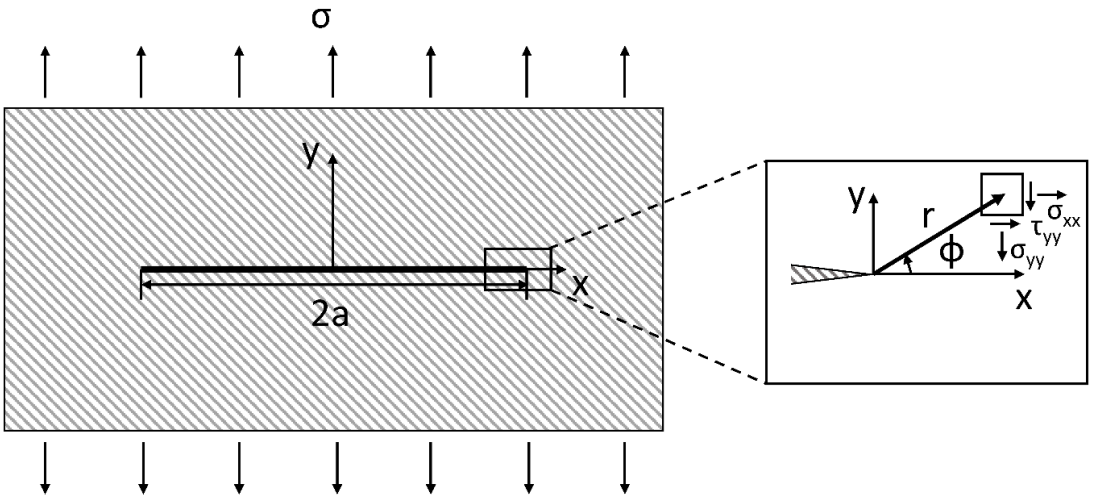

Figure 2.12 A pure type I fracture and the local polar coordinate system at fracture's edge

When the fracture suffers a shear load and therefore experiences a slip movement, it is called a shear fracture. In the type II, fracture possesses a load parallel to the shear direction, so it is called an in-plane shear fracture (the stress and displacement field can be computed through Eq. 2.23). Fracture of type III does not have load with above characteristics, thus it is called an out-of-plane or anti-plane shear fracture.

$$\begin{cases} \sigma_{xx} = -\dfrac{K_{II}}{\sqrt{2\pi r}}\sin\dfrac{\varphi}{2}\left(2+\cos\dfrac{\varphi}{2}\cos\dfrac{3\varphi}{2}\right) \\ \sigma_{yy} = -\dfrac{K_{II}}{\sqrt{2\pi r}}\cos\dfrac{\varphi}{2}\sin\dfrac{\varphi}{2}\cos\dfrac{3\varphi}{2} \\ \tau_{xy} = \dfrac{K_{II}}{\sqrt{2\pi r}}\cos\dfrac{\varphi}{2}\left(1-\sin\dfrac{\varphi}{2}\sin\dfrac{3\varphi}{2}\right) \\ u_d = \dfrac{K_{II}}{4G}\sqrt{\dfrac{r}{2\pi}}\left[(2k+3)\sin\dfrac{\varphi}{2}+\sin\dfrac{3\varphi}{2}\right] \\ u_d = \dfrac{K_{II}}{4G}\sqrt{\dfrac{r}{2\pi}}\left[(2k-2)\cos\dfrac{\varphi}{2}+\cos\dfrac{3\varphi}{2}\right] \end{cases} \tag{2.23}$$

Where σ_{xx} and σ_{yy} are the normal stress in x- and y-direction respectively [Pa], K_{II} is the stress intensity factor of fracture type II [Pa•m$^{1/2}$], r is the distance between studied element and edge of the fracture [m], φ is the angle between x-direction and direction of the studied element (from fracture edge) [°], τ_{xy} is the shear stress in xy-plane [Pa], u_d is the displacement of studied element in x-direction [m], G is the shear modulus [Pa], v_d is the displacement of studied element in y-direction [m].

Since the stress intensity factor is a certain physical quantity for particular fracture types, its value does not depend on the radius r and the angle φ. For the fractures from type I to type III the stress intensity factors can be computed through Eq. 2.24.

$$\begin{cases} K_I = \lim\limits_{r\to 0}\sigma_{yy}(r,\varphi=0)\sqrt{2\pi r} \\ K_{II} = \lim\limits_{r\to 0}\tau_{xy}(r,\varphi=0)\sqrt{2\pi r} \\ K_{III} = \lim\limits_{r\to 0}\tau_{zy}(r,\varphi=0)\sqrt{2\pi r} \end{cases} \tag{2.24}$$

Where K_I is the stress intensity factor of fracture type I [Pa•m$^{1/2}$], σ_{yy} is the normal stress in y-direction [Pa], r is the distance between studied element and edge of the fracture [m], φ is the angle between x-direction and direction of the studied element (from fracture edge)

[°], K_{II} is the stress intensity factor of fracture type II [Pa•m$^{1/2}$], τ_{xy} is the shear stress in xy-plane [Pa], K_{III} is the stress intensity factor of fracture type III [Pa•m$^{1/2}$], τ_{zy} is the shear stress in zy-plane [Pa].

2.2.4.3 Fracture propagation and its orientation

As mentioned in the theories of Griffith and Irwin, fracture within an object will expand, when certain conditions are met. In practical applications, in order to determine the extension and its direction more easily, several criteria have been summed up.

Maximum circumferential stress criterion

The maximum circumferential stress criterion narrates two phenomenon: a) the fracture will propagate, when the maximum circumferential stress exceeds the critical stress; b) the direction of propagation is perpendicular to the maximum circumferential stress.

Since the maximum circumferential stress is also a principal stress, there is no shear stress in this direction. Thus, the maximum circumferential stress can be obtained through Eq. 2.25.

$$\sigma_{\varphi\varphi} = \frac{1}{\sqrt{2\pi r}}\left[K_I cos^3\frac{\varphi_0}{2} - 3K_{II}cos^2\frac{\varphi_0}{2}sin\frac{\varphi_0}{2}\right] = \frac{K_I^{eq}}{\sqrt{2\pi r}} \tag{2.25}$$

Where $\sigma_{\varphi\varphi}$ is the maximum circumferential stress [Pa], r is the distance between studied element and edge of the fracture [m], K_I is the stress intensity factor of fracture type I [Pa•m$^{1/2}$], φ is the angle between x-direction and direction of the studied element (from fracture edge) [°], K_{II} is the stress intensity factor of fracture type II [Pa•m$^{1/2}$], K_I^{eq} is the equivalent stress intensity factor of fracture type I [Pa•m$^{1/2}$].

Maximum energy release rate criterion

Another important criterion is the maximum energy release rate criterion. It is slightly different from that of the maximum circumferential stress. This criterion also recounts two phenomenon: a) the fracture will propagate, when the maximum energy release rate exceeds the critical rate; b) direction of expansion is the same as the maximum release rate.

Since the energy release rate of a fracture (length = Δa) after its propagation in $\theta = \theta^0$ can be described through Eq. 2.26, and if Δa is infinitesimal small, the stress field can be assumed to be tending to the one before propagation (see Eq. 2.27), this criterion is derived to have the form of Eq. 2.28.

$$G_{er} = \frac{\mathrm{K}_I^2}{E^*} + \frac{\mathrm{K}_{II}^2}{E^*} \tag{2.26}$$

$$\begin{cases} \lim\limits_{\Delta a \to 0} \sigma_{\varphi\varphi|\varphi=0} = \sigma_{\varphi\varphi|\varphi=\varphi_0} \\ \lim\limits_{\Delta a \to 0} \tau_{r\varphi|\varphi=0} = \tau_{r\varphi|\varphi=\varphi_0} \end{cases} \tag{2.27}$$

$$\mathrm{G}_{er}^{(*)} = \frac{\mathrm{K}_I^{2(*)}}{E^*} \geq \mathrm{G}_{er}^{C} \tag{2.28}$$

Where G_{er} is the energy release rate [J/m^2], K_I is the stress intensity factor of fracture type I [Pa•m$^{1/2}$], $E^* = E$ for plane stress state and is equal to = $\frac{E}{1-\nu^2}$ for plane strain state [Pa], K_{II} is the stress intensity factor of fracture type II [Pa•m$^{1/2}$], φ is the angle between x-direction and direction of the studied element (from fracture edge) [°], r is the distance between studied element and edge of the fracture [m].

Crack open displacement (COD) criterion

Above criteria are all based on the linear elastic mechanism. For this reason, although they have considered the stress concentration near tip, the solution to stress singularity is still physically not reasonable. Thus, a criterion named crack opening displacement (COD) was developed. This criterion narrates one phenomena: the propagation executes after the present COD exceeding the critical COD (Eq. 2.29). Since the plastic flow has carried out around the tip and leaded to a small opening in the tip area, this characterization is considered to be reliable.

$$\delta \geq \delta_c \tag{2.29}$$

Where δ is the crack opening displacement [m], δ_c is the critical crack opening displacement [m].

At the same time, in order to overcome the singularity problem at the tip, Dugdale [15] and Barenblatt [16] proposed a cohesive zone model in their articles. This model defined two different fracture tips: a) a physical one where the cohesive traction is null and b) a mathematical one where the fracture opening is null (see Fig. 2.13). With these characterizations, the critical crack opening displacement δ_c can be calculated through the cohesive energy G_c (Eq. 2.30). When the present COD has exceeded the critical one, all of the cohesive energy in the cohesive zone will be dissipated. Thereafter, material loses all its strength in this area and tip turns to be stress-free.

$$G_c = \frac{1}{2}\sigma_{nc}\delta_c h \tag{2.30}$$

Where G_c is the cohesive energy [J], σ_{nc} is the critical stress [Pa], δ_c is the critical crack opening displacement [m], h is the thickness [m].

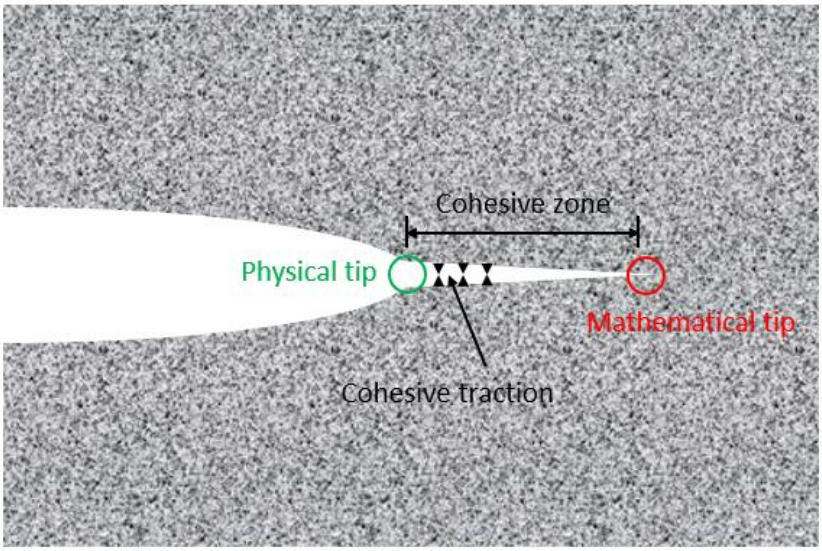

Figure 2.13 Cohesive zone and traction at the fracture tip

2.3 Fluid flow in the reservoir stimulation

Fluid's movement is another important process in the reservoir stimulation. Depending on involved domains, it can be further classified into three types, namely: a) the fluid flow

within generated fracture; b) the fluid flow in porous formation matrices; and c) the interactive flow between them. Since the flowing process is driven by pressure gradient within and between different domains, it possesses strong impacts on the change of pore pressure and effective stress and thereby affects the stress distribution in the rock formation. For this reason, implementation of corresponding theories is essential.

2.3.1 Navier-Stokes and mass conservation equations

Before further introducing the specific methods to calculate fluid motion in different domains, some more basic equations should firstly be referred. One of these is the Navier-Stokes equations.

The main purpose of Navier-Stokes equations, which are derived from the momentum conservation, is to describe the relationship between pressure change and dissipative viscous force or rather gravity in the flow field. With the assumption that the studied fluid is incompressible (the applied fluid in conventional hydraulic fracturing can be assumed to be incompressible) and it possesses a uniform density, Navier-Stokes equations could be simplified to have the form of Eq. 2.31.

$$\begin{cases} \rho_f\left(\frac{\partial v_{fx}}{\partial t}+v_{fx}\frac{\partial v_{fx}}{\partial x}+v_{fy}\frac{\partial v_{fx}}{\partial y}+v_{fz}\frac{\partial v_{fx}}{\partial z}\right)=\mu\left[\frac{\partial^2 v_{fx}}{\partial x^2}+\frac{\partial^2 v_{fx}}{\partial y^2}+\frac{\partial^2 v_{fx}}{\partial z^2}\right]-\frac{\partial P}{\partial x}+\rho_f g_x \\ \rho_f\left(\frac{\partial v_{fy}}{\partial t}+v_{fx}\frac{\partial v_{fy}}{\partial x}+v_{fy}\frac{\partial v_{fy}}{\partial y}+v_{fz}\frac{\partial v_{fy}}{\partial z}\right)=\mu\left[\frac{\partial^2 v_{fy}}{\partial x^2}+\frac{\partial^2 v_{fy}}{\partial y^2}+\frac{\partial^2 v_{fy}}{\partial z^2}\right]-\frac{\partial P}{\partial y}+\rho_f g_y \\ \rho_f\left(\frac{\partial v_{fz}}{\partial t}+v_{fx}\frac{\partial v_{fz}}{\partial x}+v_{fy}\frac{\partial v_{fz}}{\partial y}+v_{fz}\frac{\partial v_{fz}}{\partial z}\right)=\mu\left[\frac{\partial^2 v_{fz}}{\partial x^2}+\frac{\partial^2 v_{fz}}{\partial y^2}+\frac{\partial^2 v_{fz}}{\partial z^2}\right]-\frac{\partial P}{\partial z}+\rho_f g_z \end{cases} \quad (2.31)$$

Where ρ_f is the density of fluid [kg/m^3], v_{fi} is the velocity of fluid in different directions [m/s] with i = x, y, z, t is time [s], μ is viscosity [Pa•s], P is the fluid pressure [Pa], g_i is the gravity acceleration in different directions [m/s^2] with i = x, y, z.

At the same time, the mass transport in flow field should follow the principle of mass conservation as well. That is, the increased or decreased amount of mass in the observed infinitesimal small space must come from the difference between the incoming and outgoing

flow. Based on this thinking, the mass conservation equation was derived to have the form of Eq. 2.32.

$$\frac{\partial(\rho_f v_{fx})}{\partial x} + \frac{\partial(\rho_f v_{fy})}{\partial y} + \frac{\partial(\rho_f v_{fz})}{\partial z} + \frac{\partial \rho_f}{\partial t} + Q_f = 0 \tag{2.32}$$

Where ρ_f is the density of fluid [kg/m^3], v_{fi} is the velocity of fluid in different directions [m/s] with i = x, y, z, t is time [s], Q_f is the source of fluid [kg/(m^3•s)].

2.3.2 Fluid flow in a fracture

In the hydraulic fracturing that possesses a main fracture, the 3D flow in fracture can normally be approximated by some lower-dimensional problems, e.g. the fluid flow in the main fracture is analog to the flow between two parallel planes (Fig. 2.14). Thus, if the applied fluid is considered to execute a steady, incompressible and laminar flow without gravitational effects, Navier-Stokes equations in the fracture channel can be simplified to have the form of Eq. 2.33.

$$\frac{\partial P}{\partial x} = \mu \frac{\partial^2 v_{fx}}{\partial y^2} \tag{2.33}$$

Where P is the fluid pressure [Pa], μ is the viscosity [Pa•s], v_{fx} is the velocity of fluid in x-direction [m/s].

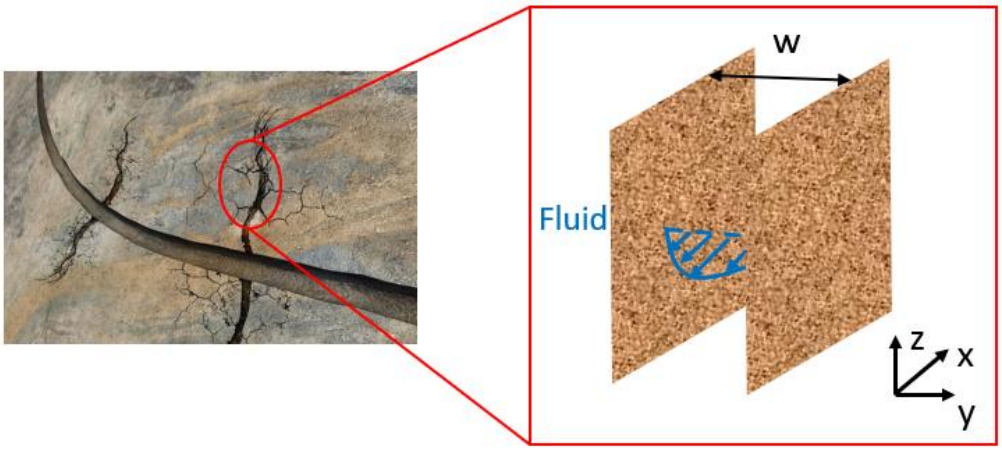

Figure 2.14 Approximation of the fracture flow field to the fluid flow between two parallel planes

Further, integrating Eq. 2.33 and considering a non-slip condition, Zimmermann et al. [17] derived the cubic law in their article (Eq. 2.34). This law describes the flow rate in the cross section perpendicular to the flow direction.

$$\mathrm{Q}_f = -\frac{\mathrm{w}^2}{12\mu}\frac{\partial P}{\partial x} \tag{2.34}$$

Where Q_f is the flow rate [m^3/s], w is the fracture width [m], μ is the viscosity [Pa•s], P is the fluid pressure [Pa].

2.3.3 Fluid flow in porous mediums

In the period from 1852 to 1855, Darcy has summed up Darcy's law through experimental research [18] (Eq. 2.35). Since then, after years of development, Darcy's equation has become the most basic and important theory in the calculation of infiltration.

$$v_f = -\frac{k_f}{\mu}\frac{\partial \mathrm{P}}{\partial i} \tag{2.35}$$

Where v_f is the flow rate of fluid [m/s], k_f is the permeability related to fluid [m^2], μ is the viscosity [Pa•s], P is the fluid pressure [Pa].

In the hydraulic fracturing, the infiltration process within the intact rock formation is considered to be in good agreement with the Darcy law. Thus, bringing Darcy equation into Eq. 2.32 while still considering the fluid as homogeneous and incompressible, Eq. 2.36 can be obtained.

$$\frac{\partial^2 P}{\partial x^2} + \frac{\partial^2 P}{\partial y^2} + \frac{\partial^2 P}{\partial z^2} = 0 \tag{2.36}$$

Where P is the fluid pressure [Pa].

2.3.4 Mass transport in fluid

In addition to the above-described several processes, in the hydraulic fracturing for oil and gas reservoirs it is often necessary to add additional solid proppant so that the artificial

fracture can still obtain sufficient permeability after the fluid being lost. For research purposes, the corresponding process should also be modeled in study.

Considering that the solid proppant moving with fluid is mainly affected by following effects, namely the diffusive, advection and settling effects, by using the superposition principle the total transport velocity can be described by Eq. 2.37 [19].

$$v_p = v_{dp} + v_{fp} + v_{sp} = -D_p \frac{\partial C}{\partial i} + k_{wc} v_f + f(F_{grav}, F_{buoy}, F_{drag}) \tag{2.37}$$

Where v_p is the total transport velocity of proppant [m/s], v_{dp} is the diffusive velocity of proppant [m/s], v_{fp} is the advection velocity of proppant [m/s], v_{sp} is the settling velocity of proppant [m/s], D_p is the diffusivity of proppant [m^2/s], C is the volumetric concentration of proppant [-], k_{wc} is the coefficient to describe the advection effects [-], v_f is the flow rate of fluid [m/s], F_{grav} is the gravitational force [N], F_{buoy} is the buoyancy force [N], F_{drag} is the drag force [N].

2.4 Heat transport in the reservoir stimulation

Apart from the geomechanical and hydraulic processes, the heat transport in reservoir stimulation and its resulted changes in material properties should also be considered in the research. Unlike hydraulic process, heat transport in an operation is mainly characterized according to different transport mechanisms. For this reason, several heat transport theories would be introduced in this section.

2.4.1 Heat conduction

The mechanism of heat conduction mainly concerns the heat transport driven by temperature gradient within the system (Fig. 2.15). In order to describe the process mathematically, the heat flow equation (Eq. 2.38) [20], the continuity condition (Eq. 2.39) [21] and the thermal constitutive equation of materials (Eq. 2.40) [22] are integrated.

$$q_i = -\lambda \frac{\partial T}{\partial i} \tag{2.38}$$

$$-\left(\frac{\partial q_x}{\partial x}+\frac{\partial q_x}{\partial x}+\frac{\partial q_x}{\partial x}\right)+q_v=\frac{\partial H}{\partial t} \tag{2.39}$$

$$\frac{\partial H}{\partial t}=\rho c_v\frac{\partial T}{\partial t} \tag{2.40}$$

Where q_i is the heat flow in the i direction [W/m^2] with $i = x, y, z$, λ is the thermal conductivity [W/(m·°C)], T is the temperature [°C], q_v is the heat source of volume [W/m^3], H is the stored heat per unit volume [J/m^3], ρ is the density [kg/m^3], c_v is the specific heat capacity [J/(kg·°C)].

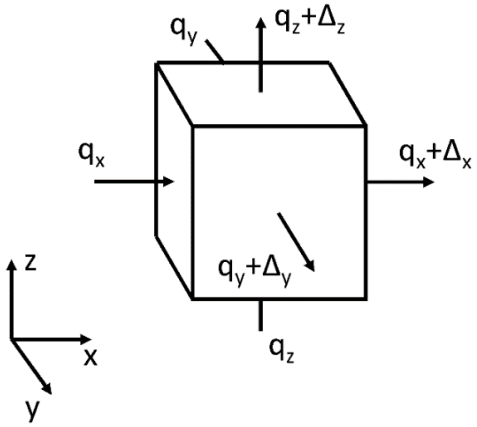

Figure 2.15 Unit volume with inflow and outflow of heat

The integral result is the heat conduction equation (Eq. 2.41).

$$\lambda\frac{\partial^2 T}{\partial x^2}+\lambda\frac{\partial^2 T}{\partial y^2}+\lambda\frac{\partial^2 T}{\partial z^2}+q_v=\rho c_v\frac{\partial T}{\partial t} \tag{2.41}$$

Where λ is the thermal conductivity [W/(m·°C)], T is the temperature [°C], q_v is the heat source of volume [W/m^3], ρ is the density [kg/m^3], c_v is the specific heat capacity [J/(kg·°C)].

2.4.2 Solid-fluid heat exchange

The second mechanism describes the convective heat exchange between flowing fluid (in fracture) and solid rock formation (Fig. 2.16). This is a process in which two systems with different phases exchange thermal energy. Although the driving force is still the temperature gradient, the intensity of heat exchange could be influenced by several other factors, including the rate of fluid flow and the surface roughness of the fracture walls. However, all the

influencing factors can also be taken into account through an overall convective heat transfer coefficient, as described by Eq. (2.42) [23].

$$q_n = h(T_s - T_e) \tag{2.42}$$

Where q_n is the heat flux component normal to the boundary in the direction of the exterior normal [W/m^2], h is the convective heat-transfer coefficient [W/(m·°C)], T_s is the temperature at the surface of the solid body [°C], T_e is the temperature of the surrounding fluid [°C].

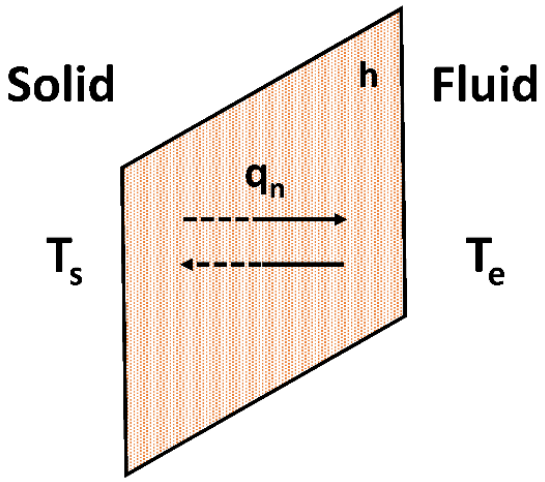

Figure 2.16 Convective heat exchange between the flowing fluid and the solid mass.

2.5 Numerical methods for implementing the theoretical models

To transfer various THM theories from mathematical equations to numerical tools of modeling, different numerical methods need to be adopted. As most of the THM equations are partial differential equations (PDEs) of second order, depending on the number of eigenvalues of their coefficient matrices A, the PDEs of second order could firstly be classified into three different types: a) for the elliptical form, A can only have non-zero eigenvalues; b) if the equation is the parabolic form, at least one eigenvalue of A is 0; c) in the hyperbolic form, one eigenvalue is larger than 0, while all the others are smaller than 0. Then, with the help of Finite Difference Method (FDM) and Finite Volume Method (FVM), the equations of elliptical form can be solved numerically. Additionally, adopting the Explicit and Implicit Euler method, the parabolic FDEs with time derivative of can also be solved.

2.5.1 Finite Difference Method and Finite Volume Method

2.5.1.1 Finite Difference Method

The FDM method is proposed to solve the boundary value problems of elliptical PDEs. Its main thought is that, when the discrete interval is small enough, the differential quotient on the observed point can be approximated through the difference quotient (Eq. 2.43 and Fig. 2.17 (a)) [24]. In this way, a differential equations system is converted into a linear equations system. Since the central difference quotient of y'' on the point x_i is $(y_{i+1}-2y_i+y_{i-1})/h^2$ (Fig. 2.17 (b)), i.e. the difference quotient of $(y_i-y_{i-1})/h$ and $(y_{i+1}-y_i)/h$, the approximation also fits the definition of second derivative.

$$\frac{dy}{dx} = \lim_{\Delta x \to 0} \frac{\Delta y}{\Delta x} \approx \frac{\Delta y}{\Delta x} \tag{2.43}$$

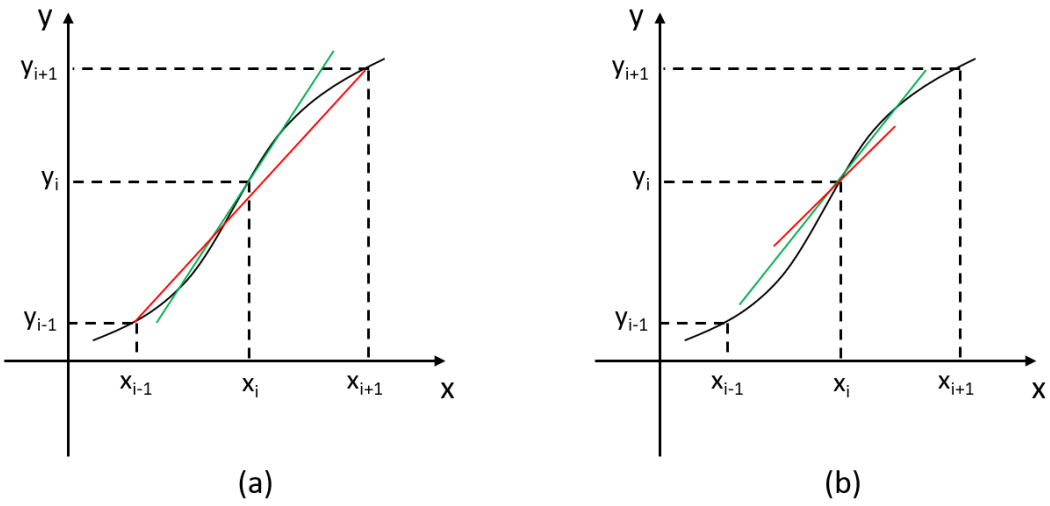

Figure 2.17 Central difference quotient of a) y' and b) y''

Because the general form of elliptical PDEs is actually Eq. 2.44, conducting FDM in 2D situation becomes essential. As shown in Fig. 2.18, Ω is the study area in numerical calculation. T = ∂Ω denotes the boundary, on which the value of u is given in a boundary value problem.

$$\frac{\partial^2 u}{\partial x^2} + \frac{\partial^2 u}{\partial y^2} = f(u, x, y) \tag{2.44}$$

In the solution of FDM, Ω is discretized by a grid with equi-distance (Fig. 2.21, where $x_{i+1} - x_i = h$ and $y_{i+1} - y_i = h$). Then the unknowns are only $u_{i,j}$ with the coordinate of (x_i, y_i). Considering an observed point (central point of a subzone) and its four ambient points, the differential quotient of second derivative (in x- and y-direction respectively) could be approximated through Eq. 2.45 and Eq. 2.46. Thus, bringing these equations to Eq. 2.44 for all the central points, a linear equations system formed by Eq. 2.47 can be obtained.

$$\frac{\partial^2 u}{\partial x^2} = \frac{u_{i+1,j} - 2u_{i,j} + u_{i-1,j}}{h^2} \tag{2.45}$$

$$\frac{\partial^2 u}{\partial y^2} = \frac{u_{i,j+1} - 2u_{i,j} + u_{i,j-1}}{h^2} \tag{2.46}$$

$$\frac{u_{i+!,j} + u_{i,j+1} + u_{i-1,j} + u_{i,j-1} - 4u_{i,j}}{h^2} = f(u_{i,j}, x_i, y_j) \tag{2.47}$$

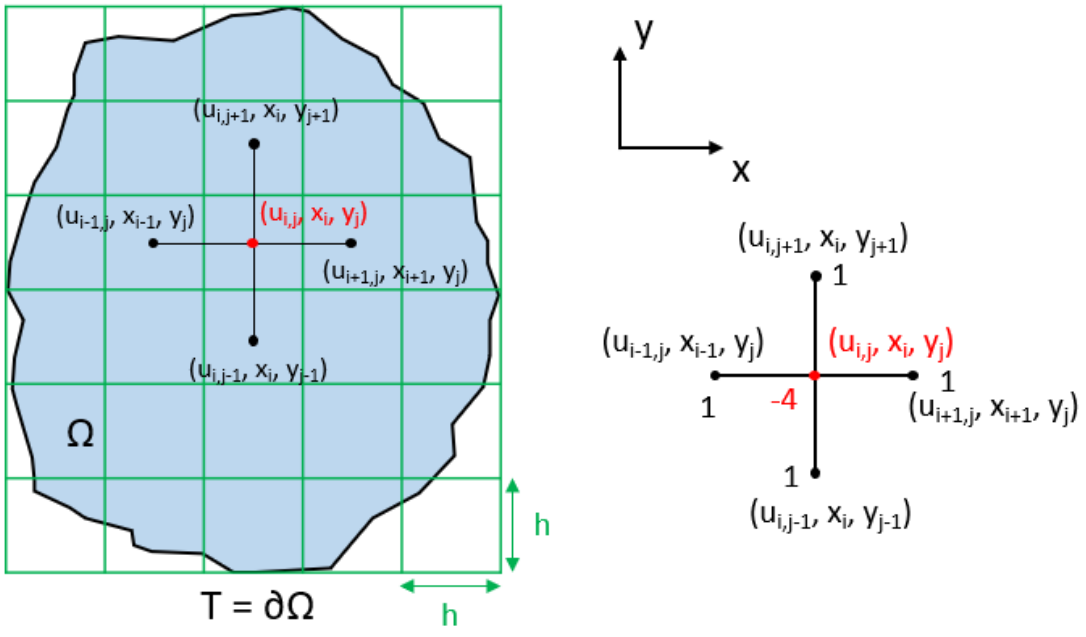

Figure 2.18 Discretization of the observed zone and derivation of the difference quotient

2.5.1.2 Finite Volume Method

The FVM method is another method to solve the boundary value problems. However, its procedure is different from that of the FDM.

In this method a concept of control volume is raised [24]. That means, for each study point there is an associated surrounding surface (2D) or volume (3D) called "control surface/volume" (see Fig. 2.19, the area enclosed by blue lines). Thus, when Eq. 2.44 is integrated over the control volume, the integration becomes Eq. 2.48.

$$\iint_{v_i} \Delta u(x,y)dxdy = \oint_{\Gamma_i} grad\, u(x,y) \cdot \vec{n} ds = \iint_{v_i} f(x,y)dxdy \tag{2.48}$$

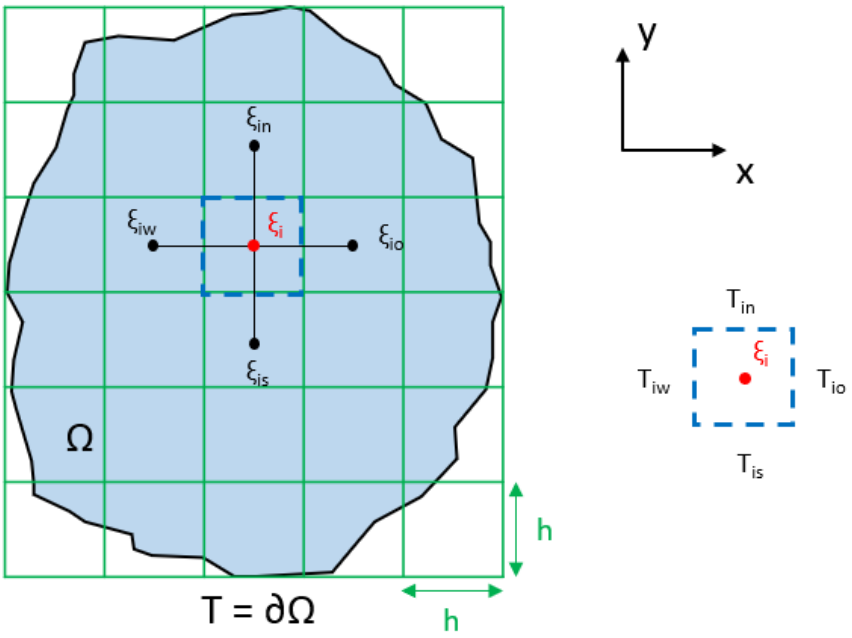

Figure 2.19 Central difference quotient of a) y' and b) y"

Further, performing the boundary integral for Eq. 2.48 (Eq. 2.49) and introducing the approximations described by Eq. 2.50 and 2.51. Another linear equations system formed by Eq. 2.52 was obtained.

$$\oint_{\Gamma_i} grad\, u(x,y) \cdot \vec{n} ds = -\int_{\Gamma_{iw}} u_x^{iw} - \int_{\Gamma_{is}} u_y^{is} + \int_{\Gamma_{io}} u_x^{io} + \int_{\Gamma_{in}} u_y^{in} \tag{2.49}$$

$$\int_{\Gamma_{ij}} u_x^{ij} \approx h u_x \left(\frac{\xi_i + \xi_{ij}}{2} \right) \approx h \frac{u(\xi_i) - u(\xi_{ij})}{h} = u(\xi_i) - u(\xi_{ij}) \tag{2.50}$$

$$\iint_{v_i} f(x,y)dxdy \approx h^2 f(\xi_i) \tag{2.51}$$

$$u(\xi_{iw}) + u(\xi_{in}) + u(\xi_{is}) + u(\xi_{io}) - 4u(\xi_i) = h^2 f(\xi_i) \tag{2.52}$$

2.5.2 Explicit and Implicit Euler Methods

The methods to solve elliptical PDEs have been introduced in 2.5.1. However, it is still not enough to perform the numerical modeling in reservoir stimulation. Since e.g. the heat transport equation in the simulation is actually a parabolic PDE with time variable and can be handled separately with spatial and temporal derivative, i.e. a differential equation with temporal derivative and an elliptical PDE with spatial derivative (Eq. 2.53 and Fig. 2.20), two methods, namely the Explicit (Forward) and Implicit (Backward) Euler methods are proposed to complete the time-related calculations.

$$\frac{\partial u}{\partial t} = \sum_{j,k=1}^{m} b_{jk} \frac{\partial^2 u}{\partial x^j \partial x^k} + \sum_{i=1}^{n} b_j \frac{\partial u}{\partial x^j} + bu + g = Eu + g \tag{2.53}$$

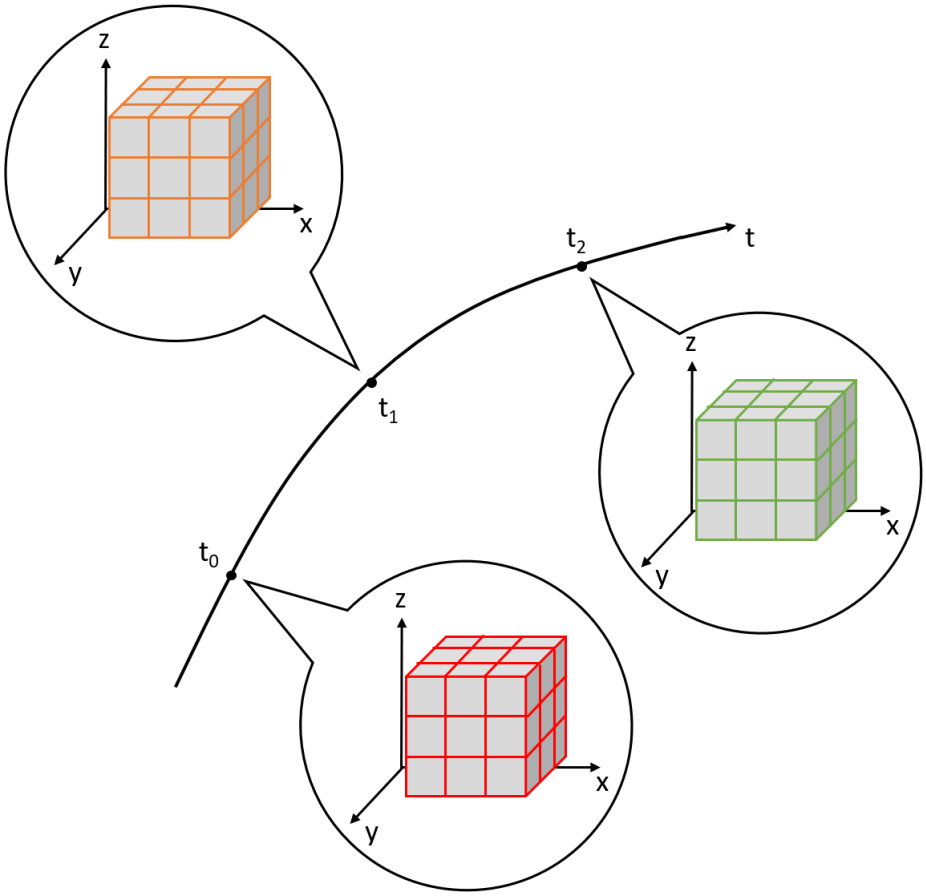

Figure 2.20 Graphical representation of the spatial and temporal discretization

2.5.1.1 Explicit Euler Method

The Explicit Euler method is also known as the Forward Euler method. In Buthcer's work of 2003 [25] it was described through following 1D example: a particle is supposed to have a movement in one dimension. At the time point t it possesses a position of y_t and a velocity of v_t. Since the velocity is assumed to have no significant change in an infinitesimal small time period, the position change is approximately equal to the time duration multiplying the velocity (Eq. 2.54).

$$y_{t+1} = y_t + ((t+1) - 1)v_t \tag{2.54}$$

$$v_t = f'(t, y_t) \tag{2.55}$$

If the motion of the particle is governed by a differential equation, i.e. the velocity v_t is a function of time t and position y_t (Eq. 2.55), the parabolic PDE could have a general form of Eq. 2.56 by applying the Explicit Euler method.

$$u_{t+1} = u_t + \Delta t \cdot E u_t + \Delta t \cdot g(t) \tag{2.56}$$

2.5.2.2 Implicit Euler Method

The Implicit Euler method is also known as the Backward Euler method. In comparison with the explicit one, it can be used to solve some more stiff PDEs. This method is called implicit, since no explicit equations will be given to calculate u_{t+1}. Instead, a matrix that describes the interactions between each element must be solved in this method. Such a solution endows the method another advantage, namely this method is more stable when a large time step is applied. A general form of Implicit Euler method can be given through Eq. 2.57.

$$u_{t+1} = u_t + \Delta t \cdot f(t, u_{t+1}) \tag{2.57}$$

2.6 Simulation concept for modeling the coupled THM processes in reservoir stimulation

All the theoretical basis of mechanical, hydraulic and thermal calculations have been introduced. Additionally, different numerical methods to implement them into the simulators are also explained. For the concrete modeling, their coupled equations would be numerically solved using different simulation concepts/frameworks, e.g. in this thesis two sets of simulation codes, namely FLAC3D^{plus} and TOUGH2MP-FLAC3D, have been adopted.

Although these different concepts work differently, however, they can still be described by a uniform flow chart (Fig. 2.21). 1) The geometric model for carrying out the simulation must firstly be constructed. The construction tools can be FLAC3D, ANSYS or other appropriate programs; 2) After that, the mechanical, hydraulic or rather thermal parameters

for defining the initial and boundary conditions should be imported using different documents. The formats depend on the types of simulation codes (TOUGH2MP or FLAC3D); 3) As all the preparation works have been finished, the simulation can be executed under different frameworks (FLAC3D^{plus} or TOUGH2MP-FLAC3D). Because of different domains, the simulations in each module can be further divided into three parts, i.e. the part in the fracture, the part in the formations and the part modeling of interaction between them.

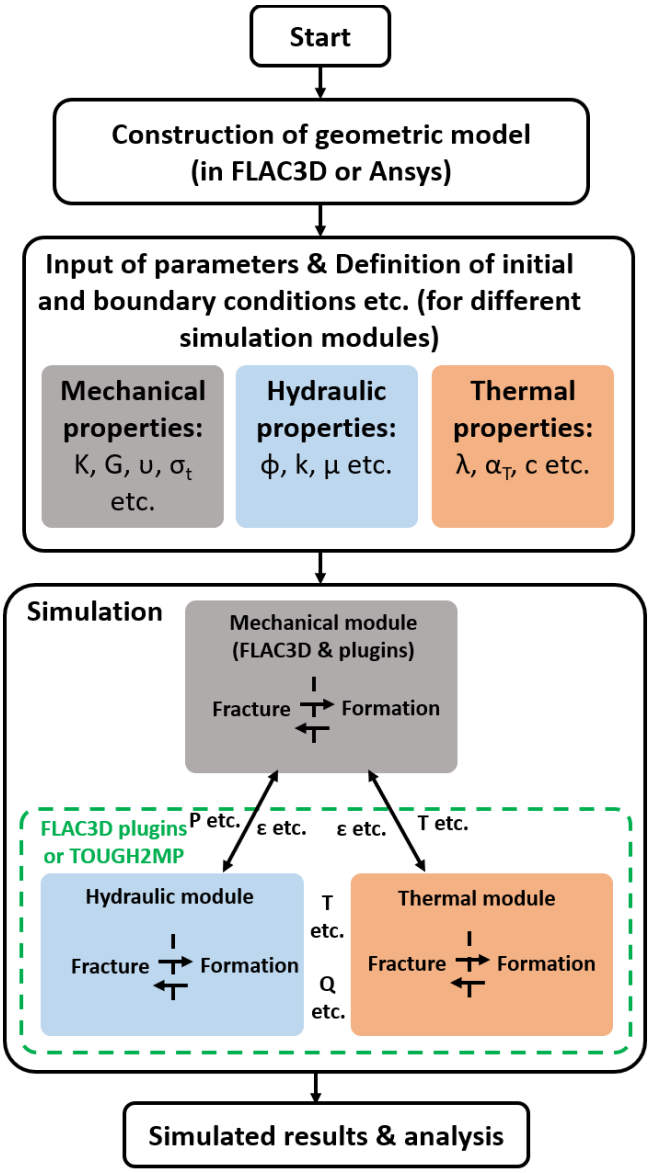

Figure 2.21 Numerical modeling concept

3 Numerical study of the fluid viscosity's influences on shaping of a stimulated fracture in tight sandstone in consideration of thermal effects and THM coupled processes

As the world's energy consumption increases and the climate changes, exploitation of unconventional energy resources, including tight gas/oil, shale gas/oil and the geothermal energy stored in the deep tight reservoirs, has become crucial issue [26]. However, in contrast with conventional resources, unconventional energy resources are usually located in a complex, hypotonic geological environment (Fig. 3.1). Tight gas, for example, which is an important type of unconventional energy resource, has reservoirs possessing extremely low porosity and permeability (usually below 0.1 mD) [27, 28]. Therefore, it is generally difficult to attain economical production from these energy sources without stimulation operations.

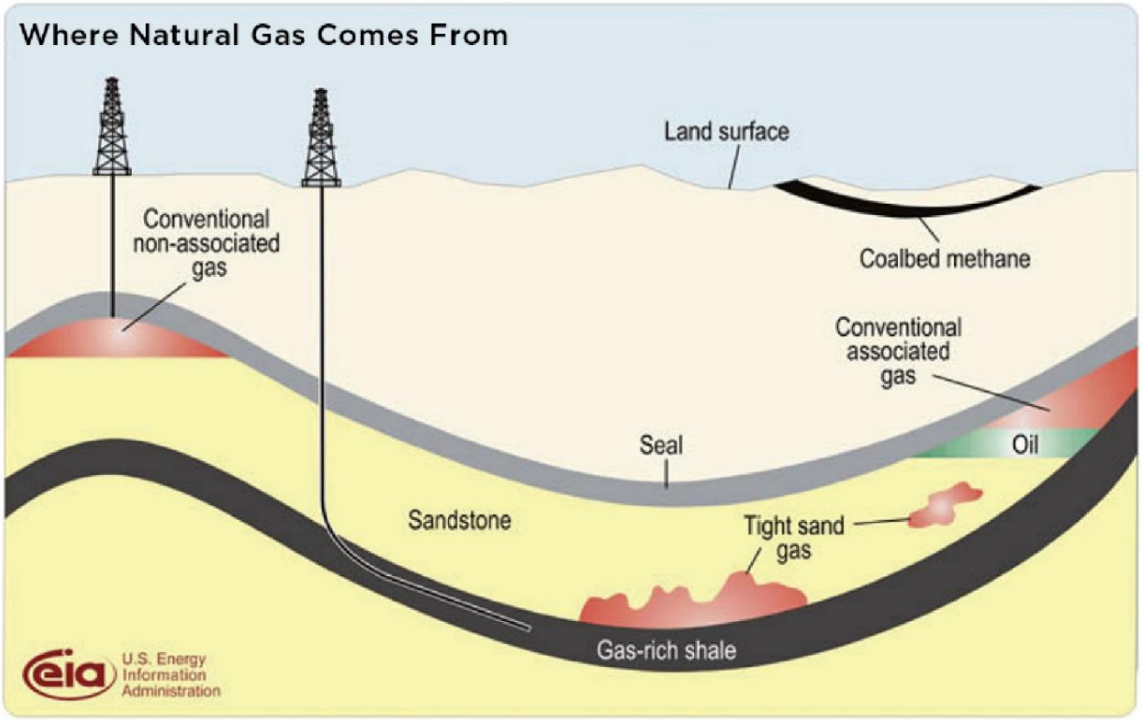

Figure 3.1 Graphical presentation of differences between conventional and unconventional gas reservoirs (source: ucsusa.com)

3.1 Overview of the modeling methods for a hydraulic fracturing and the influences from fluid's viscosity

Hydraulic fracturing is an engineering multi-process method used for stimulating the economic production of energy carriers from unconventional resources. This technique has become indispensable to the exploitation of natural gas from tight gas reservoirs. In its appropriate operation, both pressurized fluid and solid proppants are used in order to achieve increased reservoir permeability, which is absolutely necessary to obtain a reasonable production from target reservoirs. However, the new method of modeling will be crucial for improving safety, efficiency and the prediction of the consequential negative effects of hydraulic fracturing technology. Its success relies mainly on the rapid development of computer techniques in the numerical simulation.

In order to model the complete operation accurately, the process of hydraulic fracturing should first be analyzed. Hydraulic fracturing in a tight gas reservoir conventionally comprises the following physical processes: a) mechanical deformation induced by pressure changes in the reservoir fractures and pores; b) fluid flow within fractures and formation matrices (including their interactions); c) fracture propagation; and d) proppant transport (and settling) inside the fractures [29]. In addition, the influence of the thermal process should be taken into account. In an attempt to describe the process of fracture creation, propagation and proppant transport, a series of models has been developed since the 1950s which are comprehensively reviewed in the works of several authors including Zhou et al. [29], Perkins and Kern [30], Nordgren [31], Khristianovic and Zheltov [32], Geertsma and de Klerk [33], Adachi et al. [34], Barree and Conway [35], Gadde et al. [36], Gadde and Sharma [37], Liu [38], Hsu et al. [39]. Since most of the previous models are unable to represent the real processes, Zhou and Hou [40] formulated a set of models to characterize fracture propagation and proppant transport more realistically. In the recent past, they have also developed calculation modules, which are based on their new models, for FLAC3D simulators [29, 40].

However, for a long time the influences of fluid's viscosity on shaping of the stimulated fracture have not been studied systematically. As a medium for the pressure's transmission and a carrier for the proppant, this property of a fluid would certainly impact the operation's results uncommonly (see Fig. 3.2). In this chapter, the direct (due to the frictional force within the fluid and within the fracture) and indirect (due to impacts on the leak off) influences of fluid's viscosity will be investigated and described in detail. Additionally, its impacts on influencing the distribution of proppant will also be studied.

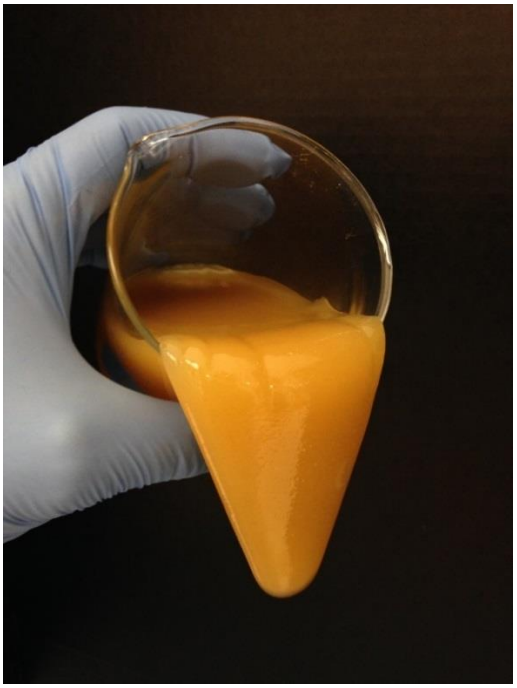

Figure 3.2 HiBrine^{TM}-XL High TDS-Based Fracturing Fluid (source: www.inno-spesinc.com)

3.2 Implemented models in FLAC3D^{plus} for modeling the hydraulic fracturing

FLAC3D is a numerical simulator that is widely used in the petroleum industry. As a basis for the simulation, numerical method FDM (Finite Difference Method) is implemented in this simulator. Since its original goals were to replicate problems in geotechnical engineering and water conservancy, mechanical processes (quasi-static and dynamic), hydraulic processes and thermal processes including their coupling effects are also considered [40].

However, the intrinsic calculation modules in FLAC3D are not as practical for the petroleum industry, especially for hydraulic fracturing. Hence, the need for further development of simulation program is indeed, such as FLAC3D^{plus}. Apart from this, although the existing thermal modules in FLAC3D were all developed for modeling thermal effects in porous medium, none of them possess the appropriate functionality to simulate the thermal processes within a fracture and between the fracture and the surrounding formations. Thus, an improved thermal module was embedded in the simulator.

3.2.1 Governing equations for HM module

The theoretical basis, verifications and practical applications of the HM (hydraulic and mechanical) modules have already been elaborated in the previous article by Zhou et al. [40]. Hence, this section predominantly aims at briefly introducing the governing equations used in the HM module.

3.2.1.1 Mechanical deformation

As introduced in Zhou's work [29], the mechanical part of FLAC3D was implemented in their new HM-module to model the corresponding effects in stimulation process. Among them, the key point is to solve the force equilibrium equation (Eq. 3.1), the continuum equation (Eq. 3.2) and the constitutive equation (Eq. 3.3, namely Hooke's law) altogether.

$$\sigma_{ij,j} + \rho_m \left(b_i - \frac{dv_i}{dt} \right) = 0 \tag{3.1}$$

$$\Delta\varepsilon_{ij} = \frac{1}{2}\left(\frac{\partial \Delta u_i}{\partial i} + \frac{\partial \Delta u_j}{\partial j} \right) \tag{3.2}$$

$$\Delta\sigma' = D\Delta\varepsilon \tag{3.3}$$

Where σ is the total stress [Pa] and $\sigma = \sigma' + \alpha I P_p$, σ' is the effective stress [Pa], α is the Biot coefficient [-], I is the unit matrix, P_p is the pore pressure [Pa], ρ_m is the rock density [kg/m^3], b_i is the volumetric acceleration [m/s^2] with $i = x, y, z$, v_i is the velocity of the rock mass

[m/s] with $i = x, y, z$, t is the time [s], ε is the strain [-], u_i and u_j are the displacements [m] with $i, j = x, y, z$, D is the physical matrix.

When it comes to the solid-liquid two phase flow in fracture, including the liquid flow in formation matrices, the processes would be calculated through the secondary developed code.

3.2.1.2 Fracture propagation and determination of fracture width

The fracture in FLAC3D^{plus} is assumed to be an aperture between two parallel plates perpendicular to the minimum horizontal stress (Fig. 3.3). Meanwhile it is considered a single fracture in modeling. According to the results obtained in the preceding experiments, e.g. which was in the work of Casas et al. in 2006 [41], the measured data during micro seismic events (as observed in the work of Dinske et al. in 2010 [42]) and the numerical simulation in the heterogeneous rock formations (for instance, in Zhou's dissertation in 2014 [12]) show conformity, and the assumptions therein are considered to be reliable. So, in FLAC3D^{plus} the tensile failure criterion was used to determine fracture propagation (Eq. 3.4) [40].

$$P_f > \sigma_3 - \sigma_t \tag{3.4}$$

Where P_f is the fluid pressure in the fracture [Pa], σ_3 is the minimum principal stress [Pa], σ_t is the tensile strength [Pa].

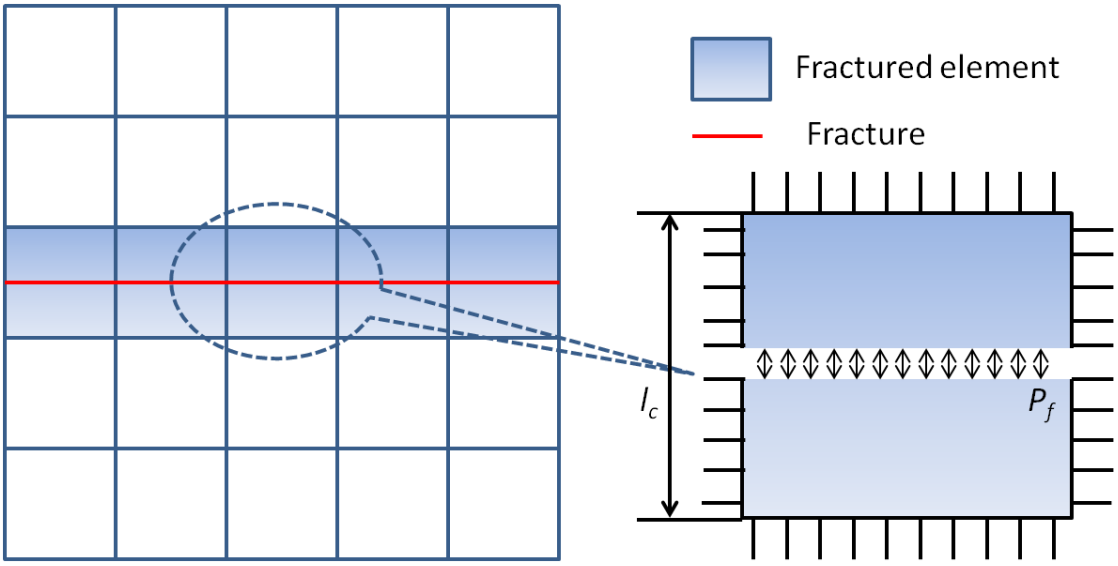

Figure 3.3 Demonstration of the fracture element [29]

When the fracture has propagated, an extra strain increment (induced by pressure change in the fracture) is added to the total strain increment to characterize the discontinuous behavior of fracture (Eq. 3.4). Therefore, the influences from the proppant are also considered.

$$\Delta\varepsilon_f = \frac{\mathrm{P}_f(t+1) + \sigma_{con}(t) + \sigma_n(t)}{a_1} \tag{3.4}$$

Where ε_f is the strain induced by the change of fluid pressure in fracture [-], P_f is the fluid pressure in the fracture [Pa], σ_n is the normal stress perpendicular to the fracture [Pa], σ_{con} is the contact stress [Pa] with

$$\begin{cases} \sigma_{con}(t+1) = 0 & if\ C \le C_{max}\ and\ w \ge w_{res} \\ \sigma_{con}(t+1) = \sigma_{con}(t) + \alpha_1 \cdot \Delta\varepsilon_0 & if\ C > C_{max}\ or\ w < w_{res} \end{cases}.$$

3.2.1.3 Solid-liquid two phase flow in fracture

Proppant concentration and diameter also influence the flowing of slurry. Firstly, FLAC3D^{plus} uses the model developed by Eissa et al. (Eq. 3.5) [43] to describe the relationship between slurry viscosity and proppant concentration, since the injected slurry in the fracture is a mixture of fluid and solid proppant. The equation of average velocity (Eq. 3.6), based on the study by Zimmerman et al. [17], is then implemented to characterize slurry flow in fracture. In Eq. 3.7 the influence of fracture aperture, pressure gradient, slurry density variation and apparent slurry viscosity are all taken into consideration.

$$\mu_a = \mu_0 \left(1 - \frac{C}{C_{max}}\right)^{-a} \frac{tan^{-1}\left(\frac{\gamma}{\gamma_L}\right)^{n-1}}{tan^{-1}\left(\frac{\gamma}{\gamma_H}\right)^{n-1}} \tag{3.5}$$

$$v_s = -\frac{w^2}{12\mu_a}\frac{\partial\left(P_f + \rho_f g z\right)}{\partial x} \tag{3.6}$$

$$w\left(Q_{inje.} + Q_{leak}\right) + \frac{\partial w}{\partial t} = \nabla \cdot \left[\frac{w^3}{12\mu_a}\nabla\left(P_f + \rho_f g z\right)\right] \tag{3.7}$$

Where μ_a is the apparent viscosity [Pa·s], μ_0 is the liquid viscosity [Pa·s], C is the proppant concentration [kg/m^3], C_{max} is the maximum proppant concentration [kg/m^3], a is the correlation coefficient [-], γ is the apparent shear rate [1/s], γ_L and γ_H are the parameters [1/s], n

is the power law coefficient [-], v_s is the slurry velocity [m/s], w is the fracture width [m], μ_a is the apparent viscosity [Pa·s], P_f is the fluid pressure in fracture [Pa], ρ_f is the fluid density [kg/m^3], g is the gravity acceleration [m/s^2], z is the elevation [m], t is the time [s], Q_s is the source [1/s], $Q_{inje.}$ is the injection source [1/s], Q_{leak} is the leak off source [1/s].

To describe the proppant transport, the mass conservation equation (Eq. 3.8) [Zhou et al. 2017] has been used. In this case, proppant velocity is calculated by using the model introduced by Gadde et al. [36], Gadde and Sharma [37], and Liu [38].

$$\frac{\partial(Cw)}{\partial t} + \nabla \cdot \left(Cv_p w\right) + wC_{inje}Q_{inje} = 0 \tag{3.8}$$

Where C is the proppant concentration [%], w is the fracture width [m], t is the time [s], v_p is the proppant velocity [m/s], C_{inje} is the proppant injection concentration [%], $Q_{inje.}$ is the injection source [1/s].

3.2.1.4 Fluid flow in rock matrices

Interactions between the fracture and the formation pores cause leak off. Thus, FLAC3D^{plus} uses the method introduced by Eq. (3.9) to describe the infiltration process. In this method Darcy's stationary flow between fracture and formation would be presumed for each time step.

$$Q_{leak}^{t+1} = \frac{K_m S}{\mu V_i} f\left(P_p^t - P_f^t\right) \tag{3.9}$$

Where Q_{leak} is the leak off source [1/s], K_m is the permeability of the matrix [m^2], S is the exchange area [m^2], μ is the viscosity [Pa·s], V_i is the volume of the element [m^3], f is the infiltration coefficient [1/s], P is the pressure [Pa] with p denotes "pore pressure in matrix", f denotes "fracture pressure".

3.2.2 Governing equations for heat transport

Heat transport mechanisms and corresponding governing equations have been introduced in details in 2.4. For the new thermal module of FLAC3D^{plus} these theories are implemented

in the codes using the FVM and Implicit Euler methods. Therefore, in this section the equations will not be repeated.

3.2.3 THM coupled processes

In addition to the thermal processes mentioned before, interactions between the mechanical, hydraulic and thermal processes have been considered in the improved module as well. Fig. 3.4 shows the interactions between the three THM coupled processes including their corresponding state parameters. The coupling between the mechanical and hydraulic processes (HM) has been exhaustively explained elsewhere in 3.2.1. Thus, in this section only the TH- and TM-couplings will be introduced and elucidated.

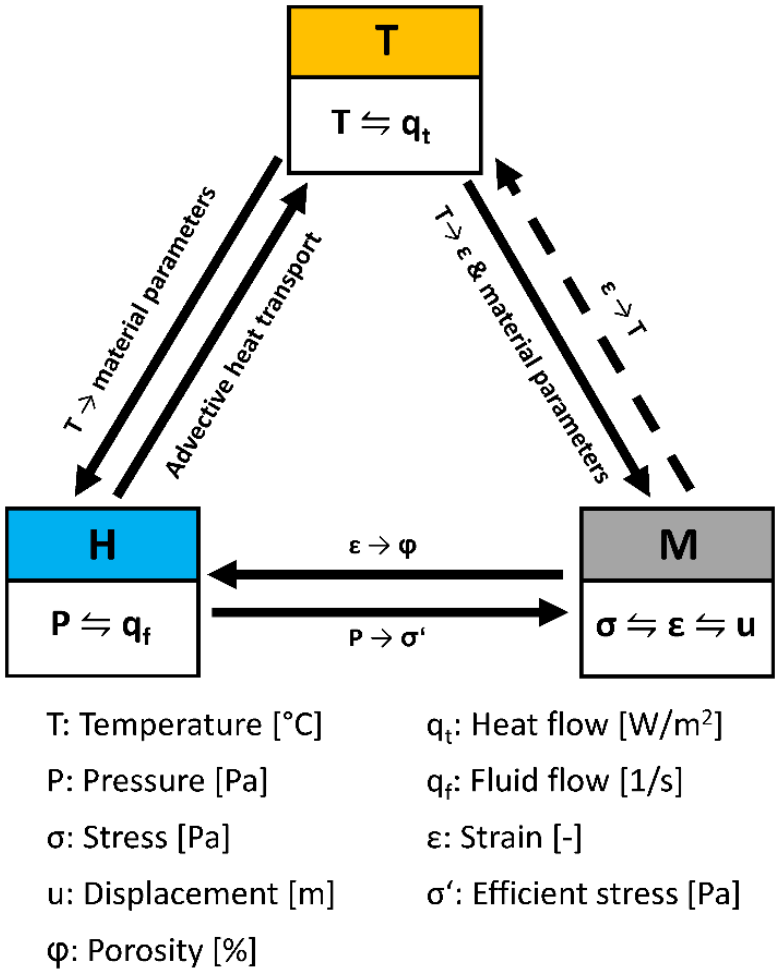

Figure 3.4 THM interactions in hydraulic fracturing

3.2.3.1 Advective heat transport

In the improved module, the influence of advective heat transport and temperature on the material properties is considered separately. The heat carried by the flowing fluid as it enters and leaves the corresponding element is considered here to be the heat inflow and outflow, respectively. Thus, the heat transport through conduction and advective processes is described by Eq. 3.10.

$$\lambda\frac{\partial^2 T}{\partial x^2}+\lambda\frac{\partial^2 T}{\partial y^2}+\lambda\frac{\partial^2 T}{\partial z^2}+\rho c_V v_x\frac{\partial T}{\partial x}+\rho c_V v_y\frac{\partial T}{\partial y}+\rho c_V v_z\frac{\partial T}{\partial z}+q_v=\rho c_V\frac{\partial T}{\partial t} \qquad (3.10)$$

Where λ is the thermal conductivity [W/(m·°C)], T is the temperature [°C], ρ is the density [kg/m^3], c_v is the specific heat capacity [J/(kg·°C)], v_i is the fluid flow velocity in the i direction [m/s], $i = x, y, z$, q_v is the heat source of volume [W/m^3].

3.2.3.2 Influences from the thermal stress

In the framework of the new thermal module, not all coupled processes are considered. The coupling between heat transport and mechanical process is considered as a one-way process. This means that the heat transfer may be coupled to the thermal stress calculation at any time during the transient simulation (Eq. 3.11). The temperature may result in stress changes, but the stress/strain changes within the object will not cause any changes in the temperature. Since the energy changes for the quasi-static mechanical problem are usually negligible, this approximation is believed to be reliable [23].

$$\frac{\partial \varepsilon}{\partial t}=\alpha_t\frac{\partial T}{\partial t} \qquad (3.11)$$

Where ε is the strain [-], t is the time [s], α_t is the thermal expansion coefficient of the solid matrix [1/°C], T is the temperature [°C].

Besides, the variations in fluid properties are induced by complex chemical processes which are not only heat-related, but also time-related, e.g. the viscosity of the fracture fluid could attenuate with time. Thus, influence of the temperature on the fluid can only be modeled, when there is enough experimental data on the fluid available to express the relationship

between its properties and temperature or time. In this regard, the approach on this process will not be carried out through the embedded numerical code but conducted using the instant imported function based on experimental data.

3.2.4 Numerical formulation of the THM coupling in FLAC3D^{plus}

In the previous approach of FLAC3D^{plus} [40], fracture propagation was assumed to be a planar problem (Fig. 3.5, the section in the yellow frame). Thus, in the improved thermal approach, the heat transport in an artificial fracture will be simplified to be two-dimensional. Unlike FLAC3D, the improved thermal module for FLAC3D^{plus} has been implemented in the simulator using the Finite Volume Method (Fig. 3.5, the section in red) with consideration of the normal and advective heat conduction (both 3D in the rock formations and 2D within the stimulated fracture), as well as the heat transfer between the injection fluid and the rock formations. In other words, the thermal influence on mechanical behavior of the rock formations has been taken into consideration through the intrinsic thermal module in FLAC3D.

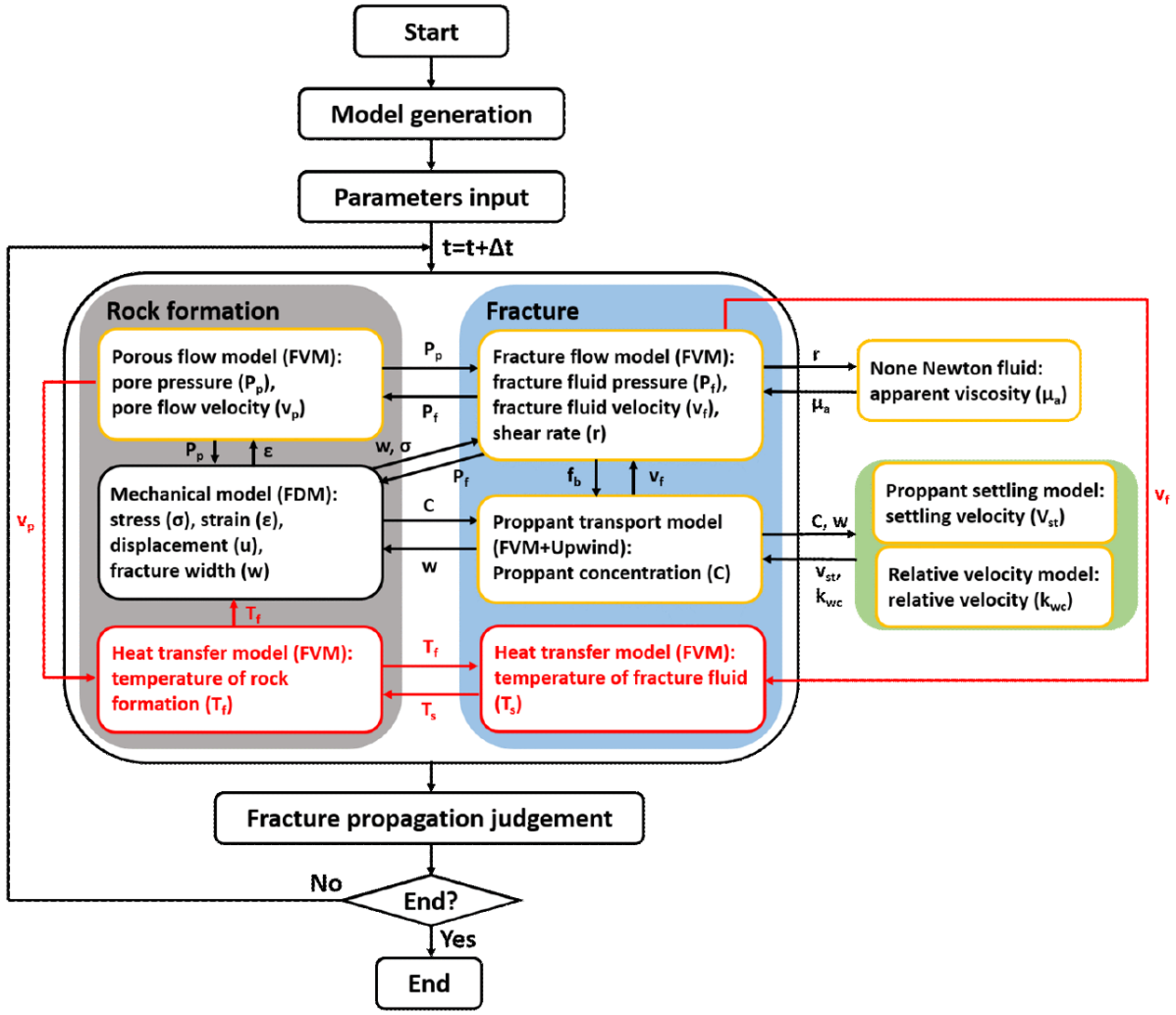

Figure 3.5 Modeling concept of FLAC3D^{plus} with the improved thermal module

Specifically, in order to simulate the TH-process in the hydraulic fracturing, the finite volume method and the implicit Euler methods were used. Therefore, both sides of Eq. 3.10 can be integrated in a control volume (Fig. 3.6 and Eq. 3.12).

$$\int_V \lambda \frac{\partial^2 T}{\partial x^2} + \int_V \lambda \frac{\partial^2 T}{\partial y^2} + \int_V \lambda \frac{\partial^2 T}{\partial z^2} + \int_V \rho c_V v_x \frac{\partial T}{\partial x} + \int_V \rho c_V v_y \frac{\partial T}{\partial y} + \int_V \rho c_V v_z \frac{\partial T}{\partial z} + \int_V q_v = \int_V \rho c_V \frac{\partial T}{\partial t} \tag{3.12}$$

Where λ is the thermal conductivity [W/(m·°C)], T is the temperature [°C], ρ is the density [kg/m^3], c_v is the specific heat capacity [J/(kg·°C)], v_i is the fluid flow velocity in the i direction [m/s], $i = x, y, z$, q_v is the heat source of volume [W/m^3].

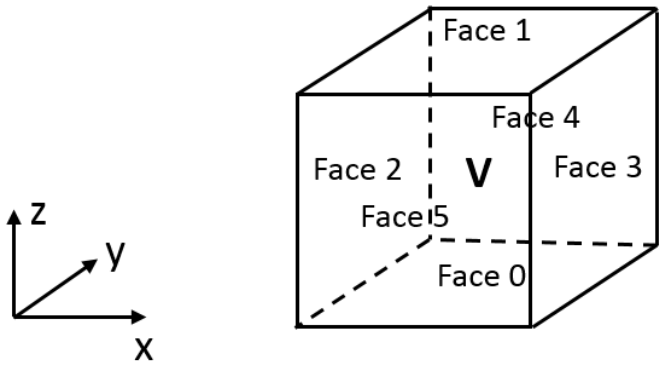

Figure 3.6Face numbering of a control volume in numerical model

According to different ways of heat conduction, the relationship between two adjacent elements in a numerical model can be divided into three different types (Fig. 3.7): 1. Both of the elements are fractured ones. In this type, heat transport is contained by the normal and advective conduction. Moreover, the heat flux is achieved through the laminar fluid flow within the fracture; 2. A fractured element and a formation element are adjacent. In this type the convective heat exchange and heat flux happens; 3. Both elements are formation ones. In this case the heat transport is the same as in the first type. However, the fluid flow is porous flow.

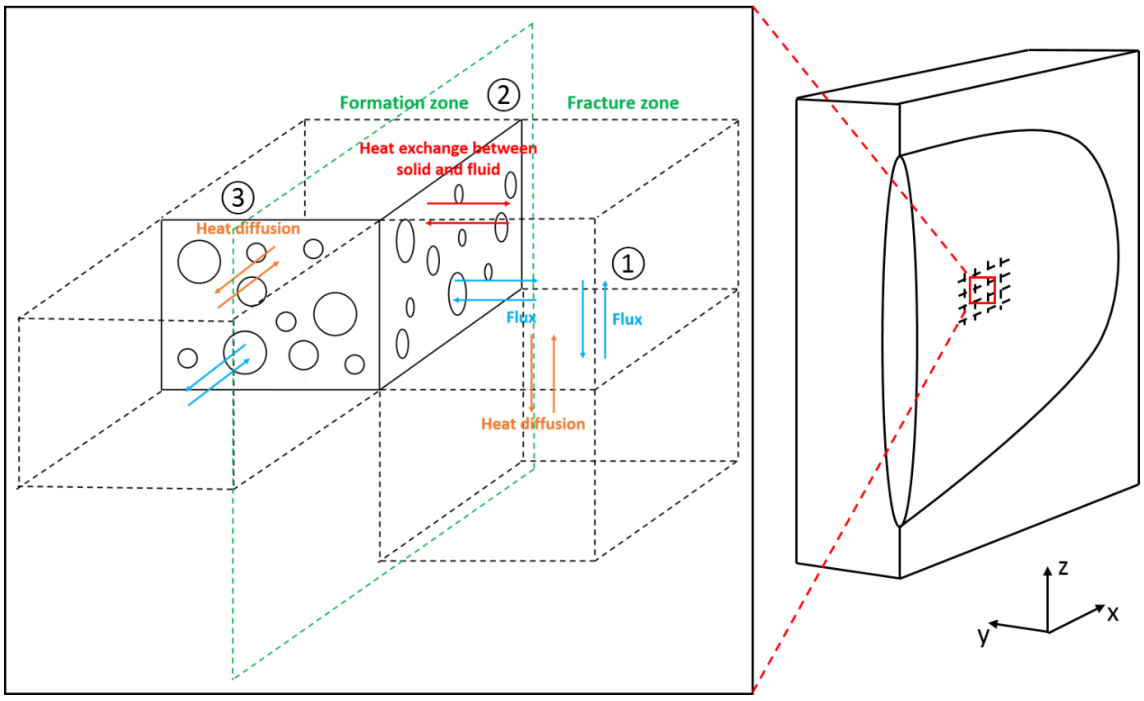

Figure 3.7 Different types of heat transport between adjacent elements

3.2.5 Verifications of the heat transport

In order to verify the reliability of improved module, three different verifications (in 1D and 2D) have been carried out. In these validations the simulation results are compared with their analytical solutions.

3.2.5.1 1D-Heat diffusion (T)

The discussion for the analytical solution of the initial verification borrows heavily from the manual of FLAC3D [23]. It considers the heat transported in a 1 m thickness sheet by conduction process (see Fig. 3.8). Table 3.1 provides the essential parameters used in the calculation.

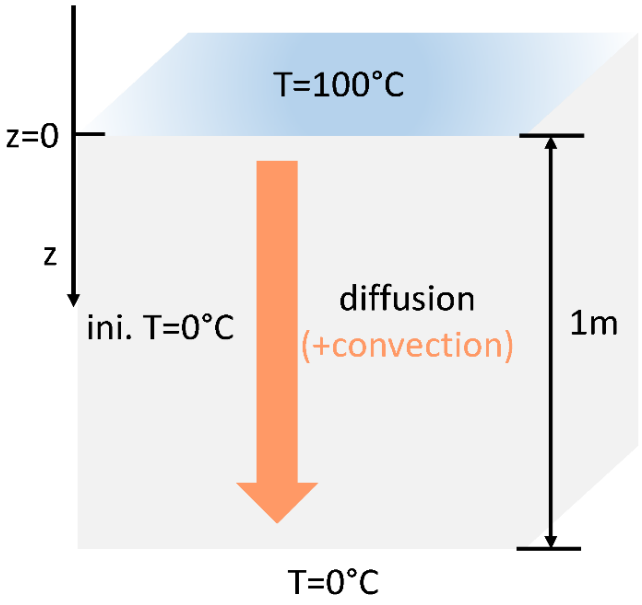

Figure 3.8 Thermal boundary condition of the 1 m thickness sheet

Table 3.1 Material properties of the heat transfer medium

Density [kg/m^3]	2,500
Porosity [-]	0.05
Thermal conductivity [W/(m·°C)]	3.2

Specific heat capacity [J/(kg·°C)]	1,000

The analytical solution for this example is given by Crank [44] (Eq. 3.13).

$$T(z,t) = T_1 + \frac{z}{L}(T_2 - T_1) + \frac{2}{\pi}\sum_{n=1}^{\infty} e^{-\alpha_d n^2 \pi^2 t/L^2}\left(\frac{T_2\cos(n\pi) - T_1}{n}\right)\sin\frac{n\pi z}{L} \qquad (3.13)$$

Where T_1 is the temperature at the top of the sheet [°C], T_2 is the temperature at the bottom of the sheet [°C], L is the thickness of the sheet [m], z is the distance to the top of the sheet [m], α_d is the thermal diffusivity [m^2/s], t is the time [s].

Fig. 3.9 shows the comparison between the analytical solution and the numerical solution. It is clear that the numerical simulation results match well with the analytical results.

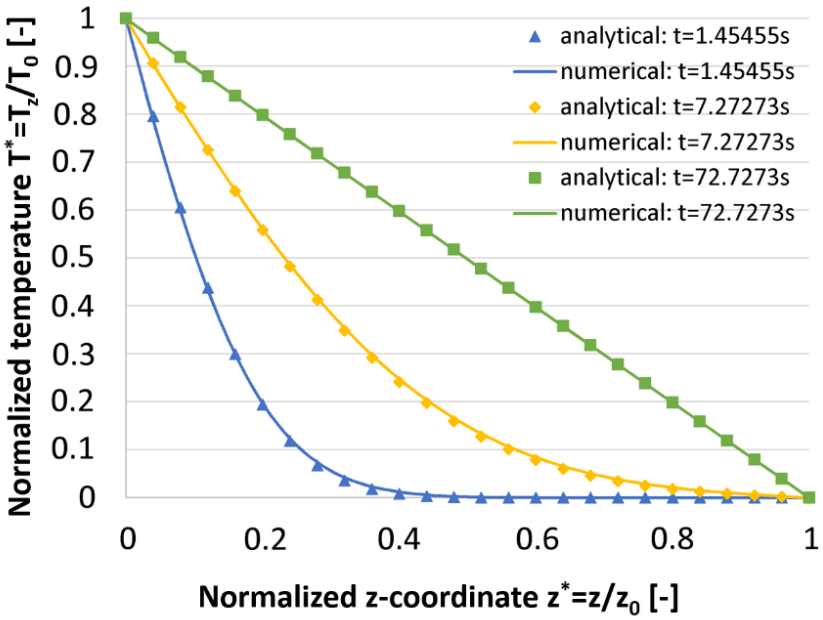

Figure 3.9 Comparison between the analytical solution and the numerical solution

3.2.5.2 1D-Heat transport by conduction and forced convection (TH)

The second example is a further extension of the first one. In this example the heat transport is considered to contain both conduction and convection processes (Fig. 3.8). However, there is no analytical solution for the transient state. For this reason, the numerical solution can only be compared with an analytical solution for the final stationary state (Eq. 3.14 and 3.15). Further parameters about the fluid flow are given in Table 3.2.

$$T^* = \frac{e^{Pex^*} - 1}{e^{Pe} - 1} \tag{3.14}$$

$$Pe = \frac{v\rho c_v L}{\lambda} \tag{3.15}$$

Where $T^* = (T\text{-}T_0)/(T_1\text{-}T_0)$ [-], with T is the temperature at the observation point in the model, T_0 is the temperature at the top (i.e. 100 °C), while T_1 is the temperature at the bottom of the model (i.e. 0°C), $x^* = x/L$ [-], with x is the distance from the observation point to the top of the model and L is the thickness of the sheet (i.e. 1 m), Pe is the Peclet's value [-], which describes the ratio between convective and conductive heat transfer, Pe is of great importance in TH-coupling, if Pe is greater than 1, the convective process is dominant, if Pe is less than 1, the conductive process will be the dominant process, v is flowing velocity of the fluid [m/s], ρ is the density [kg/m^3], c_v is the specific heat capacity [J/(kg·°C)], λ is the thermal conductivity [W/(m·°C)].

Table 3.2 Material properties and flow rate of the fluid

Water	Density [kg/m^3]	1,000
	Thermal conductivity [W/(m·°C)]	0
	Specific heat capacity [J/(kg·°C)]	4200
Flowing	Velocity [m/s]	$1\cdot10^{-6}$

Fig. 3.10 (a) shows the comparison between the analytical solution (only involving the heat conduction process) and the numerical solution (involving both the convection and conduction processes). Through this comparison the temperature of the model increased largely through heat convection. Fig. 3.10 (b) shows the temperature distribution for the stationary state. In this case the two solutions are observed to yield a good match.

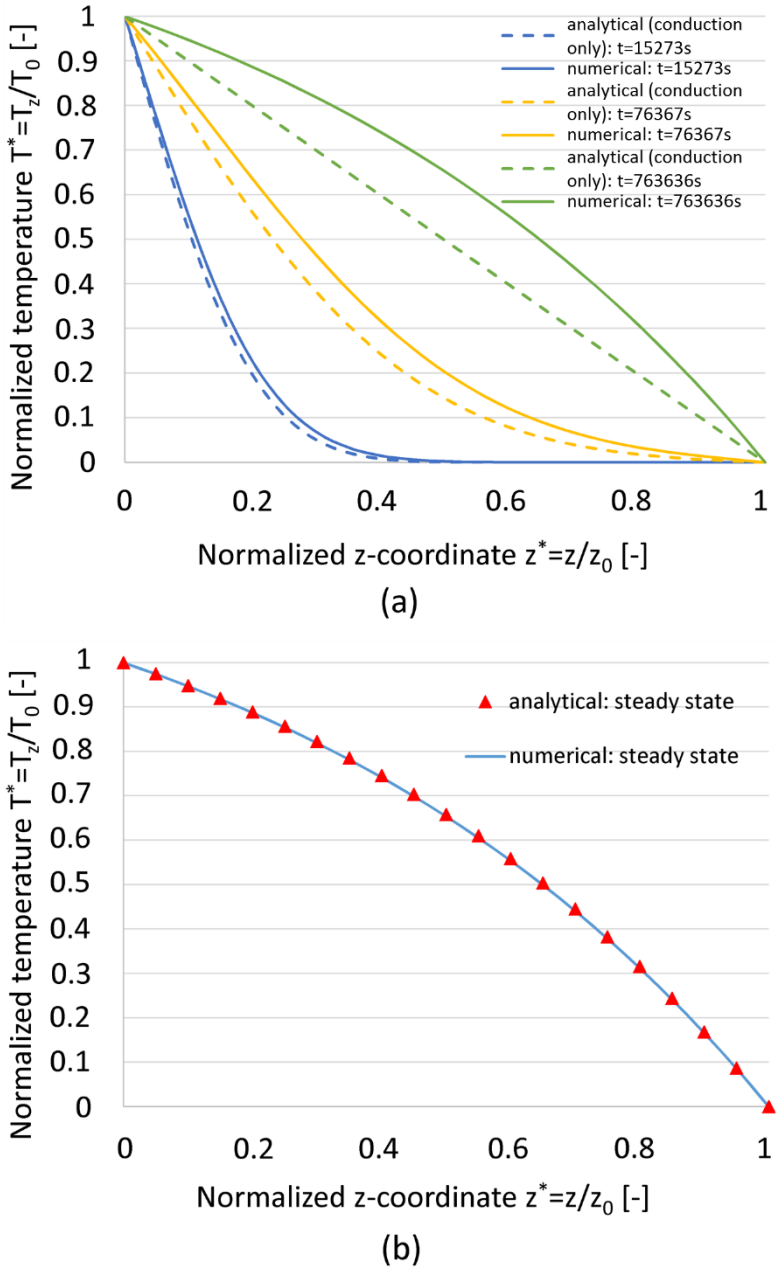

Figure 3.10 (a) Comparison between the analytical solution (for the conduction process only) and the numerical solution (for both conduction and convection), (b) comparison between the analytical and numerical solutions in a stationary state

3.2.5.3 2D-Heat diffusion (T)

The analytical solution of the third validation borrows heavily from Holman [45], who derived a model (Eq. 3.16) for the analytical solution of 2D-Heat conduction in a steady state.

$$T = T_m \frac{e^{\frac{\pi z}{W}} - e^{-\frac{\pi z}{W}}}{e^{\frac{\pi H}{W}} - e^{-\frac{\pi H}{W}}} \sin\left(\frac{\pi x}{W}\right) + T_1 \tag{3.16}$$

Where T is the temperature [°C], T_m is the temperature of the upper edge [°C], W is the width of the plate [m], H is the height of the plate [m], T_1 is the temperature of other three edges [°C].

In this verification, a sine-wave temperature distribution is considered on the upper edge of the plate (when y = W), see Fig. 3.11. The initial temperature at the upper edge can be described through the equation f(x) = 20 °C · sin(πx/W) + 0 °C. On the other three edges (i.e. x = 0, y = 0, x = W) the initial temperature is 0 °C. The temperature remains unchanged during the simulation.

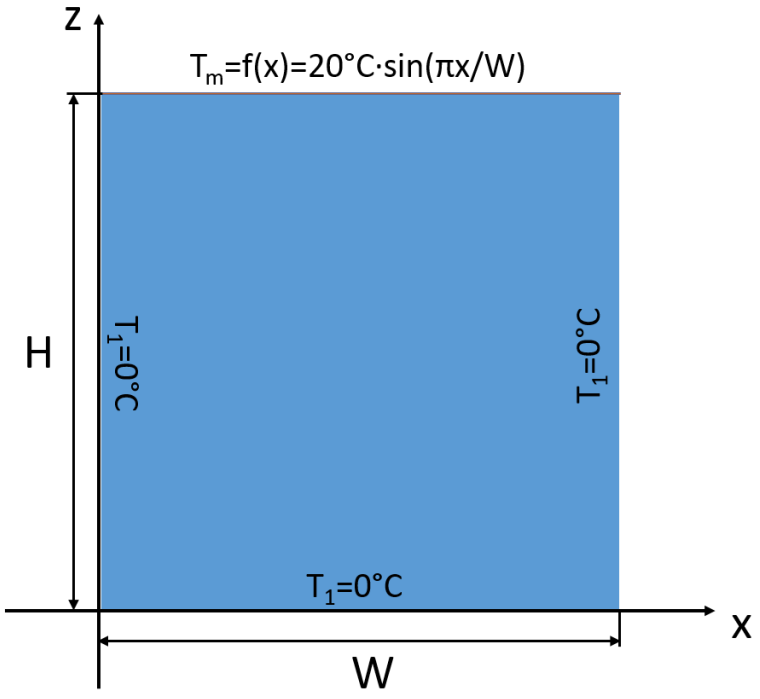

Figure 3.11 Thermal boundary condition of the plate

Fig. 3.12 shows the comparison between the analytical and numerical solutions. Both numerical and analytical solutions have the same trend of temperature distribution at a steady state. Fig. 3.12 (c) shows that their differences are negligible. This result implies that the

verification using a 2D-model yields a perfect match for the two solutions (numerical and analytical).

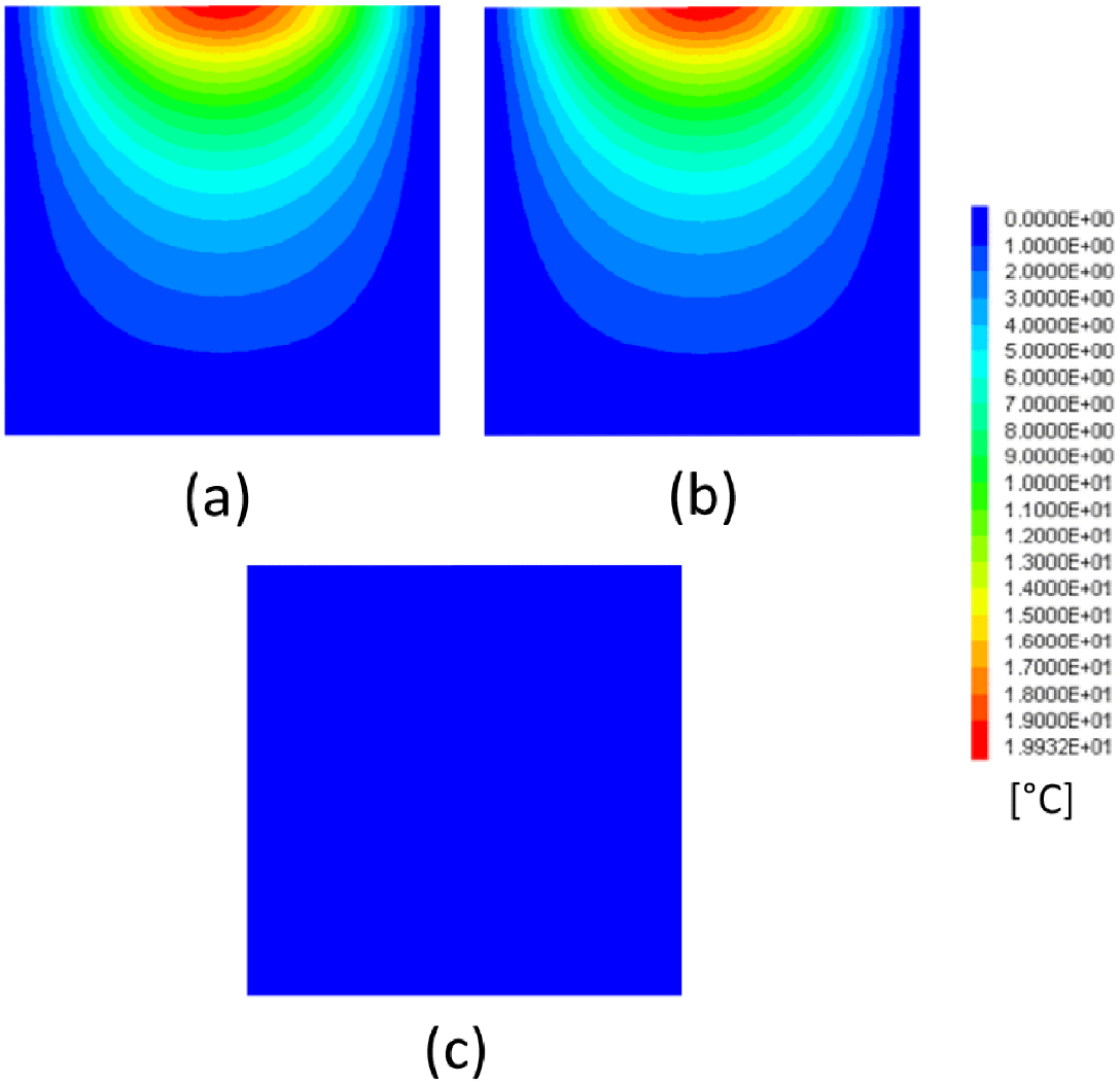

Figure 3.12 (a) Numerical solution at steady state, (b) analytical solution at steady state, (c) temperature difference between the two solutions

3.3 Numerical study of the fluid viscosity's influences on shaping of a stimulated fracture based on a fictive model

In this section, a numerical study based on a fictive fracture system is conducted through FLAC3D^{plus} (without the improved thermal module) in order to reveal the direct and indirect

influences of the fluid's viscosity on shaping of the stimulated fracture. As the given geological conditions are uncomplicated, some analysis results are more obvious.

3.3.1 Model generation and parameters

Fig. 3.13 shows the stratigraphy of the fictive reservoir, which is composed of tight sandstone. Meanwhile, it also presents a geometric model that was used in the numerical simulation. Since the geological environment in this modeling is assumed to be symmetric, a 1/4 model (200m × 300m × 200m) was utilized.

In this model the fictive reservoir is composed of three different formations. The uppermost is the caprock (from -3,000 m to -3,050 m, Δz = 50 m) that possesses a very low permeability (see Tab. 3.1). A pay zone formation, in which the stimulation is carried out, lies in the middle (form -3,050 m to -3,150 m, Δz = 100 m). The lowermost is the basement (from -3,150m to -3,200m, Δz = 50 m). This formation holds identical mechanical and hydraulic properties to those of the caprock.

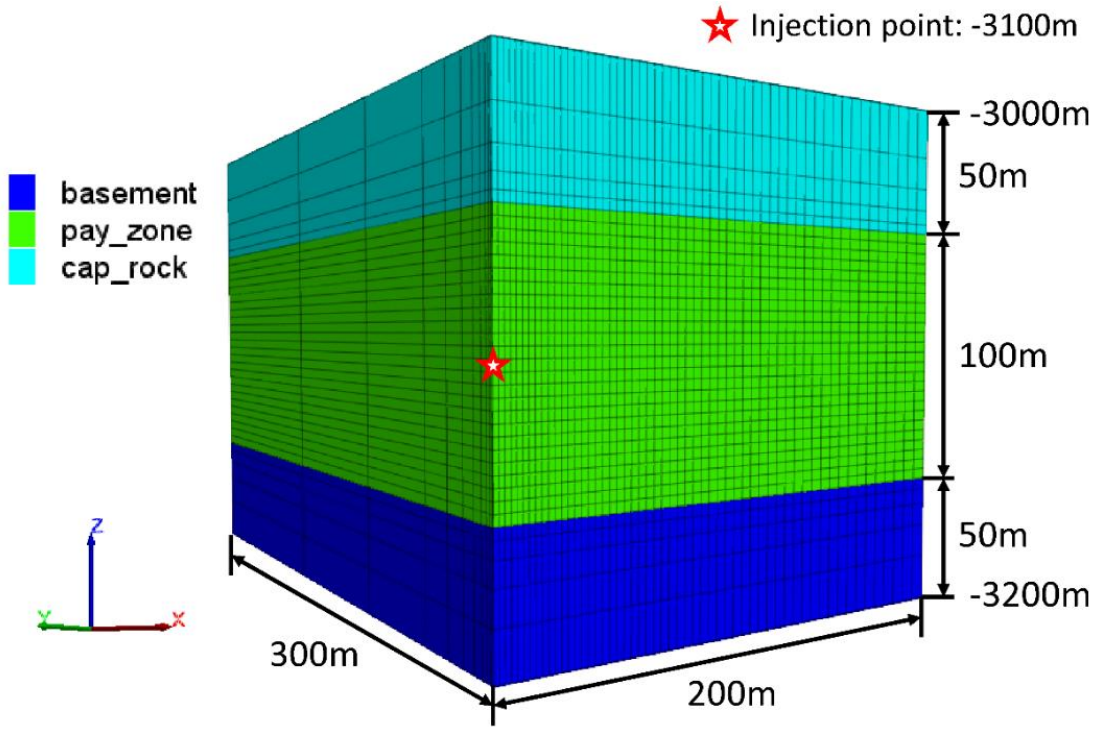

Figure 3.13 Graphical presentation of the stratigraphy and the geometric model of the fictive reservoir

All the mechanical and hydraulic parameters of geological formations have been given in Tab. 3.1. As mentioned before, it can be observed that both the caprock and the basement formations own a very low permeability. That means they are very appropriate to serve as hydraulic barriers.

Table 3.3 Mechanical and hydraulic properties of the rock formations

Rock formation	Density [kg/m^3]	Young's Modulus [GPa]	Poisson ratio [-]	Tensile strength [MPa]	Porosity [-]	Permeability [m^2]
	ρ	E	υ	σ_t	Φ	K_f
Caprock	2,600	25	0.3	1.0	0.025	1×10^{-17}
Payzone	2,600	30	0.25	1.0	0.1	1×10^{-15}
Basement	2,600	25	0.3	1.0	0.025	1×10^{-17}

In addition, Fig. 3.14 shows variation of the primary stress (vertical stress σ_v and minimum/maximum horizontal stress σ_h and σ_H) and the pore pressure P_p with depth. The minimum horizontal stress in the pay zone (from -3,050m to -3,150m) decreases significantly (ca. 8 MPa). Mechanically, the giant difference of minimum in-situ stress provides a good resistance to prevent the fracture from propagating upwards and downwards.

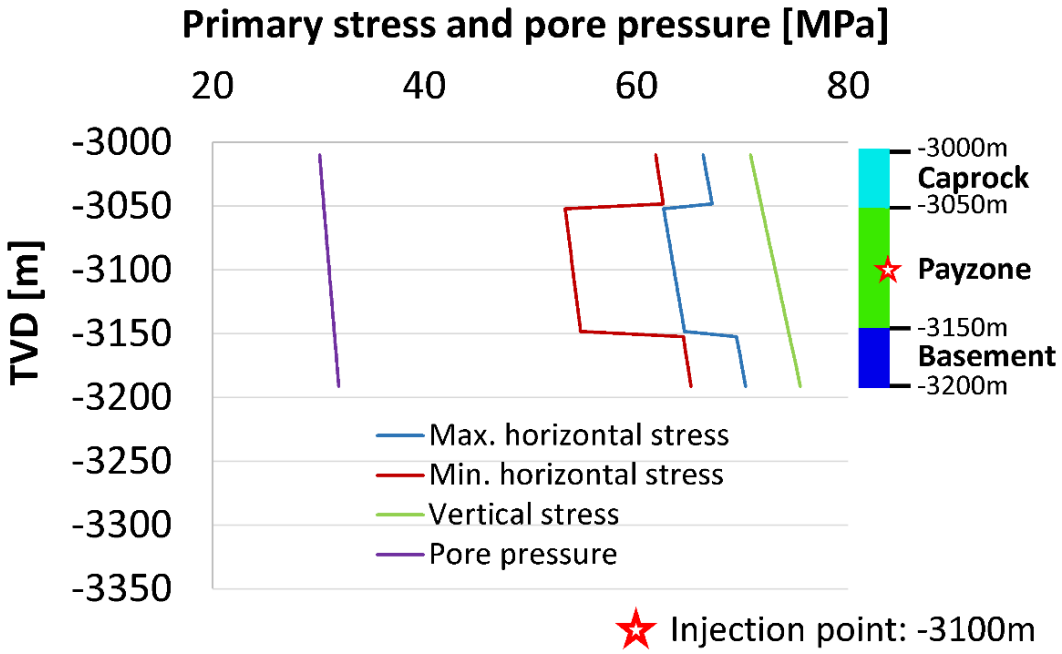

Figure 3.14 Variation of the primary stress (vertical and minimum/maximum horizontal) and the pore pressure with depth in the reservoir and barrier formations

3.3.2 Treatment schedule

As shown in Fig. 3.13, the injection position of this operation is located at a depth of -3,100m. It is 50 m below the caprock. In an 80 minutes' operation with a constant injection rate of 6 m^3/min (see Fig. 3.15), a total of 480 m^3 fluid is injected into the target formation (pay zone). The density of the operation fluid is 1,040 kg/m^3. Since impacts from the fluid viscosity are the focus of research, various simulations with different parameters were carried out.

In the later part of the study, in order to introduce the impacts from the fluid viscosity on the sand-carrying ability, the simulation also considered a sanding process, i.e. starting from t = 30 min, proppant is added with a stepwise increasing concentration from 0 to 500 kg/m^3. The properties of proppant will be given in the subsequent content.

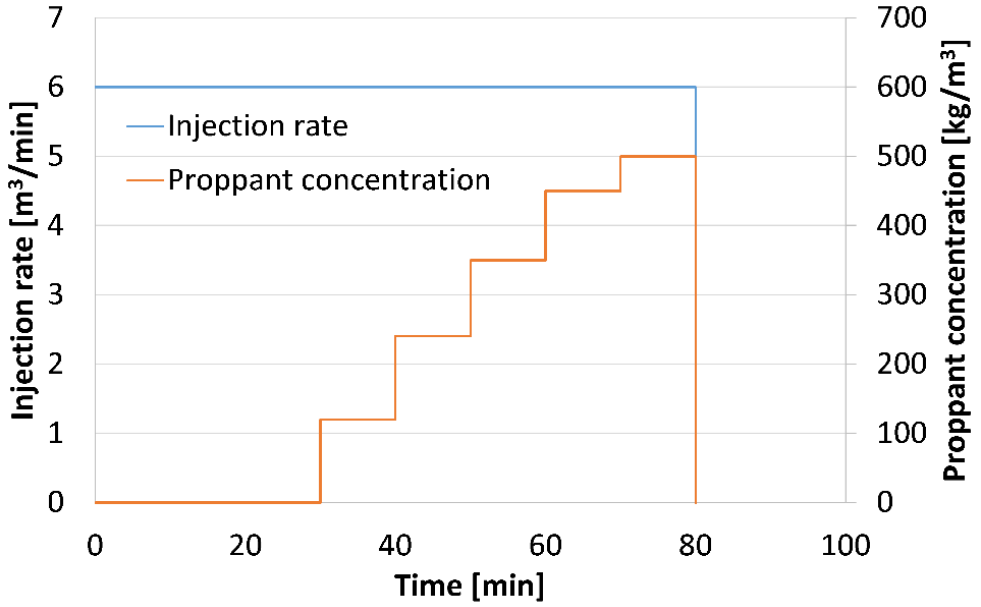

Figure 3.15 Variation of the injection rate and proppant concentration during the hydraulic fracturing

3.3.3 Modeling results of the operation with various fluid viscosity but without leak off

In the first phase of this study, 6 simulations with different fluid viscosity are conducted. Among them, μ = 1 cP (i.e. pure water) is chosen as the basic value. One thing must be pointed out that in this phase, in order to eliminate the impacts from other factors (e.g. the influences of permeability on the leak off), the leak off process has not been taken into consideration, i.e. leak off in each case is 0.

Under above premise, Fig. 3.16 shows width distribution within the stimulated fracture for the basic situation (Fig. 3.16 (a)) and each variation (Fig. 3.16 (b) to (f)). Time point is the end of the stimulation (t = 80 min). In this figure it can be observed that in all the variations, the fracture propagated within the pay zone and eventually formed an elliptical fracture. In other words, the finally achieved fracture heights in these variations are similar. This proves that the geological barrier integrity worked very well, so that the fracture is prevented from extending upwards and downwards. However, compared to those of μ = 1 cP to 10 cP, μ = 50 cP and 100 cP clearly possess shorter and wider fracture forms.

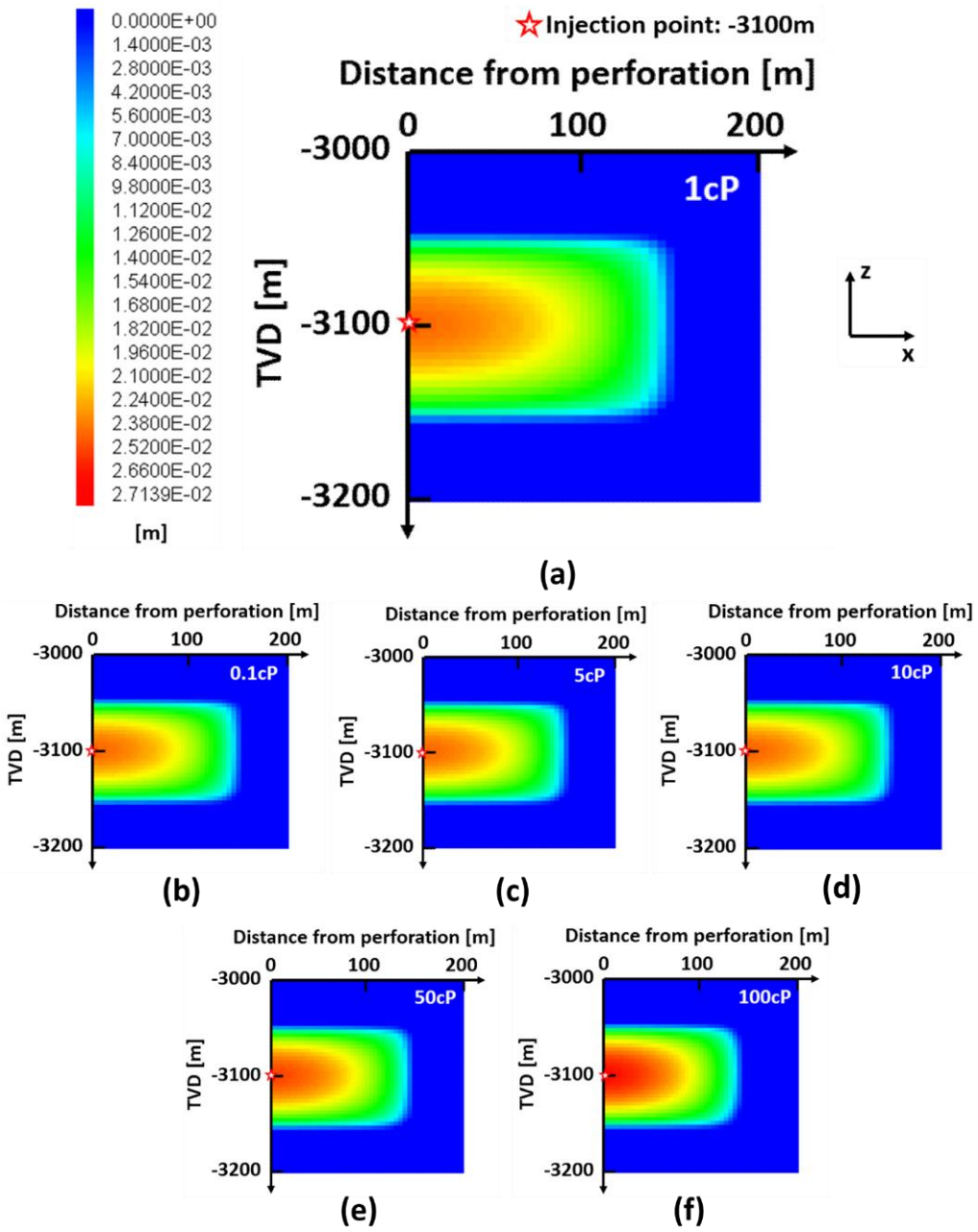

Figure 3.16 Comparison of fracture's width distributions for operations with different fluid viscosities ((a): μ = 1 cP; (b): μ = 0.1 cP; (c): μ = 5 cP; (d): μ = 10 cP; (e): μ = 50 cP; (f): μ = 100 cP) at the end of stimulation (without leak off)

Fig. 3.17 and 3.18 give more detailed comparisons in the fracture height, the maximum 1/2 fracture length, the actual fracture width at the perforation and the average fracture width. Simultaneously the width profiles (at the depth of -3,100 m) at the end of each operation

are also illustrated (Fig. 3.19). Through these comparisons some more obvious common points and differences of fracture propagation are found.

In Fig. 3.17 the achieved fracture heights with different viscosities are almost the same. Only the operation with 100 cP viscosity obtained a slightly higher fracture. The difference in the development can be summarized as, the more viscous the fluid, the faster the fracture expands in the vertical direction. Thus, the maximum fracture height was earlier achieved, when the fluid viscosity is 100 cP.

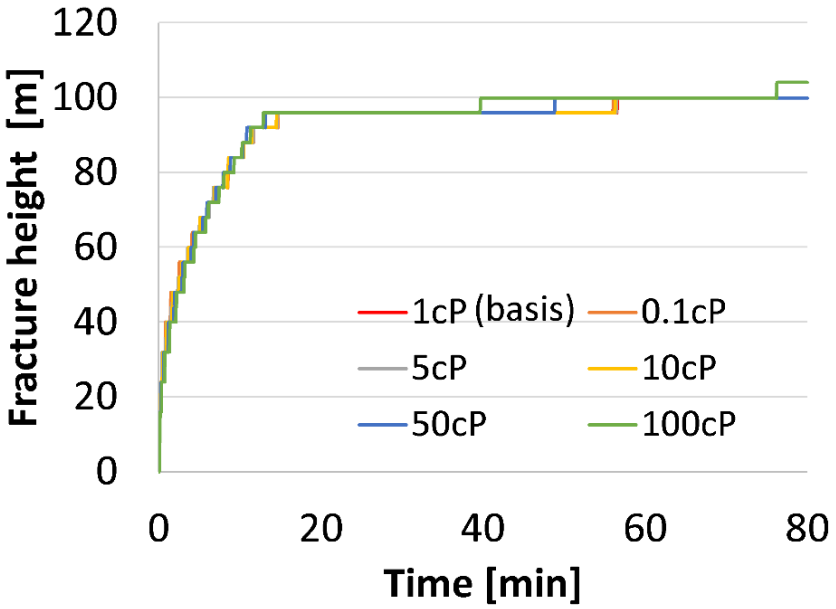

Figure 3.17 Comparison of the fracture height development with different fluid viscosities (without leak off)

A converse phenomenon appears in the evolution of fracture length. In Fig. 3.18 (a)-1, the larger the fluid viscosity, the slower the fracture expands in length direction. Therefore, a shorter fracture is finally achieved with a more viscous fluid. Fig. 3.18 (a)-2 shows the relationship between finally obtained fracture length and fluid viscosity. When, the fluid viscosity increases from 0.1 cP to 10 cP, the results do not change significantly. However, when the fluid viscosity increases further, specifically from 10 cP to 100 cP, the decreasing trend of fracture length is more compelling.

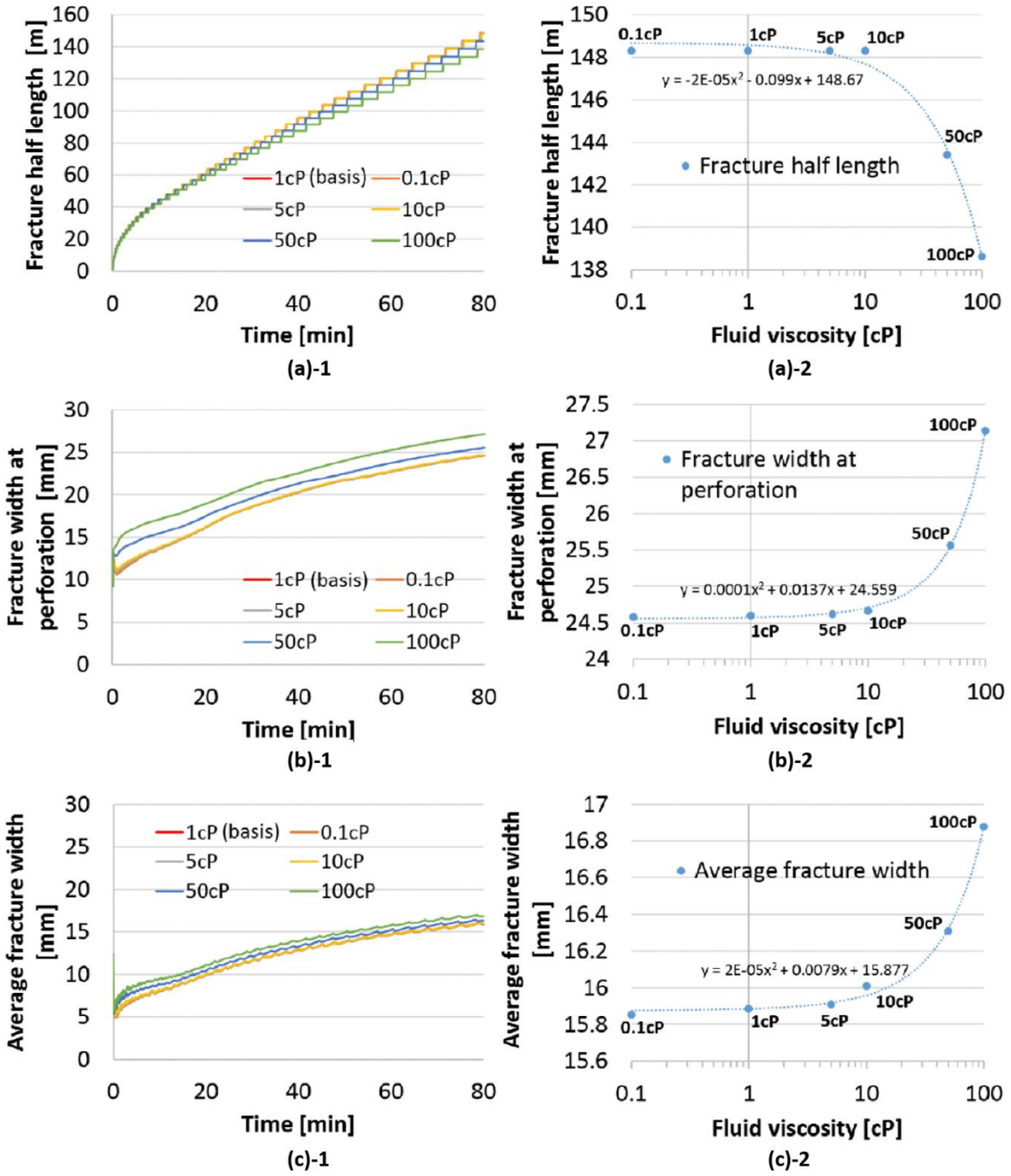

Figure 3.18 Evolution of (a) the maximum fracture half-length, (b) the actual fracture width at the perforation and (c) the average fracture width with time for different fluid viscosities and the functional curve to describe the relationship between finally achieved results (t = 80 min) and the fluid viscosity (without leak off)

Turning attention towards the temporal growth of fracture width, following phenomenon can be discovered in Fig. 3.18 (b) and (c). The fracture with a larger fluid viscosity has obtained a wider form at the beginning. This trend was maintained to the end of operation. That is to say, the nexus between finally obtained fracture width and viscosity is opposite to that between length and viscosity. In Fig. 3.18 (b)-2 and (c)-2, when the viscosity increases from 0.1 cP to 10 cP, the final widths of fracture are almost unchanged. When the fluid's viscosity increases further from 10 cP to 100 cP, the widths increase significantly. The above conclusions can also be derived from Fig. 3.19.

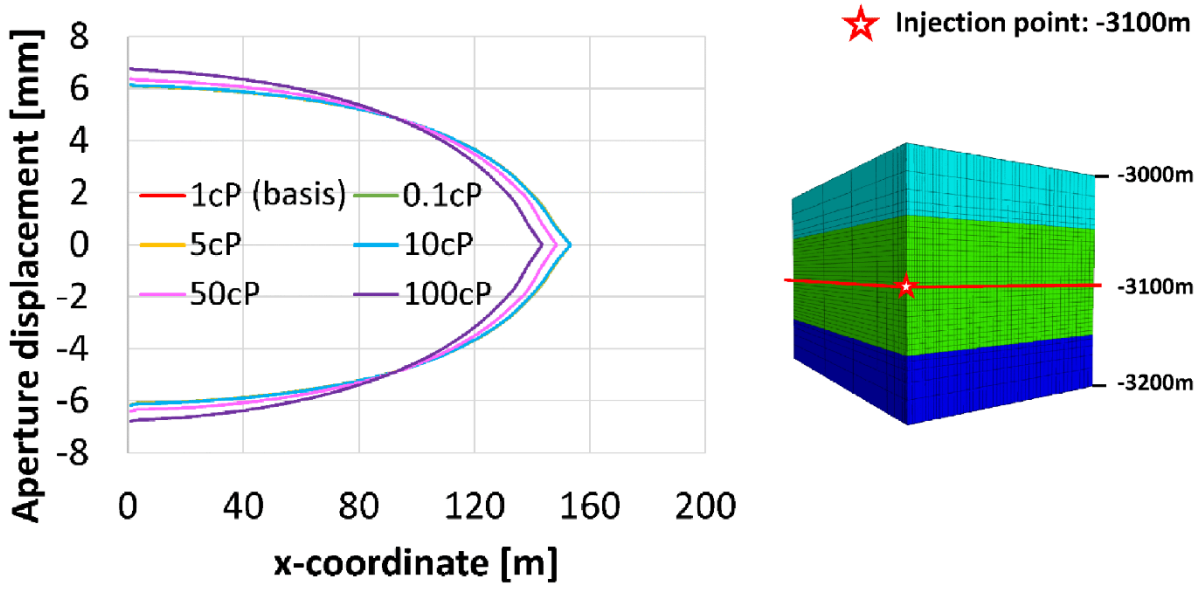

Figure 3.19 Comparison of the width profiles with different fluid viscosities at the end of stimulation (at the depth of -3100 m, without leak off)

Here the question arises that how to explain the above described phenomenon? By combing some prerequisites with the phenomenon in Fig. 3.20 and 3.21 the answers can be drawn. Firstly, as mentioned in the beginning, since the influence from leak off has been eliminated, and the fluid used in the simulations is assumed to be incompressible (an assumption in FLAC3D^{plus}), the finally obtained fracture volume in all variations should be the same, i.e. the same as the injected volume. Under this premise Fig. 3.20 show the changes in the

minimum horizontal stress σ_h and the pore pressure P_p. The time point is the end of operation. In Fig. 3.20 (a), σ_h increases in the area perpendicular to the opened fracture (the sign of a pressure is negative in FLAC3D) and, meanwhile, decrease outside the fracture front. In contrast, the pore pressure is almost unchanged (Fig. 3.20 (b)). This is because there is no leak off in the operation.

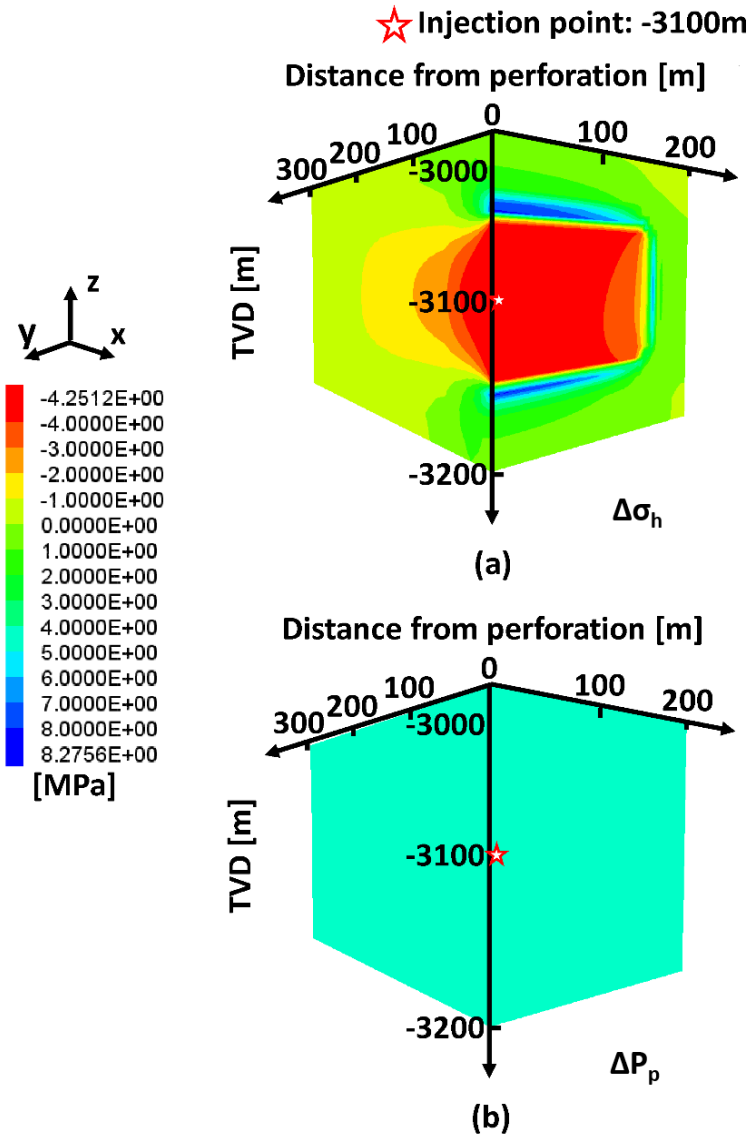

Figure 3.20 Change of the minimum horizontal stress (a) and the pore pressure (b) at the end of the operation (t = 80 min) (without leak off)

Then continue to focus on the increase in σ_h for different operations (Fig. 3.21). When the viscosity becomes larger, the increasing of σ_h near the perforation becomes more severe

(Fig. 3.21 (e) and (f)). The reason is that the fluid is less likely to flow away from the perforation, when it owns a larger viscosity. Thus, a congested situation was formed around the perforation point. As a result, in this area the fracture obtained a greater supporting force to expand in the direction perpendicular to its surface. For the same reason the change in σ_h became greater. Under this trend, a wider and shorter fracture will eventually be obtained.

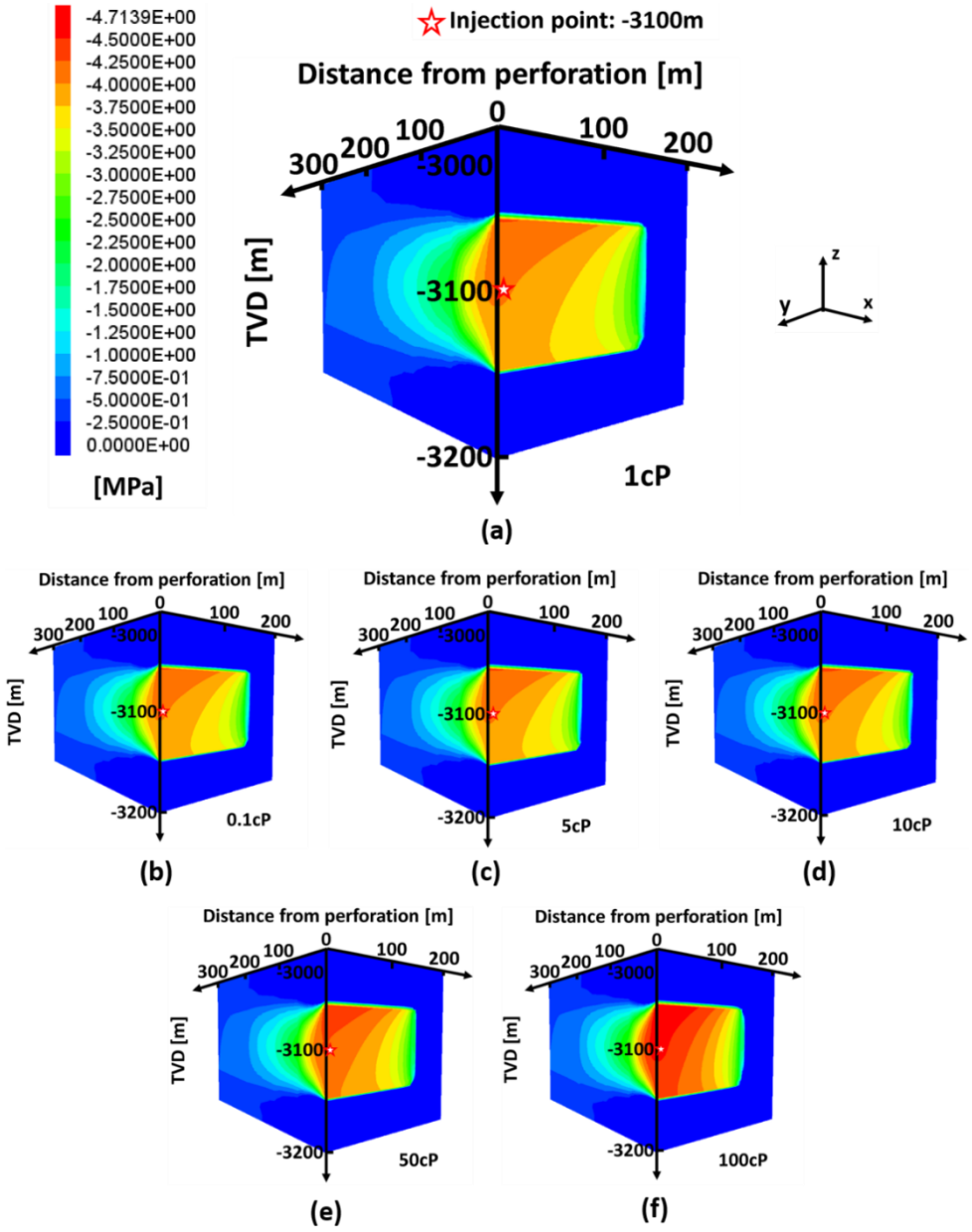

Figure 3.21 Increases of the minimum horizontal stress for simulations with different fluid viscosities ((a): μ = 1 cP; (b): μ = 0.1 cP; (c): μ = 5 cP; (d): μ = 10 cP; (e): μ = 50 cP; (f): μ = 100 cP) at the end of the operation (t = 80 min) (without leak off)

3.3.4 Modeling results of the operation with various pay zone permeabilities and constant fluid viscosity

In the second phase, operations with various pay zone permeability and constant fluid viscosity (μ = 1 cP) were simulated. The viscosity is set to be identical, in order to eliminate its impacts on the results. Among the simulation, k_f = 1 mD (i.e. 1×10^{-15} m^2) is chosen as the basis situation, i.e. the conditions are given in Tab. 3.1. Also, in this phase, the leak off of injected fluid is taken into account as an indirect influence.

Fig. 3.22 shows the fracture's width distribution for basis situation (Fig. 3.22 (a)) and each variation (Fig. 3.22 (b) to (d)) (t = 80min). In these variations, the fracture's propagations were also restricted in the pay zone formation. But unlike before, since the pay zone permeability in each operation are different, i.e. the trends to leak off are unequal, although the final fracture heights in these simulations are still similar, the length and width of the fracture have changed drastically.

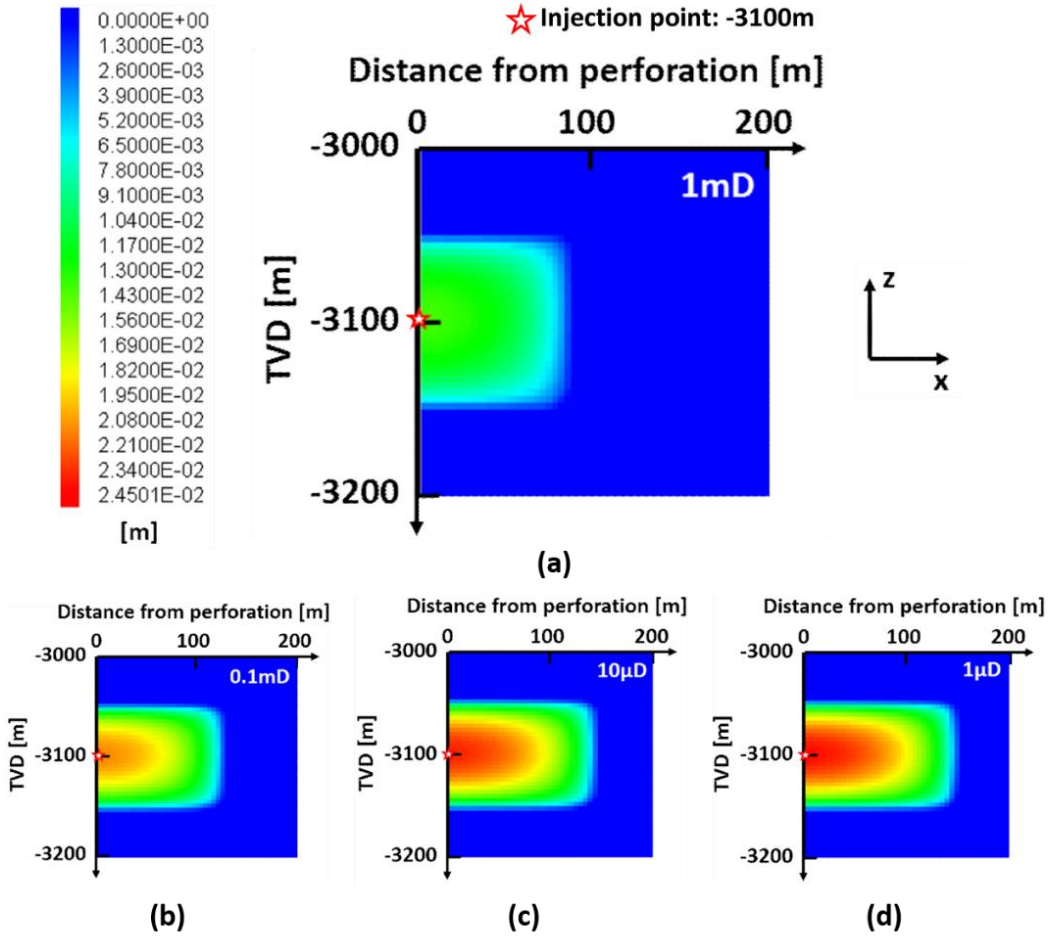

Figure 3.22 Comparison of fracture's width distributions for operations with different pay zone permeability ((a): k_f = 1 mD; (b): k_f = 0.1 mD; (c): k_f = 10 µD; (d): k_f = 1 µD) and constant fluid's viscosity at the end of stimulation (with leak off)

Fig. 3.23 and 3.24 provide some more detailed comparisons. In Fig. 3.23, the finally achieved fracture heights are still almost the same. Only in the basis situation the fracture is a bit shorter. However, as the trend of leak off decays, i.e. the pay zone permeability decreases, fracture's growth in the vertical direction became faster and faster. In the variations of k_f = 10 µD and 1 µD, the rates are almost the same. This means that the leak off trends in these two variations have been reduced to an extreme low extent.

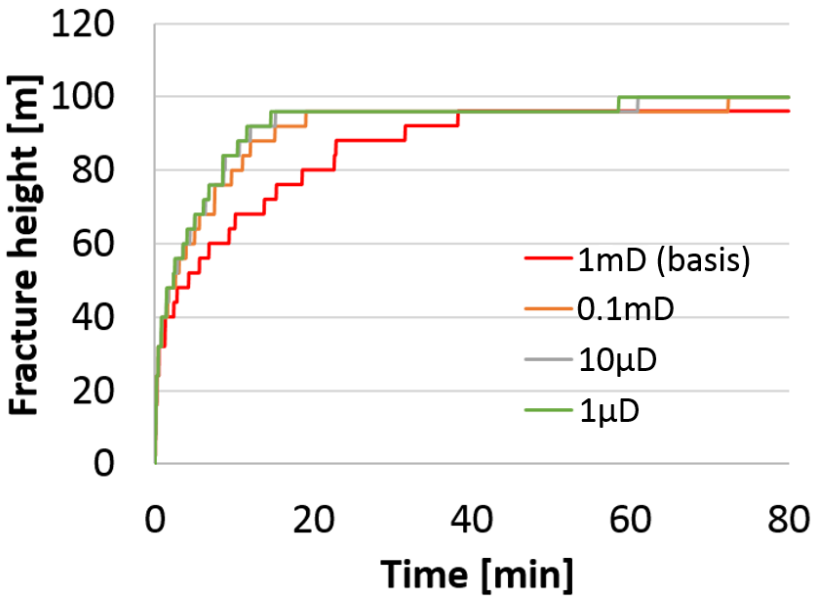

Figure 3.23 Comparison of the fracture height development with different pay zone permeability and constant fluid viscosity (with leak off)

Different from that in the first phase, the change in fracture length with various pay zone permeability shows a similar trend to that of height, i.e. the weaker the trend of the leak off (see Fig. 3.24 (a)), the faster the fracture expands in the x-direction. Finally, a longer fracture was achieved in the system with a smaller permeability. Studying the relation between the length and the leak off ability (Fig. 3.24 (a)-2 and Fig. 3.26), a phenomenon can be drawn out that, when the pay zone permeability decreases from 1 mD to 10 µD (leak off ability decreases from 70%/80 min to 6%/80 min), the finally obtained length increases significantly. However, when the leak off ability is extreme low (10 µD: 6%/80 min, 1 µD: <1%/80 min), final fracture length reduces slightly as the permeability further decreases.

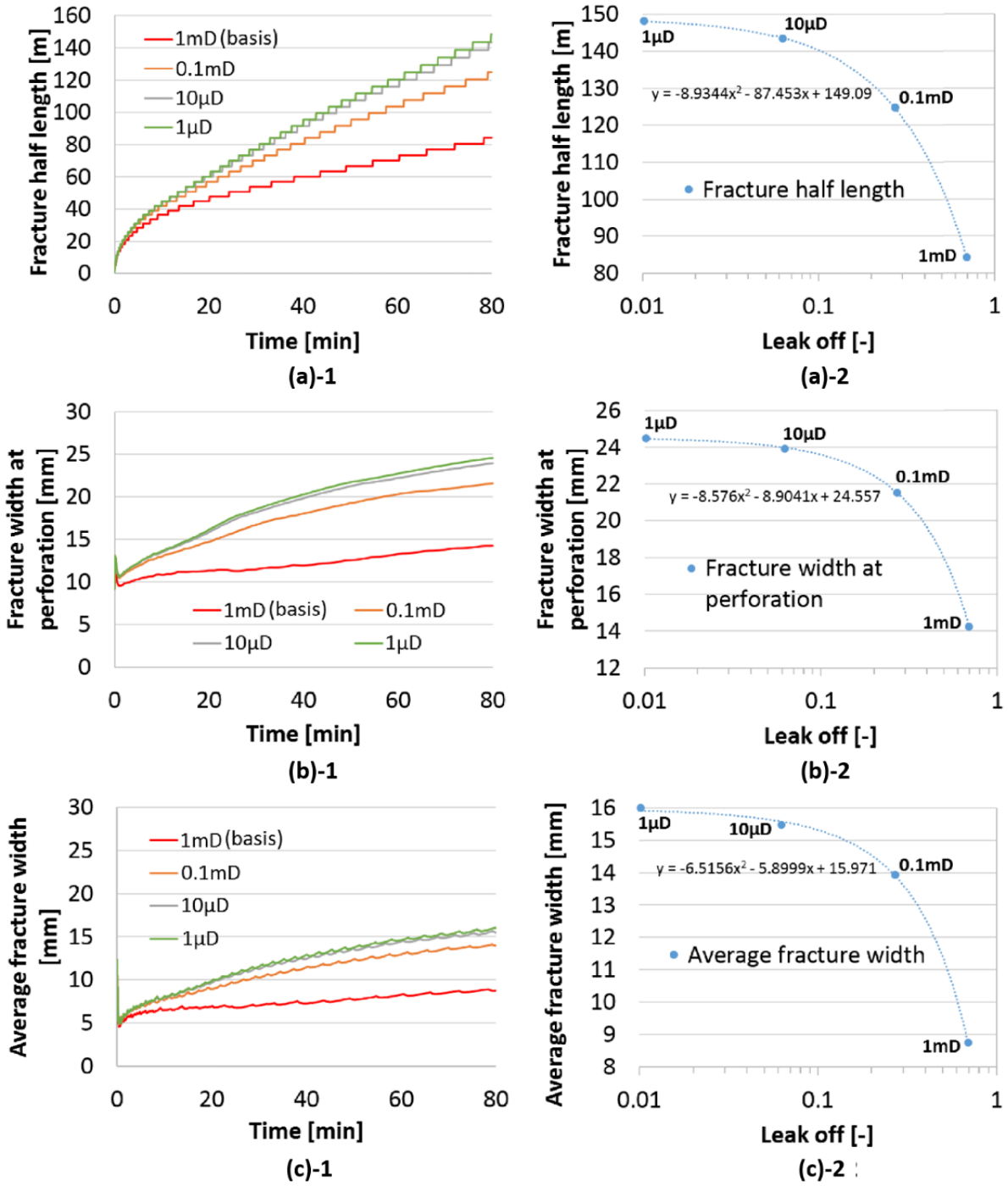

Figure 3.24 Evolution of (a) the maximum fracture half-length, (b) the actual fracture width at the perforation and (c) the average fracture width with time for different pay zone permeability and constant fluid viscosity, the functional curves describe the relationship between finally achieved results (t = 80min) and the permeability (with leak off)

Turning the attention towards the fracture widths, the evolution of fracture widths over time (Figure 3.24 (b) and (c)) shows the same trend as that in height and length. Similarly, when the leak off ability is reduced to an extreme low extent, the change of final result became very slight as the pay zone permeability varies. In Fig. 3.25 the representation of the width profiles makes a summary for the previous comparison.

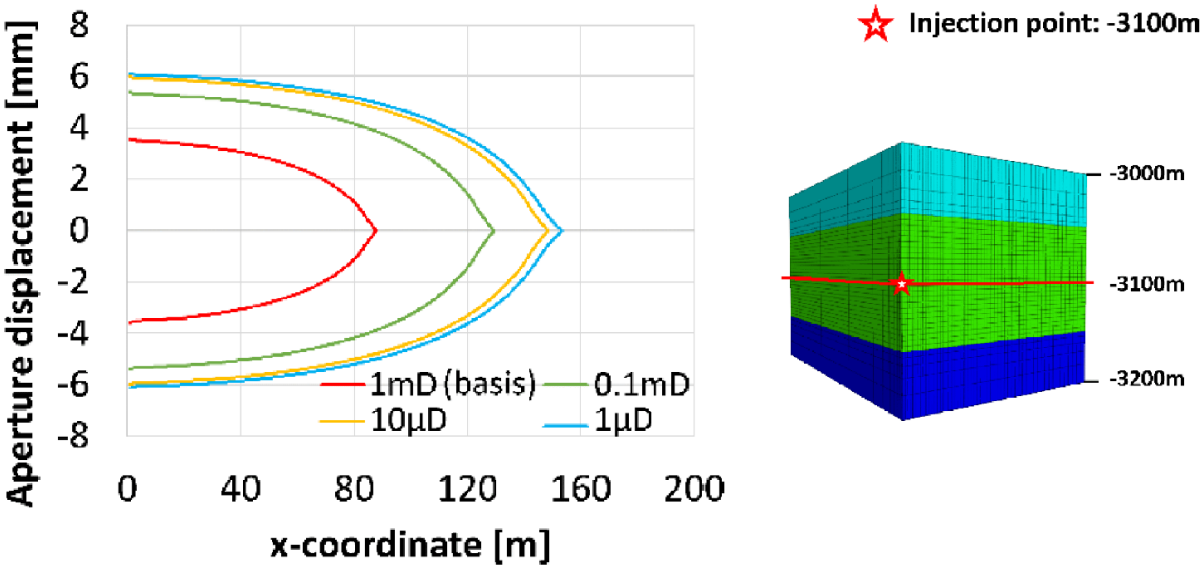

Figure 3.25 Comparison of the width profiles with different pay zone permeability and constant fluid viscosity at the end of stimulation (at the depth of -3100m, with leak off)

Refer to the derivation in 3.3.3, the phenomenon here is also easy to explain. Since different pay zone permeability in various operations indicates that the leak off tendency also varies, the finally obtained fracture volume in each modeling differs (Fig. 3.26). Simultaneously, because of identical fluid viscosity, the trends of fluid's flowing to the distal fracture front are the same. For these two reasons, the fracture's propagation ability in different directions should be the same in different variations. Thus, the fracture's width profiles present an identical shape (see Fig. 3.25). The sizes of fracture in length and width direction depend only on the pay zone permeability.

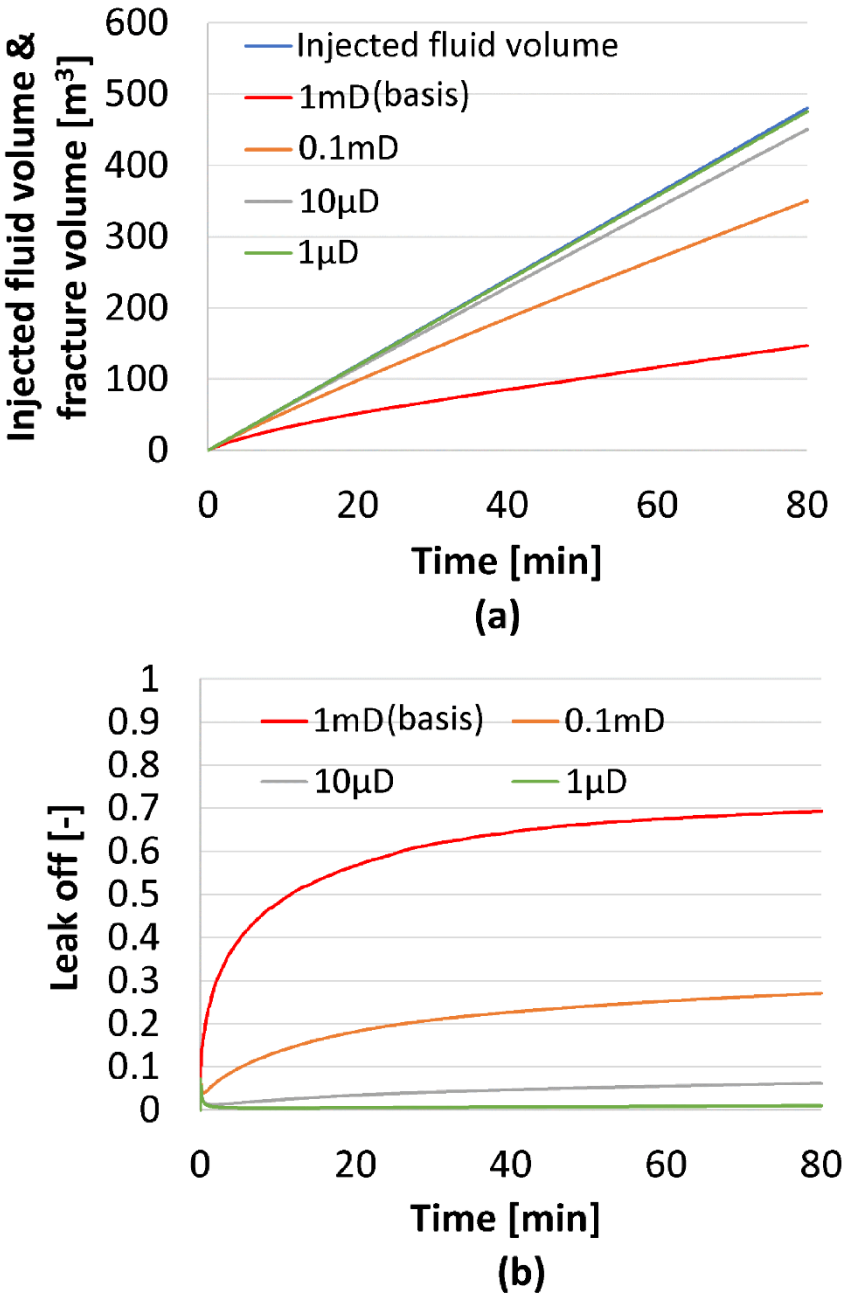

Figure 3.26 Evolution of (a) the volume of the injected fluid and the fracture volume over time for operations with different pay zone permeability and constant fluid viscosity and (b) the corresponding leak off percentage (with leak off)

Fig. 3.27 confirms above explanation as well. In other words, the increase of minimum horizontal stress around the fracture and the increase of pore pressure in surrounding formations should be in two opposite directions. Similar statement is also mentioned in the article of Carrier et al. [46].

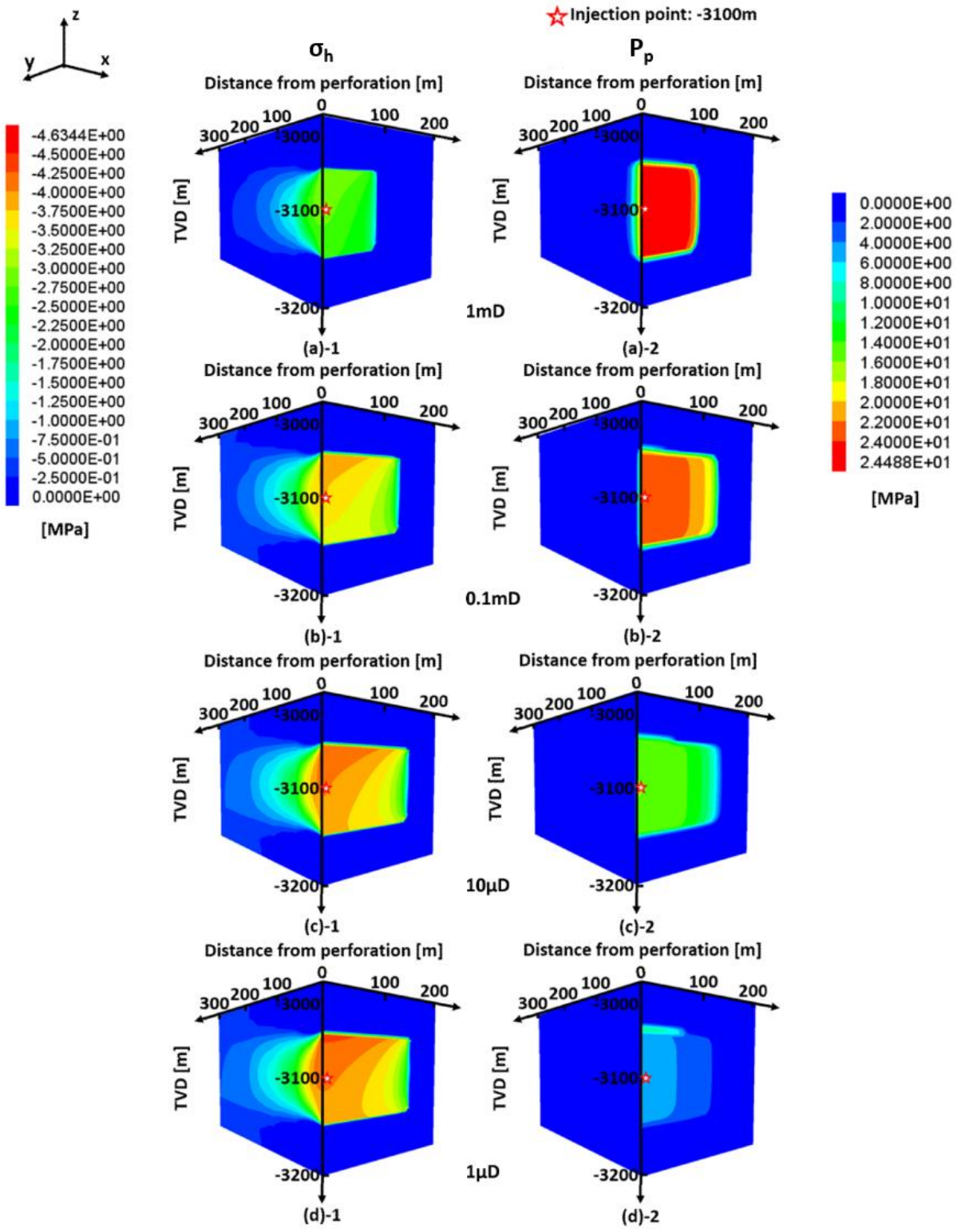

Figure 3.27 Increases of the minimum horizontal stress and the pore pressure for simulations with different pay zone permeability ((a): k_f = 1 mD; (b): k_f = 0.1 mD; (c): k_f = 10 μD; (d): k_f = 1 μD) and constant fluid viscosity at the end of stimulation (t = 80 min) (with leak off)

Fig. 3.28 shows a two-dimensional parameter space composed of dimensionless toughness K and dimensionless leak-off coefficient C. In a general stimulation work, the fracture's propagation is governed by two competing energy dissipation mechanisms (viscous flow and fracturation) and two competing storage mechanisms (in the fracture or in the porous formation).

In conjunction with the results in 3.3.3, when the system is dominated by a storage mechanism (storage in the fracture), the final shaping of a fracture would be impacted by viscosity itself significantly, i.e. the more viscous the injected fluid, the more the fracture tends to expand in the width direction (viscous flow) rather in the length direction (fracturation). However, when same fluid is used to carry out stimulation under different permeable conditions (geological conditions should also be identical), the stronger the trend to leak into the formations, the smaller the final fracture would be. Correspondingly, the increase in P_p (see Fig. 3-27 (a)-2, (b)-2, (c)-2, (d)-2) becomes greater, and the increase in σ_h becomes smaller (see Fig. 3-27 (a)-1, (b)-1, (c)-1, (d)-1).

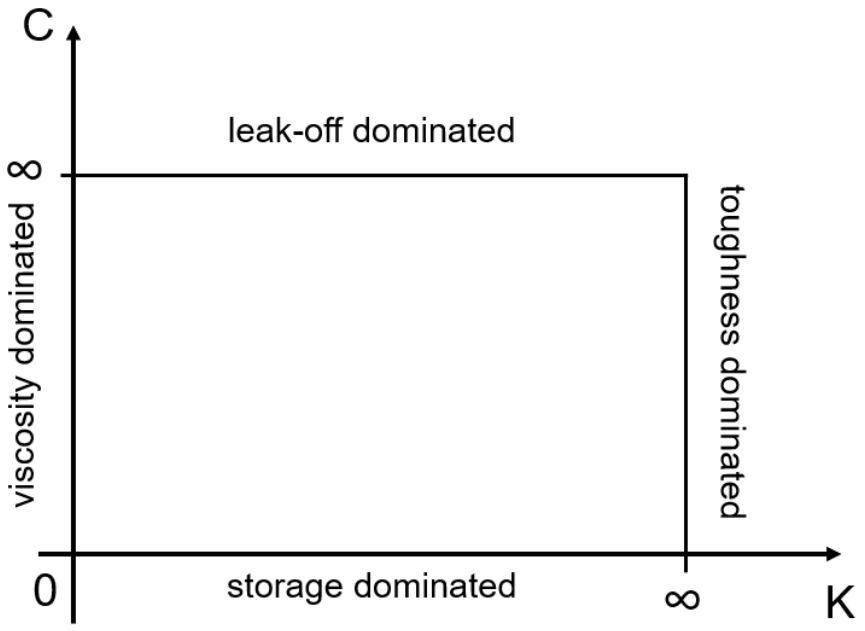

Figure 3.28 Hydraulic fracture parametric space (modified from the work of Carrier et al. 2012 [46])

3.3.5 Modeling results of the operation with various fluid viscosity and leak off

In the previous phases, the impacts from fluid viscosity (ignore the leak off process) and leak off on the stimulated results have been studied separately. However, in actual operations the viscosity of fluid will not only influence the shape of fracture, but also affect the leak off. Thus, a question would be, if both the effects are considered, which would be more significant?

In this section, operations with various fluid viscosities (μ = 1 cP is still the basic value) were simulated again. The difference to 3.3.3 is that the leak off process was also considered. Fig. 3.29 shows the width distribution of each variation at the end of operation (t = 80min). Unlike before, although the final heights of fracture in these variations are almost the same, the length and width of fracture have changed drastically with the diversity of viscosity. Considering that the pay zone permeability in all variations are identical, impacts on the results could only come from the fluid viscosity. That is, in this phase the change in fluid viscosity takes a huge impact on the leak off process. Thus, the diverse viscosity of fluid resulted in dramatic changes in the shaping of fracture.

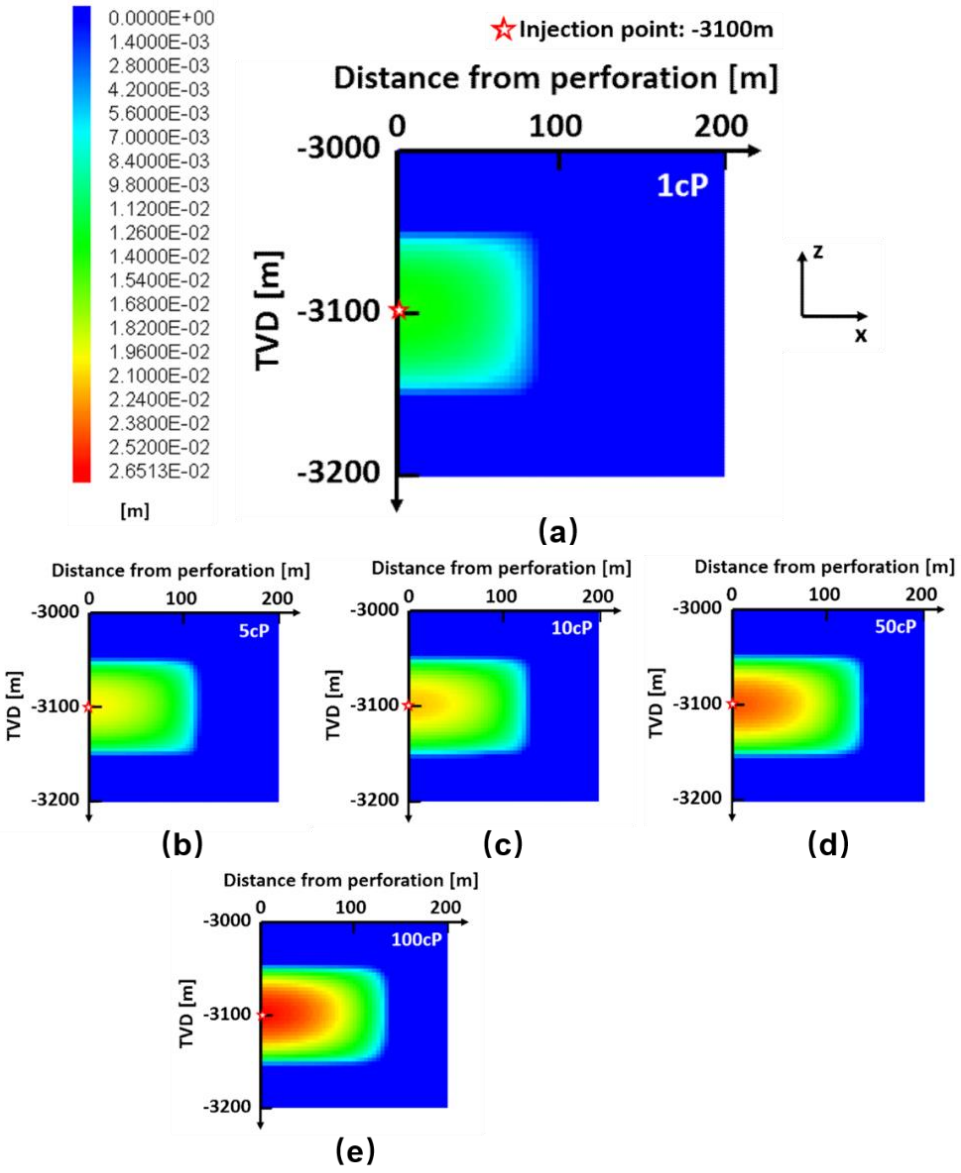

Figure 3.29 Comparison of width distributions for simulations with different fluid viscosities ((a): μ = 1cP; (b): μ = 5cP; (c): μ = 10cP; (d): μ = 50cP; (e): μ = 100cP) at the end of the hydraulic fracturing operation (with leak off)

Fig. 3.30 to 3.32 gives more detailed comparisons. From the three figures it can be drawn out that not only the increasing of fracture length but also the evolution of fracture widths shows similar trends to those in 3.3.4. With a more detailed description: when the injected fluid possesses a higher viscosity (from 1 cP to 50 cP), the fracture expands faster not only in the length direction (Fig. 3.30 (a)) but also in the width direction (see Fig. 3.30 (b) and (c)).

This manifested an opposite trend to those of the first phase. In 3.3.3, since leak off process was ignored, the final shaping of the fracture was only controlled by the viscosity. Under such premise, the relation between the obtained fracture width and viscosity is proved to be opposite to that between the length and the viscosity, i.e. the larger the fluid viscosity, the slower the fracture expands in length direction, but the fracture would obtain a larger width since the beginning of the operation. Therefore, when the viscosity of fluid is in at a lower level, as it becomes more viscous, its impacts on the final shape by affecting the leak off is more significant than its direct influence. This is well confirmed by comparing with the results of the first and second phases.

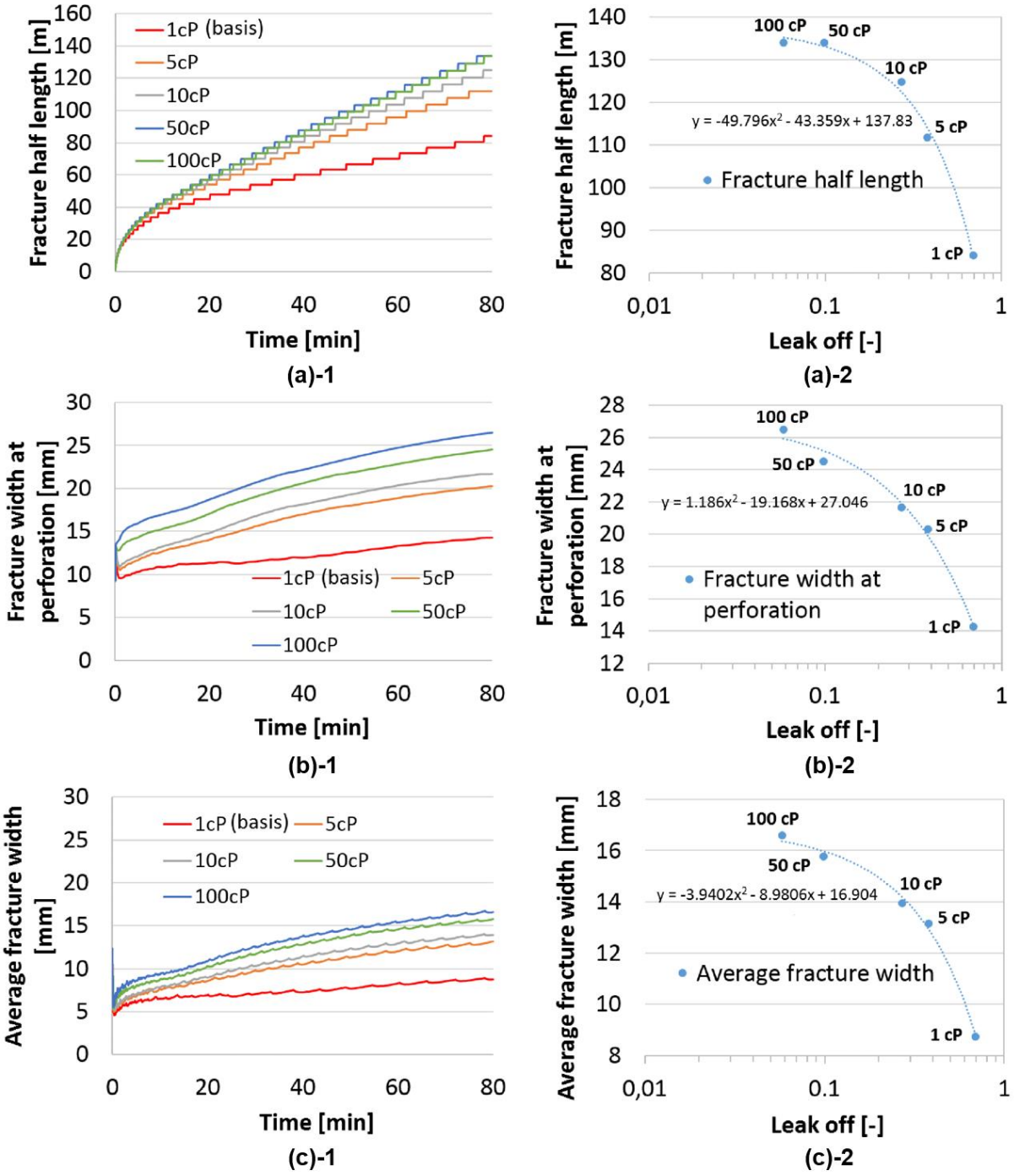

Figure 3.30 Evolution of (a) the maximum fracture half-length, (b) the actual fracture width at the perforation and (c) the average fracture width with time for different fluid viscosities, the functional curves describe the relationship between finally achieved results (t = 80min) and the fluid viscosity (with leak off)

However, in conjunction with Fig. 3.30 to 3.32, it must be pointed out that the above phenomenon will become insignificant (in Fig. 3.30 (a) and Fig. 3.31 the fracture half-lengths of 50 cP and 100 cP are the same) when the leak off is slow due to more viscous fluid (see Fig. 3.32, the leak off ability reduced from 10%/80 min to about 6%/80 min, as the fluid viscosity increased from 50 cP to 100 cP). Or, this moment, the dominated storage mechanism changes from leak off (in porous formation) to storage (in fracture) [46]. Thus, decisive impacts on the final shaping come from the competition results between two energy dissipation mechanisms (viscous flow and fracturation).

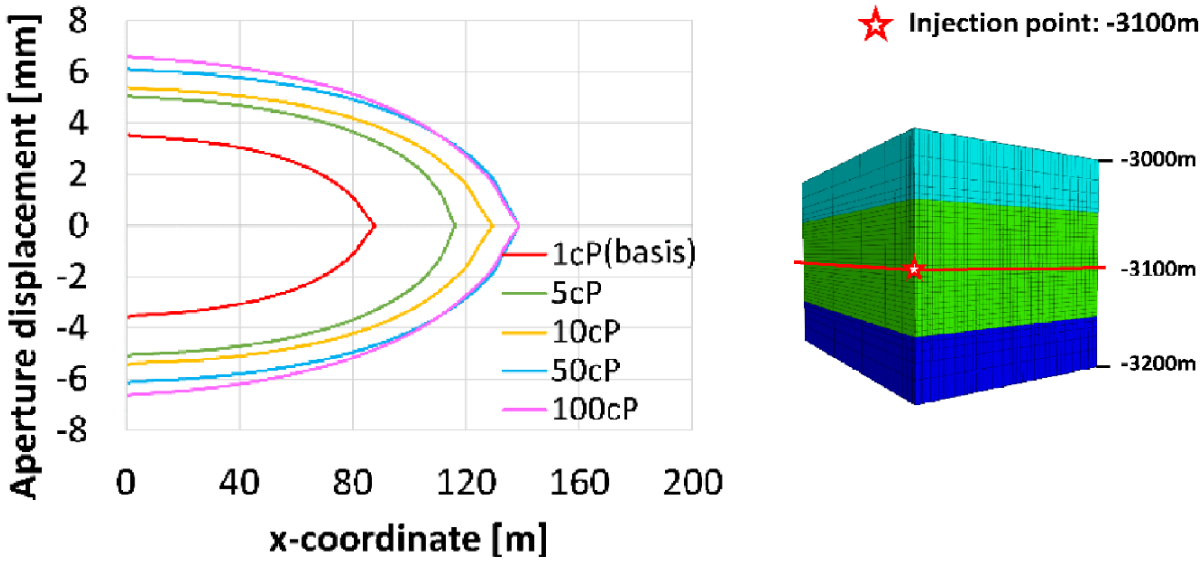

Figure 3.31 Comparison of the width profiles with different fluid viscosities at the end of stimulation (at the depth of -3100 m, with leak off)

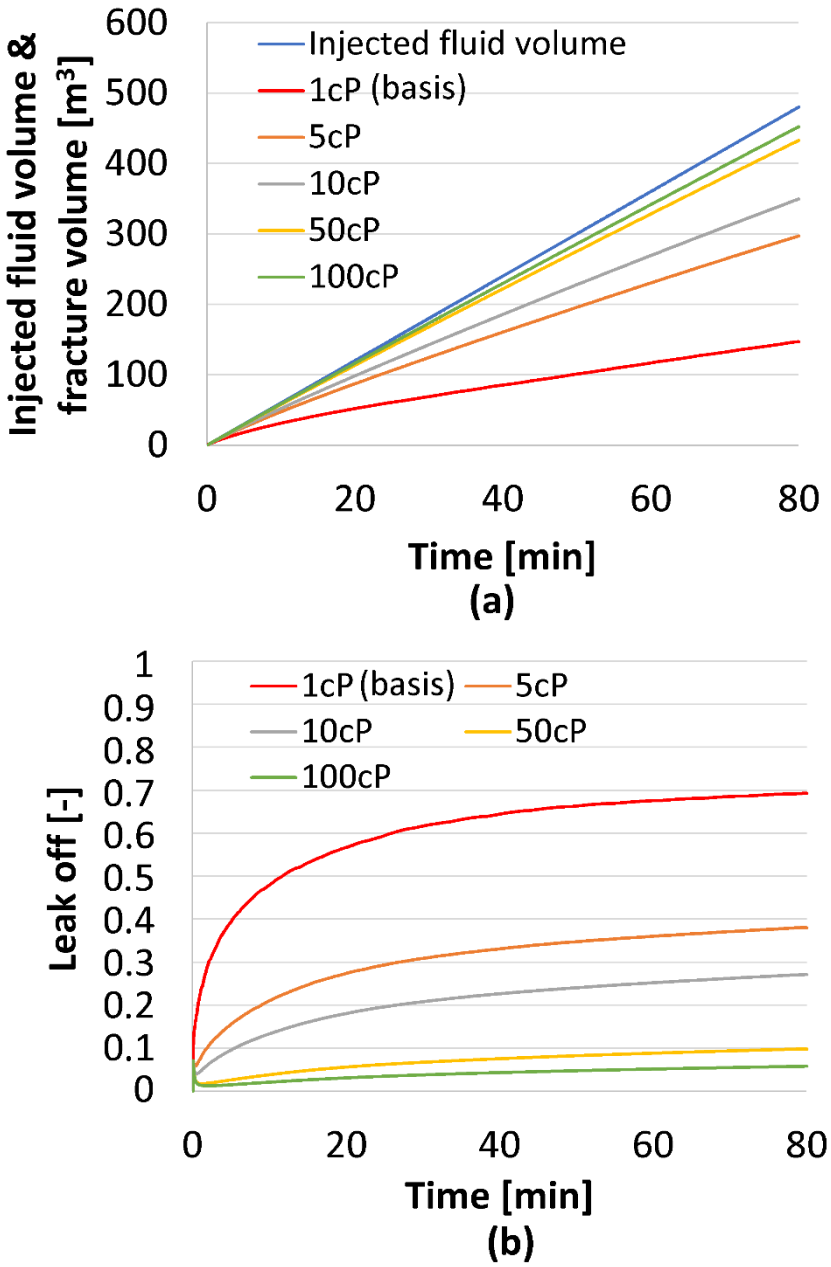

Figure 3.32 Evolution of (a) the volume of the injected fluid and the fracture volume over time for operations with different fluid viscosities and (b) the corresponding leak off coefficient (with leak off)

Then, Fig. 3.33 continues to show the changes of minimum horizontal stress and pore pressure. As with the previously described developing trend in fracture length and width, whether it is σ_h or P_p, when the fluid viscosity is still in at lower level, their changes will be affected significantly. These effects are caused by the stronger leak off ability (Fig. 3.32).

More specifically, when the fluid is not so viscous, the increase in σ_h will be weakened by the increase of leak off significantly (Fig. 3.33 (a)-1 to (c)-1). The increase of P_p will be significantly enhanced for the same reason (Fig. 3.33 (a)-2 to (c)-2). Once the fluid becomes more viscous, the leak off during the operation is greatly reduced. Currently, the growth of the minimum horizontal stress with increasing viscosity becomes less noticeable (Fig. 3.33 (c)-1 to (d)-1). The same trend applies to changes in pore pressure (Fig. 3.33 (c)-2 to (d)-2).

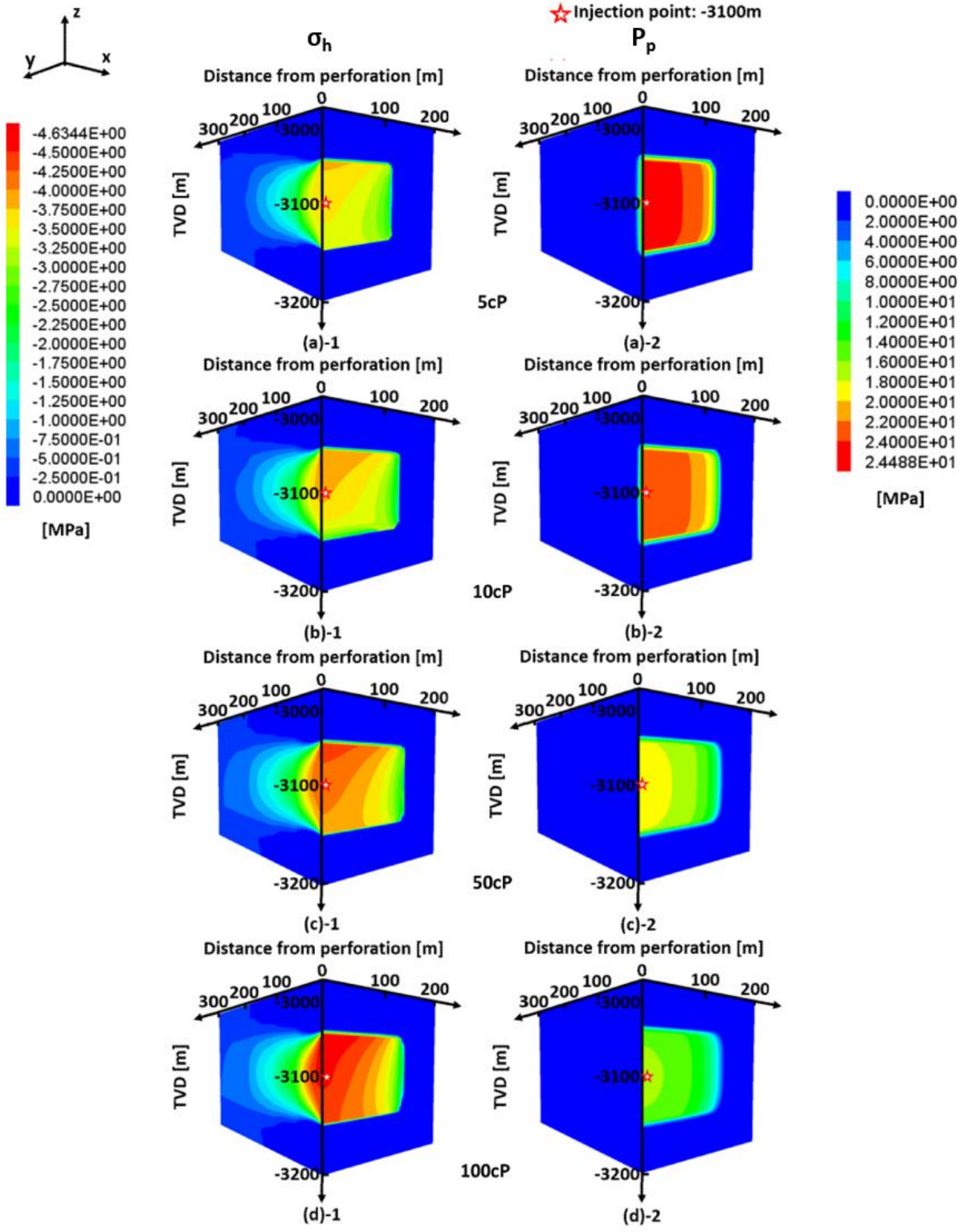

Figure 3.33 Increases of the minimum horizontal stress and the pore pressure for simulations with different fluid viscosities ((a): μ = 5 cP; (b): μ = 10 cP; (c): μ = 50 cP; (d): μ = 100 cP) at the end of the operation (t = 80 min) (with leak off)

3.3.6 Influences from the proppant

The research of previous phases has mainly focused on the fluid viscosity's affecting on the final shaping of artificial fracture in tight sandstone. In those cases, only the presence of fracturing fluid was considered. Conclusions from such premises have undoubtedly important guiding significance for the actual stimulation work, especially for those performed at the Hot Dry Rock (HDR) geothermal. Since the operation phase of these systems must inject and extract the heat-exchange medium continuously, they possess high requirement for the fracture shape after shut in.

However, in other exploitation projects that are also carried out in tight sandstone, such as the extraction of tight gas, man often need to add proppant during the fracturing process (the mixture of fluid and solid proppant is called as slurry) so that the fracture can still maintain a certain shape (not completely close) after the fluid being totally lost (see Fig. 3.34). Thus, considering the fluid viscosity's influences on the final distribution of the proppant, e.g. through its proppant-carrying ability and the impacts on leak off process, becomes the research focus of the last phase.

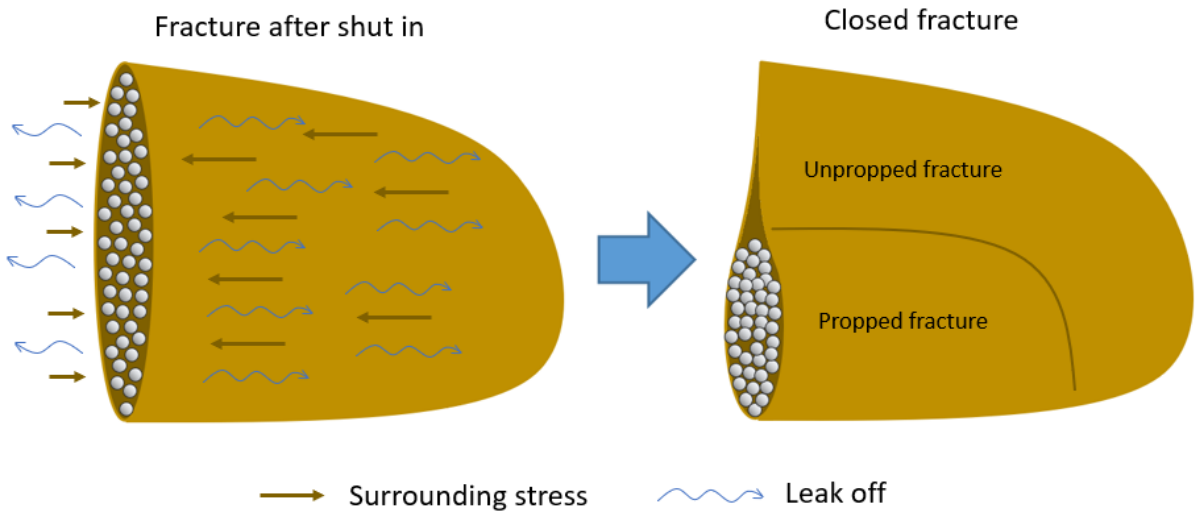

Figure 3.34 A schematic of the proppant's placement before and after the fracture closure: actions of the leak off and the surrounding stress lead to uneven distribution of proppant

3.3.6.1 Governing equations in FLAC3D^{plus} to describe the relationship between proppant concentration and slurry viscosity

In FLAC3D^{plus}, in order to describe the relationship between the slurry viscosity and the proppant concentration, a mathematical model (Eq. 3.19) derived from the works of Barree et al. [35] (Eq. 3.17) and Eissa et al. [43] (Eq. 3.18) is used. In this equation, the correlation coefficient possesses a value between 1 and 3, whereas C_{max} has a value between 0.59 and 0.65. C_{max} means that with this concentration the fracture system has entered a compacted/closure status. Through this model, not only the lower (in this region the slurry behaves more like a Newtonian fluid) and higher (in this region the slurry is more like a shear thin fluid) shear rate region, but also the transition region is taken into account. To better demonstrate the situations described by Eq. 3.20, Fig. 3.35 is illustrated, in which the value of C_{max} is 0.65.

$$\mu_a = \mu_0 \left(1 - {}^{C}/_{C_{max}}\right)^{-a} \tag{3.17}$$

$$\mu_a = \mu_0 \frac{tan^{-1}\left(\frac{\gamma}{\gamma_L}\right)^{n-1}}{tan^{-1}\left(\frac{\gamma}{\gamma_H}\right)^{n-1}} \tag{3.18}$$

$$\mu_a = \mu_0 \left(1 - {}^{C}/_{C_{max}}\right)^{-a} \frac{tan^{-1}\left(\frac{\gamma}{\gamma_L}\right)^{n-1}}{tan^{-1}\left(\frac{\gamma}{\gamma_H}\right)^{n-1}} \tag{3.19}$$

Where μ_a is the apparent viscosity [Pa·s], μ_0 is the fluid viscosity [Pa·s], C is the proppant concentration [kg/m^3], C_{max} is the maximum proppant concentration [kg/m^3], a is the correlation coefficient [-], γ is the apparent shear rate [1/s], γ_L is the critical shear rate to limit low shear rate region [1/s], γ_H is the critical shear rate to limit high shear rate region [1/s], n is the coefficient [-].

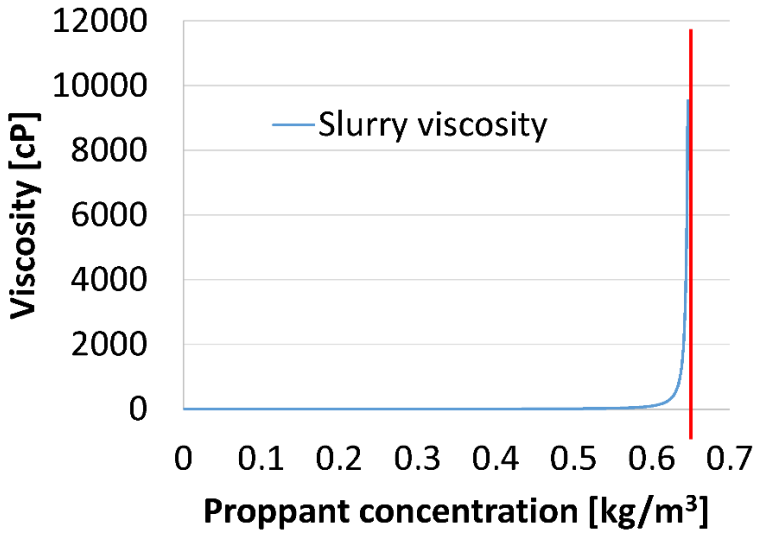

Figure 3.35 Evolution of the slurry viscosity with increasing of the proppant concentration

3.3.6.2 Results of further modeling

Based on above model, applying the same values of viscosity in 3.3.5, various simulations were performed again. However, in order to inspect the fracture shape at the compacted status, the simulation time of μ = 1 cP to 10 cP were extended to 1000 min, for μ = 50 cP and 100 cP it was extended to 5000 min. Thus, the modeled results shown in Fig. 3.36, 3.37 and Appendix A were obtained.

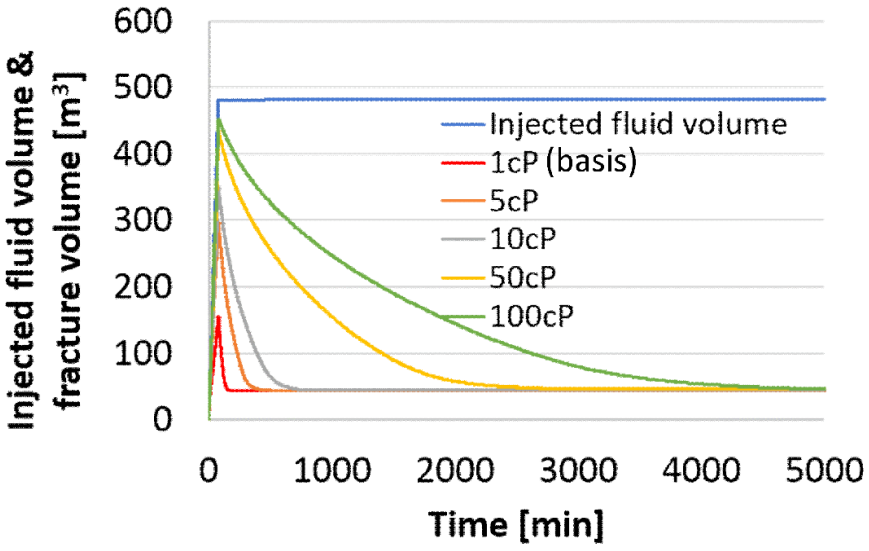

Figure 3.36 Evolution of the fracture volume with time considering various viscosities of fracturing fluid

Since the generated fracture with different fluid entered the compacted status at different times (Fig. 3.38), but the final achieved facture volumes are the same, i.e. it should be the actual volume of the solid proppant considering C_{max} = 65%, in Fig. 3.39 and Appendix A, the fracture shapes (length, height and width distribution) at the end of stimulation (shut in) and at the compacted status are presented. Through detailed comparison, a series of phenomena can be figured out. The increased viscosity of fluid enhances its proppant-carrying and weakens the leak off ability. Combined with the previous results, this trend on the one hand makes the fracture be larger in length and width (Fig. 3.37 (a)), when the slurry possesses a higher viscosity, on the other hand, stronger proppant-carrying ability makes the proppant more tend to distribute in the length direction. As shown in Appendix A, in all the variations the distribution of proppant in length direction is equivalent to the length of the fracture. Since amount of the added proppant is constant and the closure widths of the fracture are almost the same (Fig. 3.37 (b)), when the proppant has a larger distribution in the longitudinal direction, its distribution in the height direction will be reduced (Appendix A). When the amount of proppant is below a reasonable value, its distribution in height will eventually be farther away from the injection/production point. However, for practical operation in a tight gas reservoir, the fluid viscosity changes due to time and temperature conditions. Therefore, for a more accurate simulation of the fracturing work in tight gas, the influences from gel breaking process should be considered.

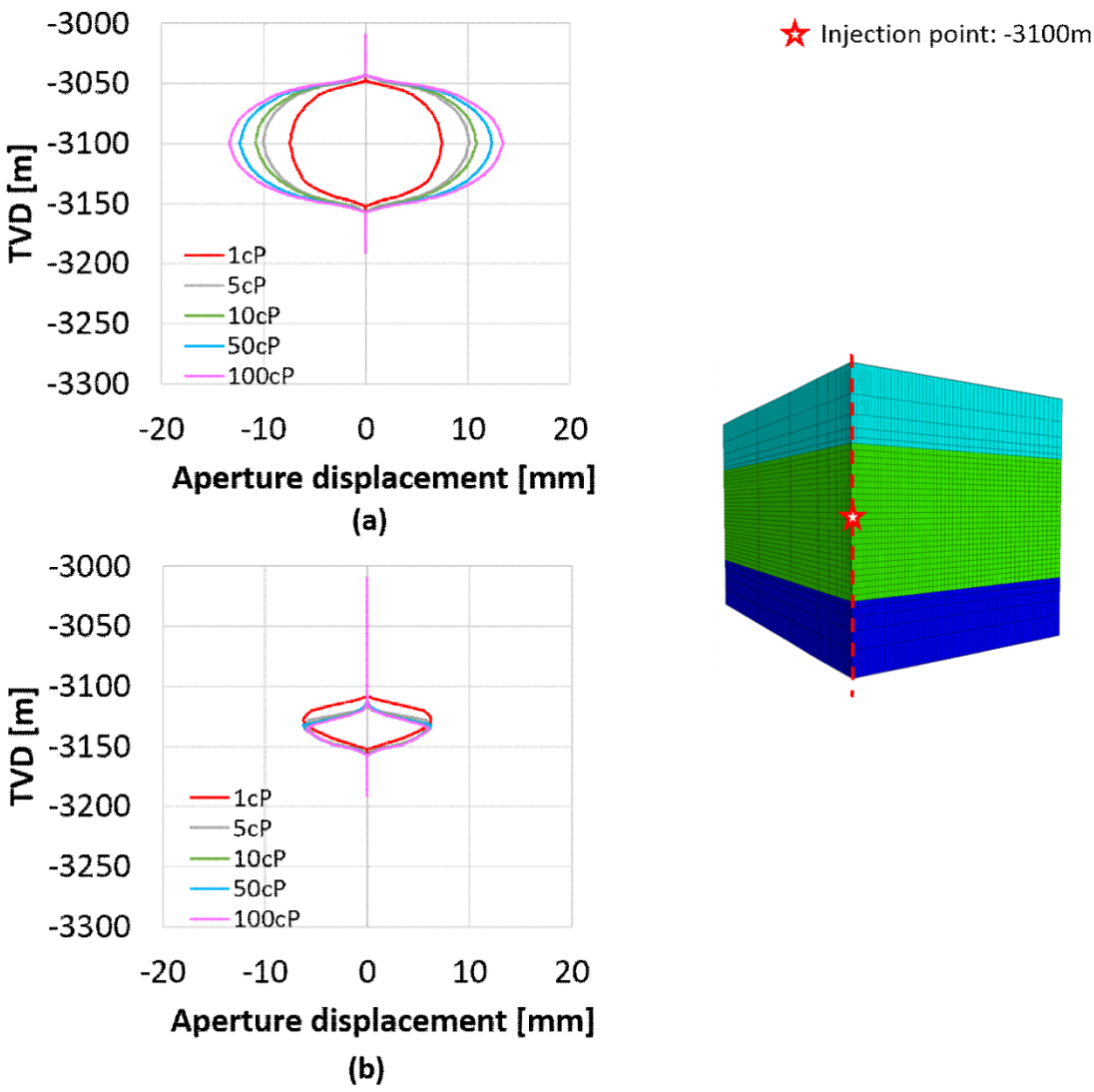

Figure 3.37 Comparison of the width profiles with different fluid viscosities (a) at the end of stimulation and (b) at the compacted status (at the position of x = 0 m, with leak off)

3.4 A real case study to investigate the fluid viscosity's influences in practical operation in consideration of thermal effects and THM coupled processes - stimulation operation in tight gas reservoir Leer

After introducing the theoretical background and giving a detailed and systematical numerical study using the fictive model, what follows is a real case study to investigate the fluid viscosity's impacts on the results of the stimulation work in consideration of the thermal effects and THM coupled processes.

3.4.1 Information of the gas field Leer

Leer is a natural gas field lying in the North German Basin (see Fig. 3.38). According to the work of Koehler et al. [47], its structure is located about 5 km SSE to the city of the same name.

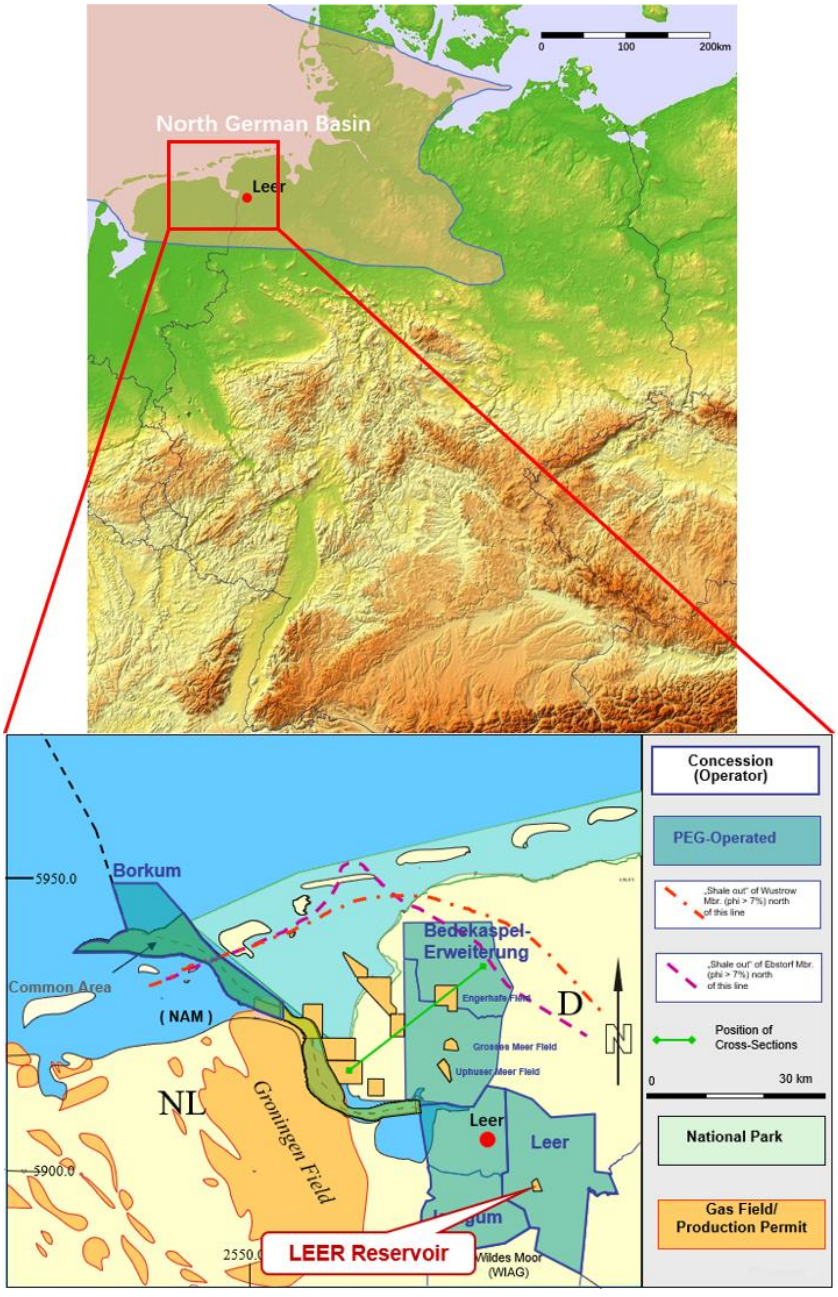

Figure 3.38 Location of the North German Basin relative to Germany and the prospect location map of Ostfriedsland licenses and gas fields with the positions of Leer city and corresponding gas field (modified from www.scilands.de and Koehler's work of 2004 [48])

The exploitation of Leer field started from the beginning of 1970s. Since its subordinate gas reservoirs were proved to lie primarily in the "tight" sandstone formations (Fig. 3.39), namely the Bahsen- and Wustrow-Member in this area (through the exploration well Leer Z2) [49], which only possesses very low permeability, the application of stimulation methods becomes crucial.

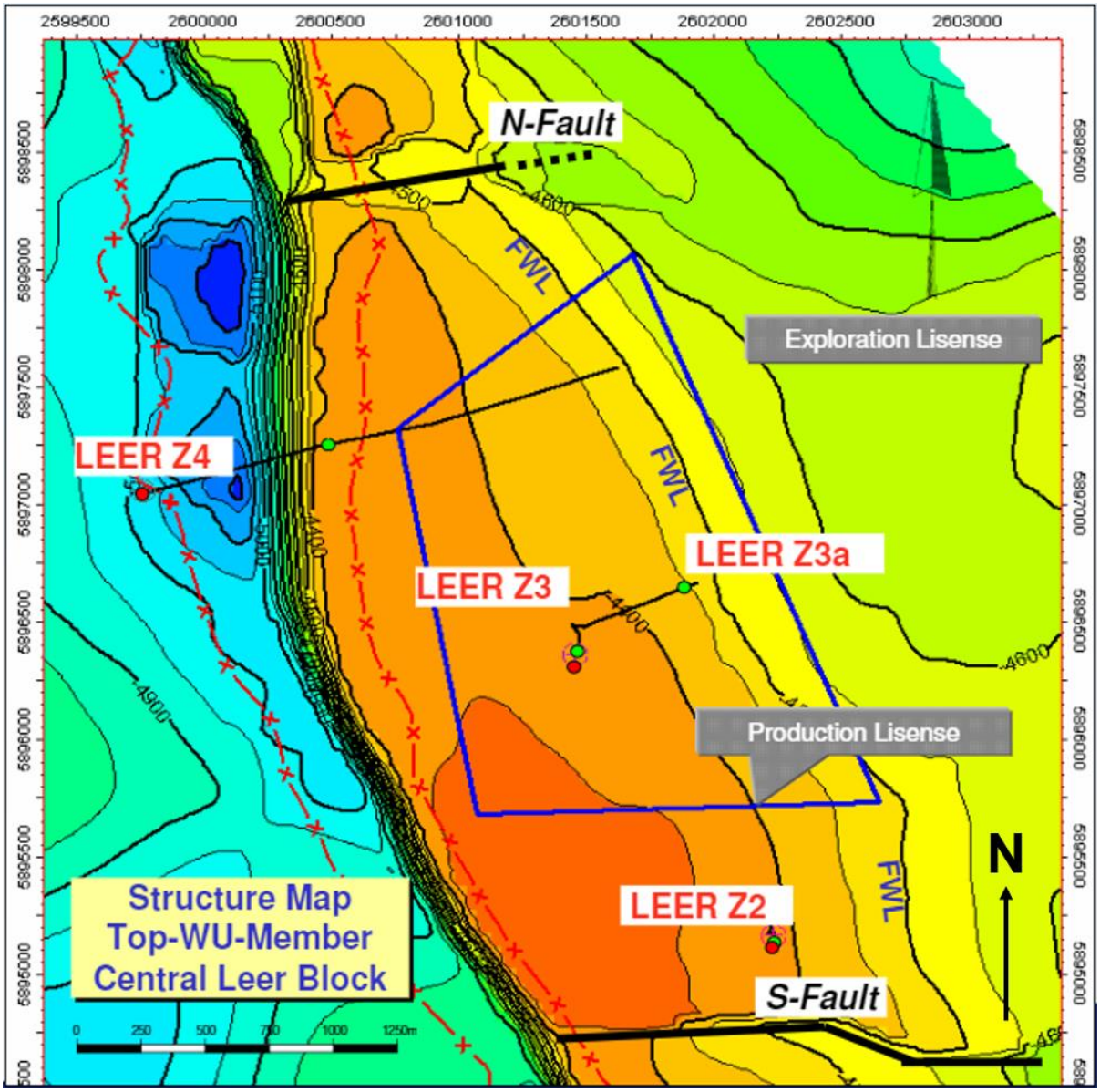

Figure 3.39 Structure map of Top-WU-Member in Central Leer Block at 11/2015 (modified from Gaz de France [50])

3.4.2 Model generation and parameters of Leer reservoir

In this dissertation, in order to investigate the influences from fluid viscosity on the stimulated results, also considering the thermal effects and THM coupled processes, one stage of hydraulic fracturing at the reservoir Leer was modeled.

To achieve this goal, a 1/2 model in Fig. 3.40 (l × w × h: 150 m × 170 m × 215 m) was used. Simultaneously it presents the stratigraphy of the target area. In the actual work, the target pay zone of the well is located at the depth from -4310 to -4409 m. Just like other wells (in this field), the reservoir is mainly composed of sandstone. Apart from this, the uppermost (from -4,290 to -4,347 m, Δz = 57 m) and the lowest (from -4,394 to -4,505 m, Δz = 109 m) formations are intercalated with shaly interlayers, this structure is believed that can provide efficient hydraulic barrier in the stimulation operation.

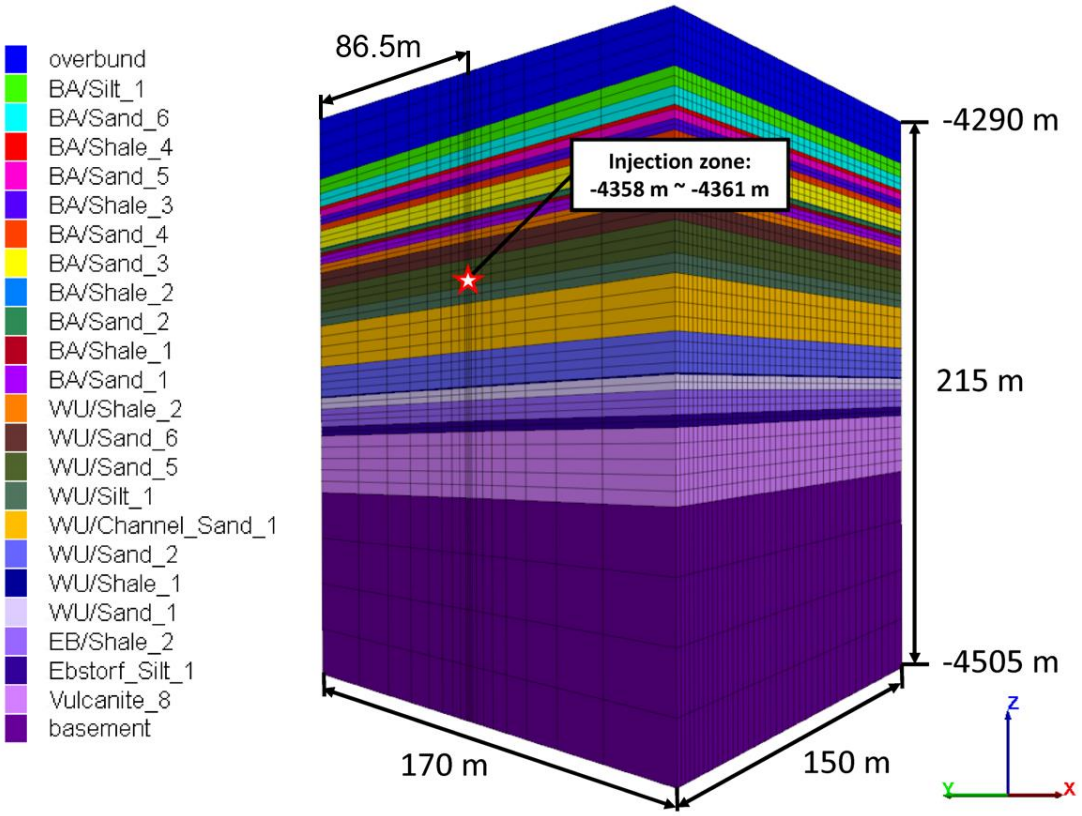

Figure 3.40 Graphic presentation of the stratigraphy and the geometric model of the tight gas reservoir Leer

Fig. 3.41 shows the variations of primary vertical stress, minimum horizontal stress and pore pressure. The minimum horizontal stress in the shale layers, overburden (mainly composed of anhydrite) and basement (mainly composed of granite) are larger in comparison with those in other formations. Meanwhile the pore pressure gradient in the entire target area is considered to be relatively low. The thickness of overburden and basement is also large enough. It is for this reason that these formations are considered as barriers for preventing the fracture from propagating above and below the reservoir. The corresponding mechanical, hydraulic and thermal properties of the formations are listed in Appendices B and C.

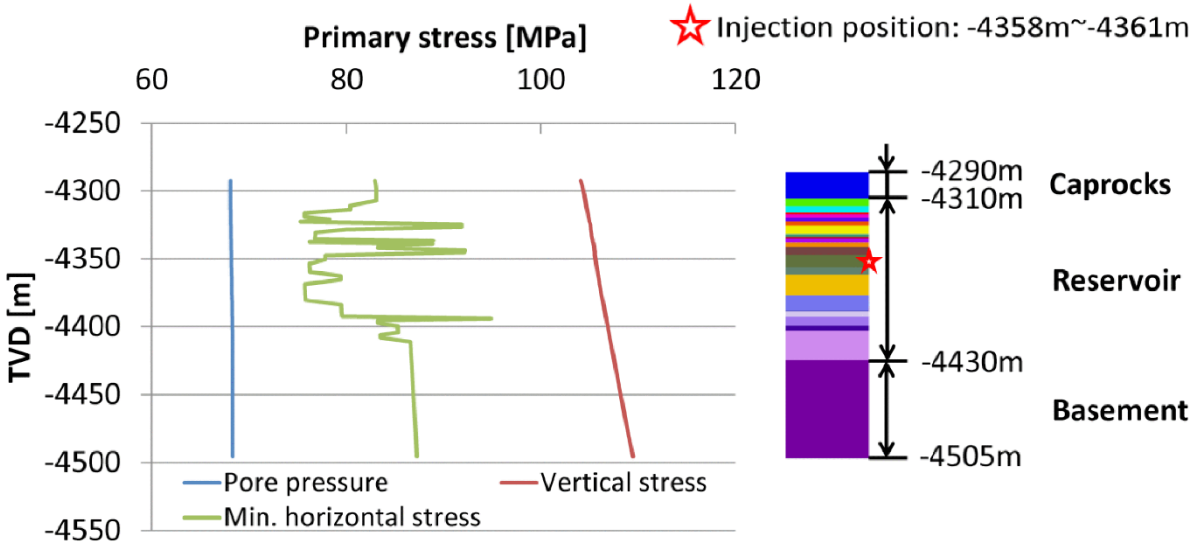

Figure 3.41 Variation of the primary vertical stress, the minimum horizontal stress and the pore pressure with depth in the reservoir and barrier formations of Leer

For considering the thermal or rather THM effects during the stimulation process, the temperature data must be applied to the model. As the area of Leer possesses a thermal gradient of 2.271 °C/100 m, its initial top to bottom temperature before the treatment ranges from 146 °C to 151 °C (see Fig. 3.42).

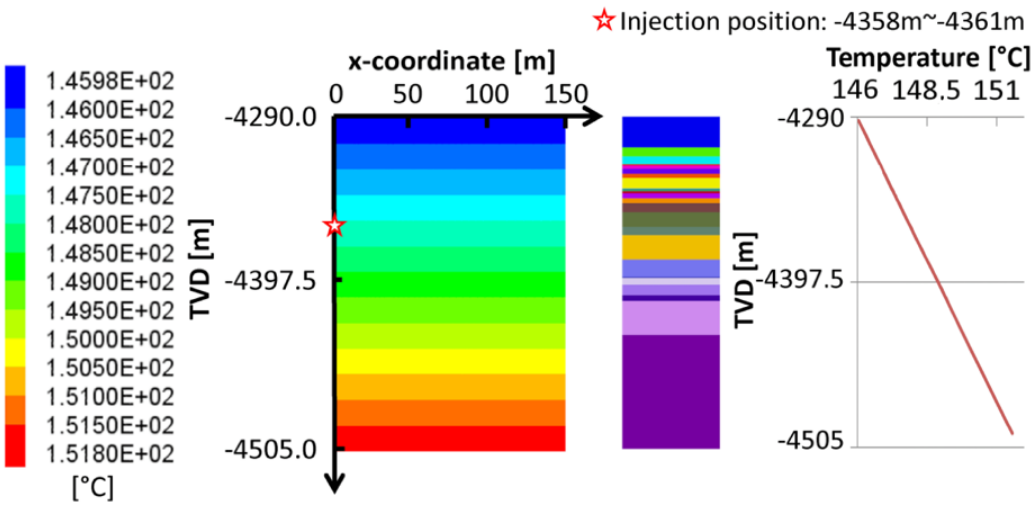

Figure 3.42 Temperature distribution in the reservoir Leer before stimulation operation

3.4.3 Injection schedule and change of the fluid viscosity with time and temperature

On the specific treatment schedule, during the operation which lasted for 86 min, a total volume of 427 m^3 fracturing fluid (density 1040 kg/m^3 and temperature 50 °C) loaded with 142,000 kg of proppant was injected into the target formation. Later (after ca. 27 minutes), solid proppant with a radius of 0.67 mm was added. The actual variations in injection rate and proppant concentration with time are represented graphically in Fig. 3.43. The data derived from these treatment schedules was used for the subsequent simulation.

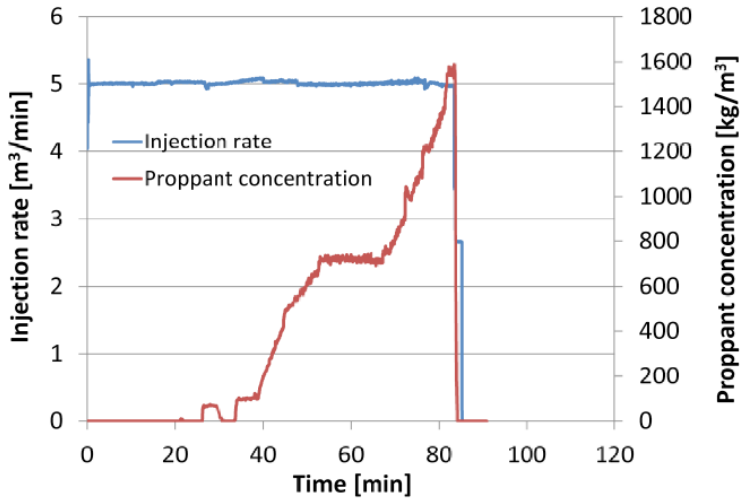

Figure 3.43 Variation of the injection rate and proppant concentration with time during stimulation operation in the target pay zone of Leer

At the same time, in order to model the influences of time and temperature on the fluid viscosity (thermal effects on fluid's properties), the viscosity was implemented to the simulator as a binary function of these two variables (see Fig. 3.44). Specifically, as time goes by and temperature raises, the fluid viscosity gradually decreases from 870 cP (80 °C, t = 0.1h) to 4.2 cP (160 °C, t = 10 h), i.e. becomes smoother. And, it should be noted that this process is irreversible.

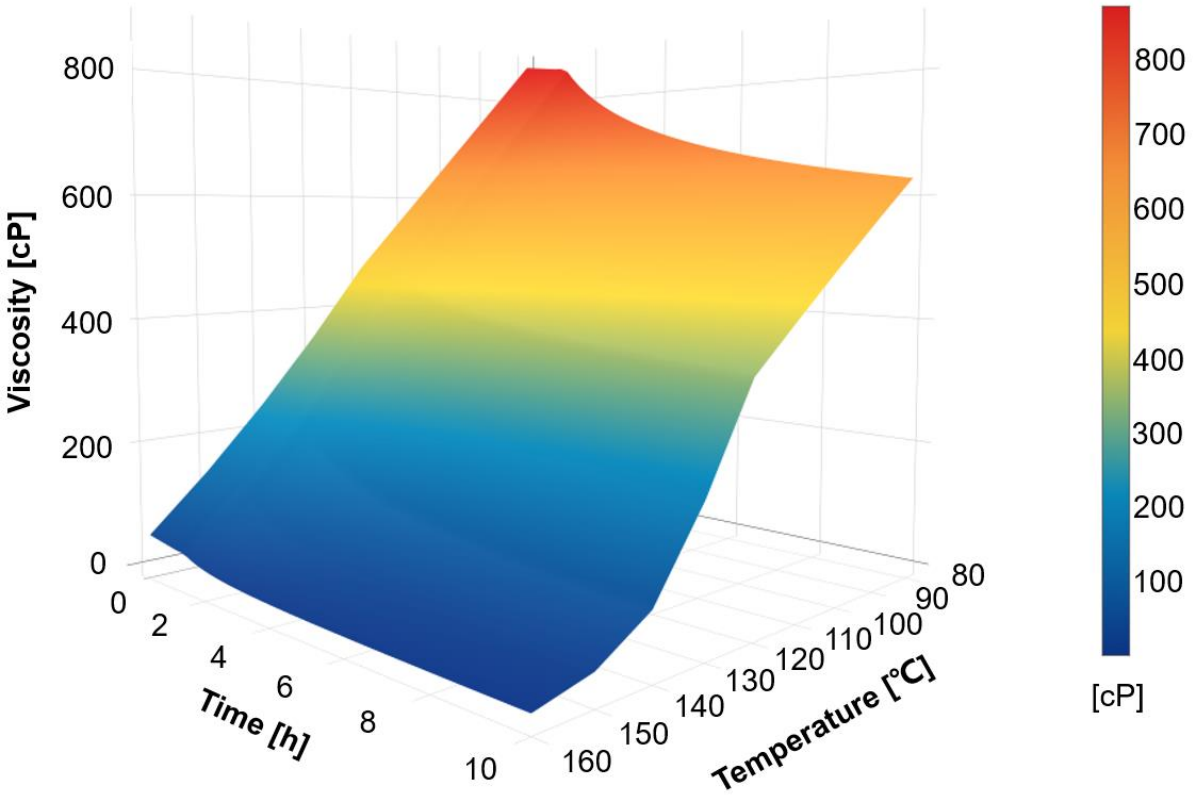

Figure 3.44 Variation of the fluid viscosity depending on temporal evolution and change of temperature

3.4.4 Modeling results

The simulation with consideration of thermal effects and THM coupled processes was based on history-matching of the in-situ measured wellhead pressure (WHP) obtained by logging data (120 minutes). However, for more practical analysis the hydrostatic pressure in the borehole and the friction loss along the path are added to the WHP so that it can be trans-

ferred to the bottom hole pressure (BHP). Fig. 3.45 reveals that the calculated BHP reasonably match the WHP measured in-situ (here transferred to the BHP). The unstable section at the end of operation is caused by pre-mature screen out [49].

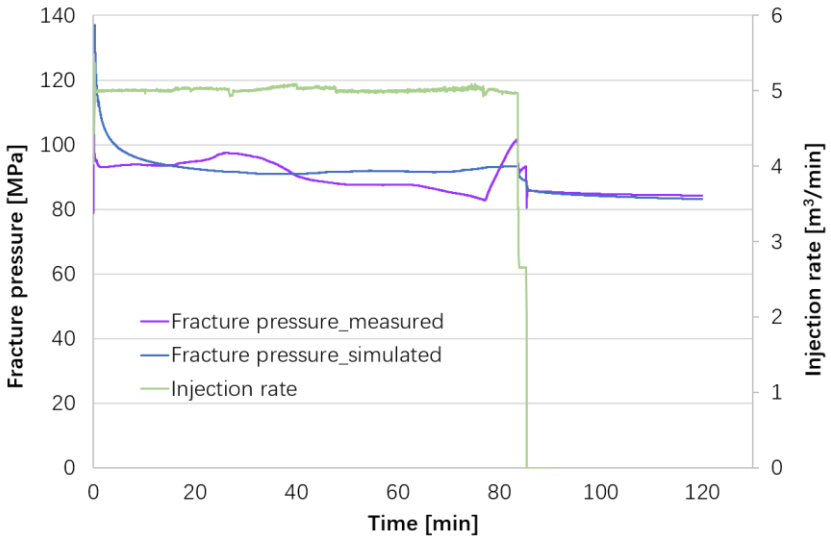

Figure 3.45 Comparison of the trends of the in-situ measured wellhead pressures with consideration of hydrostatic pressure and friction loss and the calculated bottom hole fracture pressures in consideration of thermal effects over time (t = 0 - 120 min)

In this study, the total duration of numerical modeling was set to 1000 minutes so that the influences from fluid viscosity under thermal impacts on the fracture's development can be better analyzed until the full closure. Tab. 3.3 lists some key parameters that can characterize the evolution of fracture. Simultaneously, it gives a comparison between the results after shut-in and after full closure.

Table 3.4 Simulated results (average reference values) for the development of a fracture in Leer after shut-in and after full closure

Parameter	After shut-in (t = 86 min)	After full closure (t = 1000 min)	Difference [%]
1/2 Frac length [m]	92	118	+28%
Frac height [m]	104	104	0%

Frac width (at perf.) [mm]	34.7	6.6	-81%
Ave. Frac width [mm]	16.5	4.0	-76%
1/2 Fracture area [m^2]	15030	19280	+28%
1/2 Proppant length [m]	92	118	+28%
Max. proppant conc. [kg/m^3]	0.63	0.65	+3%
Proppant / frac length [-]	100%	100%	0%
Leak off [%]	39%	83%	+113%

In both Tab. 3.3 and Fig. 3.46 it could be found that the 1/2 fracture length has increased further (+28%) after the injection being stopped. However, one thing must be pointed out that the 1/2 fracture length here actually refers to the maximum 1/2 fracture length, i.e. the distance from the farthest end of fracture to the perforation in length-direction. Therefore, the analysis for its development should also be combined with the subsequent contour figures. So, reasonable conclusions can be derived.

Meanwhile, the fracture height stayed unchanged from the shut-in to the full closure (see Tab. 3.3 and Fig. 3.46, no difference in fracture height). It is obvious that due to the strong geological barrier integrity (higher mechanical strengths and tectonic stresses) the fracture cannot propagate beyond the upper and lower limits.

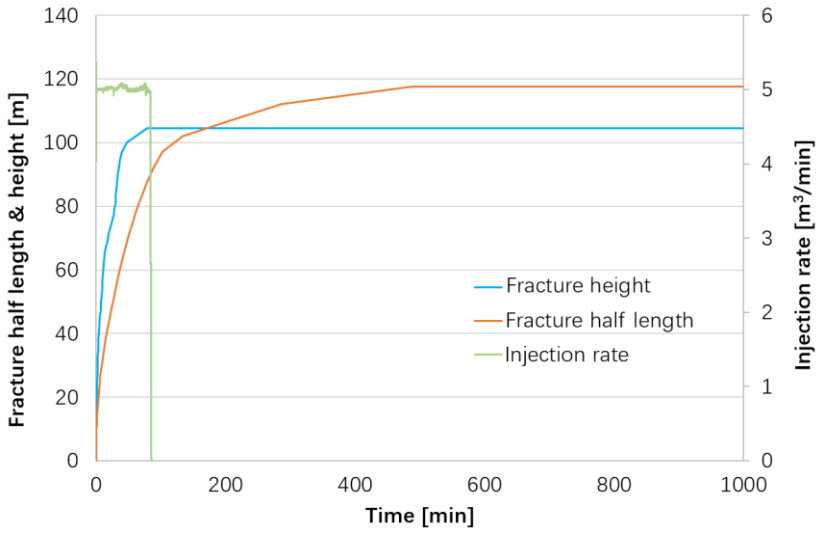

Figure 3.46 Development of the maximum fracture half-length and the height with time

Fig. 3.47 shows the temperature distribution within the generated fracture and in its surrounding rock formations (along the vertical and the horizontal directions). In order to better demonstrate the thermal development over time, some representative time points are selected, respectively t = 0 min, 22 min, 50 min, 86 min, 120 min and 1000 min. Temperature contours corresponding to these time points represent that during the injection phase the area around perforation maintains a temperature of ca. 50 °C (Fig. 3.47 (a) to (d)), same as the injected fluid. However, after the beginning of shut-in, temperature in the entire fracture area has quickly recovered (Fig. 3.47 (e) and (f)). Especially as shown in Fig. 3.47 (e), the temperature has recovered from ca. 50 °C to ca. 126 °C within only 34 minutes. For this reason, it could be believed that the cold fluid injected in the fracturing process caused no significant impacts on the thermal environment of gas reservoir.

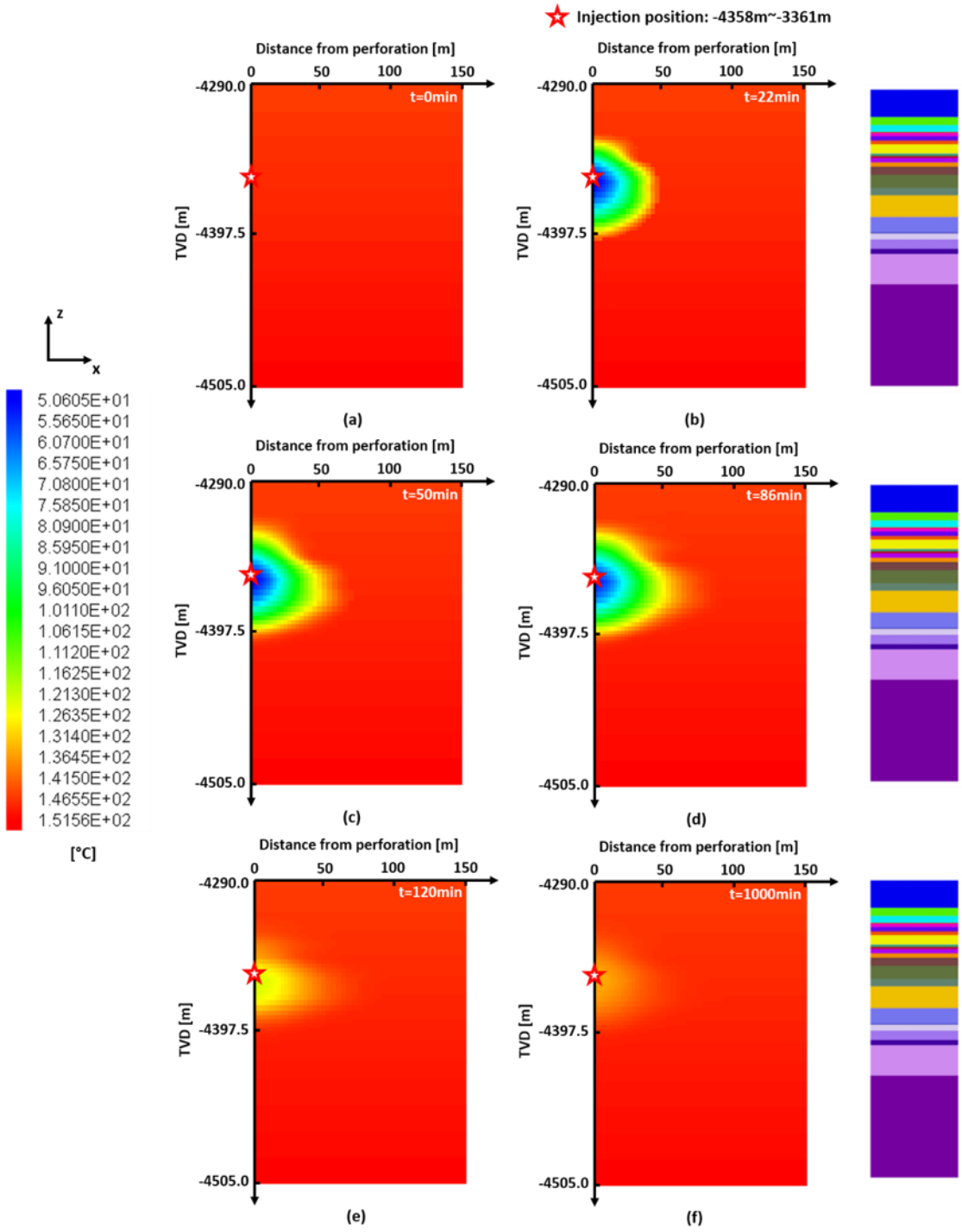

Figure 3.47 Simulated temperature distribution along the vertical and horizontal directions in reservoir Leer at time t = 0 min, 22 min, 50 min, 86 min, 120 min and 1,000 min

Despite of this fact, rapid heating of the fracture has led to major influences on other properties of the fluid. Moreover, through these impacts shape of the fracture was further changed. In this study, considering the fluid viscosity to be a binary function of temperature

and time (mentioned in 3.4.3), its temporal development within the fracture was simulated (Fig. 3.48).

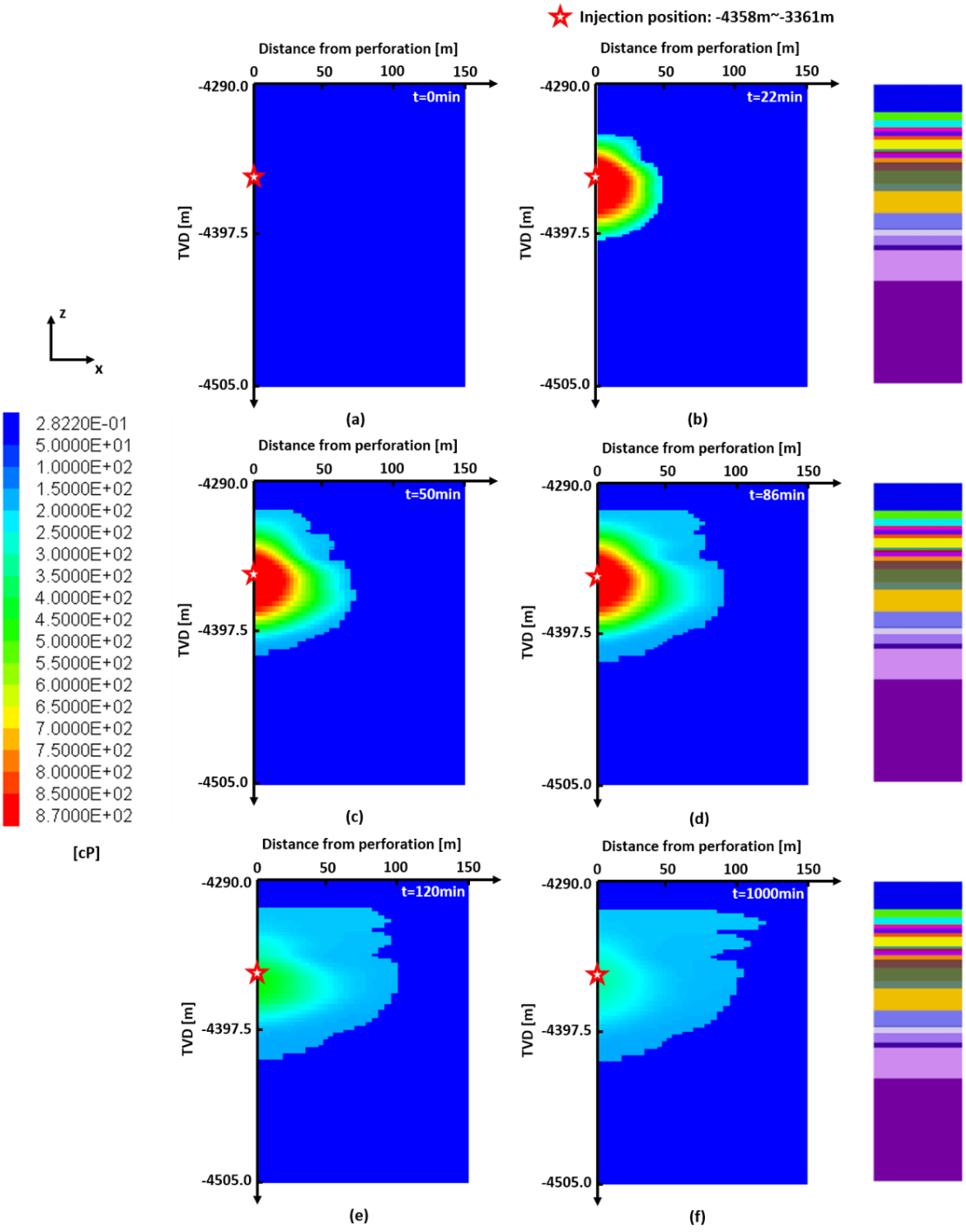

Figure 3.48 Simulated distribution of fluid viscosity in the fracture along the vertical and horizontal directions in reservoir Leer at time t = 0 min, 22 min, 50 min, 86 min, 120 min and 1,000 min

As mentioned before, analysis for the development of fracture length over time should be combined with the contour representations so that it could be more accurate. In Fig. 3.48 and 3.51, increase in the fracture length during the injection phase is mainly due to the increase of injected volume. The continuous low temperature around the perforation also makes the fluid to maintain a high viscosity. However, in the shut-in stage the continued growth of fracture length is actually concentrated at the upper area (above 4345.88 m, the lower area also expanded for a certain degree). This is on one side because some of the formations, in which the fracture's upper area is located, have a smaller minimum horizontal stress (Fig. 3.41, e.g. BA/Sand_5 and BA/Sand_3). For this reason, the propagation gained weaker restriction in these formations. On the other side, if the rock permeability listed in Appendix B is represented in the graphic form of Fig. 3.49, it is obvious that the formations above 4,345.88 m possess lower permeability (< 100 µD).

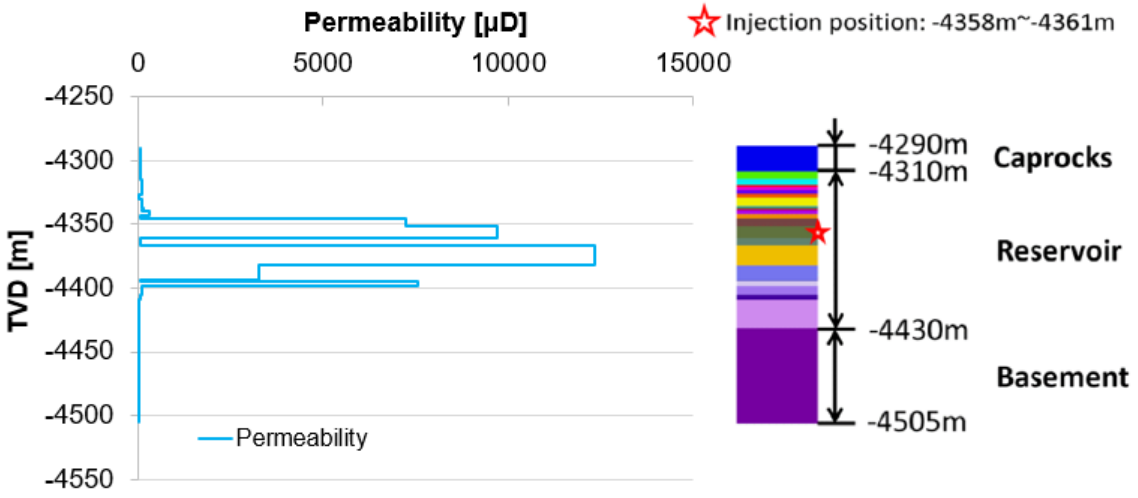

Figure 3.49 Variation of the rock permeability with depth in the reservoir and barrier formations of Leer

In conjunction with the conclusions from 3.3, i.e. the storage mechanism of a fracture tends to be in fracture-dominated, when the permeability is low enough, and with such a mechanism, impacts from the energy dissipation on final shaping would be more significant, the evolution trend of fracture length in upper area becomes more reasonable. Since infiltration ability of the upper area is obviously weaker, the fluid therein is prone to flow within the

fracture rather than leak off. Thus, because the fracture in these formations tends to propagate in the length direction rather than expand in the width direction (fluid not so viscous), it achieved a further expansion in length, after the operation has entered a shut-in stage. For the opposite reason, i.e. influences from leak off are more obvious, this trend becomes significantly weaker in other formations with greater permeability and smaller viscosity, e.g. WU/Sand_6 and BA/Channel_Sand_1 in the reservoir.

Different from the fracture's development in height and length, temporal evolution of the actual fracture width at the perforation and the average fracture width both show an increase in the injection phase and a decrease in the shut-in (Fig. 3.50). A little difference is that at the beginning of shut-in stage the fracture width at perforation reduced much faster than the average rate, since the area around perforation experienced a faster temperature recovery within this period (see Fig. 3.47 (e) and (f)), fluid viscosity in this area has also undergone more dramatic changes (see Fig. 3.48 (e) and (f)). As a result, the fracture width has changed more drastically.

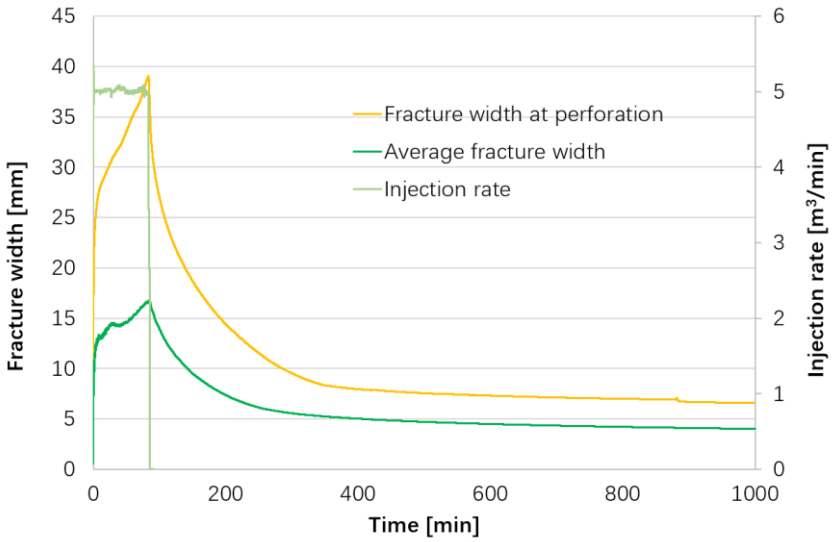

Figure 3.50 Temporal evolution of the actual fracture width at the perforation and the average fracture width

Moreover, during the shut-in stage the change of fracture width in upper area mainly comes from the forward flow of fluid inside the fracture (Fig. 3.51 (d), (e) and (f)). However, due

to the participation of leak off the artificial fracture eventually entered a compacted status (Fig. 3.51, 3.52 and 3.53).

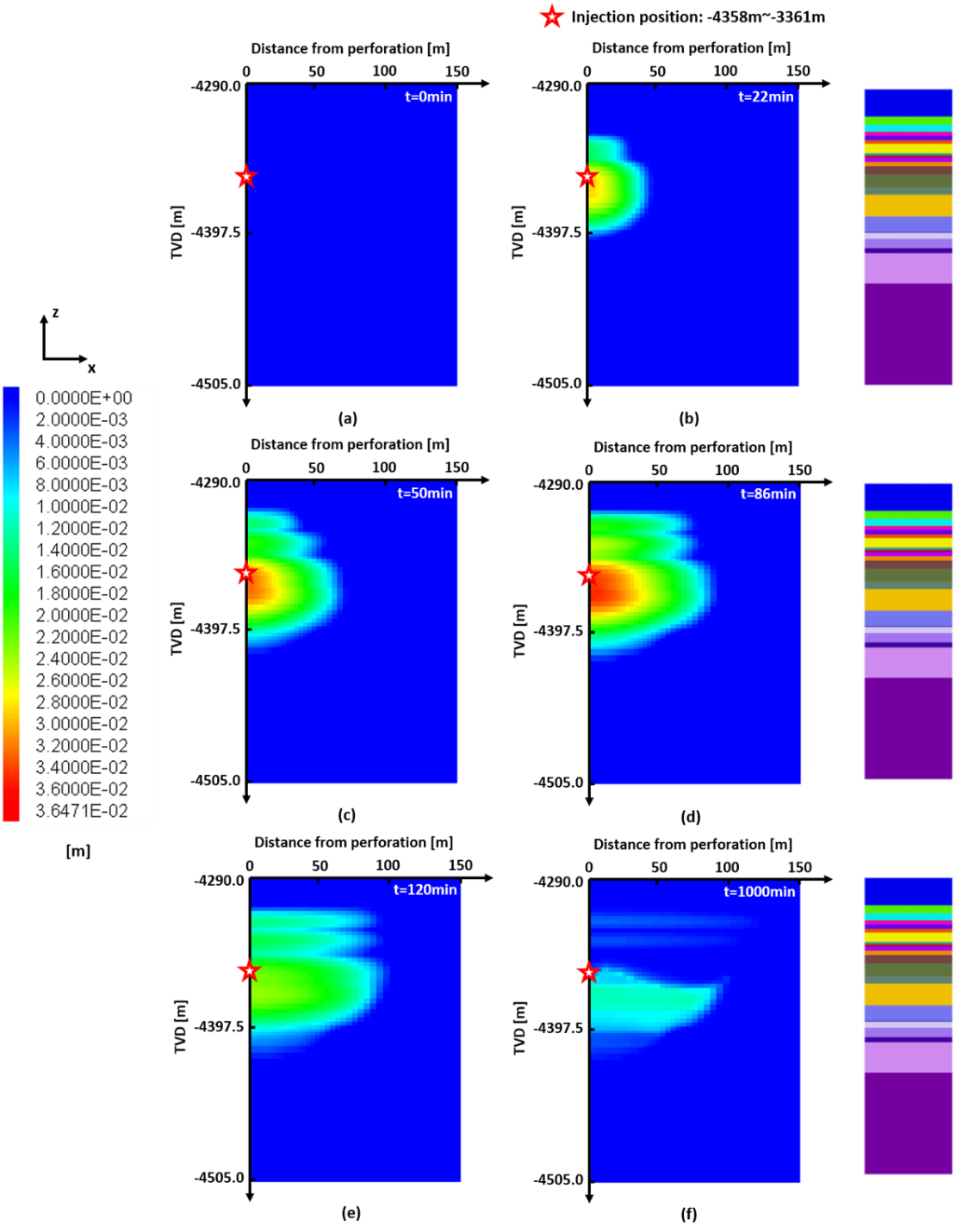

Figure 3.51 Simulated absolute fracture width along the vertical and horizontal directions in reservoir Leer at time t = 0 min, 22 min, 50 min, 86 min, 120 min and 1,000 min

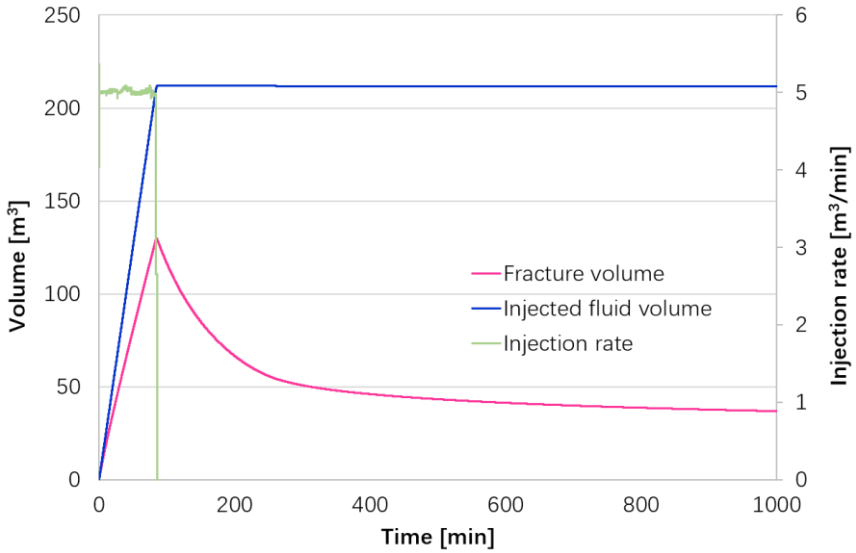

Figure 3.52 Evolution of the injection and fracture volume over time

Another point to be noted is that, as shown in Fig. 3.53, although just after adding the proppant a portion of the solid material is located above the perforation (later the production port) due to fluid's movement (see Fig. 3.53 (c) and (d)), during the process of gradually close, the proppant finally settles to a lower position due to the combination of water's friction force and gravity (Fig. 3.53 (d) to (f)). The situation in Leer is fortunate, as the final position of proppant created enough communication between the gas reservoir and the producing port. However, as mentioned in 3.3.6, in order to obtain sufficient production efficiency for every operation, a certain amount of proppant should still be added at the beginning of shut-in stage to offset the deposition impacts.

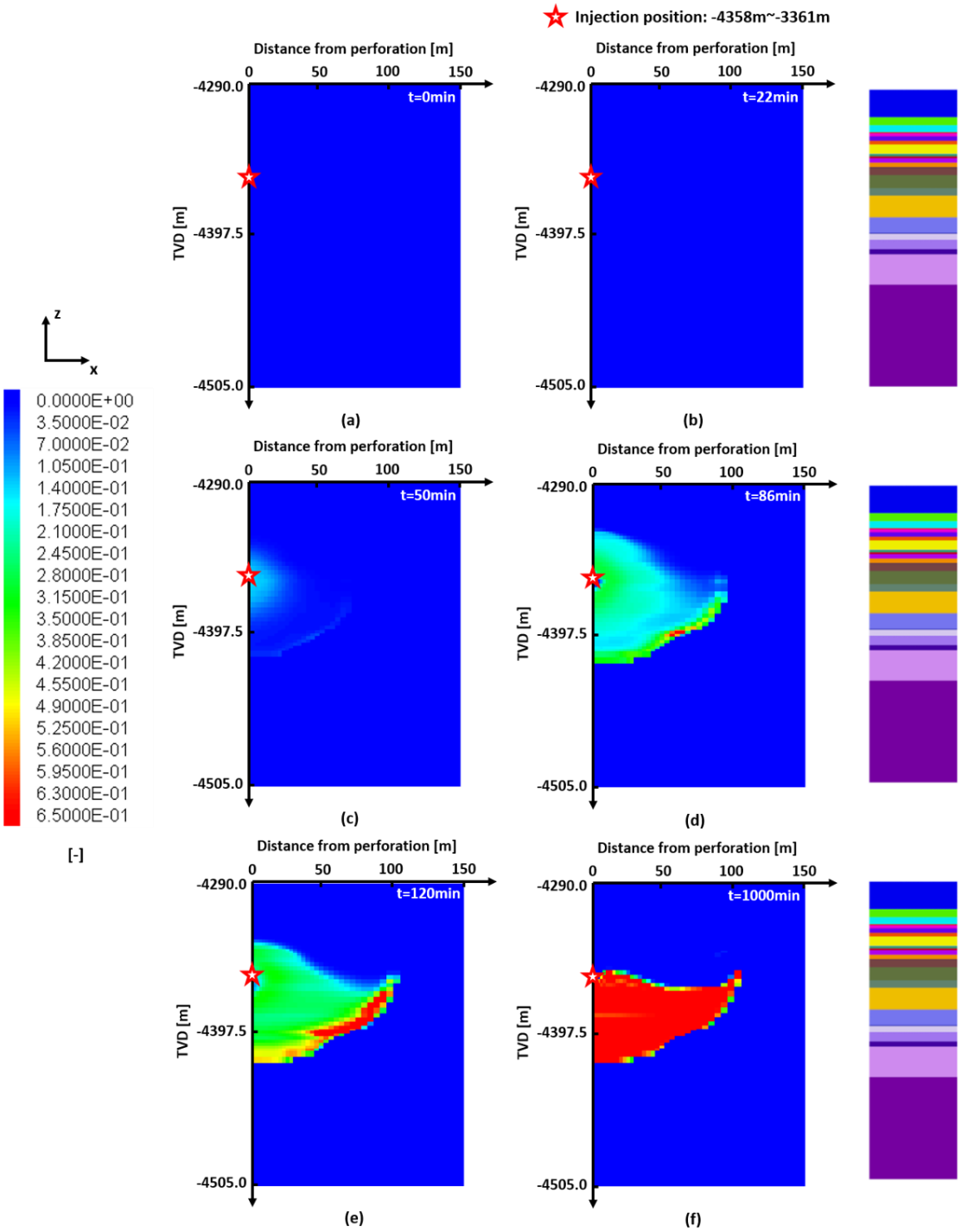

Figure 3.53 Simulated distribution of proppant concentration in the fracture along the vertical and horizontal directions in reservoir Leer at time t = 0 min, 22 min, 50 min, 86 min, 120 min and 1,000 min

Then, refocusing on the changes in minimum horizontal stress and pore pressure (Fig. 3.54 and 3.55), since the initial permeability of rock formations in Leer are not very high, and the fluid used for fracturing maintained a relatively high viscosity before the temperature begins to recover, as mentioned in 3.4, the entire fracture system tends to have a storage-dominated mechanism during the injection phase. Reflected in the variation of σ_h and P_p, σ_h increased at this stage much more than P_p (Fig. 3.54 (a) to (d) and Fig. 3.55 (a) to (d)).

After the operation has entered the shut-in stage, the system shifts from the storage-dominated mechanism to the leak off-dominated mechanism due to the continuous occurrence of leak off and the continuous reduction of fluid viscosity (no new fluid is injected). Currently, the increased σ_h of surrounding formations began to decrease gradually, and P_p therein continues to increase with the carrying out of leak off (Fig. 3.54 (d) to (f) and Fig. 3.55 (d) to (f)).

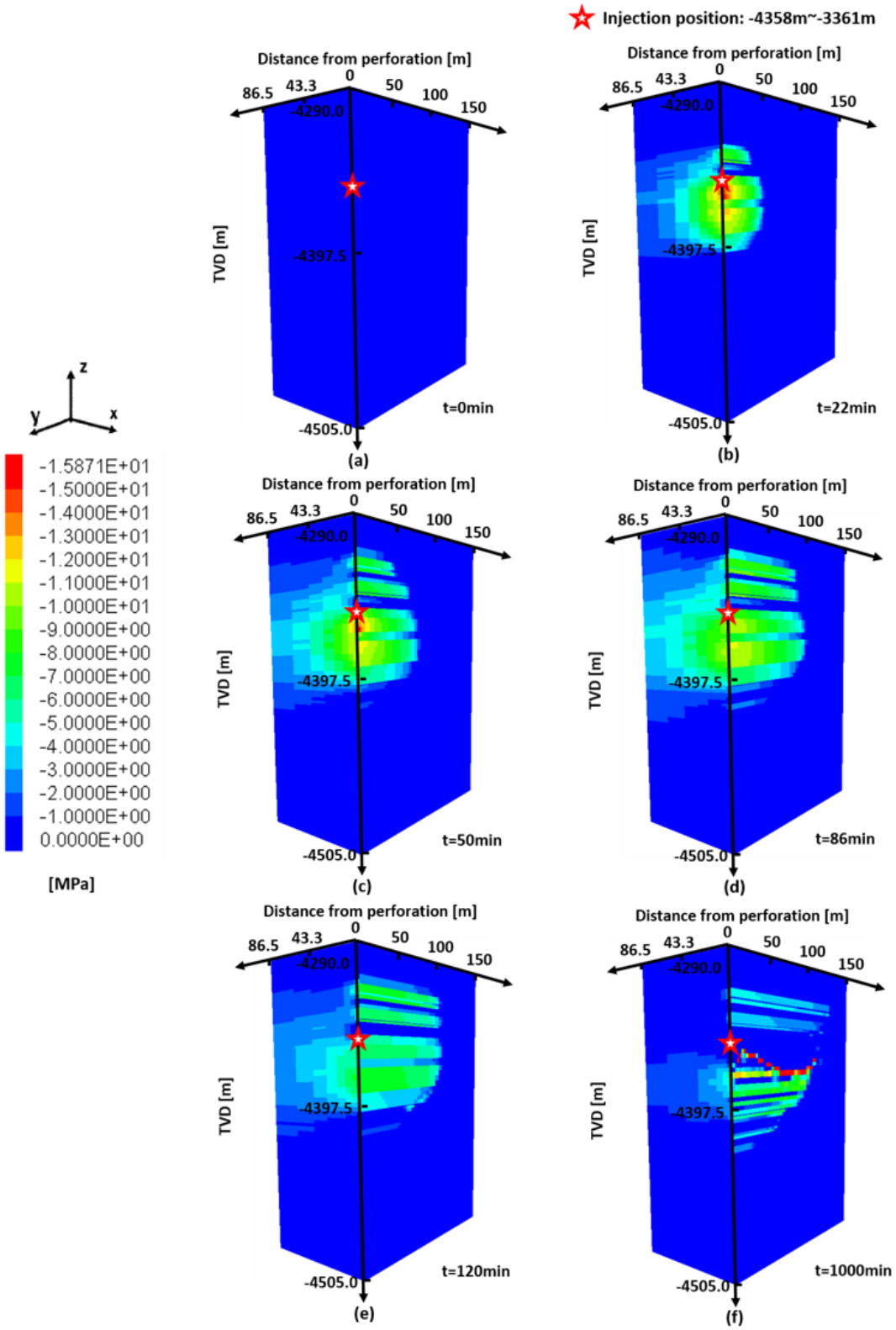

Figure 3.54 Simulated increase of the minimum horizontal stress along the vertical and two horizontal directions (x and y) in reservoir Leer at time t = 0 min, 22 min, 50 min, 86 min, 120 min and 1,000 min

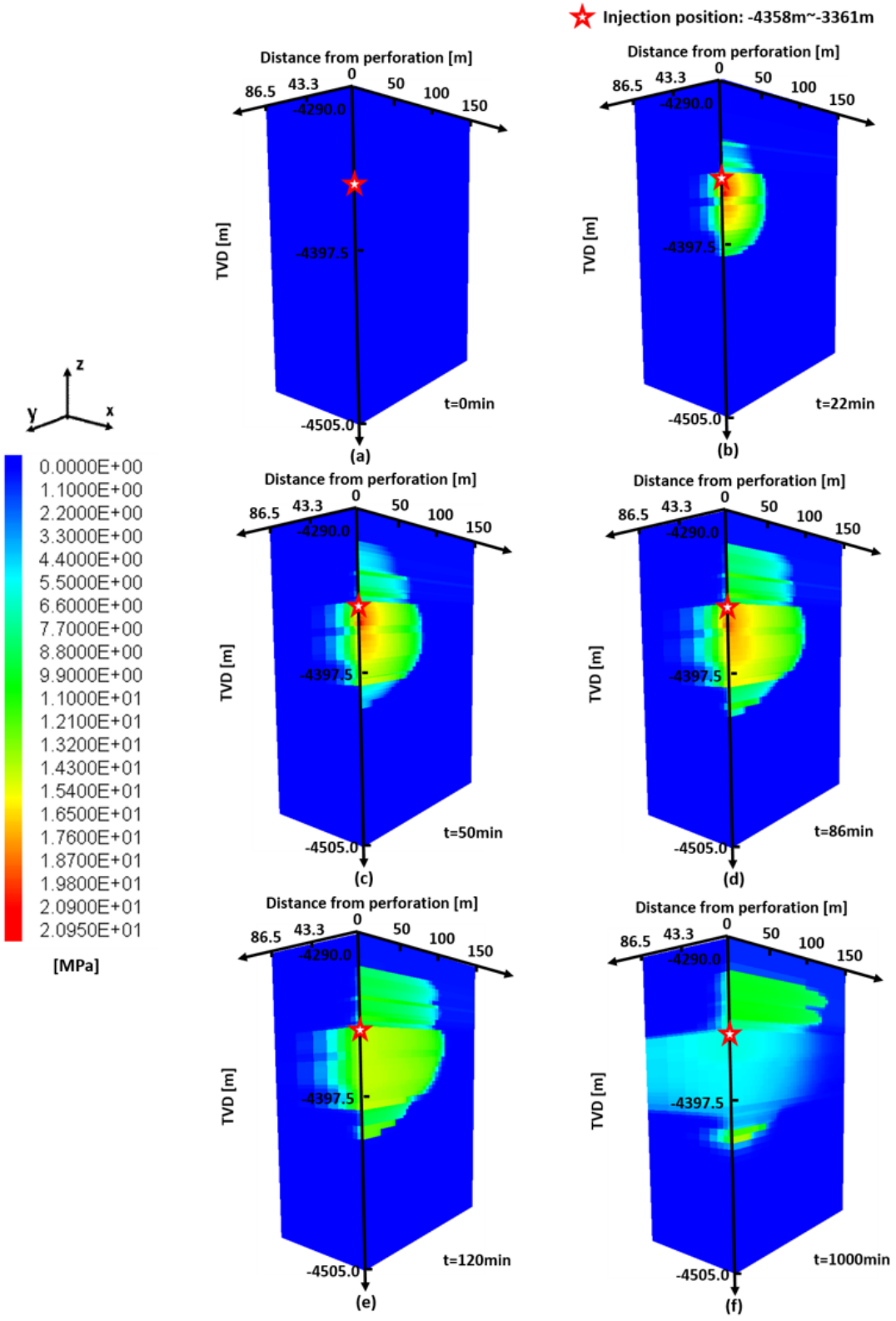

Figure 3.55 Simulated increase of the pore pressure along the vertical and two horizontal directions (x and y) in reservoir Leer at time t = 0 min, 22 min, 50 min, 86 min, 120 min and 1,000 min

It is still worth noting that, as the upper formations of the fracture are generally impermeable, even after the reduction of fluid viscosity the leak off in these formations are still at a very low level. For the changes in σ_h and P_p, their conversion executed very slowly.

3.5 Summary

In this chapter, a systematical study of fluid viscosity's influences on shaping of the stimulated fracture in tight sandstone has been carried out using the by Hou's research group self-developed numerical simulator FLAC3D^{plus}.

By applying a fictitious model at the beginning to study different factors, the statement mentioned in the article of Carrier has been confirmed and more substantiated, i.e. an artificial fracture obtains different propagation mechanisms under different viscosity conditions. Specifically, it is:

1. In a stimulation operation, the propagation of fracture is governed by two competing energy dissipation mechanisms (viscous flow and fracturation) and two competing storage mechanisms (in the fracture or in the porous formation). If the infiltration ability of a fracture system is low enough (depending on the relationship between formation permeability and fluid viscosity), storage mechanism of this system tends to be in fracture (storage)-dominated. Then, influences from the energy dissipation become more significant, namely, a more viscous fluid will tend to expand in the width direction (viscous flow) rather than in the length direction (fracturation). In other words, the fracture is prone to become wider. On contrary, if the system is dominated by a leak off-mechanism, the final shaping of fracture would be decided by its leak off ability.
2. The changes in σ_h and P_p are also affected by above phenomena. Since the main driving force for changing of the pore pressure is from the leak off process, if a fracture system tends to be storage-dominated, the change in σ_h will be more intense

than that of P_p. At the shut-in stage, as the leak off continues, the system will eventually complete the conversion between the increment in σ_h and the increment in P_p.

In addition to the direct and indirect impacts (through the leak off) on fracture system in the operation in a tight gas reservoir, the fluid viscosity also affects the final shape of fracture through its proppant-carrying ability. By further simulating the settling behavior during closing stage, it can be found that when the fracture system obtains larger geometry due to more viscous fluid, the transport of proppant will be correspondingly enhanced. Therefore, blindly increasing the geometry of fracture without adding more proppant would only result in a longer and lower distribution of proppant in the fracture, which is more detrimental to subsequent production activities. Besides, to get a modeled results closer to the practical situation, the process of gel breaking should be taken into account.

In the subsequent investigation, a real case study using the data from Leer reservoir was performed. Simultaneously the gel breaking process was also considered. Through implementing the viscosity's binary function of time and temperature into the simulator, the complete THM coupled processes were well simulated. After analyzing the results in graphical and contour forms it can be found that the fracture's propagation in Leer well followed the rules summarized earlier. However, since the stratigraphic structure in the real case is more complex, in the same operation formations with different properties also represented different propagation mechanisms. Although reduction of the viscosity in shut-in stage accelerated the closure of fracture, it has no obvious influences on the final distribution of proppant. Therefore, a possible way for changing this dilemma is to stimulate the reservoir with gas-based methods, e.g. the supercritical CO_2, since a very fast closing of fracture can make the proppant has no time to sink. But its efficiency must be further investigated.

4 Numerical investigation on the geothermal operation induced microseismic by case study and influencing factors

For extraction of the deep geothermal energy from a series of low-permeable rock formations, hydraulic fracturing plays an important role in the development of such reservoirs. However, generally in a stimulation work more than 10,000 m^3 of fluid will be injected into the underground [51]. Thus, during fracture generation in the reservoir area technically unavoidable anthropogenic seismicity also arises. For this reason, the corresponding investigations are required for the purpose to reduce such phenomenon. The goal of this chapter is to carry out a detailed analysis of fluid-induced seismicity in the course of hydraulic fracturing operations. With help of the post-developed numerical simulator TOUGH2MP-FLAC3D the work has been achieved very well. Moreover, depending on the analyzed results, methods for limiting the microseismic activities in complex geothermal fields have been obtained.

4.1 Overview of the EGS-project Landau and the induced micro seismic events

4.1.1 Location and geological conditions

The South Palatinate EGS (Enhanced Geothermal System) project Landau (maximum power output: 3.6 MW, maximum heat output: approx. 5MW) is located in the area of Upper Rhine Plain (see Fig 4.1).

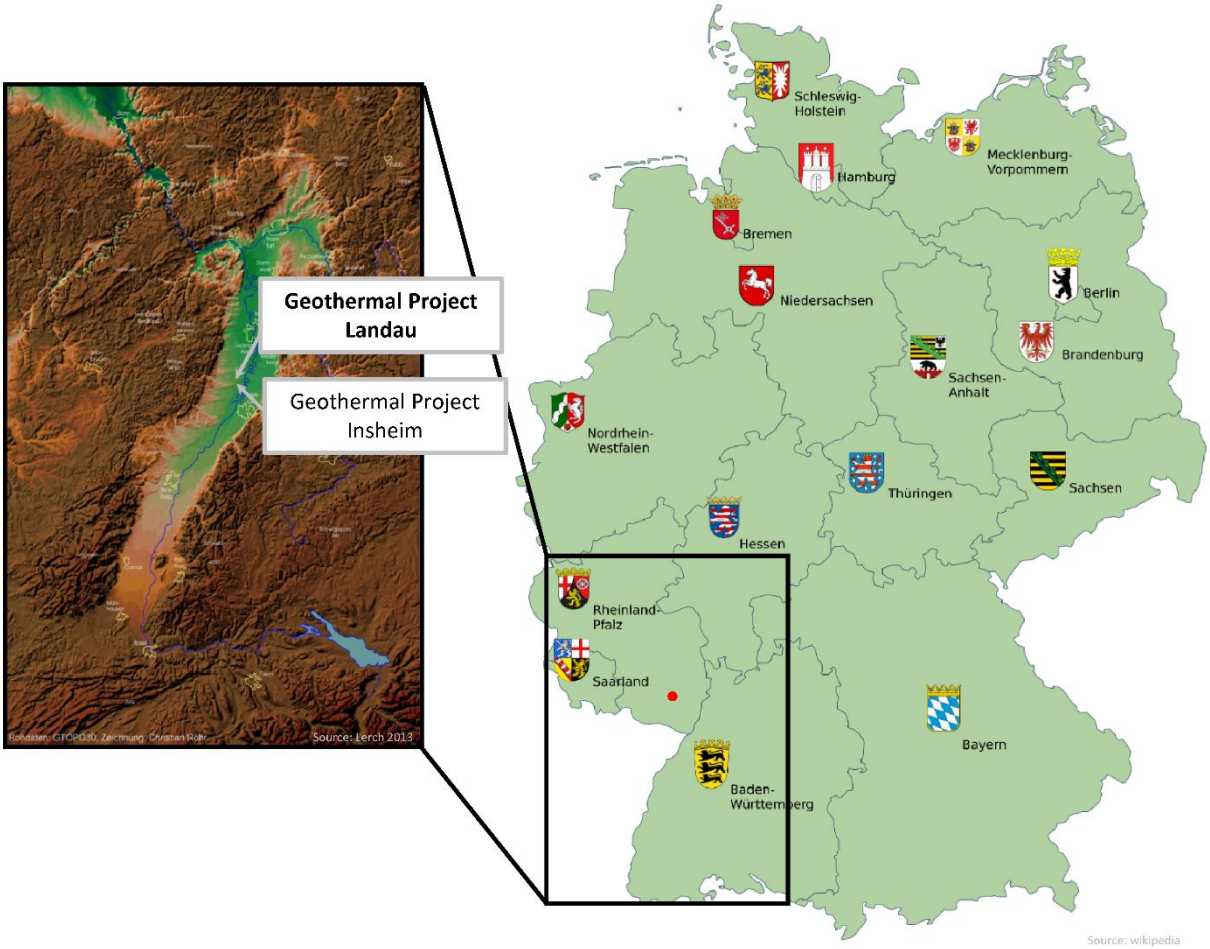

Figure 4.1 Location of the geothermal project Landau on a German map and on a geological map (modified from Baumgärtner [52])

As shown in Fig. 4.2, this region possesses a very high thermal gradient. In comparison to the normal value for Central Europe (about 30 ° C/km), the temperature increases in the Upper Rhine Plain averages 80 ° C / km. For this reason, Landau offers very good conditions for developing geothermal energy. However, the Upper Rhine Plain is proved to be a tectonic active area. There are a lot of natural faults in the area (see Fig. 4.3). That is why exploiting the geothermal resource also involves a lot of risk.

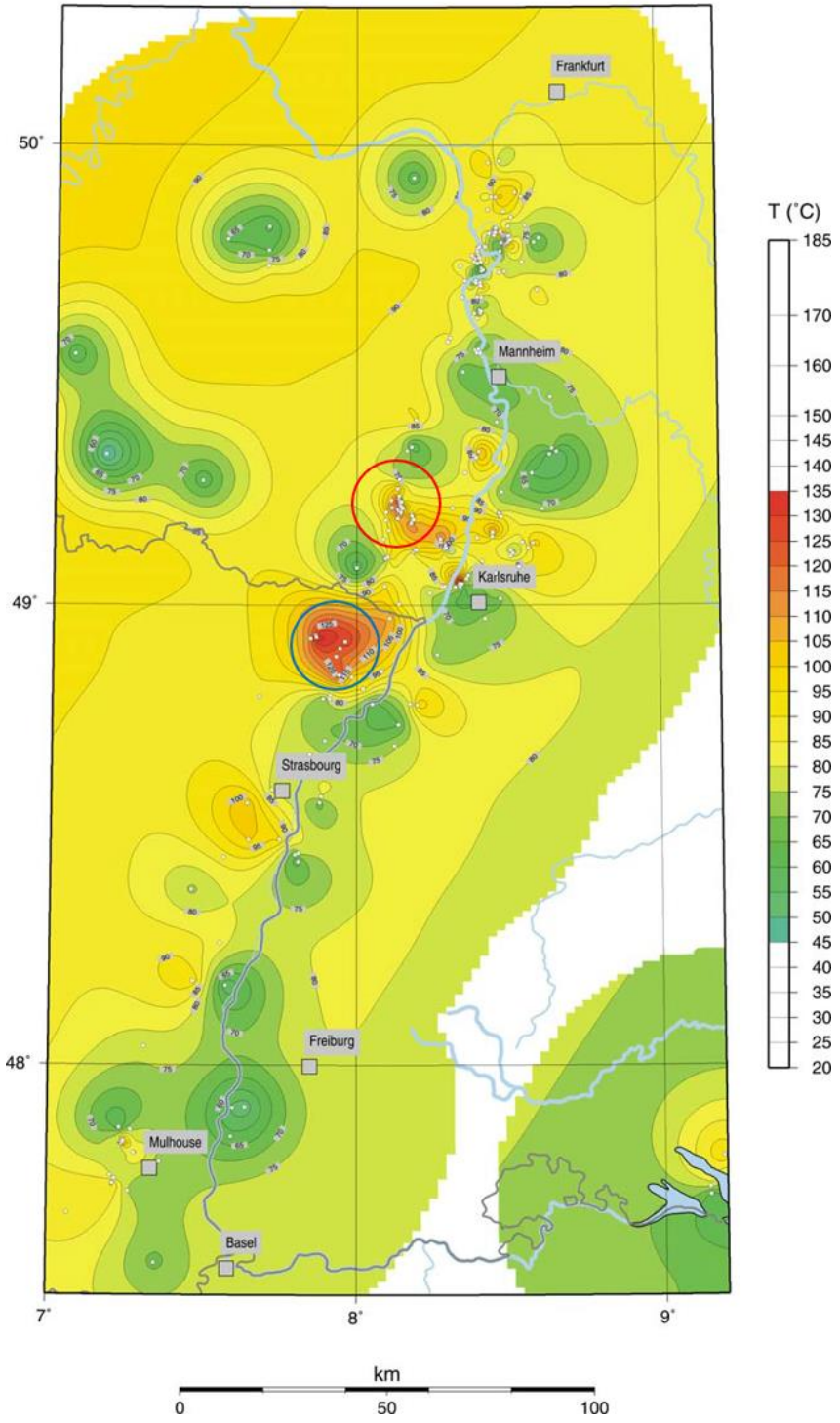

Figure 4.2 Temperature's isolines for the study area of the Upper Rhine Graben for the depth 1500 m. The white dots mark the holes with temperature information. Areas that have no temperature information over a radius of 50 km are shown in white. The red circle marks the area around Landau, the blue circle the area around Soultz-sous-Forêts. (modified from Baumgärtner [52])

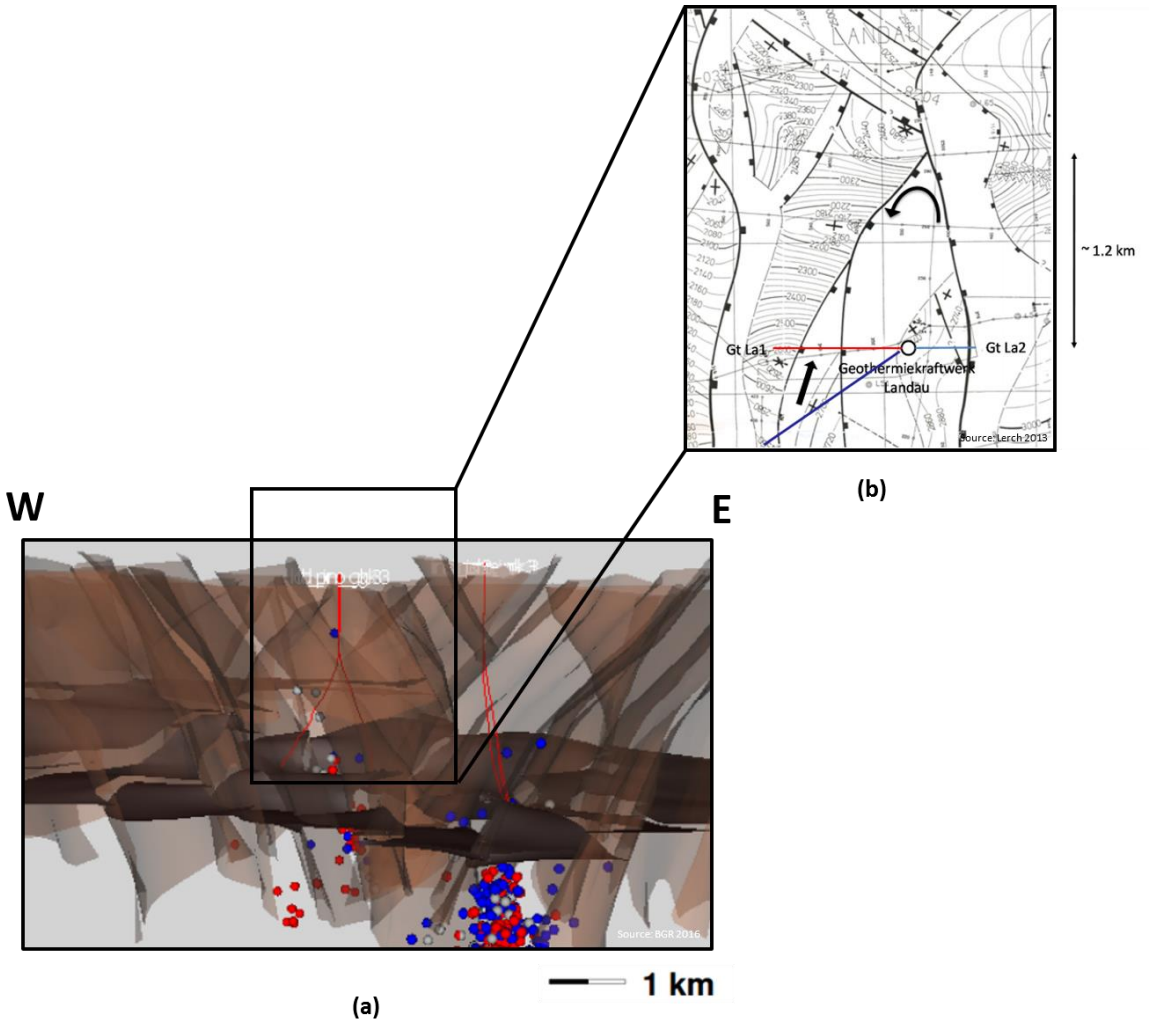

Figure 4.3 Overview of the geological situation in the area around Landau: (a) a side view of natural faults in the area of Landau (east-west section); (b) the natural faults surrounding the Landau project (modified from GeoORG-Project Model and Hou et al. [53])

4.1.2 Seismic events

On August 15th, 2009, a seismicity with a local magnitude M_L of 2.7 was occurred in Landau (Fig. 4.4). This event was clearly noticeable throughout the city and in part of the surrounding area [54]. Subsequently, between September 13th and 15th, 2009, 6 other perceptible quakes occurred, of which the event of September 14th has an M_L of 2.4. The third event with a $M_L \geq 2.0$ happened a year later (December 12th, 2010). Thus, a total of three seismic events with a $M_L \geq 2.0$ within one year took place in Landau. The geothermal energy not only brought

the energy, but also caused a great panic to general public. Therefore, the study of induced seismicity in Landau is necessary.

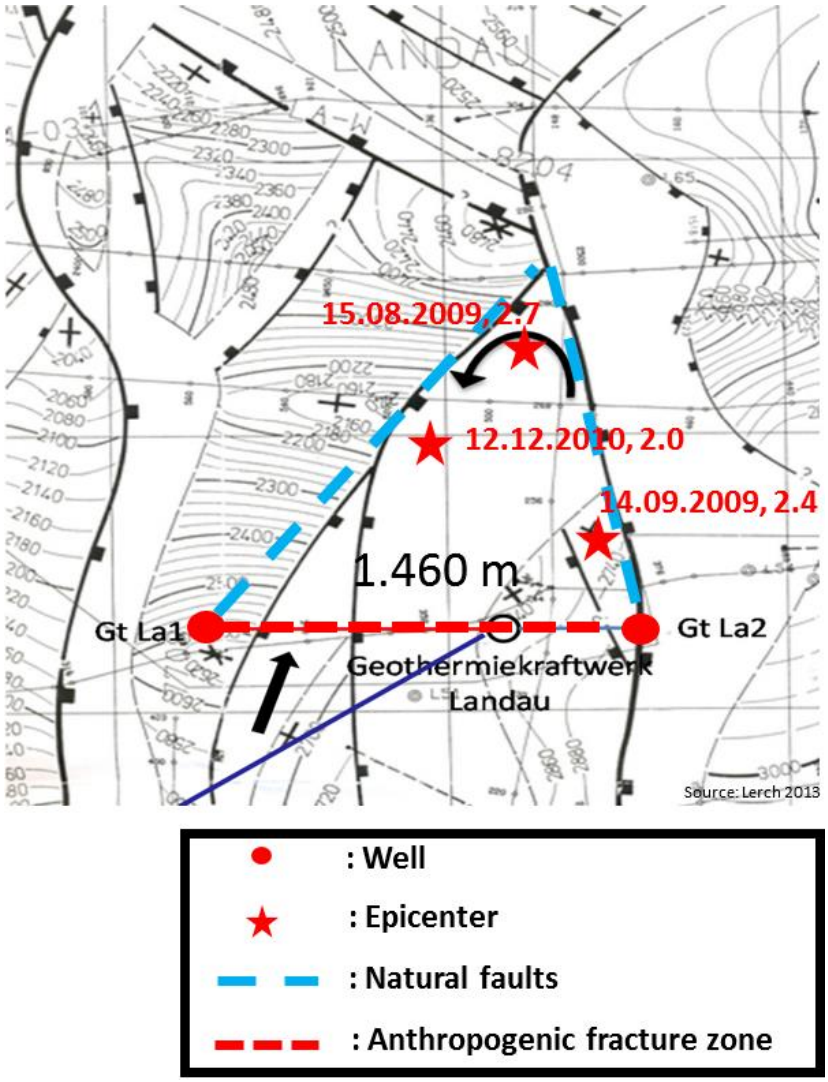

Figure 4.4 Natural faults surrounding the Landau project and the locations of the injection well (Gt La 2), the production well (Gt La 1) and the 3 induced seismicities with local magnitudes M_L over 2.0 (modified from Hou et al. [53])

If the catalog of the seismic events in Landau (see Fig. 4.5, which demonstrates the seismic events in the area of Landau and Insheim), the map of the main fault zones in Landau (see Fig. 4.6) and the map with the location information of the injection and production wells (Fig. 4.4) are overlapped, a helpful phenomenon is discovered. That is, almost all events are

in or around a triangular area constructed by two natural faults and an anthropogenic fracture zone (Figure 4.7). This supports the opinion that these seismic events have something to do with the reactivation of natural faults to a certain extent.

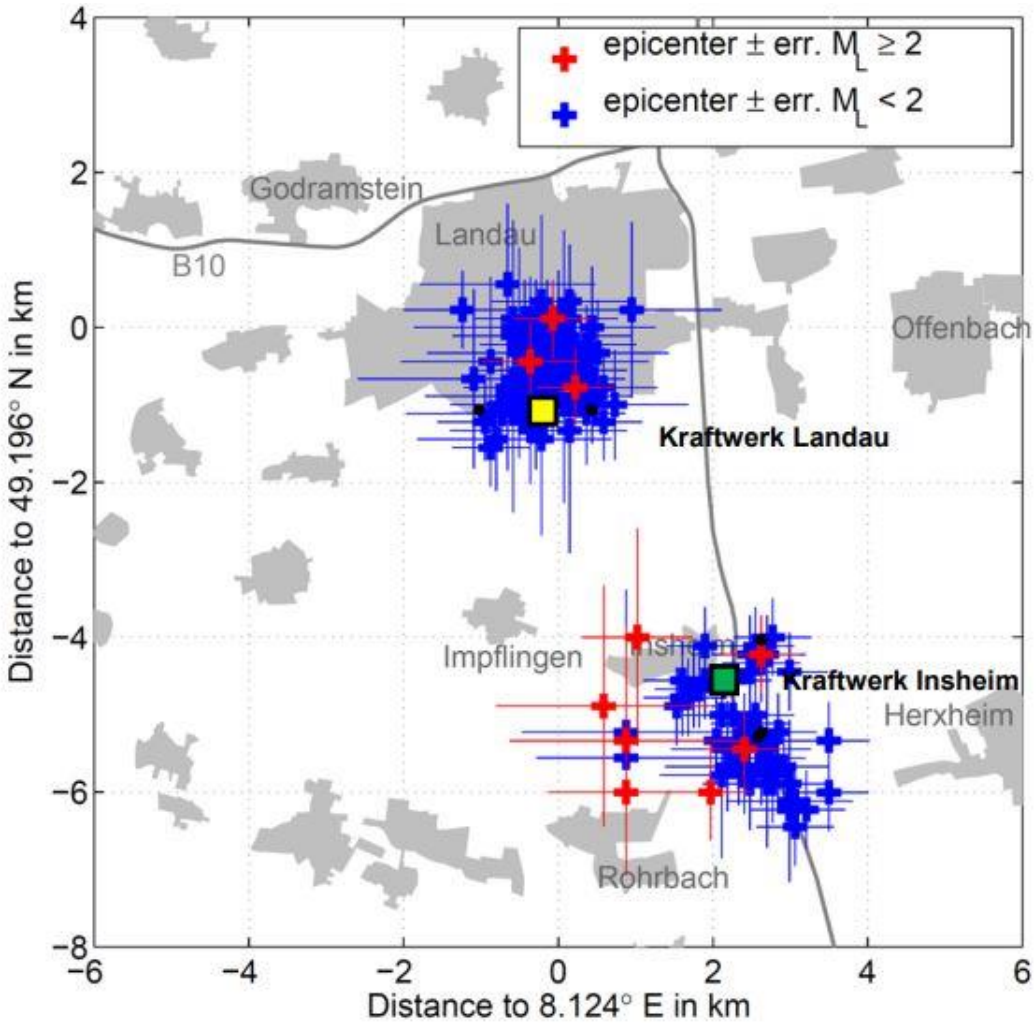

Figure 4.5 Catalog of seismic events in the area of Landau and Insheim (red: events with a magnitude ≥ 2; blue: events with a magnitude <2) (source: Abschlussbericht MAGS-EP1)

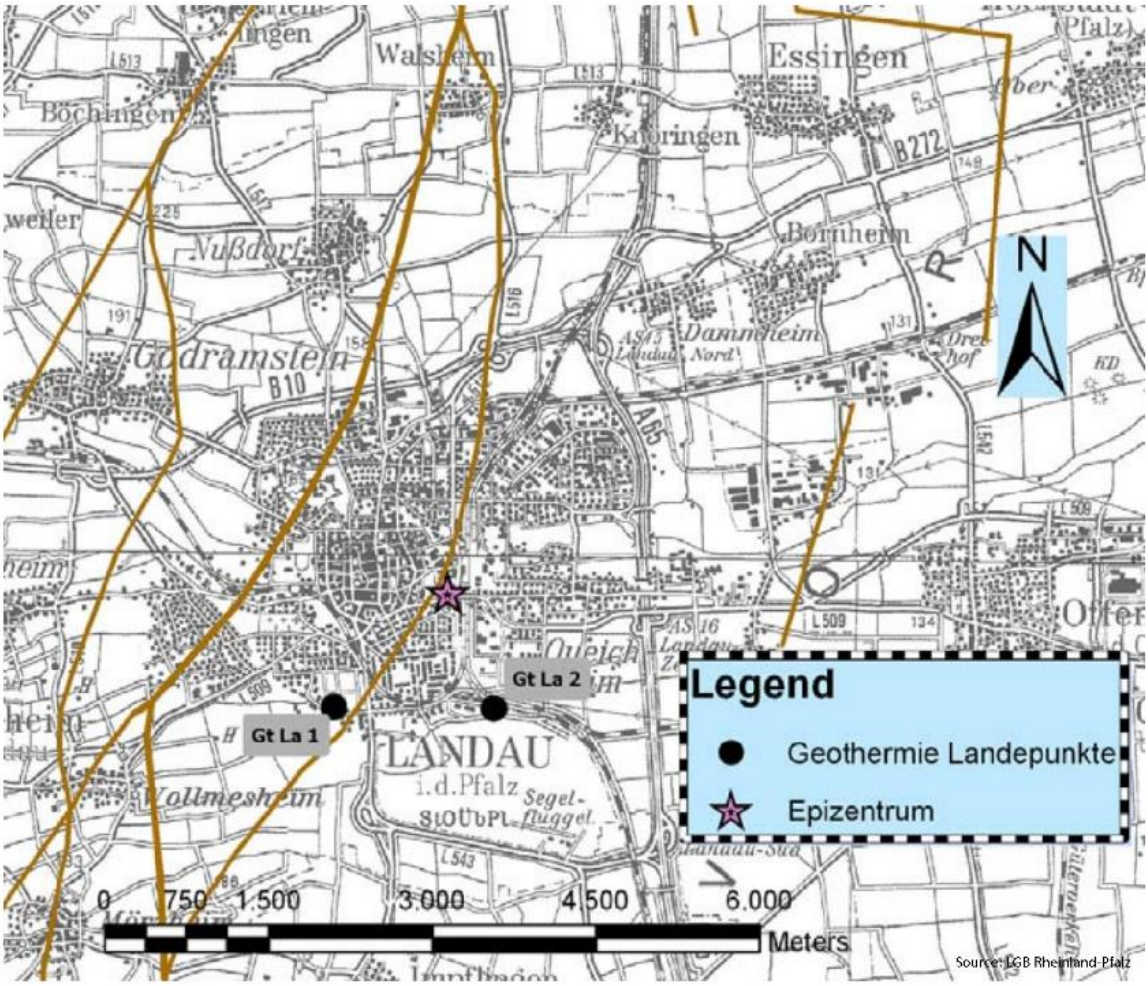

Figure 4.6 Main fault zones in the area of Landau, locations of the production well GtLa1 and the injection well GtLa2 and the epicenter of the seismicity at 15 August 2009 (source: LGB Rheinland-Pfalz)

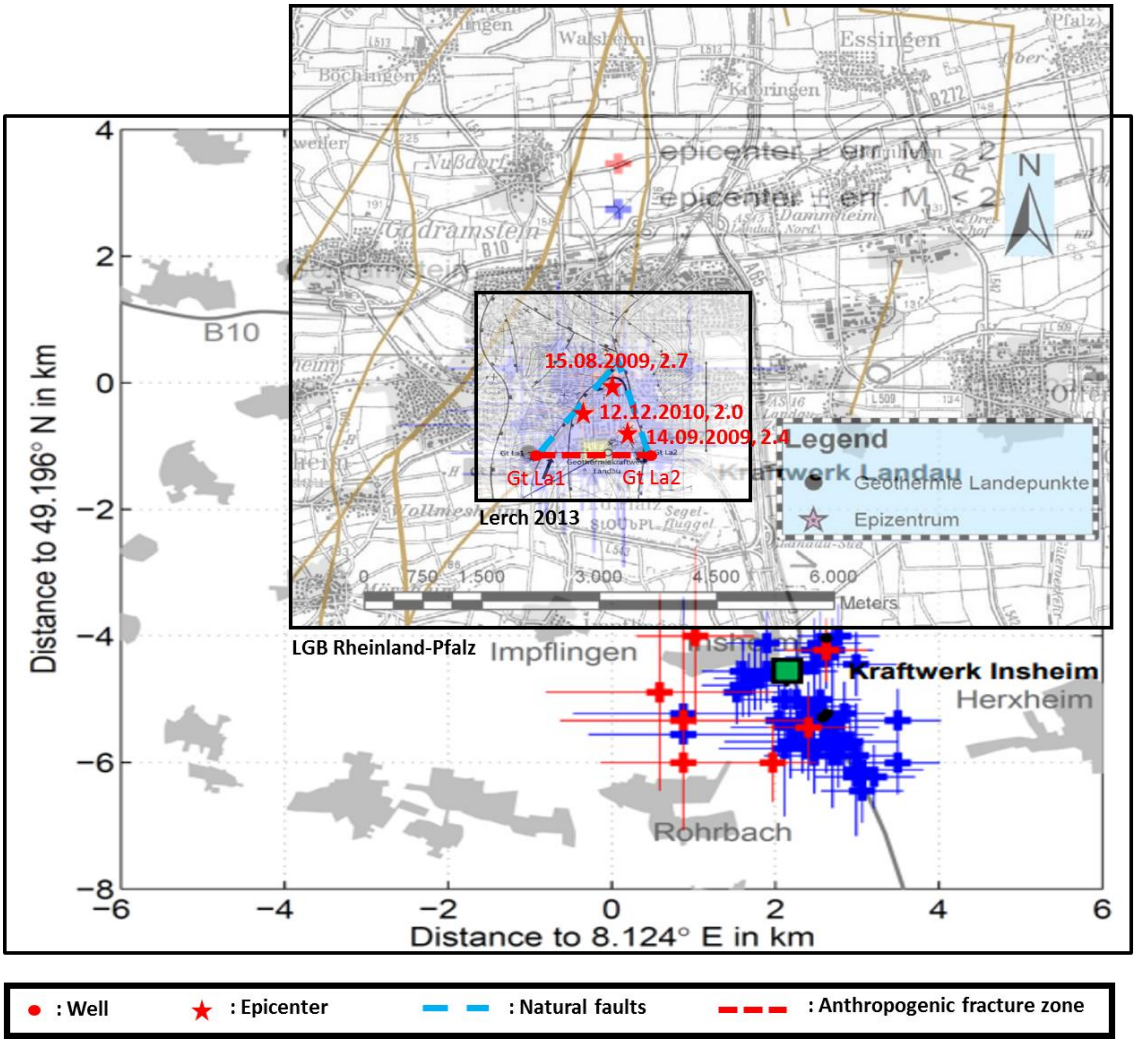

Figure 4.7 Overlapping of Fig. 4.4, Fig. 4.5 and Fig. 4.6, with locations of the anthropogenic fracture zone and natural faults crossing with the fracture zone, locations of the production well GtLa1 and the injection well GtLa2 and the epicenter of the seismic events at August 15, 2009, September 14, 2009 and December 12, 2010

The depth locations of the larger events also contribute in favor to this assumption. In Fig. 4.8, the three events with a $M_L \geq 2.0$ were very close to the huge natural faults.

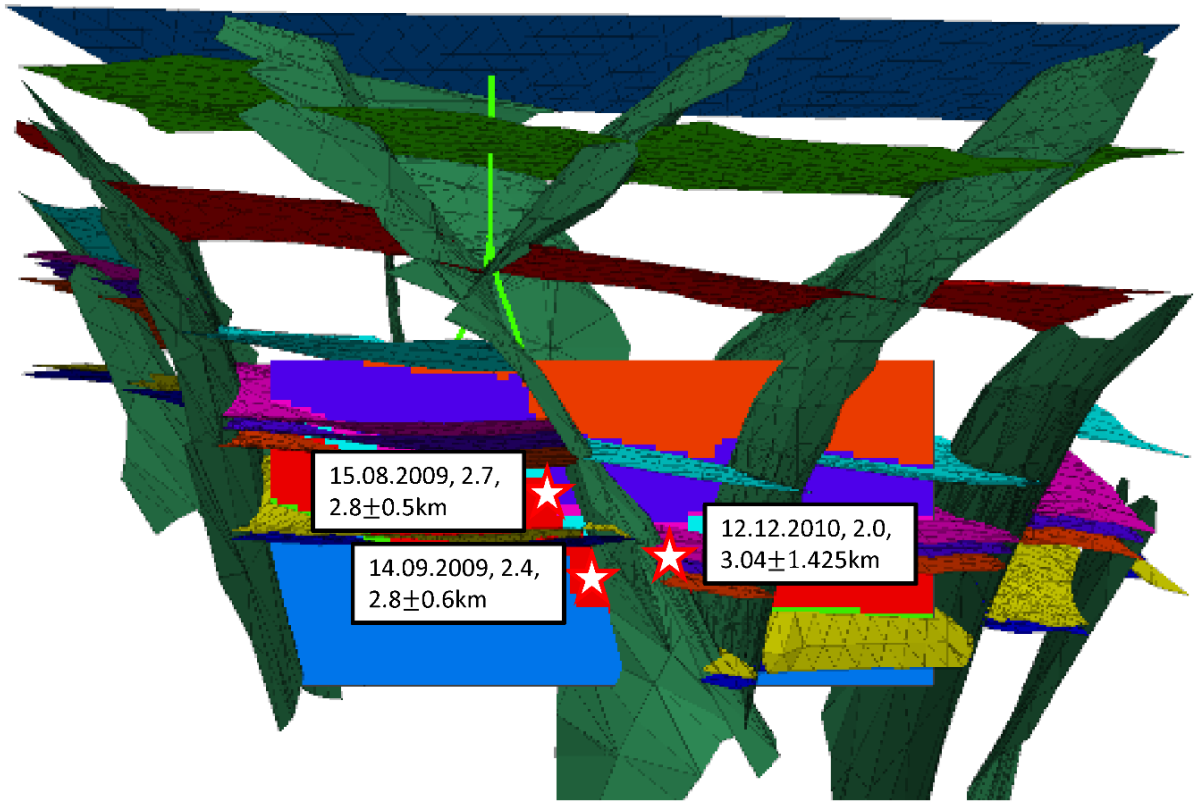

Figure 4.8 Positional relationship between the formations and the model used in the simulation (side view), with depths of the seismic events at August 15, 2009, September 14, 2009 and December 12, 2010 (modified from Hou et al. [53])

4.2 The coupled simulator TOUGH2MP-FLAC3D

In order to verify above assumption and find out reasonable solutions, several numerical modeling were conducted in this study using a powerful research tool: TOUGH2MP-FLAC3D.

4.2.1 Coupled concept of TOUGH2MP-FLAC3D

TOUGH2MP-FLAC3D is an advanced numerical simulator developed by Gou since 2014 [55], whose intent is to study the coupled geo-processes within the geo-energy production. Its basic thought comes from the coupling concept of TOUGH-FLAC (Fig. 4.9), which was developed by Rutqvist & Tsang as well as Rutqvist et al. at 2012 [56, 57].

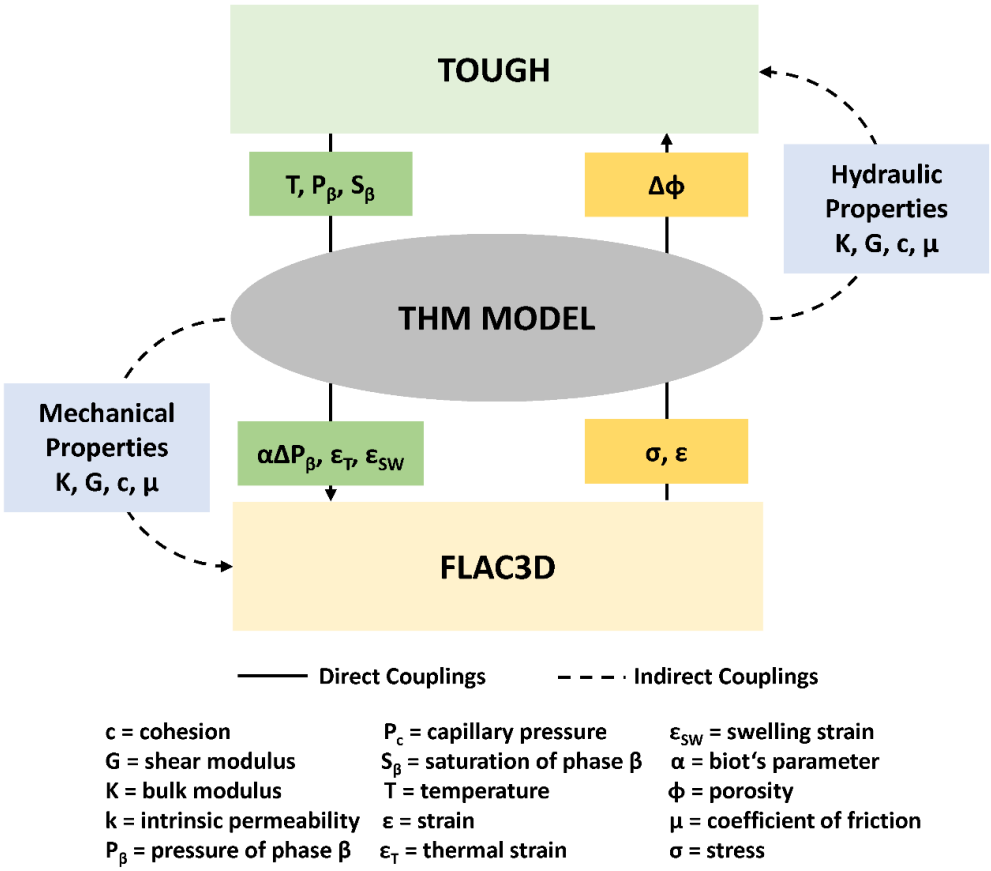

Figure 4.9 Schematic representation of the coupling concept between TOUGH2 and FLAC3D for a coupled THM simulation (Modified from Rutqvist [58])

However, for improving the computing performance a parallel version of TOUGH2, namely TOUGH2MP is adopted in the new simulator. TOUGH2MP is written in FORTRAN 90 and provides many new features, e.g. dynamic memory allocation and array operation [5]. But the most attractive and important evolution is that the code in TOUGH2MP has introduced a parallel algorithm (Fig. 4.10). That is, during the simulation the whole grid in a model would be divided into several sub-domains (domain decomposition). Correspondingly, their calculation work is distributed to multiple threads (logical CPUs). Through this advancement, the performance of TOUGH2MP-FLAC3D is strongly improved.

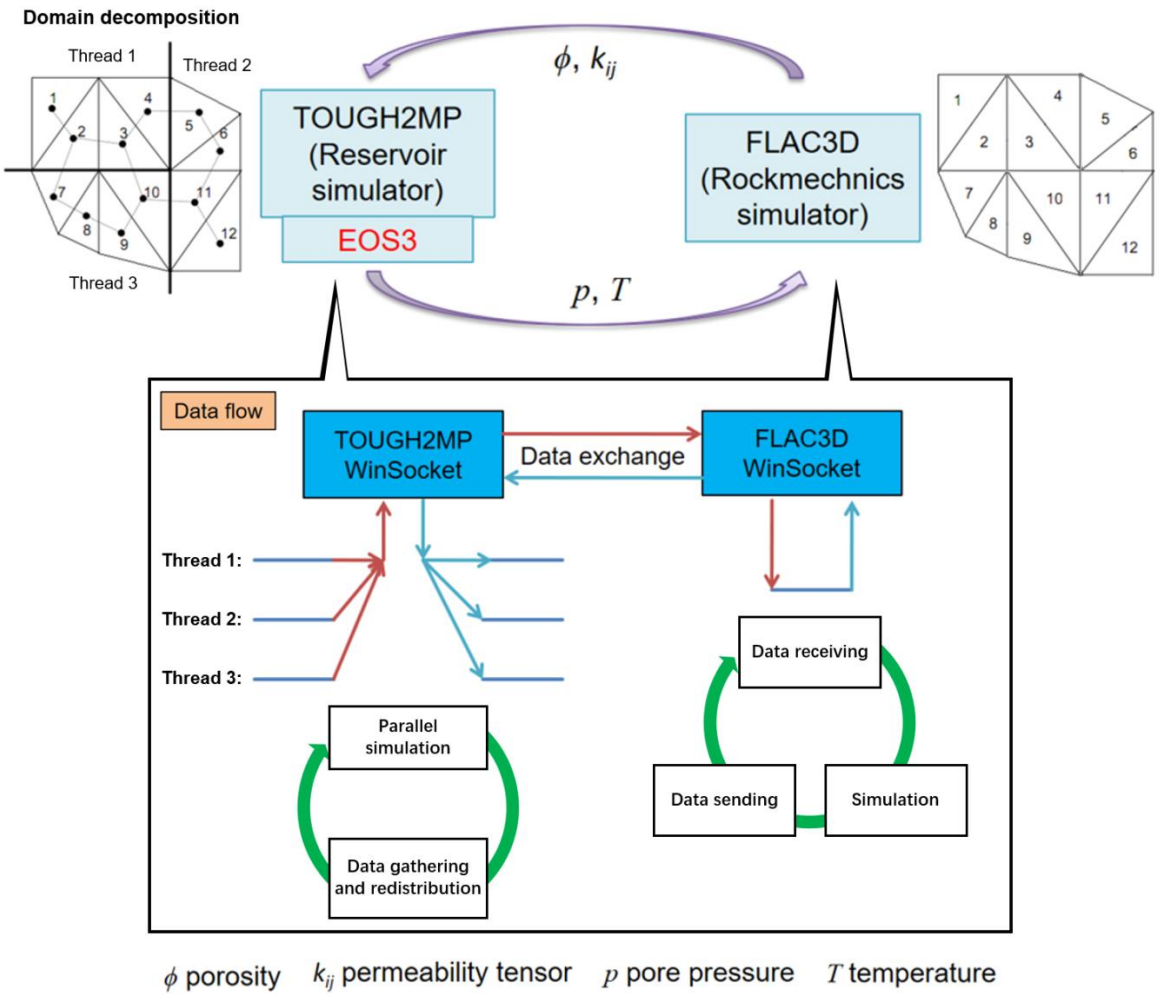

Figure 4.10 Concept of the coupling and parallel computing in TOUGH2MP-FLAC3D

4.2.2 Introduction of the damage concept to the HM coupled model

In order to simulate the rock's softening in the fractured area (Fig. 4.11) more logically and also consider the resulted enhancement in permeability, the damage concept is introduced into the poro-plastic model "subiquitous" (Bilinear, Strain-Hardening/Softening Ubiquitous-Joint) of FLAC3D. Thereafter, the modified code was implemented into FLAC3D as a new damage module.

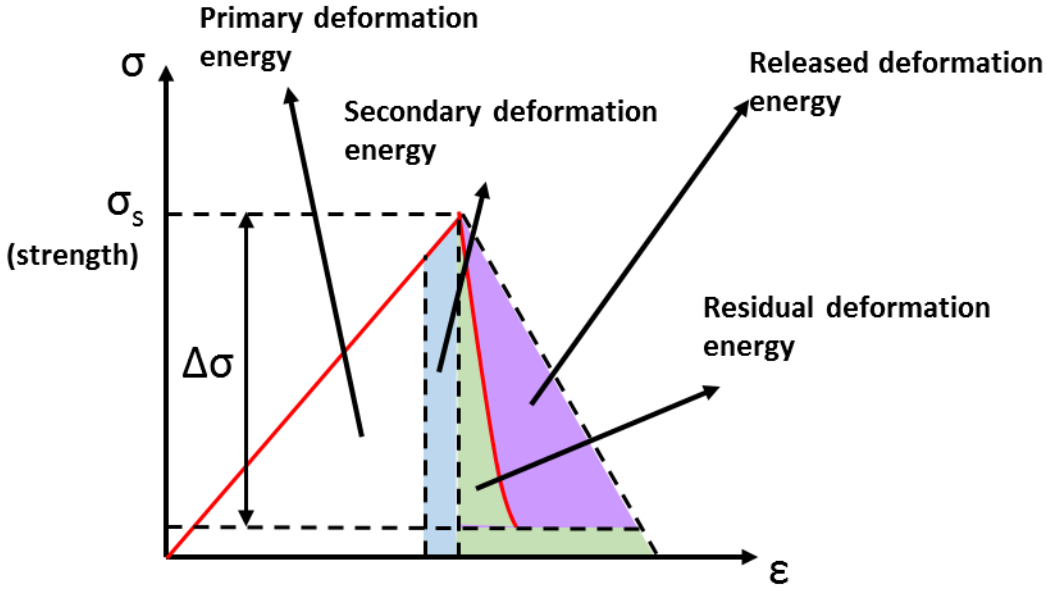

Figure 4.11 Principle of the deformation energy release

The concrete theory of damage is given in Pogacnik's work in 2014 [59] and described by Eq. 4.1. In this model, the damage is an isotropic scalar and based on elasticity. Such a model is easy to implement and can simultaneously well describe the behavior of material.

$$D = \begin{cases} 0 & if \quad \tilde{x} < \tilde{x}_c \\ \dfrac{D_{max}}{\tilde{x}_{off} - \tilde{x}_c}\tilde{x} - D_{max}\dfrac{\tilde{x}_c}{\tilde{x}_{off} - \tilde{x}_c} & if \quad \tilde{x}_c \le \tilde{x} \le \tilde{x}_{off} \\ 1 - (1 - D_{max})\dfrac{\tilde{x}_{off}}{\tilde{x}} & if \quad \tilde{x} > \tilde{x}_{off} \end{cases} \tag{4.1}$$

Where $\tilde{x}_c$ is the critical value of strain ε (damage starts) [-], $\tilde{x}_{off}$ is the cutoff value of strain ε which corresponds to the damage D_{off} [-], and D_{max} is the limit value of the damage [-].

Specifically, the damage value is globally set to zero at the beginning of modeling. At the end of each time step, the scalar variable ε is calculated. If its value exceeds the critical value $\tilde{x}_c$, the damage increases linearly until ε reaches a maximum value $\tilde{x}_{off}$. Therefore, according to the constitutive law, the material softens when ε becomes larges.

In Pogacnik's article of 2015 [60], the permeability is formulated as a function of strain and damage. As the total increment in permeability is controlled by a strain part k_s (Eq. 4.2,

reversible) and a damage part k_D (Eq. 4.3, irreversible, since the damage is permanent), the evolution of permeability can be calculated through Eq. 4.4 (Fig. 4.12).

$$k_s = \frac{k_0}{2} + \left(\frac{\frac{\kappa_{max}}{2} - \frac{\kappa_0}{2}}{1 + exp[-\lambda_\varepsilon(\tilde{\varepsilon} - \tilde{\varepsilon}_{on})]} \right) \tag{4.2}$$

$$\kappa_D = \frac{\kappa_0}{2} + \left(\frac{\frac{\kappa_{max}}{2} - \frac{\kappa_0}{2}}{1 + exp[-\lambda_D(D - D_{on})]} \right) \tag{4.3}$$

$$\kappa = \kappa_\varepsilon I + \kappa_D I \tag{4.4}$$

Where k_s is the part of permeability controlled by strain [mD], k_0 is the initial permeability before stimulation [mD], k_{max} is the maximum permeability [mD], λ_ε, ε_{on}, λ_D and D_{on} are the curve fit parameters to describe the evolution of permeability (adjusted according to experimental data), ε is the strain [-], k_D is the part of permeability controlled by damage [mD], k is the permeability [mD].

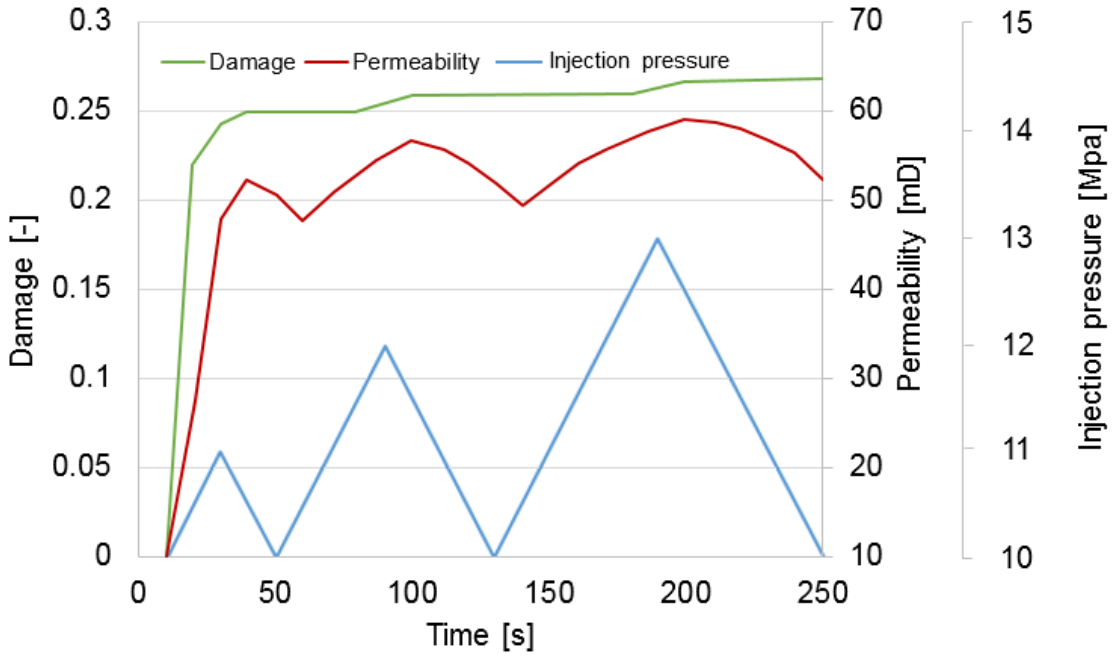

Figure 4.12 Temporal evolution of the injection pressure, rock damage and the enhanced permeability for a 1D column injection scenario

4.3 Numerical investigation of the induced seismicity during the stimulation in Landau

As mentioned above, the purpose of this dissertation is to clarify the seismic mechanisms during its exploitation by studying the stimulation in Landau. At the same time, some reasonable suggestions to mitigate the frequency and intensity of the induced seismicity will also be derived.

Therefore, in accordance with the research framework proposed by the MAGS (German: Mikroseismische Aktivität geothermischer Systeme) project, this study used TOUGH2MP-FLAC3D to numerically simulate the stimulation and then analyzed the changes in stress and deformation. Based on these results, the synthetic seismic catalog and further the slip tendency were also calculated. In this way, combining simulating a series of alternative injection schedules, some countermeasures were obtained (Fig. 4.13).

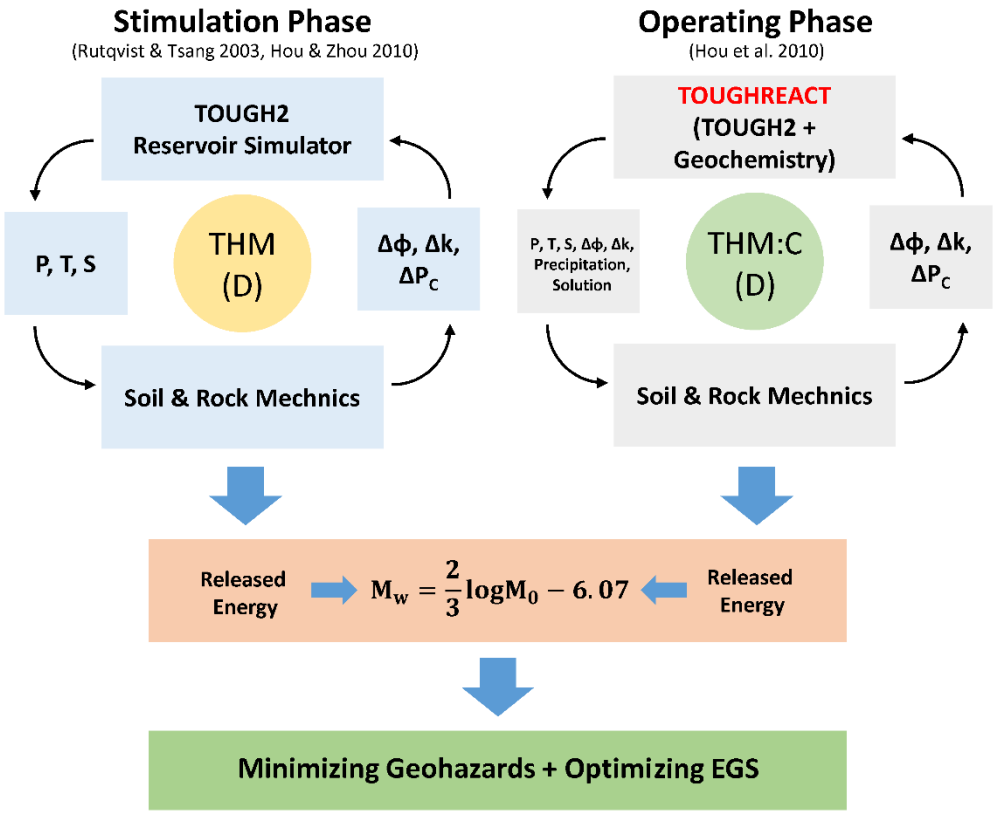

Figure 4.13 Simulation concept proposed by research group Hou to investigate the induced seismicity during the exploitation of geothermal system

4.3.1 Construction of a model for the site

For the purpose of modeling the Landau project, a full model is used due to the reason of asymmetry (Fig. 4.14 (a)). The structure of this 3D model is based on the geometric and coordinate data introduced in Hou et al. of 2016 [53] (Fig. 4.8). The model possesses a height of 2,000 m (z-direction), which corresponds to the real depth section from -1,800 m to -3,800 m. The width is 600 m (y-direction) and the length 4,000 m (x-direction). The injection position is located at a depth of -3,340 m (Fig. 4.14 (b)).

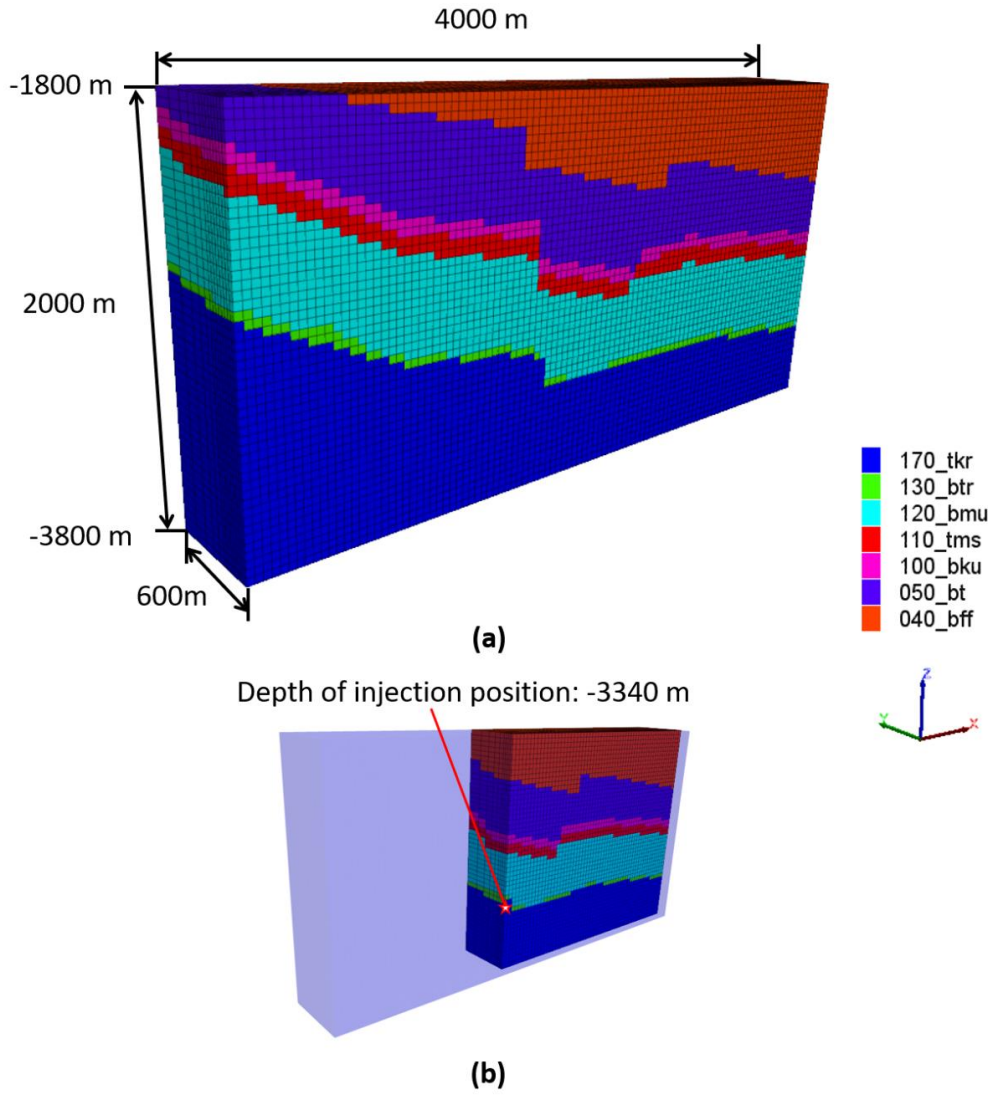

Figure 4.14 Graphical representation of (a) the stratigraphy and the geometric model used in the simulation and (b) the depth of injection position

According to the stratigraphic information, the model is divided into seven groups of elements (Fig. 4.14). Simultaneously the classification through natural faults is also included (Fig. 4.15). The concrete geological formations of each group are given in Tab. 4.1. Their corresponding mechanical, hydraulic and thermal properties are explained in 4.3.2.

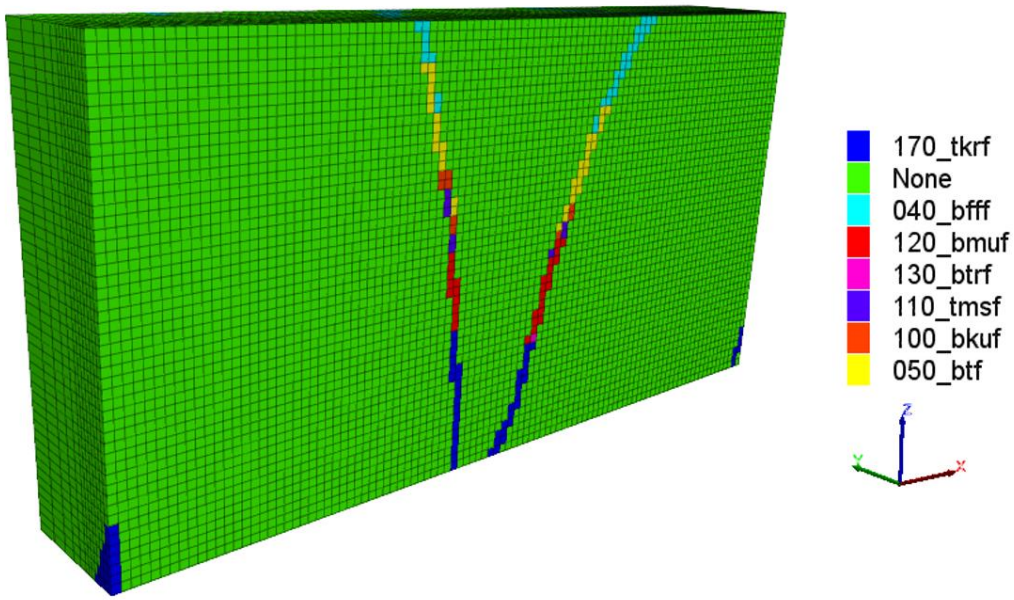

Figure 4.15 Graphical representation of fault elements included in the geometric model

Table 4.1 Element groups and the corresponding formations

Groups	Formation
040_bff, 040_bfff	Middle and early Jurassic
050_bt, 050_btf	Keuper
100_bku, 100_bkuf	Upper Muschelkalk
110_tms, 110_tmsf	Middle and Lower Muschelkalk
120_bmu, 120_bmuf	Buntsandstein
130_btr, 130_btrf	Permian
170_tkr, 170_tkrf	Granite

4.3.2 Parameter determination

All the parameters required in the modeling are determined by the literature study, the personal communication or the supervisor and the adaptation. In the mechanical parameters (Tab. 4.2) the cohesion and tensile strength are different in matrix and joint. The hydraulic and thermal parameters are given in Tab. 4.3 and Tab 4.4.

Table 4.2 Mechanical parameters for the simulation of EGS project Landau

Group	Young's modulus	Poisson ratio	Cohesion		Tensile strength		Friction angle
			Matrix	Joint	Matrix	Joint	
	[GPa]	[-]	[MPa]		[MPa]		[°]
040_bff	38.7	0.313	6.01	4.01	2.5	1.7	36.99
050_bt	24.2	0.326	6.5	4.3	3	2	37.37
100_bku	35.0	0.301	10.51	7.01	2.5	1.7	38.03
110_tms	35.0	0.301	10.51	7.01	2.5	1.7	38.03
120_bmu	30.0	0.334	7.7	1	2	1	35.5
130_btr	27.7	0.332	7.5	1	2.5	1	36.1
170_tkr	54.0	0.225	4.5	1	5	1	40.0

Table 4.3Hydraulic parameters for the simulation of EGS project Landau

Group	Porosity	Permeability	Biot modulus
	[%]	[mD]	[GPa]
040_bff	11	0.25	72.73
050_bt	10.7	20	74.77

100_bku	2.7	1.3	296.30
110_tms	1.97	0.096	406.09
120_bmu	4	0.1	84.12
130_btr	4	0.1	123.08
170_tkr	2	3.5×10^{-3}	400

Table 4.4 Thermal parameters for the simulation of EGS project Landau

Group	Thermal conductivity	Hear capacity
	[W/(m•K)]	[J/K]
040_bff	2.5	900
050_bt	2.5	900
100_bku	2.7	900
110_tms	1.97	900
120_bmu	9.51	900
130_btr	6.5	900
170_tkr	1.18	900

Table 4.5 Parameters related to damage

D_{off}	λ_{ε}	λ_D	k_{max}
[-]	[-]	[-]	[mD]
0.6	10000	5	100

4.3.3 Initial and boundary conditions

During the numerical calculation, all lateral edges and the lower edge of model are fixed, i.e. the moving speeds of lattice points along the respective edges remain zero in the normal direction. At the same time, the model is loaded from the upper edge with a corresponding rock pressure in the vertical direction downwards. In addition, for each model element, the primary stress state resulting from the Soultz project and the hydrostatic pressure are initialized (see Fig. 4.16 and 4.17).

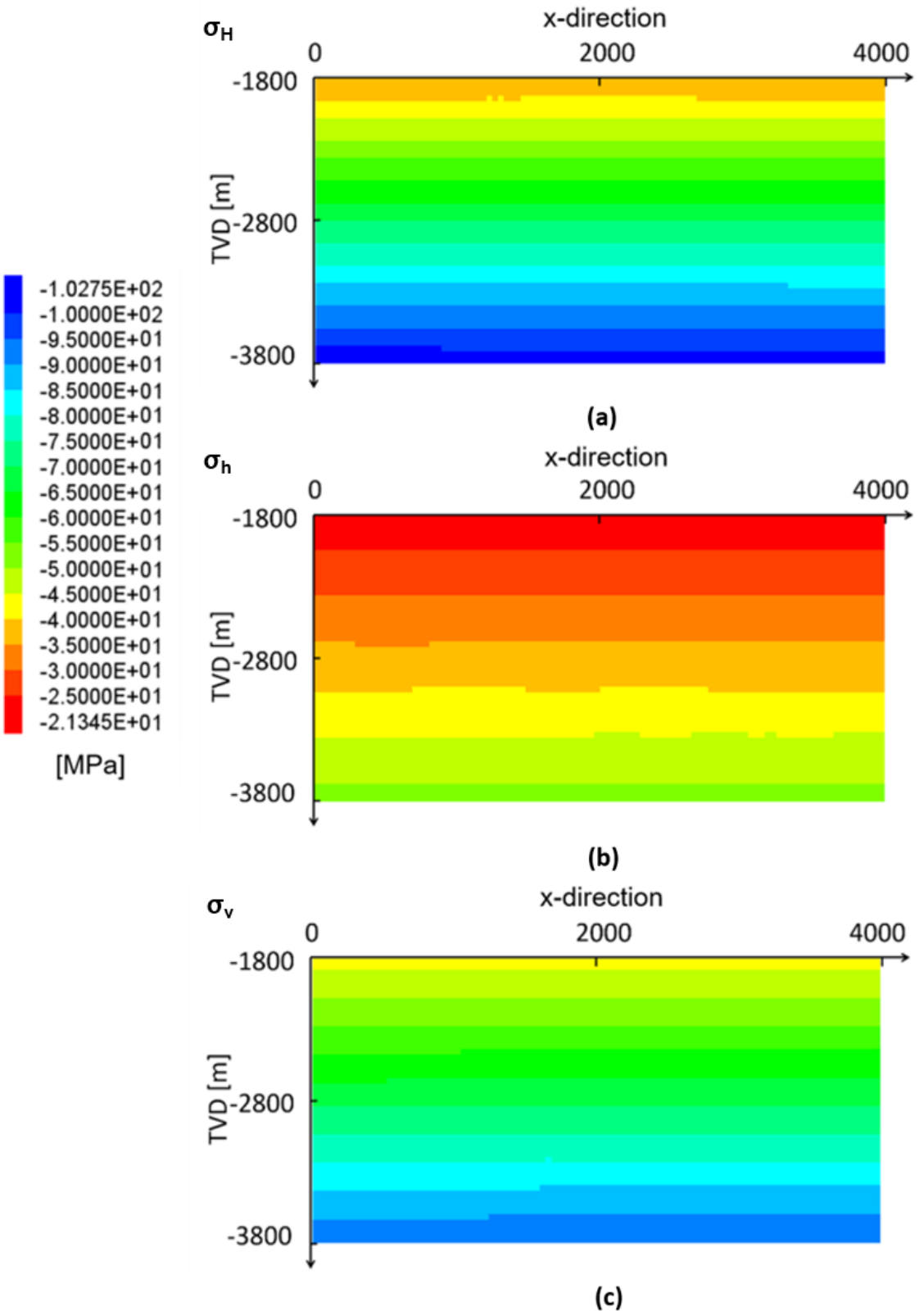

Figure 4.16 Variation of (a) the maximum horizontal stress, (b) the minimum horizontal stress and (c) the primary vertical stress in the research area of EGS project Landau

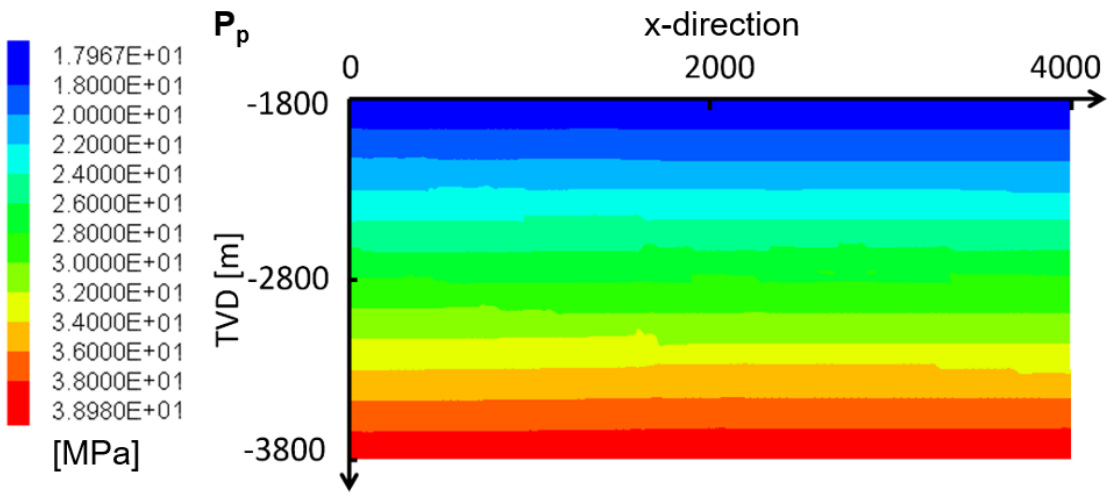

Figure 4.17 Variation of the primary hydrostatic pressure in the research area of EGS project Landau

4.3.4 Treatment schedule and modeling results

4.3.4.1 Treatment schedule of the hydraulic fracturing

The hydraulic fracturing for Landau was divided into four parts, namely the hydraulic preliminary test, the hydraulic stimulation, the stimulation with a high speed and the acid stimulation. In this study, only hydraulic stimulation and stimulation with a high speed were simulated (data comes from Hou et al. of 2016 [53]). In Fig. 4.18, Phase 1 is the hydraulic stimulation. In this phase, a total of 6,552.3 m^3 of water was injected at a rate of 0.906, 1.236 to 5.16 m^3/min. Phase 2 represents stimulation with a high injection rate. In this phase, a total of 8,615.2 m^3 of water was injected within 7 days at a rate of 1.2, 4.2, 9.42, 9.48 and 11.4 m^3/min respectively.

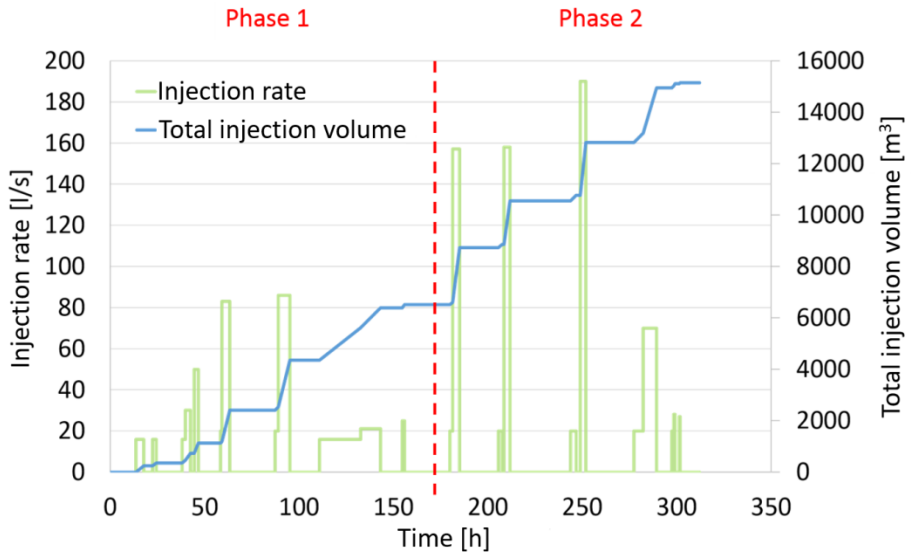

Figure 4.18 Variation of the injection rate and the corresponding total injected volume with time during stimulation work in Landau

4.3.4.2 Modeling results of the hydraulic fracturing

As a good reference to describe the operation process, the numerically calculated Bottom Hole Pressure (BHP) is compared to the data measured locally at Landau (see Fig. 4.19, in situ measured wellhead pressure is transferred into BHP with consideration of friction loss and hydrostatic pressure). This adaptation makes the following discussions more reliable.

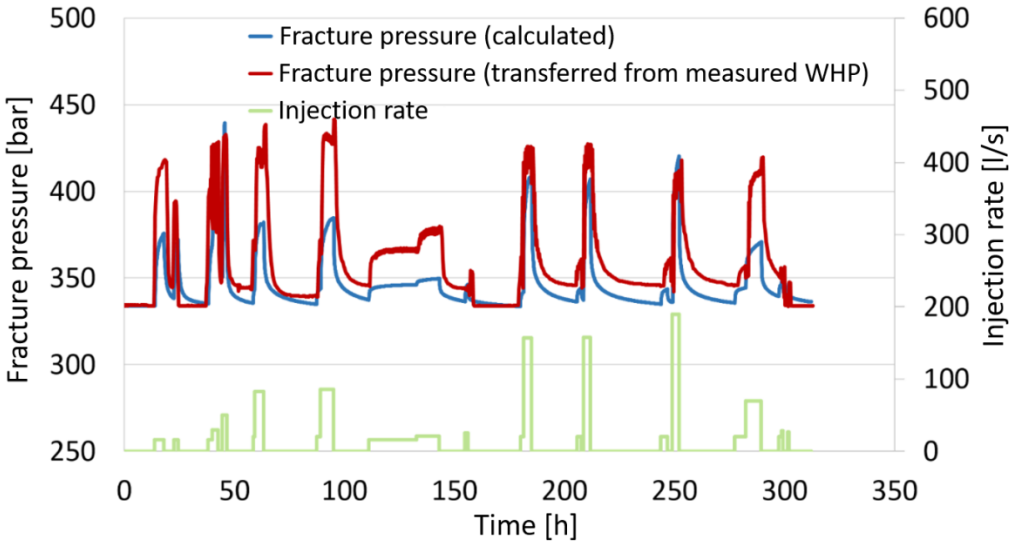

Figure 4.19 Comparison of the in-situ measured wellhead pressure considering hydro-static pressure and friction loss and the calculated bottom hole fracture pressure over time

In the simulation results, a fracture zone with a geometry of 2,780 m in x direction, 90 m in y direction and 1,070 m in z direction was generated (Fig. 4.20 (a)). Since operation was carried out mainly in the formation of granites, the shear fracture was the only single type of failure.

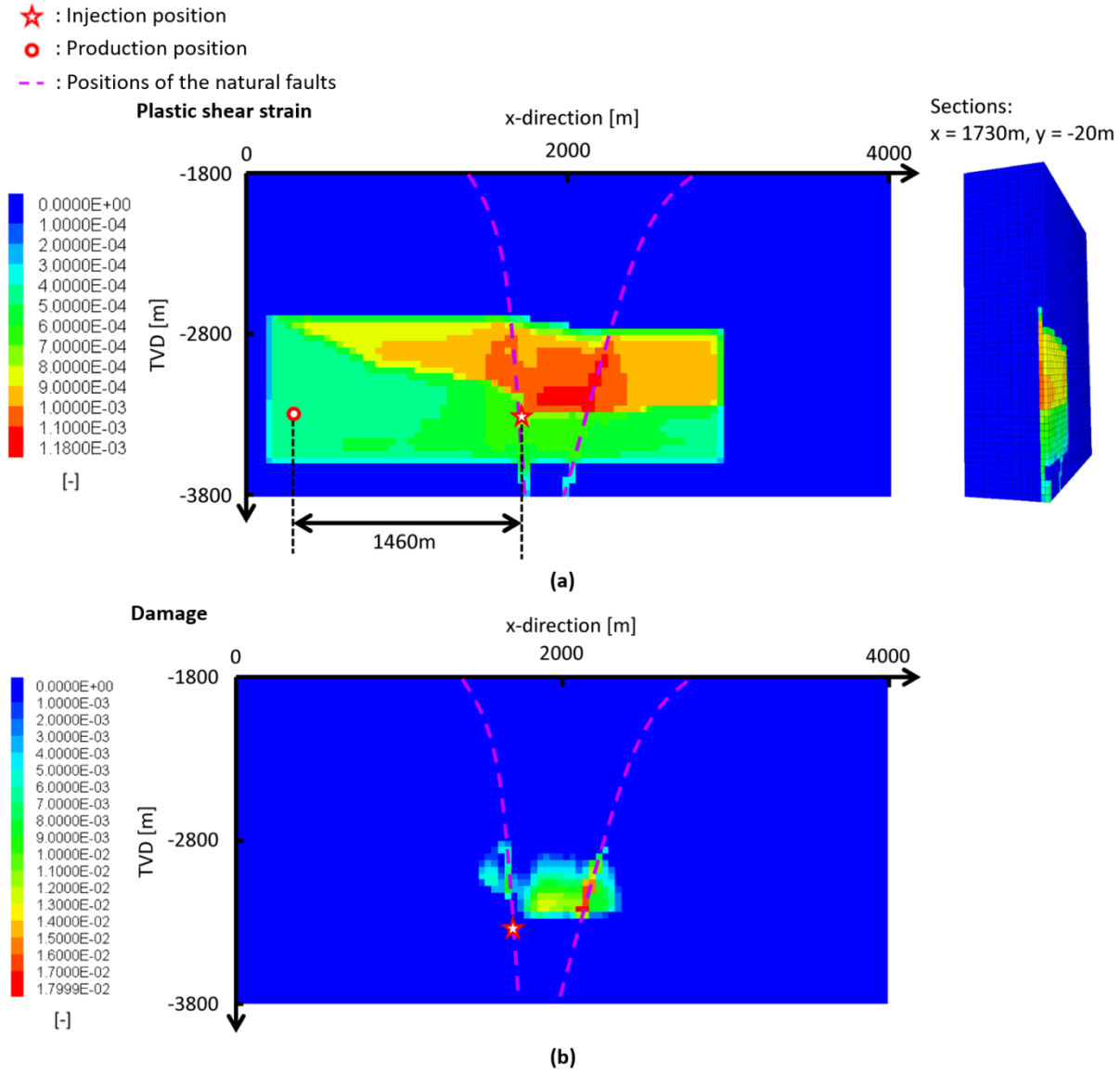

Figure 4.20 Variation of the injection rate and the corresponding total injected volume with time during stimulation work in Landau

Fig. 4.20 (b) shows the damage formed in vertical and horizontal directions. The most important phenomenon in Fig. 4.20 is the occurrence of the greatest plastic shear strain and

damage mainly in the region between or within the natural faults. It can be depicted that, these areas were severely influenced by the operation.

By using Equations from 4.5 to 4.8 (in Aki et al. 2002 [61] Eq. 4.5 was used to calculate the seismic moment tensor M_{ij}; in Shearer 2009 [62] Eq. 4.6 was used to calculate the scalar seismic moment M_0; Eq. 4.8 was defined in Kanamori et al. [63] 1975 and Hanks et al. 1979 [64]), Fig. 4.21 illustrates the temporal evolution of synthetic seismic magnitude (moment-magnitude) during the operation. In addition, the status of fracture propagation at certain time points is also represented.

$$M_{ij} = \mathrm{G}\left(\mathrm{n}_i s_j + \mathrm{n}_j s_i\right) + \lambda \delta_{ij} \vec{s} \cdot \vec{n} \tag{4.5}$$

$$M_0 = \sqrt{\frac{1}{2}\sum_{ii} M_{ij}^2} \tag{4.6}$$

$$M = \sum_i M_0^i \tag{4.7}$$

$$M_w = \frac{2}{3} log_{10} M\text{-}6.07 \tag{4.8}$$

Where M_{ij} is the seismic moment tensor [N•m], G is the shear modulus [Pa], n_i is the surface normal of the fracture area [-], s_i is the plastic displacement [m], λ is the Lamé constant [Pa], M_0 is the scalar seismic moment [N•m], M_w is the moment magnitude [-].

In the representations, two phenomena are important:

1) The large-scale fracture zone was already formed at a very early stage. Subsequently, the enlargement of the entire surface stops. But the area of core zone, i.e. the area with greatest plastic strain which mainly appear around or within the natural faults, continues to grow (Fig. 4.19 (b) to (e)).

2) The seismic events also occurred even after stopping the injection, i.e. if the stress redistribution was not achieved, the deformation or fracturing process continued (Fig. 4.19 (a)).

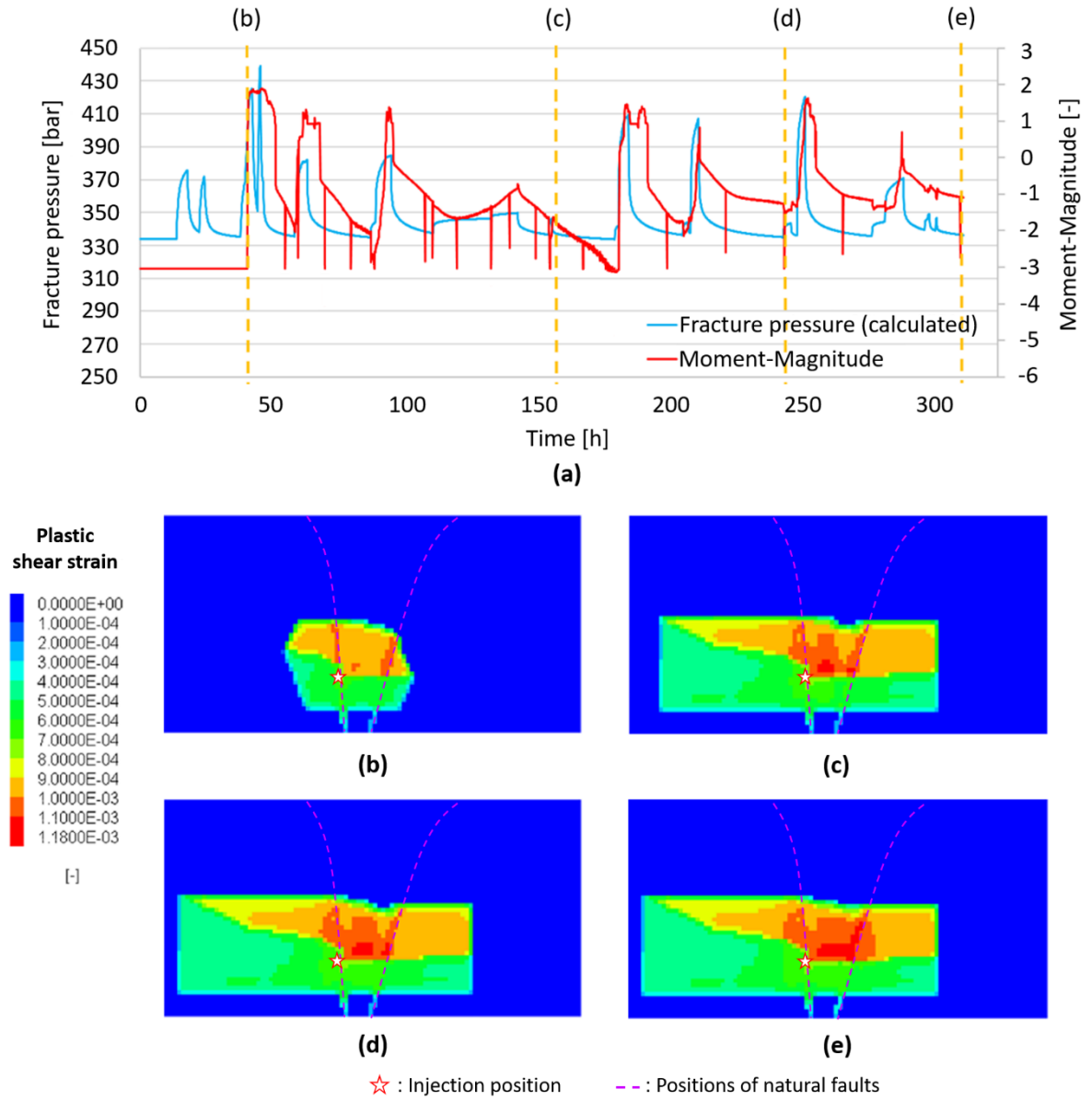

Figure 4.21 Development of (a) the fracture pressure and the synthetic seismic magnitude during operation in contrast to (b) to (e) the fracture propagations (development of the plastic shear strain) at certain time points (t = 42 h, 158 h, 243 h and 312 h in (a)).

4.3.4.3 Treatment schedule of the production phase

The injection and production schedules of production phase were also derived from the actual operating scheme (Fig. 4.22) [53]. However, in order to reduce the computational effort, the applied schedules to numerical modeling were simplified. In the following study, only the production work from 2008 to 2009 was modeled. The injection rates are 60 l/s and 70

l/s in the year of 2008 and 2009 respectively. The production rate in 2008 is initially very high (100 l/s), but after about 120 days, the rate is dropped to 60 l/s. In 2009, the production rate is the same as that of injection rate.

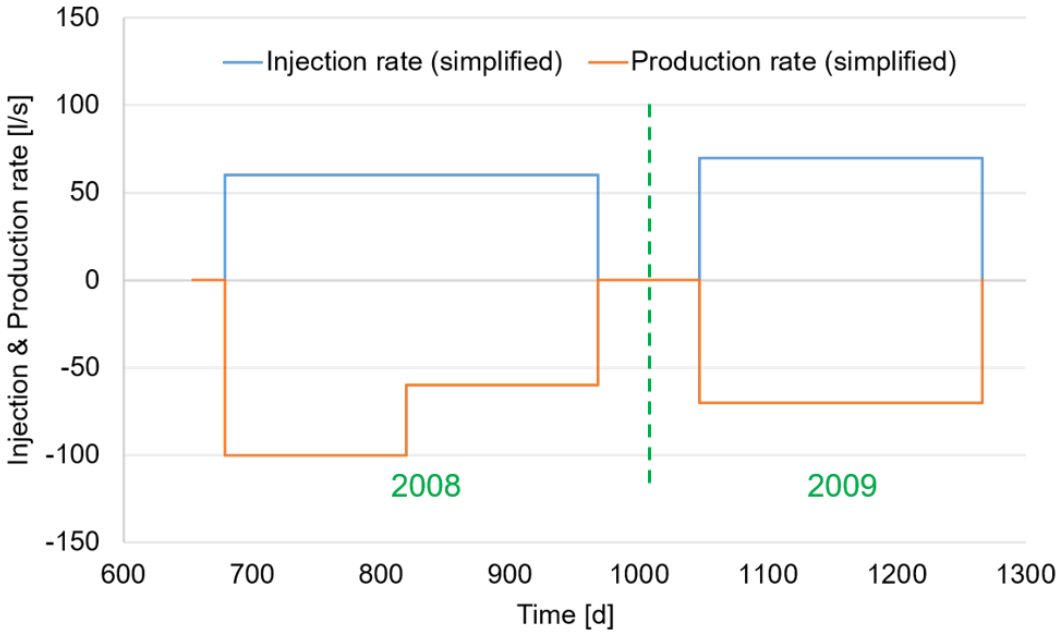

Figure 4.22 In simulation used injection and production schedules

At the same time, since the thermal effects are not significant in the geo-mechanical processes [65], here only the HM-coupled simulation was considered.

4.3.4.4 Modeling results of the production phase

Fig. 4.23 shows the comparison between the numerically calculated BHP and the in situ measured values of production phase. In this simulation, the BHP was approximately matched.

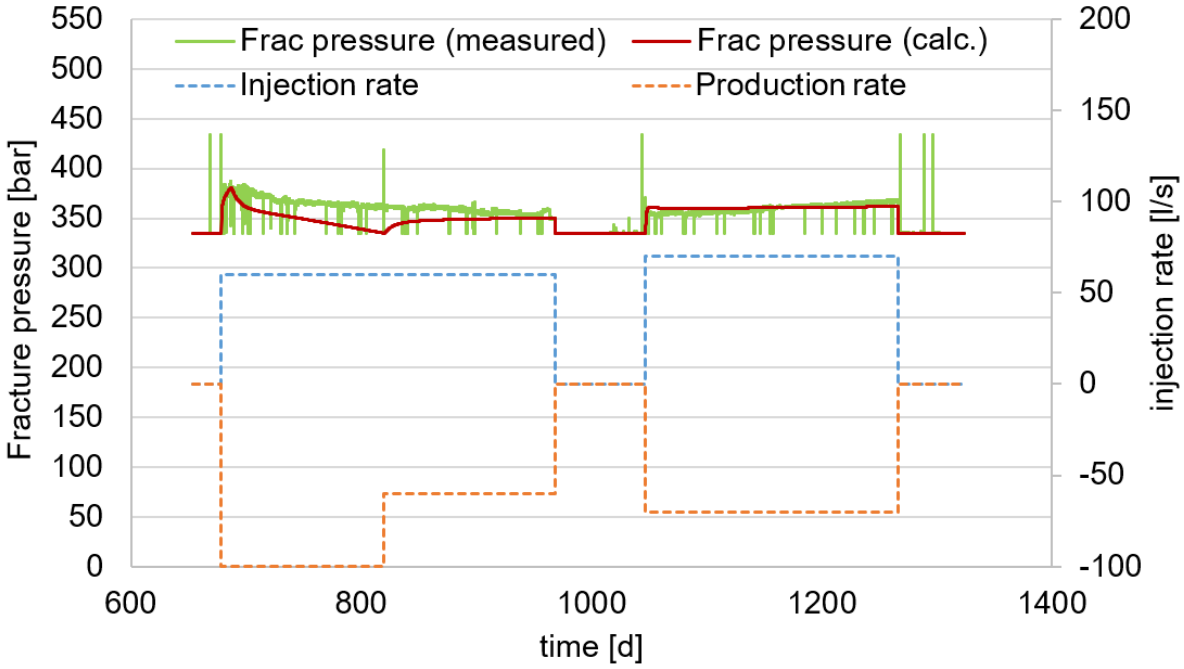

Figure 4.23 Comparison of the measured and calculated bottom hole pressure in contrast to the injection and production rate

After getting confirmation that the analysis possesses a good foundation (history matching), the development of calculated seismic magnitude during the production phase is shown in Fig. 4.24. In addition, the injection and production schedules are also presented. It can be noted that the seismic events occurred only at the beginning and after the stop of the production (Fig. 4.24 (a)). In Fig. 4.24 (b) to (f), it can also be observed that the pore pressure in the reservoir area changes during the operating process. The pressure around injection position is increased. At the same time, the pressure around production position is dropped. Such a stress change leads to secondary “injuries” at the time of beginning and after the production phase.

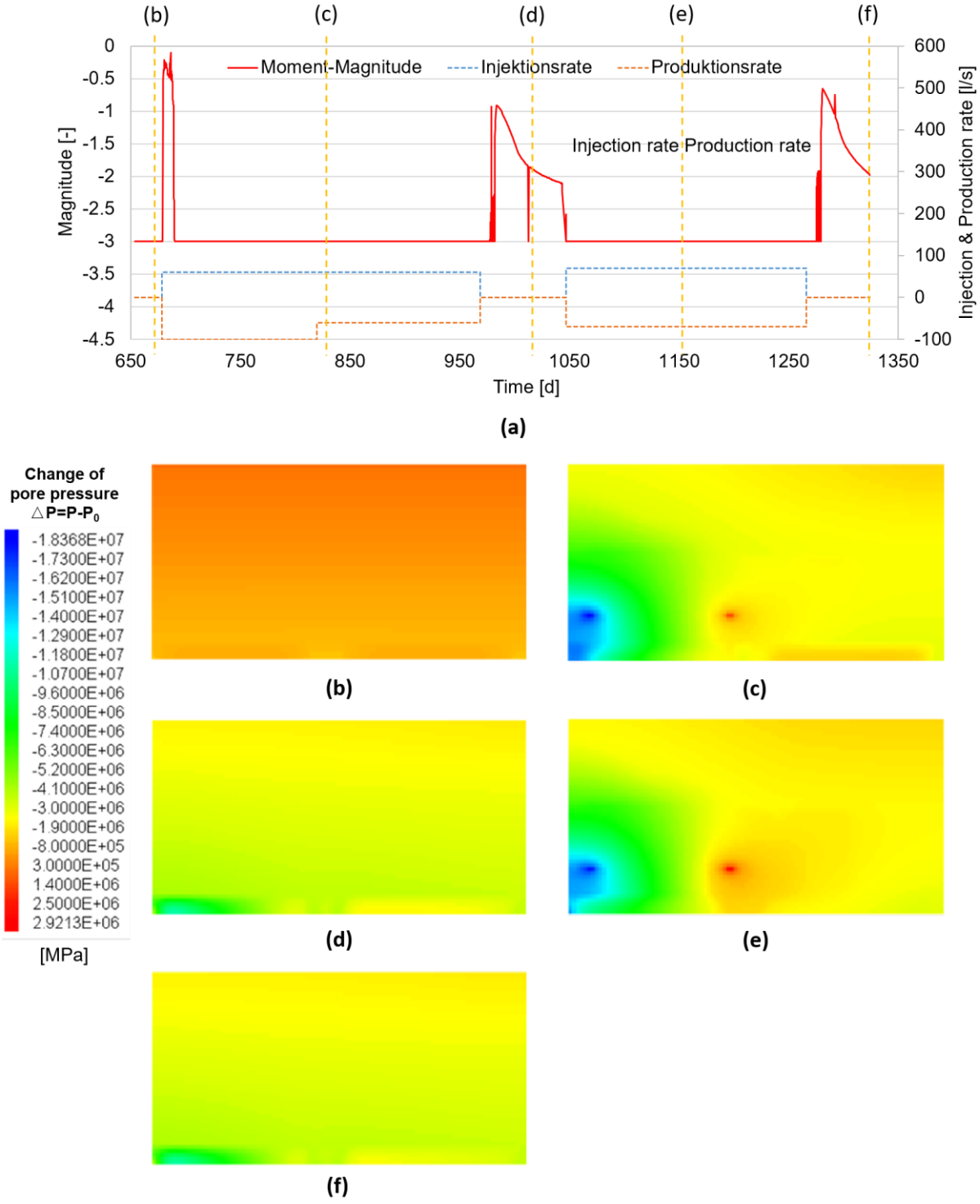

Figure 4.24 Development of (a) the calculated seismic magnitude and the injection and production rate during the production phase in contrast to (b) to (f) the change of pore pressure change at certain time points (t = 680 d, 825 d, 1020 d, 1160 d and 1320 d in (a))

Further, in order to study the relationship between the geothermal production process and the reactivation of natural faults (caused by the "triggered" earthquakes), a parameter called the slip tendency was introduced to describe the activation's trend. The slip tendency was originally defined as the ratio of shear stress to effective normal stress on cohesion-less fault surfaces [66]. However, the definition was updated by Gou in his doctoral dissertation [5]. Thus, slip tendency becomes the ratio between shear stress and shear strength of fault surfaces (Eq. 4.9).

$$\eta = \frac{\tau(\sigma_{ij}, n_i)}{\tau_f(\sigma_{ij}, n_i, \varphi, c)} \tag{4.9}$$

Where τ is the shear stress on the fault plane [Pa], σ_{ij} is the stress tensor of fault element [Pa], n_i is the normal vector [-], τ_f is the shear strength of fault plane [Pa], φ is the friction angle [°], c is the cohesion [Pa].

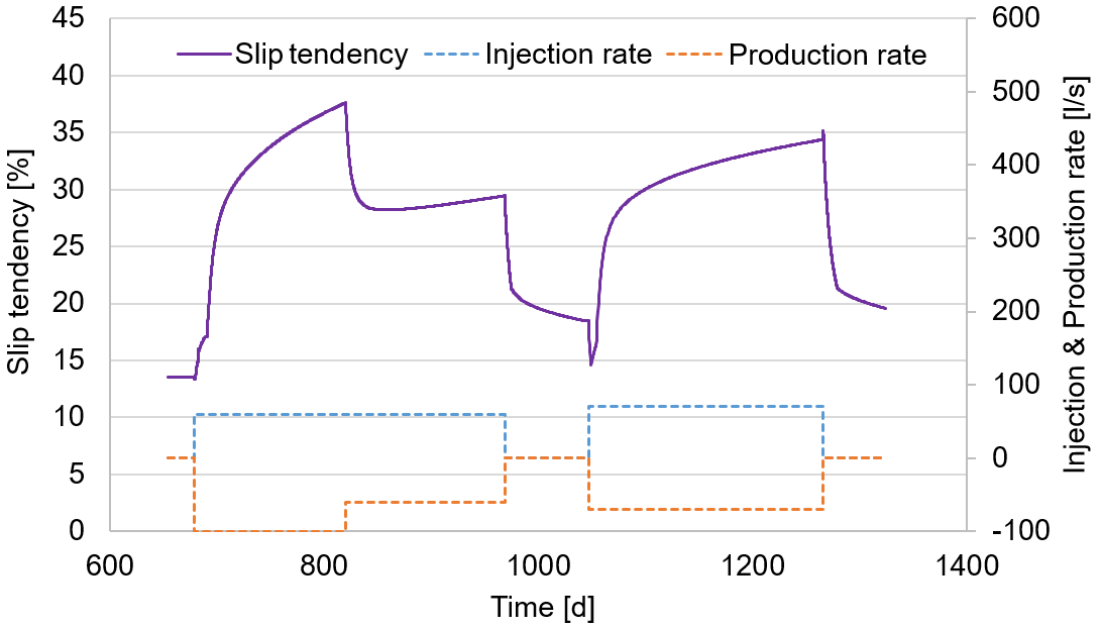

Figure 4.25 Development of the slip tendency for natural faults in contrast to the injection and production rate

Figure 4.25 describes the change in slip tendency for natural faults with reference to time, injection and production rate. Although due to technical reasons the simulation for Landau did not take the tectonic shear stress on natural faults into account, therefore the initial slip

tendency of model system is actually very small (only about 15%). Even so, the increase in slip tendency caused by geothermal production is very high (about 35%). Simultaneously, it can be found from Fig. 4.25 that the growth of slip tendency should be significantly correlated with the production rate, since the slip tendency was substantially reduced during the decreased production rate in mid-2008.

Therefore, combined with the analysis of induced earthquakes, it can be concluded that the injection and production processes in the production of geothermal projects have a clear connection with another two different processes. The first connection is between production process and induced earthquake. The production process and its corresponding stopping induces pressure's change within the artificial fracture and will cause obvious secondary disturbance. The induced earthquakes during production phase come mainly from this mechanism. The second important connection exists between the natural fault's reactivation and the production process. Since the production process will redistribute the water volume within the entire reservoir area (it should be noted here that the Landau project is not a complete HDR geothermal, its output in the first half of 2008 is significantly larger than the injection volume), the lost water from fractures will inevitably increase the slip tendency of natural faults.

4.3.5 Modified schedules for reducing the risks of induced seismicity

After analyzing the connections between production work and different geo-mechanical processes, several pairs of modified injection and production schedules are being proposed to reduce the risks from induced seismicity and reactivation of natural faults. However, their performance must firstly be confirmed by the numerical study.

4.3.5.1 Jagged injection with unchanged total volume

Fig. 4.26 illustrates a pair of modified injection and production schedules, in which the injection rate represents a serrated form (a-type). Despite of this, the total injected water

maintains an unchanged volume. As only the injection schedule has been modified, this variation can be related with the reduction of induced seismicity.

The purpose of this modification is that, since the induced seismicity during the production phase mainly comes from the disturbance caused by change of the fracture pressure, enough time should be there for the system to encounter the change. Thus, a serrated injection schedule was proposed. During the falling time, the pressure and stress redistributions get time to carry out.

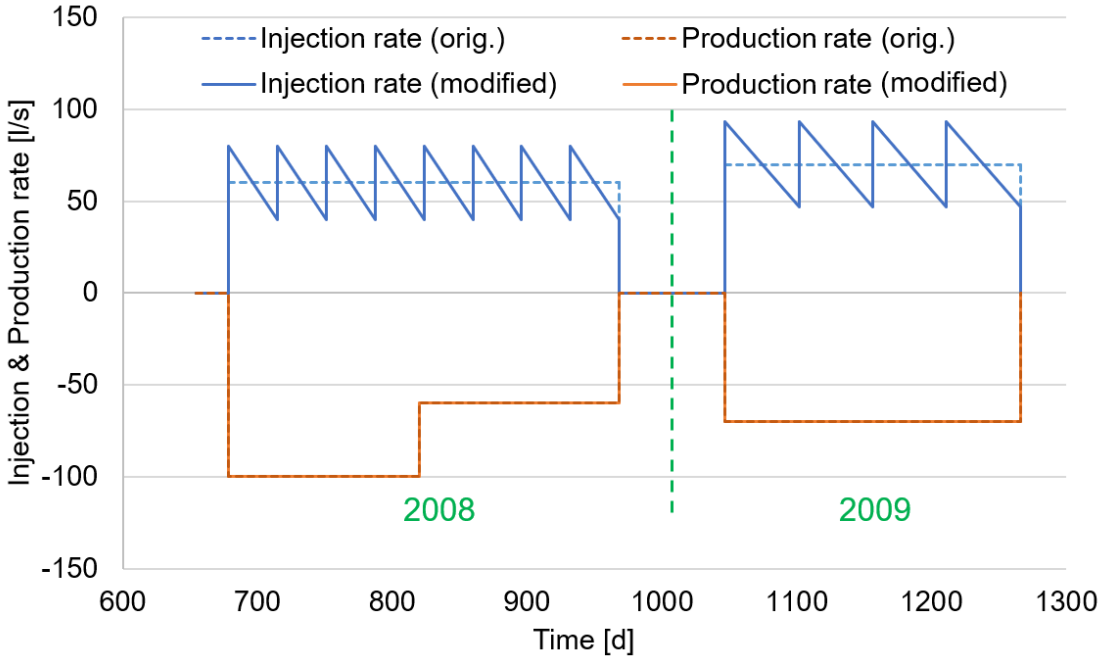

Figure 4.26 A-type modification of injection and production schedules comparing with the original schedules for simulation

However, results shown in Fig. 4.27 demonstrates that the performance of this modification is not so obvious. Although the induced seismicity during paused time and the slip tendency of first phase (2008) are both reduced for the serrated injection, but once the time of each jagged form becomes longer (2009), changes become almost negligible. This is mainly because of the total injected volume which has not been reduced in this modification. Thus, the weakening in pressure change is also very limited.

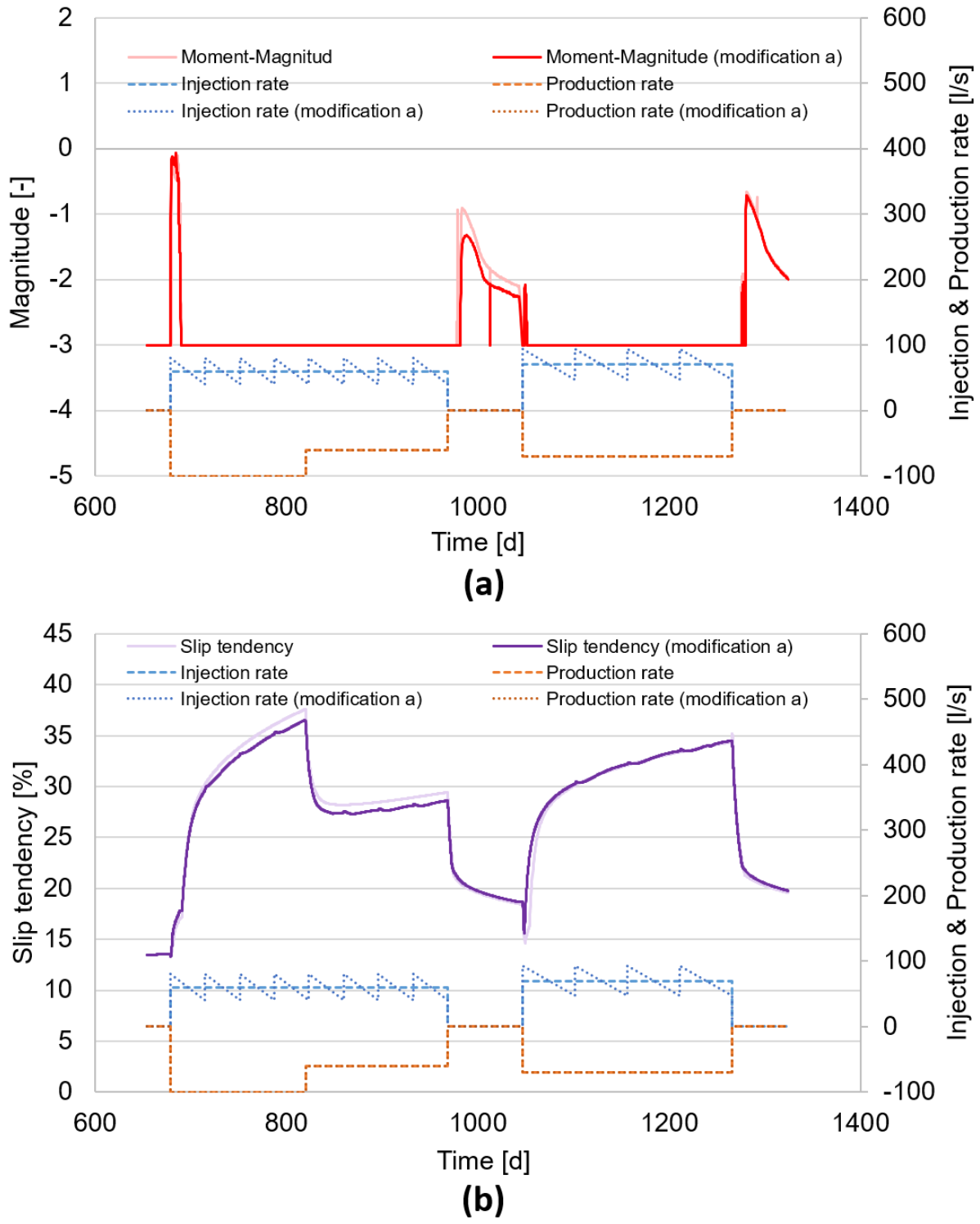

Figure 4.27 Comparison of the development of (a) synthetic seismic magnitude and (b) slip tendency caused by original and modified injection schedule (a-type) in contrast to the injection rate.

4.3.5.2 Production with a reduced rate

In the second modification (b-type), the production rate was reduced to appeal a weakening of the slip tendency (Fig. 4.28). One thing should be noted that, appeal the total produced volume was also decreased due to the modified reduced rate.

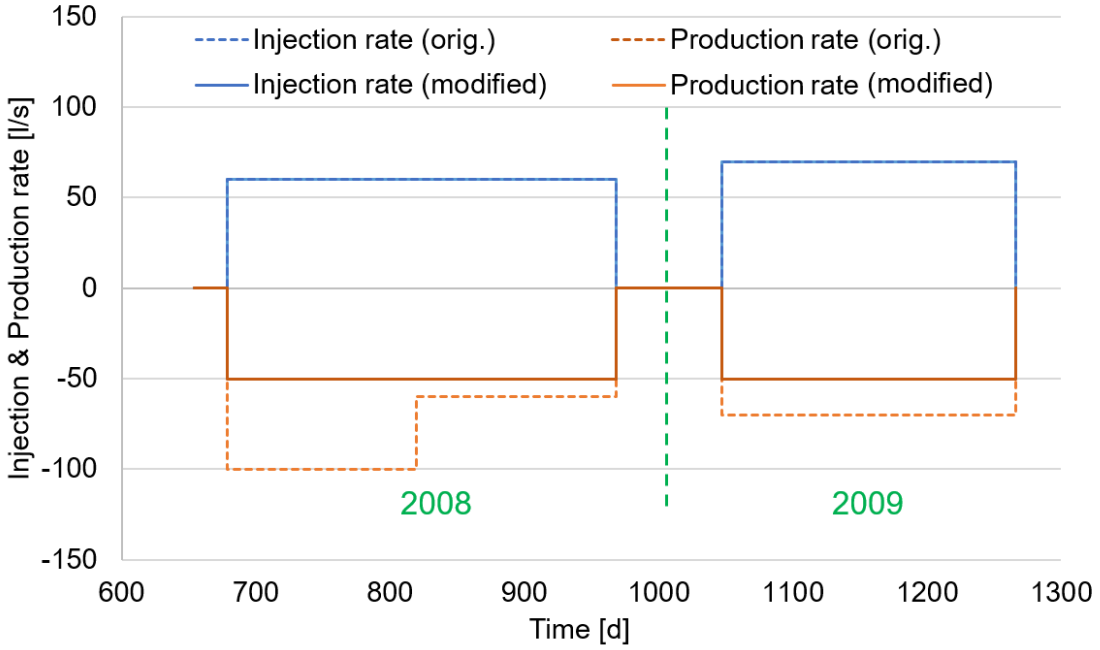

Figure 4.28 B-type modification of injection and production schedules comparing with the original schedules for simulation

Fig. 4.29 (b) reveals that this modification is very useful to reduce the slip tendency. Through the decreased production rate, the growth of slip tendency in the early stage of production is effectively suppressed. But unfortunately, since only the production rate is reduced, this modification on the contrary causes stronger pressure change (more input but less output), or unbalance. Thus, more intensive induced seismicity is occurred during the production phase (see Fig. 4.29 (b), at the beginning of 2009 even some events with magnitude larger than 0 appeared).

At the same time, there is still one thing that is not clear here, i.e. the weakening of slip tendency is because of the production process alone or also influenced by the operation's intensity of entire system?

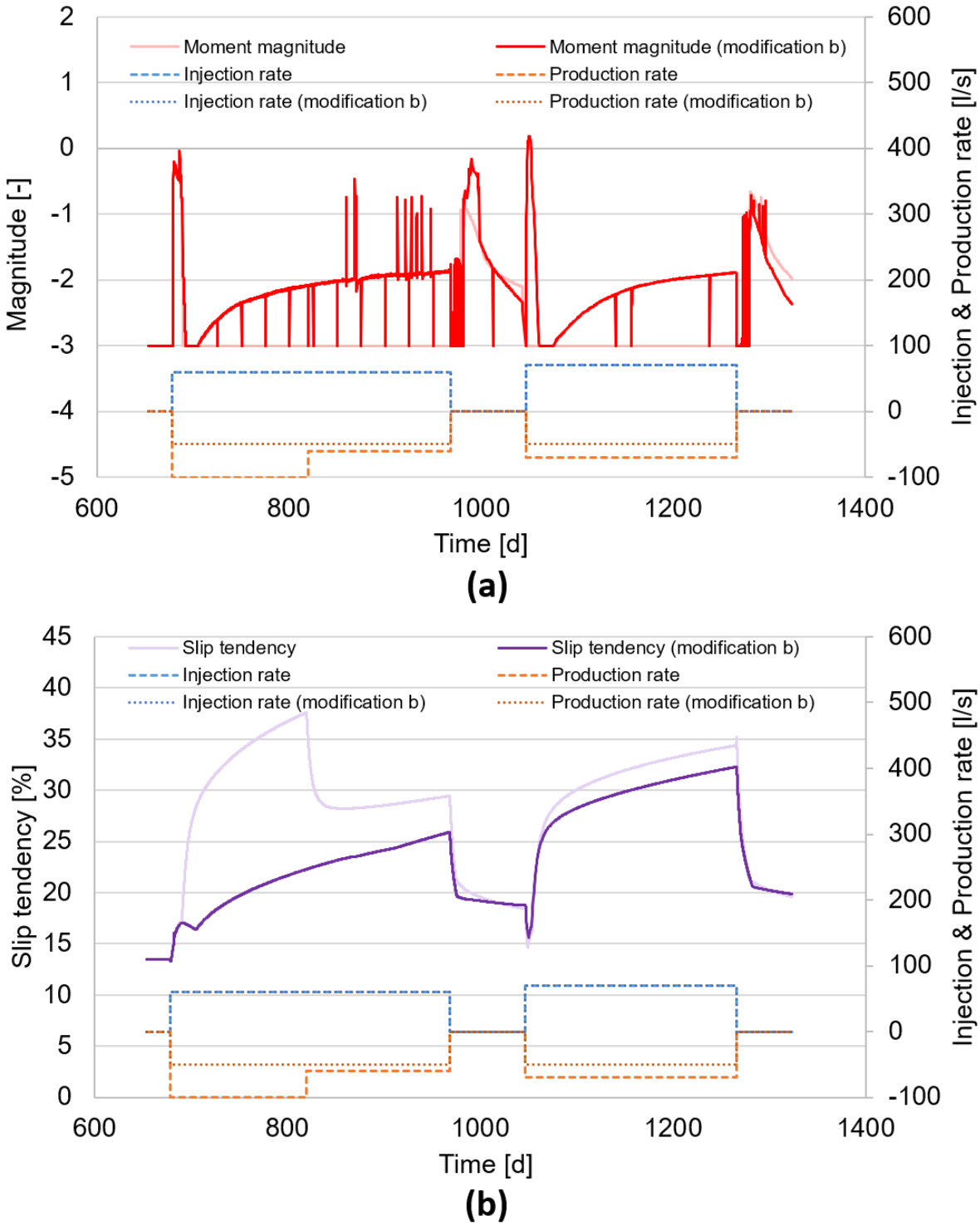

Figure 4.29 Comparison of the development of (a) synthetic seismic magnitude and (b) slip tendency caused by original and modified injection schedule (b-type) in contrast to the injection rate.

4.3.5.3 Injection and production with reduced rates

Above question can be answered by adopting the third modification (c-type). In this improvement, in order to mitigate the intensity of induced earthquakes, the injection rate is also reduced (still with a serrated form) along with the reduced production rate (Fig. 4.30).

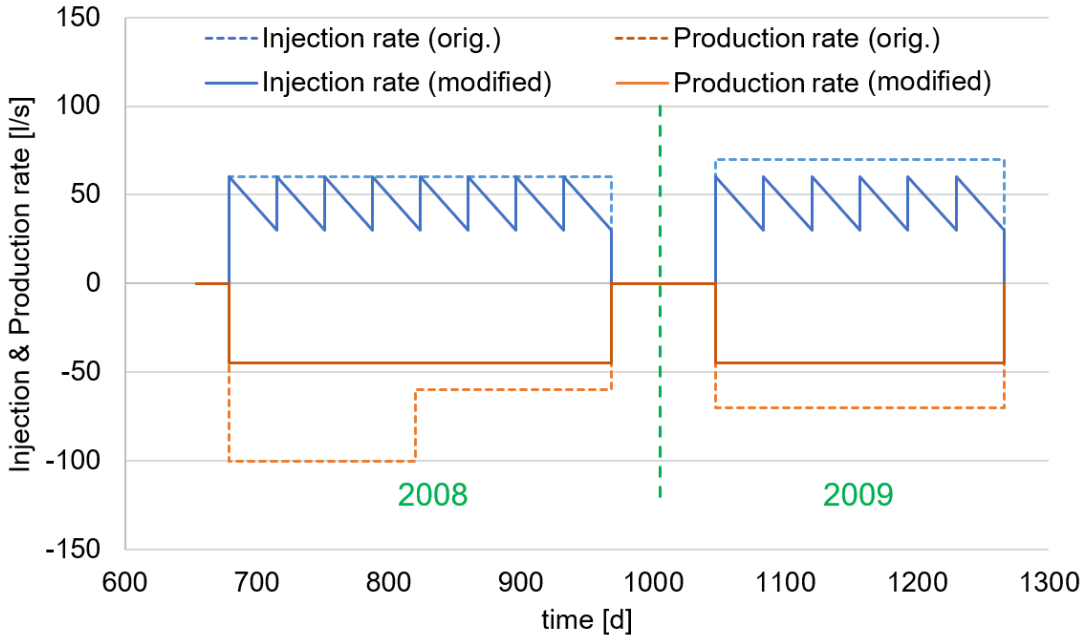

Figure 4.30 C-type modification of injection and production schedules comparing with the original schedules for simulation

As shown in Fig. 4.31 (a), since the injection rate has been reduced to avoid strong disturbances, there are no intensive events in the synthetic seismic magnitude generated by improved schedules.

Further, the slip tendency during whole production phase was reduced on the basis of modification b. This indicates that, production rate is not the only factor affecting the change of slip tendency. More important is the operating intensity of entire system. Therefore, reduction in the risk of destructive geological disasters in a geothermal system can be achieved by improving and coordinating the injection and production schedules.

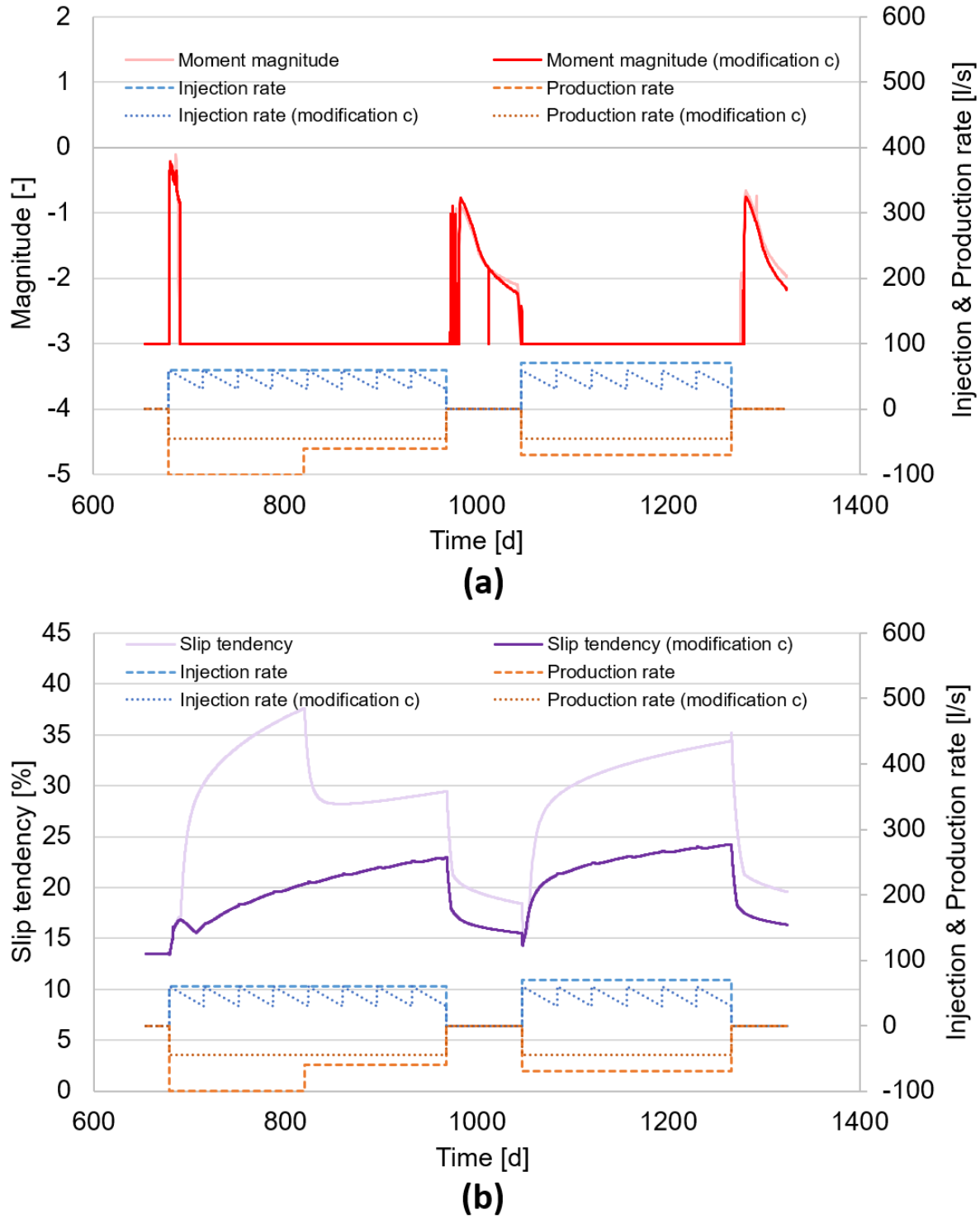

Figure 4.31 Comparison of the development of (a) synthetic seismic magnitude and (b) slip tendency caused by original and modified injection schedule (c-type) in contrast to the injection rate.

4.4 Summary

In this chapter the simulator TOUGH2MP-FLAC3D was used to achieve the modeling of EGS project Landau. From the well-matched temporal evolution of BHP ("history matching") the simulated results are believed to be reliable. Thus, three important phenomenon can be found in the contour presentations, the synthetic catalog and the graphic illustration of slip tendency:

1. The area of entire fracture zone at the beginning increased very rapidly and then remained unchanged. However, the core area within and around the natural faults is more susceptible to the injection work. Thus, its plastic strain increased further.
2. Seismic events occurred even after stopping the injection. This is because of change in the pore pressure was delayed. For this reason, the mechanic and hydraulic equilibrium state cannot be achieved immediately. The after failure process (fracturing and seismic) therefore continued until the end of stress redistribution.
3. During the production phase the seismic events occurred only at the beginning and after the stop of operation. The reason is an intense rise and fall in injection and production rate (system need time and carrying out corresponding geo-mechanical or rather -hydraulic processes to digest the change in fracture volume and pressure), which induces disturbance in the system. This causes further fracture process. The stronger the disturbance, the more intensive the seismic events could be.

Hence the conclusion is, unbalanced production work (fast rise and fall of injection rate and huge difference between injection and production rate) lead to induced seismicity, while the reactivation trend of natural faults (slip tendency) is impacted by the system's operating intensity (absolute values of the injection and production rate). Thus, the recommended countermeasures were derived from the study, i.e. the injection and production rates should be reduced immediately with a moderate and equal rate when critical seismicity magnitude (e.g., $M_L \geq 2.0$) occurs.

5 Advanced FLAC3D^{plus} - a further developed 3D-Simulator for modeling of hydraulic fracturing in consideration of fracture propagation with arbitrary orientation and hydro-mechanical coupling effects

Models and methods mentioned in Chapter 3 have been implemented into FLAC3D^{plus} to simulate and analyze the generation of artificial fracturing. However, there exist still many more complex problems in the actual engineering that need to be solved. Since the modeling executing in FLAC3D^{plus} are all based on a core assumption, i.e. orientations of the in-situ stresses are throughout the same, the simulated results would express as straight fractures propagating perpendicular to the minimum principal stress. Although this assumption can on one hand avoid heavy computational works, but on the other hand it ignores the unevenness and anisotropy of in-situ stresses. The simulated results under complex geological conditions will be different from the actual situation. For this reason, some improvements must be carried out for this powerful simulator.

5.1 Fracture's propagation in stimulation operation

In order to better improve FLAC3D^{plus}, the first thing that should be figured out is what happened to the fracture when it's propagation direction changes. Thereafter, coping modifications can be applied to the simulator.

As a highly oriented simulator, the purpose of FLAC3D^{plus} is to simulate the generation of artificial fracture in tight sandstone. From an environmental background of stimulation work, the failure morphology corresponding to tight sandstone possesses a significant feature, that is, tensile fracture occurs as dominated failure instead of shear failure. Since the sandstone is mainly composed of fine sand particles bonded to each other (see Fig. 5.1(a)), for such a structure the tensile strength is much smaller than the shear strength. So, the tensile failure is more likely to occur.

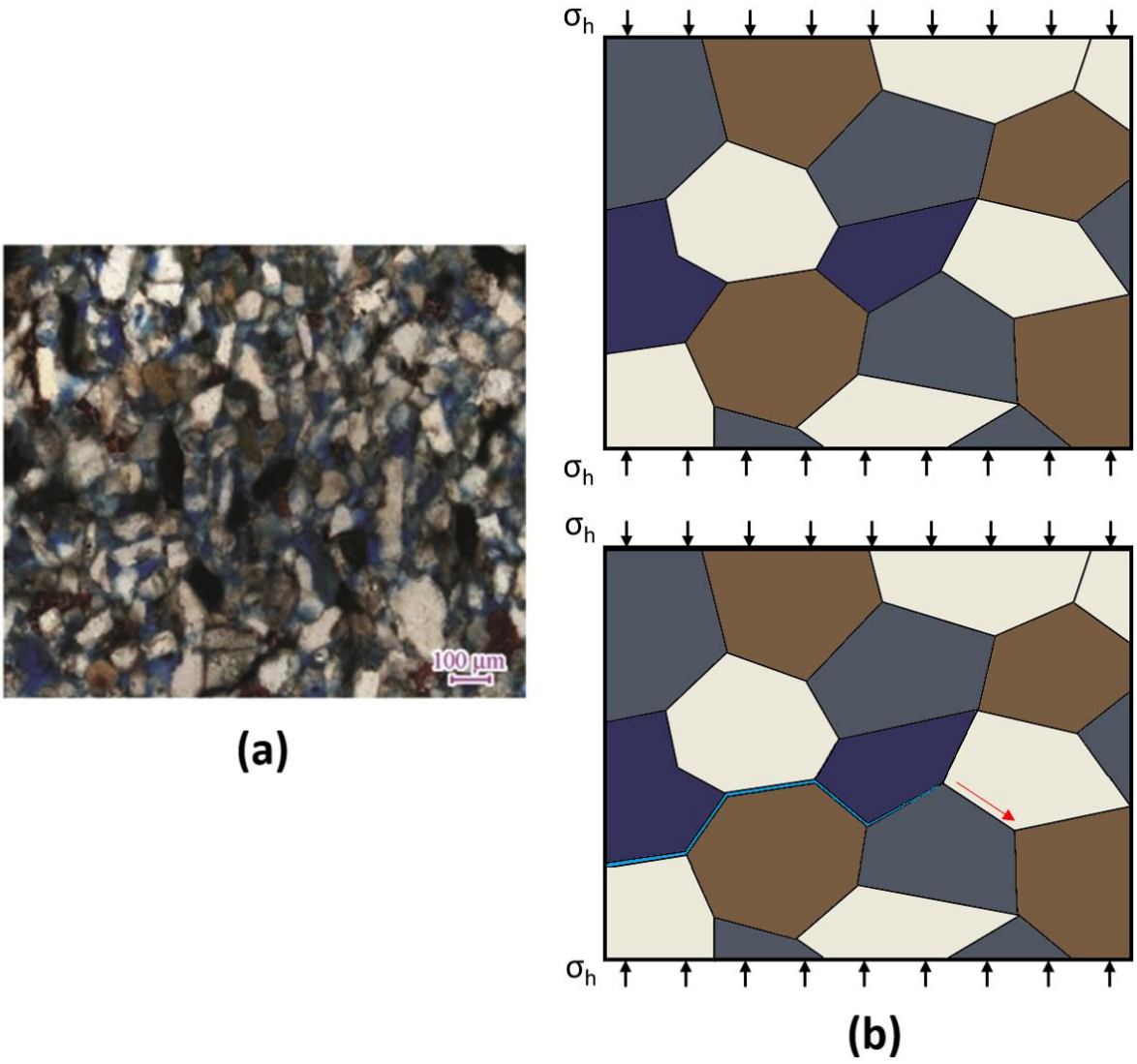

Figure 5.1 Demonstration of (a) the bonded structure in sandstone [67] and (b) the fracture's propagation within

Another point to note is that the fracture in a destructed rock expands not indiscriminately. Its direction always tends to be perpendicular to the direction of minimum principal stress at its location (Fig. 5.2 (b)). This is also easy to understand. According to the principle of minimum energy, the rock after destruction must restore the equilibrium (of system) by external work. The easiest way to achieve this goal is that the fracture opens in the direction of the minimum principal stress. Thus, the fracture will propagate in a path that is closest to the direction perpendicular to the minimum principal stress.

5.2 The further developed hydro-mechanical simulator for modeling fracture's propagation with arbitrary orientation

The objective of this study is to improve FLAC3D^{plus} so that it possesses the capability to model fracture's propagation with arbitrary orientation. At the same time, it has been explained above that the propagation's direction always tends to be perpendicular to the minimum principal stress. Thus, the governing equations of improved simulator are still based on the original system (of FLAC3D^{plus}, see Chapter 3). The modification is done mainly in their numerical formulation and implementation.

5.2.1 Realization of fracture's propagation with arbitrary orientation in FLAC3D^{plus}

5.2.2.1 Model element of triangular prism

To achieve better direction's change especially from the perspective of geometry, the improved FLAC3D^{plus} (more willing to call it advanced FLAC3D^{plus}) uses completely the model composition consisting of triangular prisms (Fig. 5.2 (b)). This is because, since the fracture in previous FLAC3D^{plus} is assumed to propagate only in one direction, i.e. perpendicular to the minimum principal stress, the elements of geometric model can be set as a rectangular parallelepiped that contains single preset split (Fig. 5.2 (a)). Through the arrangement of triangle element, two preset splits within are enabled to be activated as the fracture expands further. More importantly, the elements in the emphasized area will normally be set as equilateral triangular prisms, whereby three preset splits are of equal length and at an angle of 120º. Thus, the influences from geometry (of the element) are minimized and the impacts of induced stress are apparent. In more extreme cases, all the three splits can be activated in the simulation.

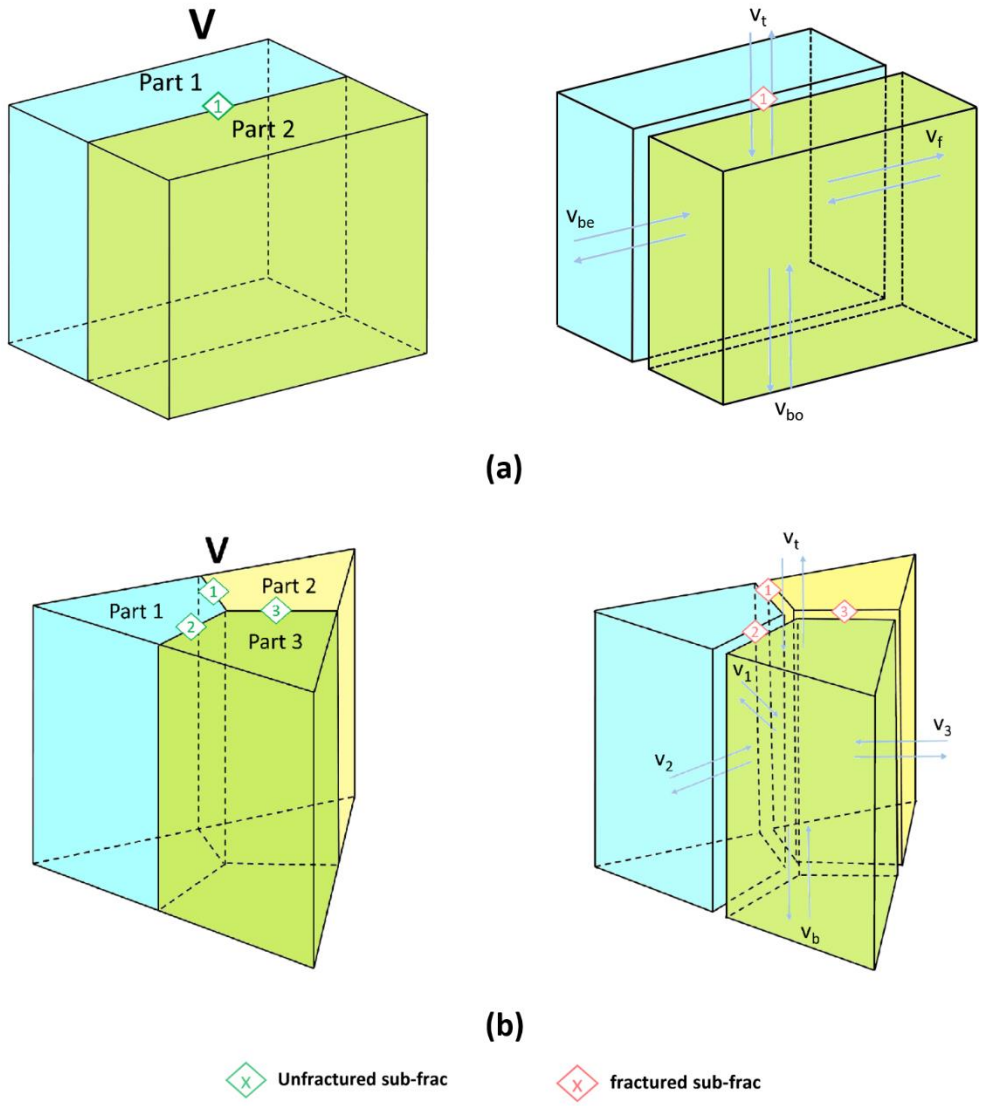

Figure 5.2 Comparison between (a) the rectangular parallelepiped element with single preset split (FLAC3D^{plus}) and (b) the improved prism element with three preset splits (advanced FLAC3D^{plus})

5.2.2.2 Alteration of the fracture width

As introduced in Zhou et al. 2014 [29], in FLAC3D^{plus} an extra strain increment induced by fracture's pressure change (due to fluid flow or leak off) is added in the total strain increment so that the discontinuous behavior can be described. This idea has also been retained in advanced FLAC3D^{plus} (see Fig. 5.3). That means, for each of the sub-fracs (subprime fracture) its actual width would be controlled by the interaction between fluid pressure and surrounding stress (Eq. 5.1 and 5.2).

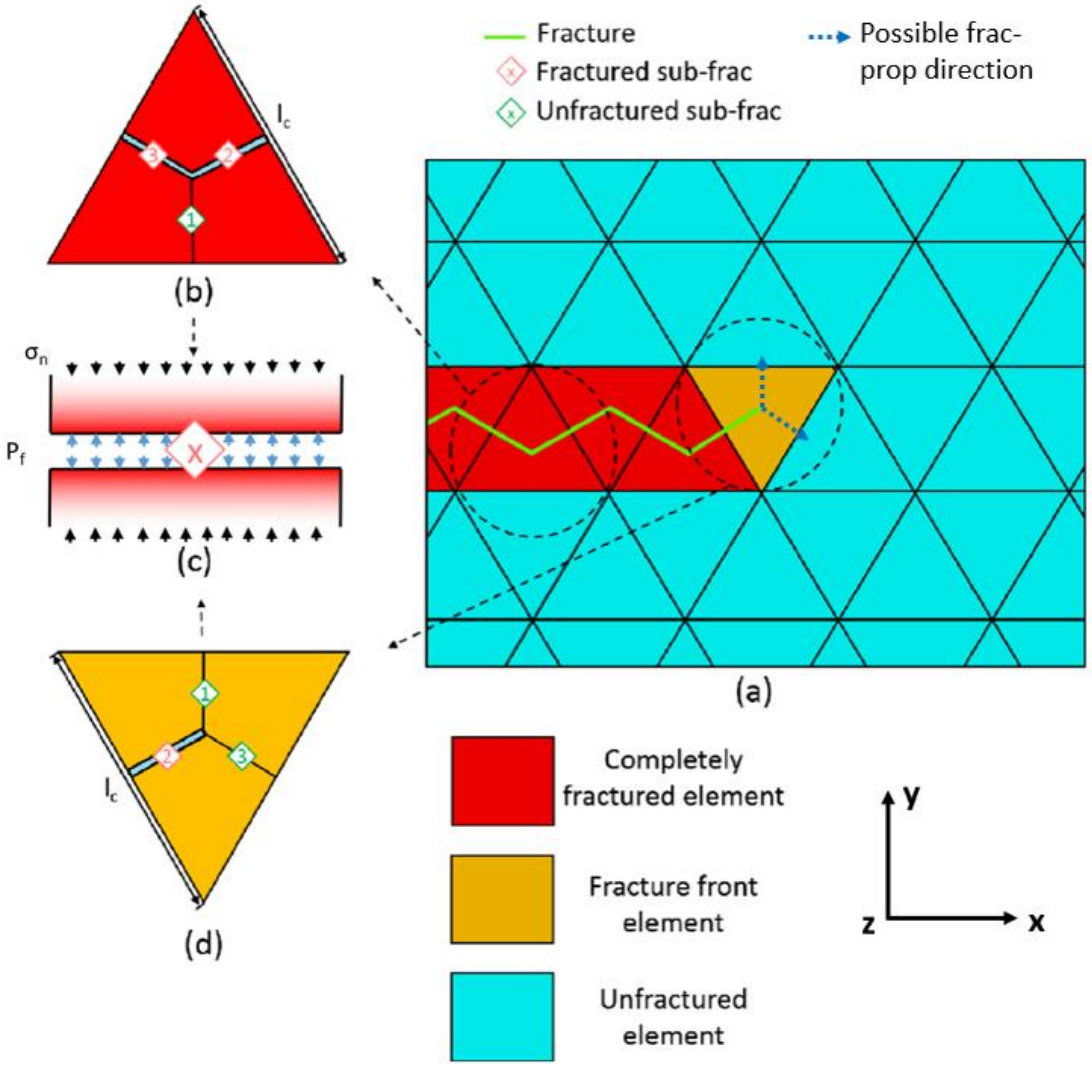

Figure 5.3 Demonstrations of (b) and (d) the fracture elements in (a) the geometric model as well as the interaction between fluid pressure and surrounding stress at a certain time point

$$\Delta\varepsilon_f = \frac{P_f(t+1) + \sigma_n(t)}{\alpha_1} \tag{5.1}$$

$$\Delta \mathrm{w} = \Delta\varepsilon_f l_c a_{geo} = \frac{P_f(t+1) + \sigma_n(t)}{\alpha_1} l_c a_{geo} \tag{5.2}$$

Where ε_f is the strain induced by change of the fluid pressure and the stress [-], P_f is the fluid pressure within the fracture [Pa], σ_n is the normal stress perpendicular to fracture [Pa], α_1 is the elastic parameter [-] and = K + 4G/3, w is the fracture width of sub-frac

[m], l_c is the length of corresponding side [m], and a_{geo} is the coefficient to describe the geometric effect [m] (value between 0.5 and 1).

Further, change of the stress in three orthogonal directions (of the sub-frac, the so called induced stress) (Eq. 5.3 and 5.4) also affect the fracture's expanding of next step.

$$\sigma_n^{new} = \sigma_n^{old} - \alpha_1 \Delta\varepsilon_f \tag{5.3}$$

$$\sigma_{1,2}^{new} = \sigma_{1,2}^{old} - \alpha_2 \Delta\varepsilon_f \tag{5.4}$$

Where σ_n is the normal stress perpendicular to fracture [Pa], α_1 is the elastic parameter [-] and = K + 4G/3, ε_f is the strain induced by change of the fluid pressure and the stress [-], $\sigma_{1,2}$ is the stress in another two principal directions of fracture [Pa], and α_2 is another elastic parameter [-] and = K - 2G/3.

However, the updated value must firstly be transferred to the global coordinate using Eq. 5.5.

$$[\sigma] = [C]^T [\sigma]' [C] \tag{5.5}$$

Where $[\sigma]$ is the stress tensor in the global coordinate [Pa], $[C]$ is the rotation tensor whose three columns are the direction cosines of x', y', and [n] [-], and $[\sigma]'$ is the stress tensor in the local coordinate [Pa].

5.2.2 Fracture propagation and orientation

Since induced stress has been obtained in the previous calculation, the updated stress field can be applied to determine whether the preset splits will be activated or not. As mentioned before, the elements of triangular prism are used in advanced FLAC3D^{plus}, hence different forms will be seen from the top and the side views (Fig. 5.4).

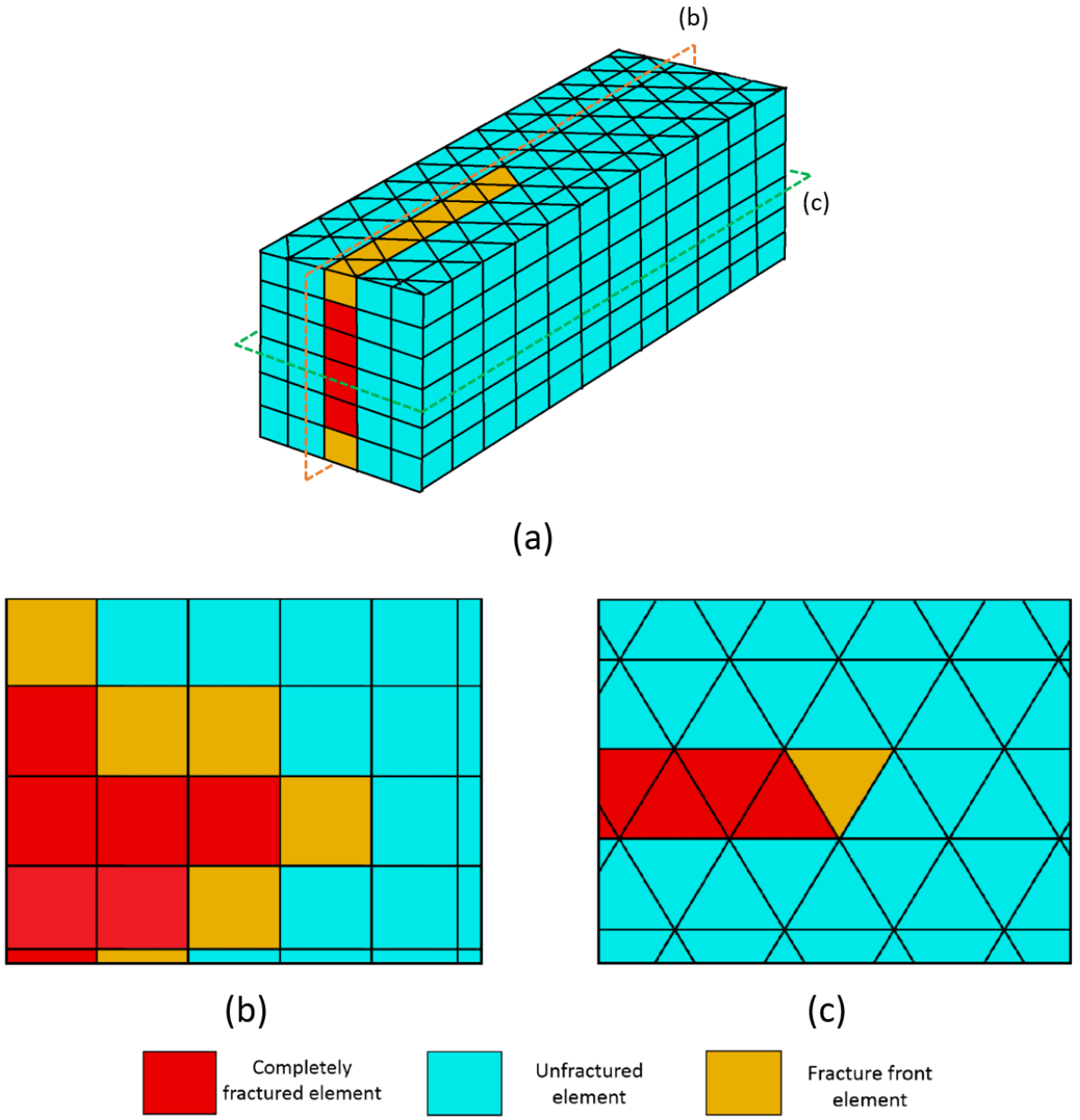

Figure 5.4 Classification (completely fractured, unfractured and fracture front) and geometric relationship of the elements: (b) for side view and (c) for top view of (a)

The same also applies to the numerical formulation. In the specific judgment, the elements in geometric model are classified into three different types, named as the completely fractured, the unfractured and the fracture front element (fracture tip). When more than two preset splits are activated in the calculation, the corresponding element would be classified into completely fractured one. Its adjacent element possessing one or less activated pre-frac is classified into fracture tip. Others would be classified into unfractured elements.

Thus, in a series of computation carried out by advanced FLAC3D^{plus}, there are always such things to be repeated (see Fig. 5.5 - the flow chart of computational calculation procedure):

a) Hydraulic and general mechanical calculations are performed in all the model elements but with different types. The unfractured elements relate the porous rock formations. However, a set of calculation procedures designed specifically for fractured elements is applied to the completely fractured elements and the fracture tips.

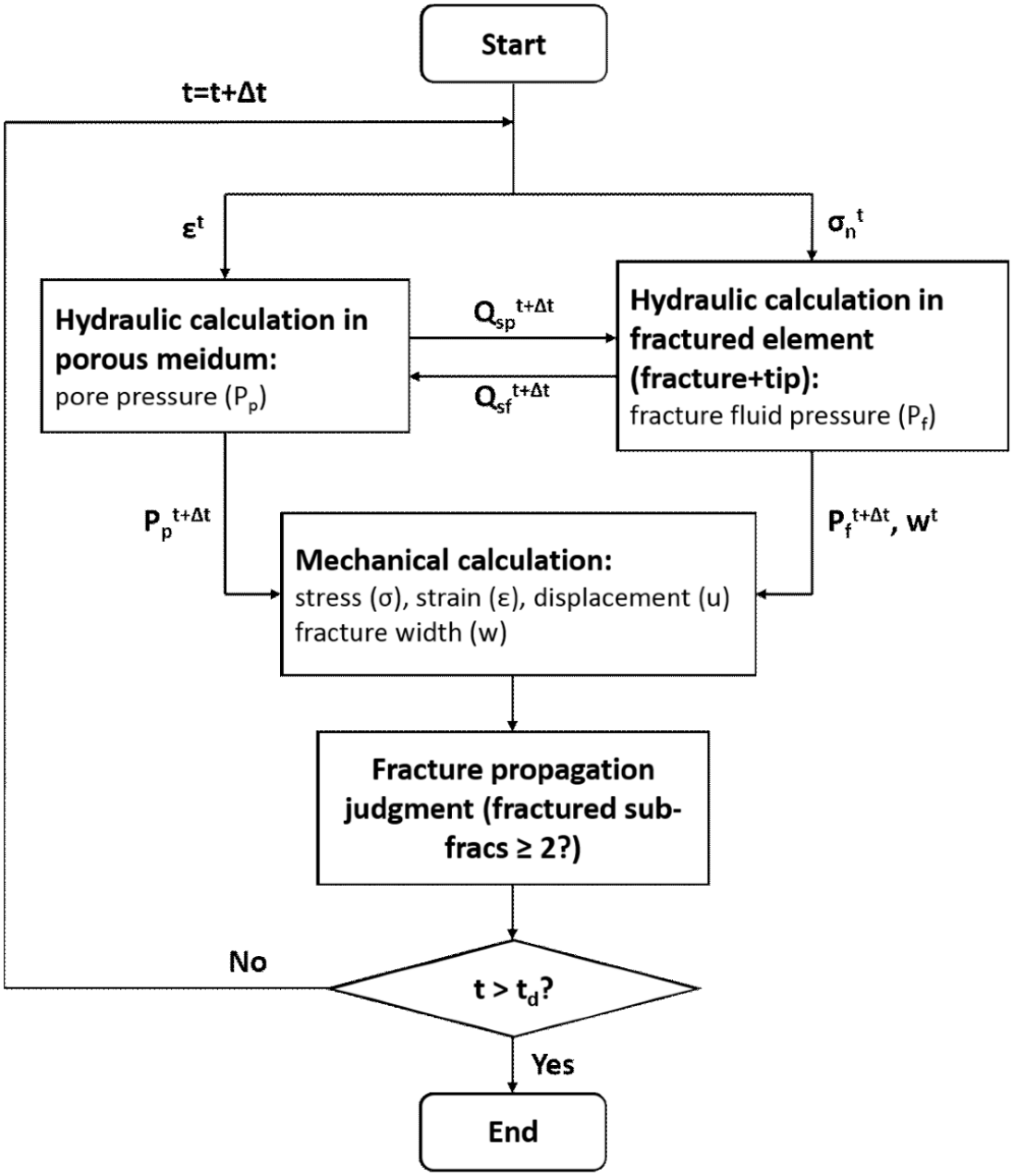

Figure 5.5 Flow chart of the computational calculation procedure

b) After the stress or rather strain has been calculated, propagation judgment would be carried out in all the fracture tip elements (Fig. 5.5 and 5.6). If a fracture tip element determines that more than two preset splits within it can be activated (all the sub-fracs are numbered according to the number of grid points, see Fig. 5.6 (b)), its classification would be updated (from (c)-1 or (c)-2 to (c)-3 or (c)-4). However, if the stimulation work is not so intensive, this element may also maintains to be as fracture tip but its status actually has turned from (c)-1 to (c)-2.

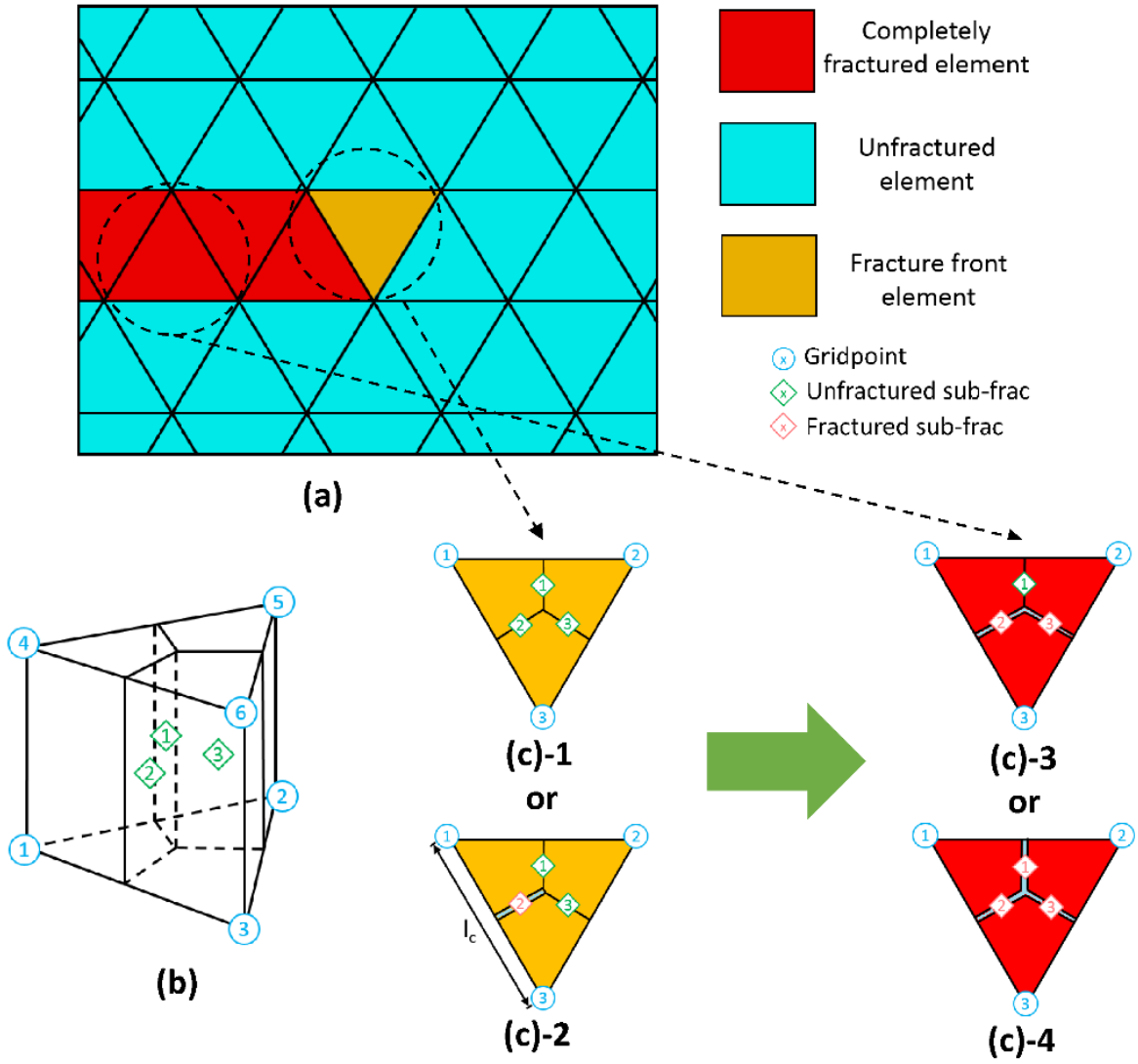

Figure 5.6 Graphic presentation of (a) the positional relationship between three types of elements, (b) the numbering of sub-fracs according to number of grid points and (c) the transformation from fracture tip to completely fractured element

5.3 Verification of the improved simulator

5.3.1 Propagation of a KGD fracture

To verify the new features of simulator, an example of KGD fracture taken from Carrier et al. 2012 [46] was firstly used for reference. Applying the parameters given in Tab. 5.1 and using the geometric model in Fig. 5.7 with all its sides being fixed, a stimulation work with an injection rate of 0.5l/s was modeled using the improved simulator.

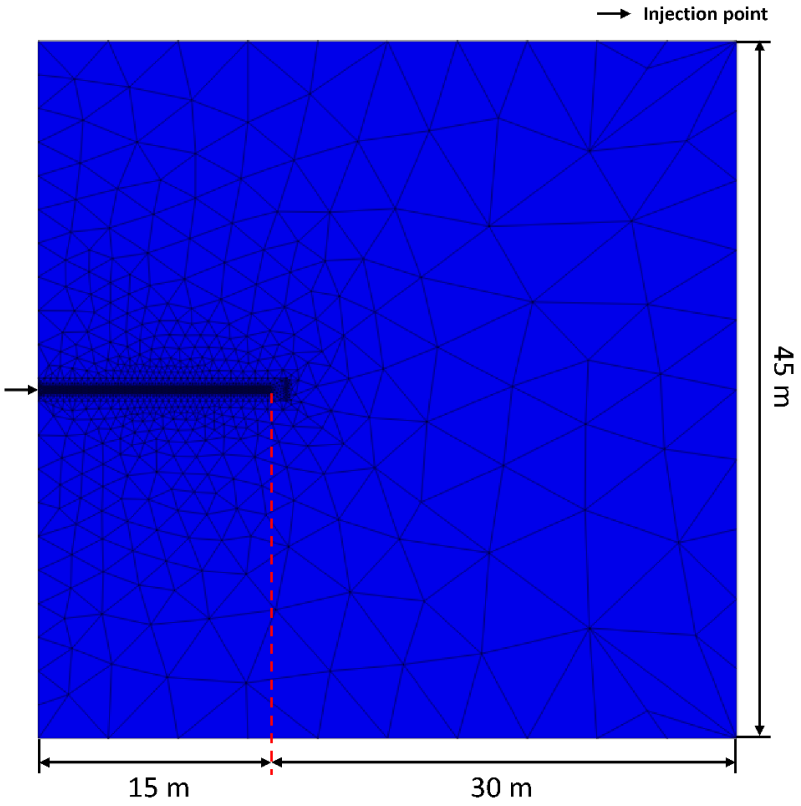

Figure 5.7 Geometric model and mesh used in numerical modeling of the propagation of a KGD fracture.

Table 5.1 Applied parameters for the numerical simulation of a dynamic growth of the KGD fracture

Parameters	Symbol	Value
Young's modulus [GPa]	*E*	17

Poisson's ratio [-]	v	0.2
Critical traction strength [MPa]	σ_c	1.25
Cohesive fracturing energy [Pa•m]	G_c	120
Injection rate [m^3/s]	Q	0.0005
Viscosity [Pa•s]	μ	0.0001
Far-field stress [MPa]	σ_0	3.7

When the numerical results were compared with the semi-analytical solution in Bunger et al. 2005 [68] (see Fig. 5.8 and 5.9), the temporal evolution of fracture length or the width envelope after 10 s' operation matches well. Thus, a preliminary verification for the functionality is achieved. The next necessary thing is to check whether advanced FLAC3D^{plus} can model the fracture's steering logically.

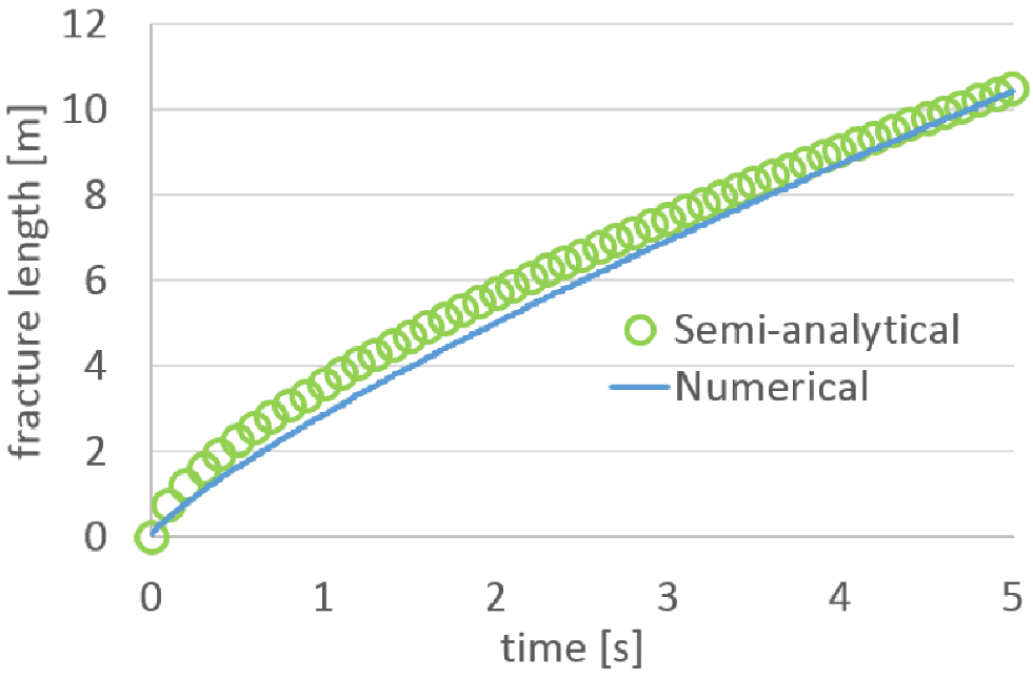

Figure 5.8 Comparison of the KGD fracture's propagation between semi-analytical and numerical solution

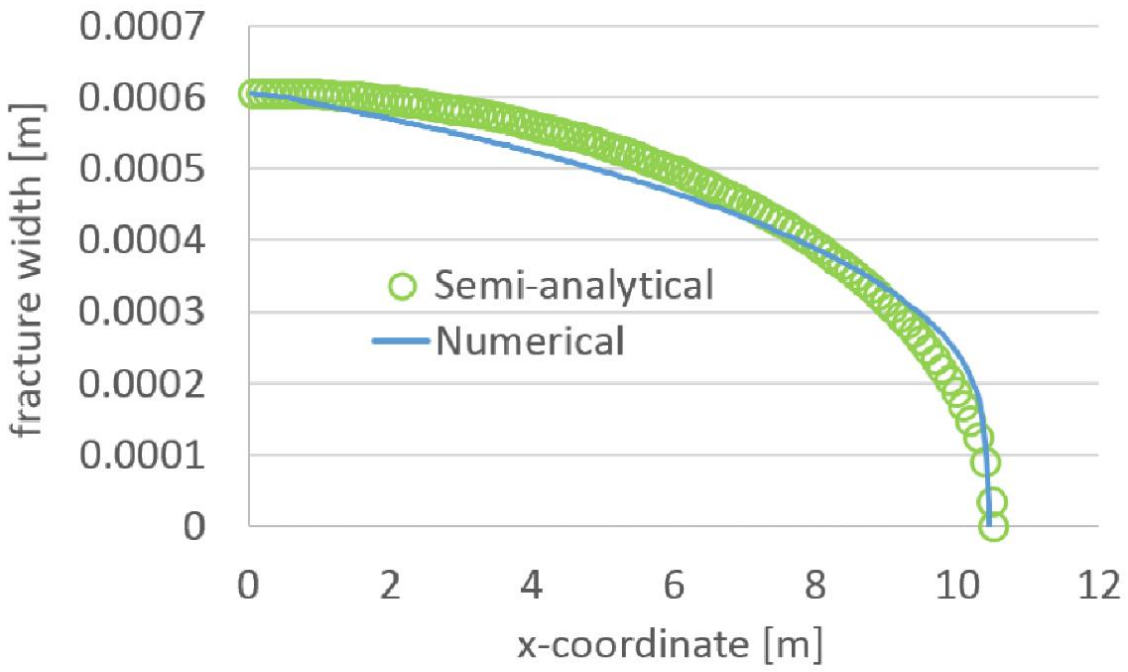

Figure 5.9 Comparison of the KGD fracture's width profile at t=10 s between semi-analytical and numerical solution.

5.3.2 Steering of a fracture

This verification is still based on the model which is presented in section 5.3.1. However, the initialized fracture is assumed to possess a direction that is not perpendicular to the minimum horizontal stress σ_h, but almost along its direction. Additionally, the maximum horizontal stress σ_H is set to be as twice as σ_h. Thus, if the feature of arbitrary direction in the improved simulator is functional, the fracture should complete the steering in a relatively short period of time and continue to expand in a direction perpendicular to σ_h.

In the simulated results, it can be seen that only in 1 second after the start of water injection, i.e. after the fracture has just begun to propagate (Fig. 5.10 (c)-1), the steering has been successfully completed. The direction of fracture turns from the direction along σ_h to the direction perpendicular to it. Checking σ_h in the computing process (Fig. 5.10 (b)-2 to (d)-2), noticeable induced stress appeared in the tip area to make the fracture complete above steering process. In addition to this, final length of the fracture is shortened by only about 8 meters due to the additional consumption of part of the energy in steering.

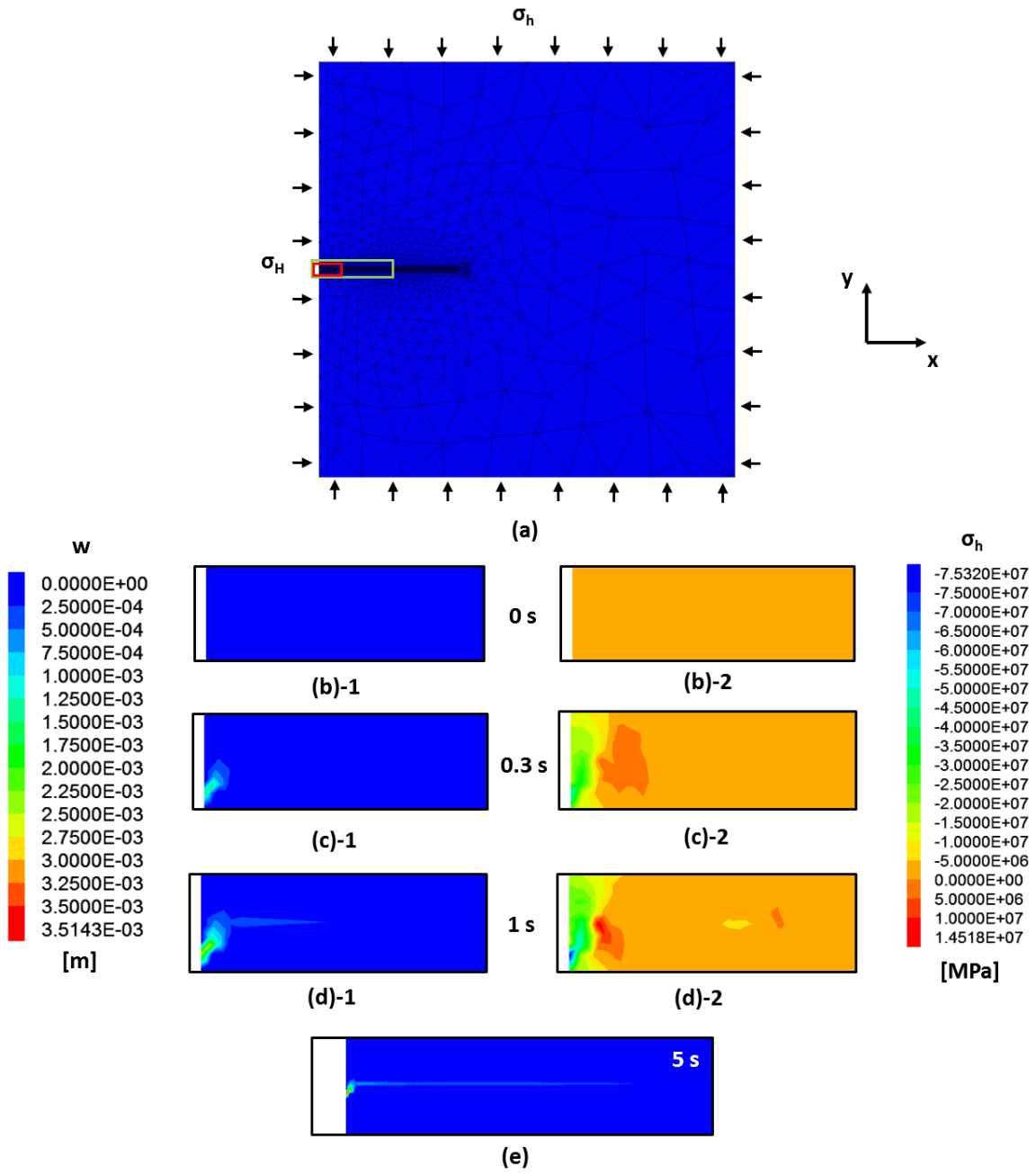

Figure 5.10 Graphic presentation of the temporal propagation of fracture ((b)-1 to (e)) and appearance of induced stress ((b)-2 to (d)-2), (a) shows the positions of magnified view

5.4 A 3D example

Since the new simulator is called an improved version of FLAC3D^{plus}, it should also have inherited some powerful features of the old simulator, e.g. FLAC3D^{plus} can simulate the

fracture's expansion on 3D level. Here, a 3D example is introduced to demonstrate this feature of advanced FLAC3D^{plus}.

As mentioned in Zhou's doctoral thesis [29], a reservoir normally does not possess a uniform geometry. For this reason, its distribution of geological stress may also be uneven. Under such premises, it is quite possible for a horizontal well not to be directly drilled into the direction of formation's minimum horizontal stress (σ_h). In this way, it needs to study whether the fracture can continue to propagate in the direction perpendicular to σ_h, especially when its initialized direction is not in this direction.

The following example has assumed such a situation. In a small model (see Fig. 5.11, x × y × z: 50 m × 50 m × 10 m) with its mechanical and hydraulic properties listed in Tab. 5.2, an artificial fracture has been initialized in the direction at a 30° angle to the direction of σ_h (3.7 MPa). The maximum horizontal stress σ_H is still twice the minimum one (7.4 MPa). Thus, even in a case of three dimensions, the propagation should be able to achieve a steering of its direction.

Table 5.2 Mechanical and hydraulic properties of the formations

Rock formation	Density [kg/m^3]	Young's Modulus [GPa]	Poisson ratio [-]	Tensile strength [MPa]	Porosity [-]	Permeability [m^2]
	ρ	E	Y	σ_t	Φ	K_f
Caprock	2,200	30	0.3	1.0	0.01	1×10^{-20}
Payzone	2,200	20	0.2	1.0	0.1	1×10^{-16}
Basement	2,200	30	0.3	1.0	0.01	1×10^{-20}

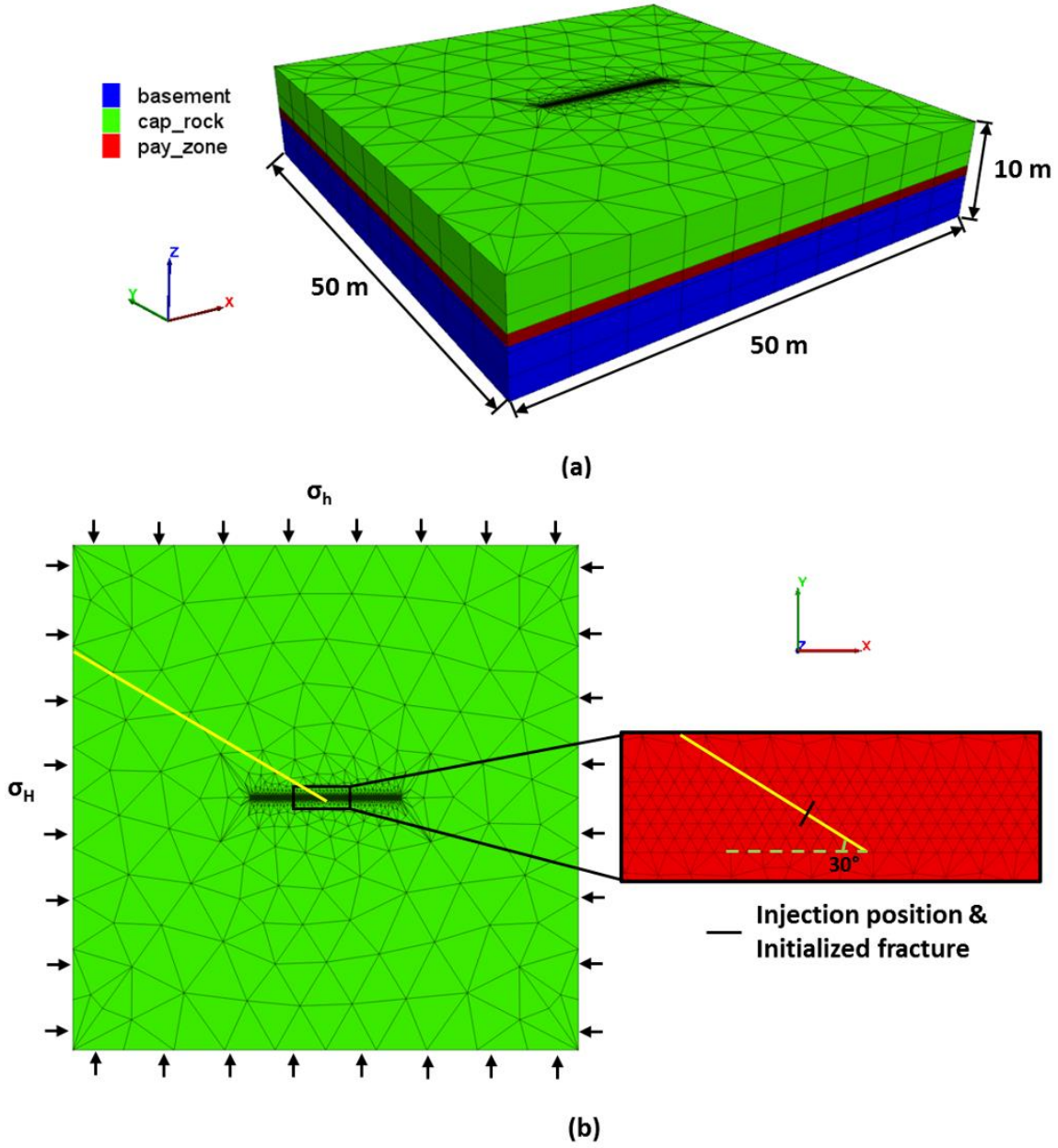

Figure 5.11 (a) The geometric model used in the simulation and (b) the position of the initialized fracture

The simulated results (Fig. 5.12) prove that above estimation is correct. In a short period of time the three-dimensional fracture has completed the steering, and because of the symmetry of the 3D model, the propagation resulted also in a symmetrical form (two-way development, see Fig. 5.12 (a)). The asymmetry of the contour image (Fig. 5.12 (b)) is due to the plotting problem of FLAC3D.

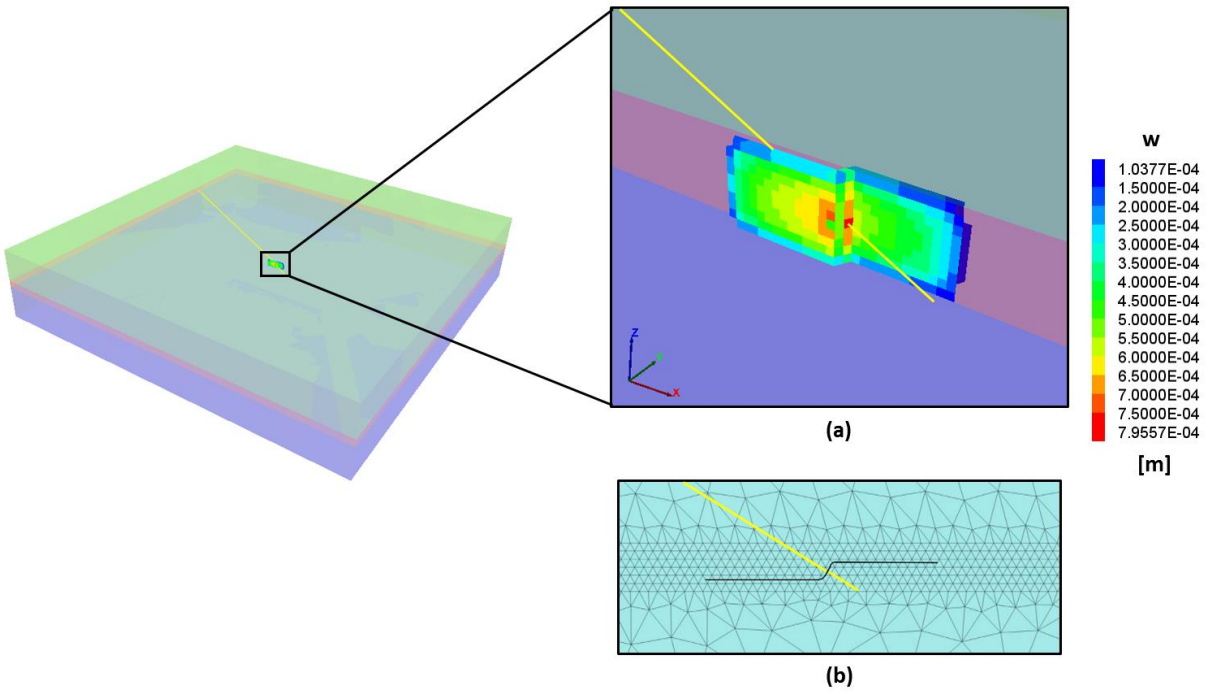

Figure 5.12 Graphic presentation of the fracture's 3D steering with (a) its width distribution, (b) is a top view of contour representation to illustrate the two-way development of fracture

5.5 Summary

In this chapter, a series of improvements to the numerical simulator FLAC3D^{plus} has been introduced. Through these modifications, e.g. the geometric model composed of triangular prisms, this powerful simulator possesses the new feature that it can model the fracture propagation with arbitrary orientation.

In the subsequent verifications, a classical KGD fracture was firstly adopted to check the functionality of improvement. The results show that the simulator can accomplish this task very well. After that, in the same model, an artificial fracture was set to initialize in a direction that is not perpendicular to σ_h. The improved simulator once again demonstrates its ability to simulate the fracture's steering due to stress unevenness. Finally, through a three dimensional example, it is proved that the simulator possesses the same functionality also in 3D situation.

In the future works, the improved simulator will be applied to some more detailed and more systematical research so that the phenomenon of fracture's expansion with arbitrary orientation can be better studied.

6 Conclusion and outlook

Hydraulic fracturing in combination with horizontal well drilling technology has played a key role in the efficient development of a large number of unconventional gas/oil reservoirs and deep geothermal resources. However, although researchers such as Adachi et al. [34] and Zhou et al. [29] have concluded that from the perspective of mechanic and hydraulic theories, the hydraulic fracturing is mainly composed of four processes, namely: a) mechanical deformation induced by pressure changes in the reservoir area (within the fracture and in the pores) as well as effective stress changes (in the porous formations); b) fluid flow in the fractures and formations, including their interactions; c) fracture expansion and d) proppant transport inside the fractures, the integral operation, especially from the perspective of THM (Thermal-Hydraulic-Mechanic) interactions have not been studied systematically.

In this thesis, in order to investigate some more targeted and important issues in the stimulation work, such as influences of the fluid's viscosity on the fracturing results and the induced seismicity during the fracturing and production operation or rather reactivation of the natural faults, several mathematical/physical models have been developed and implemented in the numerical tools (FLAC3D^{plus} and TOUGH2MP-FLAC3D). To clarify their theoretical fundamentals so that the subsequent numerical simulation and related analysis can be better performed, Chapter 2 firstly introduced the corresponding mechanic, hydraulic and thermal theories respectively. On this basis, the principle of THM coupling and the applied methods for its numerical formulation were further described. Thus, introductions of the improved simulators in each chapter become more understandable.

Using powerful FLAC3D^{plus} with a newly developed thermal module, a systematic study of the fluid viscosity's impacts on shaping of the fracture (in tight sandstone) was carried out in Chapter 3. Since this additional module is entirely based on the finite volume method (FVM) and specialized for fracture modeling, it gets the features to model heat flow in fracture, in matrix, their interactions and also the gel breaking process. After achieving the

verification, a fictitious model was firstly employed to study the influences of different factors (viscosity alone, leak off ability affected by formation permeability and viscosity). Since the statement proposed in Carrier's work [46] was confirmed and further verified in this part, following conclusions were obtained through the analysis: a) the fracture's expansion during stimulation is governed by two competing energy dissipation mechanisms (viscous flow and fracturation) and two competing storage mechanisms (in the fracture or in the porous formation). The system tends to be storage (in fracture)-dominated, when fracture's leak off ability is low enough (depending on the combined effects of formation permeability and fluid viscosity). In this case, influences from the viscous flow become more significant, i.e. an artificial fracture with more viscous fluid tends to expand in the width direction (viscous flow) rather than in the length direction (fracturation); b) Change in minimum horizontal stress (σ_h) and pore pressure (P_p) are actually two competing mechanisms. Since change of the pore pressure is mainly driven by the leak off process, but the minimum horizontal stress varies mainly due to the fracture pressure, σ_h alters more intensively when a system is difficult to leak off. Further, in a tight gas reservoir, the fluid viscosity also affects the fracture's final shape through its proppant-carrying ability. By simulating the settling behavior during fracturing process and conducting a real case study in tight gas reservoir Leer (considering the THM coupling effects and the gel breaking process), it can be found that not only the leak off but also the proppant's settling would be accelerated by the smoother fluid. A possible way to solve this problem is introducing of gas-based fracturing (e.g. supercritical CO_2), since in this method the fracture's close rate can be much faster than the settling. However, for investing this more advanced technology, a more powerful and even revolutionary simulator is required.

In Chapter 4, TOUGH2MP-FLAC3D with a damage module was used to simulate the Landau project, which is an EGS power plant located in Upper Rhine Graben. In this study, to model the softening of rock formations more logically, the damaging concept and its influences on permeability evolution was introduced to the simulation (of hydraulic fracturing) for the first time. Since the "history matching" of BHP was well achieved, the results have

revealed three important phenomena: a) the core area within and around the natural faults is more susceptible to the injection work. For this reason, its plastic strain increases further even after the area of entire fracture remained unchanged; b) Mechanic and hydraulic equilibrium cannot be achieved immediately. Thus, fracturing and seismicity also occurred even after stopping the injection. These post failure processes continued until the end of stress redistribution; c) intense rise or fall in injection/production rate and a big difference between them can both induces disturbance in the system. The stronger the disturbance, the more intensive the deformation or the fracturing would be. So, it can be concluded that disturbance in the production work (because of an immoderate change of injection/production rate or the big difference between them) can cause the induced seismic events, while the reactivation trend of natural faults is impacted by the system's operating intensity (absolute value of the injection/production rate). A reasonable response to reduce the risks is: reducing the injection and production rates immediately with a moderate and equal rate (injection/production) when critical magnitude (e.g. $M_L \geq 2.0$) occurs.

The fracture systems in the above studies (Chapter 3 and 4) were all achieved through presetting a primary fracture in the geometric model (perpendicular to the uniform σ_h). However, the practical situation is sometimes more complicated than this assumption. In Chapter 5, a series of in-depth modifications were proposed to be applied in FLAC3D^{plus}. Through implementing the triangle prism element and reprogramming corresponding mechanic and hydraulic codes, FLAC3D^{plus} has gained the new feature to model the fracture propagation with arbitrary orientation. More importantly, it overcomes the shortcomings of XFEM (extended finite element method) that cannot simulate the 3D propagation. The functionality was approved using a classical KGD fracture and a steering model based on it. Afterwards, a three-dimensional example was illustrated to represent the same ability in the 3D situation.

In the future, advancement in technology will make large- or even ultra-large-scale computing capabilities more affordable. Therefore, a more advanced simulator using Python programming (based on e.g. the fundamental package NumPy or SciPy) and GPU-accelerated

computing (e.g. the CUDA technique of NVidia) should be developed based on further developed theoretical models (e.g. a HM model based on apparent hydraulic permeability). As a result, simulations of the new fracturing techniques, e.g. the gas-based fracturing and the complex fracture net in shale gas exploitation, will become more precise and can be applied to large scale models.

7 References

[1] BP (2017). *BP Statistical Review of World Energy* 2017. BP p.l.c.

[2] REN21 (2017). *Advancing the global renewable energy transition*. Renewable Energy Policy Network for the 21st Century.

[3] IEA (2017). *World Energy Outlook*. International Energy Agency.

[4] EIA (2016). *International Energy Outlook 2016 with Projections to 2040*. U.S. Energy Information Administration.

[5] Gou Y (2017). *Numerical study of coupled THM/C processes related to geo-energy production*. Doctoral Dissertation. Cuvillier Verlag Göttingen, ISBN: 9783736998209.

[6] Economides MJ, Boney C (2000). *Chapter 1 Reservoir Stimulation in Petroleum Production*. Reservoir Stimulation 3rd Edition, Wiley, 2000, the USA, ISBN-10: 0471491926, ISBN-13: 978-0471491927.

[7] Xu ZL (2006). *Chapter 1 Introduction*. Elasticity 4th Edition, High Education Press, 2006, P.R. China, ISBN: 978-7-04-020213-7.

[8] Jaeger JC, Cook NGW, Zimmerman R (2007). *Chapter 2 Analysis of Stress and Strain*. Fundamentals of Rock Mechanics 4th Edition, Wiley Blackwell, 2007, the USA, ISBN: 978-0-632-05759-7.

[9] Li SY, He TM, Yin XC (2010). *Chapter 1 Basis of Elastic Mechanics*. Introduction of Rock Fracture Mechanics, University of Science and Technology of China Press, 2010, P.R. China, ISBN: 978-7-312-02229-6.

[10] Griffith AA (1921). *The Phenomena of Rupture and Flow in Solids*. Philosophical Transactions of the Royal Society of London. Series A, Containing Papers of a Mathematical or Physical Character, Vol. 221 (1921), 163-198.

[11] Ugural AC, Fenster SK (2011). *Chapter 2 Strain and Material Properties*. Advanced Mechanics of Materials and Applied Elasticity 5th Edition, Pearson Eduaction, Inc., 2011, the USA, ISBN-10: 0-13-707920-6, ISBN-13: 978-0-13-707920-9.

[12] Zhou L (2014). *New numerical approaches to model hydraulic fracturing in tight reservoirs with consideration of hydro-mechanical coupling effects*. Doctoral Dissertation. Cuvillier Verlag Göttingen. ISBN: 9783954046560.

[13] Irwin (1957). *Analysis of stress and strain near the end of a crack extension force*. Journal of Applied Mechanics, Vol. 24, 361-363.

[14] Bertram A (2008). Bruchenergie laufender Risse in Gestein. Doctoral Dissertation in Ruhr-University of Bochum.

[15] Dugdale DS (1960). *Yielding of steel sheets containing slits*. Journal of the Mechanics and Physics of Solids, Vol. 8(2), 100-104.

[16] Barenblatt GI (1962). *The mathematical theory of equilibrium cracks in brittle fracture*. Advances in Applied Mechanics, Vol. 7, 55-130.

[17] Zimmerman RW, Kumar S, Bodvarsson GS (1991). *Lubrication theory analysis of the permeability of rough-walled fractures*. International Journal of Rock Mechanics and Mining Sciences, Vol. 28, 325-331.

[18] Wu CG (2008). *Chapter 15 Infiltration*. Hydraulics 4th Edition, High Education Press, 2008, P.R. China, ISBN: 978-7-04-022677-5.

[19] Patankar SV (1980). *Chapter 6 Calculation of the flow field*. Numerical heat transfer and fluid flow, McGraw-Hill, 1980, the USA, ISBN: 9780891165224.

[20] Fourier J (1822). Analytical Theory of Heat, Cambridge University Press, 1878, the UK, ISBN: 9783733308831.

[21] Lamb H (1916). Hydromechanics, Cambridge University Press, 1916, the UK, ISBN: 978-0486602561.

[22] Halliday D, Resnicks R, Walker J (1960). Fundamentals of Physics, John Wiley & Sons, Inc., 2013, the USA, ISBN: 978-1118230718.

[23] Itasca (2009). FLAC3D Manual Version 4.0, ITASCA Consulting Group, Inc., 2009, the USA.

[24] Röhlig K (2013). *Differentialgleichungen in der Langzeitsicherheitsanalyse*, Courseware, 2013, Germany.

[25] Butcher JC (2008). Numerical Methods for Ordinary Differential Equations 2nd Edition. John Wiley & Sons, 2008, the USA, ISBN: 978-0470723357.

[26] Gou Y, Zhou L, Zhao X, Hou ZM, Were P (2015). *Numerical study on hydraulic fracturing in different types of georeservoirs with consideration of H^2M-coupled leak-off effects*. Environmental Earth Sciences, Vol. 72(10), 6019-6034.

[27] Lu C, Guo J, Liu Y, Yin J, Deng Y, Lu Q, Zhao X (2015). *Perforation spacing optimization for multi-stage hydraulic fracturing in Xujiahe formation: a tight sandstone formation in Sichuan Basin of China*. Environmental Earth Sciences, Vol. 73(10), 5843-5854.

[28] Hou Z, Xie H, Zhou H, Were P, Kolditz O (2015). *Unconventional gas resources in China*. Environmental Earth Sciences, Vol. 73(10), 5785-5789.

[29] Zhou L, Hou MZ, Gou Y, Li M (2014). *Numerical investigation of a low-efficient hydraulic fracturing operation in a tight gas reservoir in the North German Basin*. Journal of Petroleum Science and Engineering, Vol. 120, 119-129.

[30] Perkins TK, Kern LR (1961). *Width of Hydraulic Fractures*. Journal of Petroleum Technologies, Vol. 13(9), 937-949.

[31] Nordgren RP (1972). *Propagation of a vertical hydraulic fracture*. Society of Petroleum Engineers Journal, Vol. 12(4), 306-314.

[32] Khristianovic SA, ZheltovYP (1955). *Formation of vertical fractures by means of highly viscous liquid*. In: Proceedings of the Fourth World Petroleum Congress, Rome, Italy, 6–15 June.

[33] Geertsma J, de Klerk F (1969). *A rapid method of predicting width and extent of hydraulically induced fractures*. Journal of Petroleum Technologies, Vol. 21, 1571–1581.

[34] Adachi J, Siebrits E, Peirce A, Desroches J (2007). *Computer simulation of hydraulic fractures*. International Journal of Rock Mechanics and Mining Science, Vol. 44, 739–757.

[35] Barree RD, Conway MW (1995). *Experimental and numerical modeling of convective proppant transport*. Journal of Petroleum Technologies, Vol.47, 216–222.

[36] Gadde PB, Liu Y, Norman J, Bonnecaze R, Sharma MM (2004). *Modeling proppant settling in water-fracs*. In: Proceeding of SPE Annual Technical Conference and Exhibition, Houston, the USA, 26–29 September.

[37] Gadde PB, Sharma MM (2005) .*The impact of proppant retardation on propped fracture lengths*. In: Proceeding of SPE Annual Technical Conference and Exhibition. Dallas, USA, 9–12October.

[38] Liu Y (2006). *Settling and Hydrodynamic Retardation of Proppants in Hydraulic Fractures*. Doctoral Dissertation for University of Texas at Austin.

[39] Hsu Y, Dang XL, Chilton W, Chang P, Stelin I, Gusain D, Northington N,de Pater HJ (2012).*New physics-based 3D hydraulic fracture model*. In: Proceeding of SPE Hydraulic Fracturing Technology Conference. Woodlands, the USA, 6–8 Feburary.

[40] Zhou L, Hou ZM (2013). *A new numerical 3D-model for simulation of hydraulic fracturing in consideration of hydro-mechanical coupling effects*. International Journal of Rock Mechanics and Mining Sciences, Vol. 60, 370-380.

[41] Casas LA, Miskimins JL, Black AD, Green SJ (2006). *Laboratory hydraulic fracturing test on a rock with artificial discontinuities*. In: Proceeding of SPE Annual Technical Conference and Exhibition. SanAntonio, Texas, the USA, 24–27 September.

[42] Dinske C, Shapiro SA, Rutledge JT (2010). Interpretation of micro seismicity resulting from gel and water fracturing of tight gas reservoirs. Pure and Applied Geophysics, Vol. 167, 169–182.

[43] Eissa MS, King SU, Abdulrahman AA (2007). *Experimental and numerical investigation of proppant placement in hydraulic fractures*. In: Proceeding of SPE Latin American and Caribbean Petroleum Engineering Conference. Buenos Aires, Argentina, 15–18April.

[44] Crank J (1975). The Mathematics of Diffusion 2nd Edition. Oxford University Press, 1975, the UK, ISBN: 0-19-853411-6.

[45] Holman JP (2010). Heat transfer 10th Edition. McGraw-Hill, 2010, the USA, ISBN: 978-0073529363.

[46] Carrier B, Granet S (2012). *Numerical modeling of hydraulic fracture problem in permeable medium using cohesive zone model*. Engineering Fracture Mechanics, Vol. 79.

[47] Kohler M, Kerekes F (2006). *Rotliegend Tight Gas Field Leer: A Development with a Multiple Hydraulically Fractured Horizontal Well: Project Leer Z4*. DGMK-Frühjahrstagung 2006, ISBN: 3-936418-48-9.

[48] Kohler M (2004). *Project Leer Z4: G&G_Peer-Presentation*. Internal presentation of ENGIE E&P Deutschland GmbH.

[49] Li M (2018). *Optimization of Multistage Hydraulic Fracturing Treatment for Maximization of the Tight Gas Productivity*. Doctoral Dissertation. Cuvillier Verlag Göttingen, ISBN: 9783736999343.

[50] Gaz de France (2006). A Development with a Multiple Hydraulically Fractured Horizontal Well: Project Leer Z4. Gaz de France

[51] Hou ZM, Kracke T, Zhou L, Wang XR (2012). *Rock mechanical influences of hydraulic fracturing deep underground the North German Basin: geological integrity of the cap rock salt and maximum magnitude of induced microseismicity based on the GeneSys stimulation in May 2011*. Erdöl Erdgas Kohle, Vol. 128(11), 454-460.

[52] Baumgärtner J (2013). *Geothermie 2.0 Geothermie-Kraftwerk Insheim*. BESTEC GmbH.

[53] Hou ZM, Gou Y, Feng W, Xing W, Fiedler F (2016). *Entwicklung numerischer Analysemodelle zur lokalen seismischen Gefährdungseinschätzung vor Bohrbeginn und langfristige Bewertung von Geothermiefeldern unter Berücksichtigung THM:C gekoppelter Prozesse*.

[54] Expertengruppe „Seismische Risiko bei hydrothermaler Geothermie“ (2010). *Das seismische Ereignis bei Landau vom 15. August 2019*.

[55] Gou Y, Hou Z, Liu H, Zhou L, Were P (2014). *Numerical simulation of carbon dioxide injection for enhanced gas recovery (CO2-EGR) in Altmark natural gas field*. Acta Geotechnica, Vol. 9(1), 49-58.

[56] Rutqvist J, Tsang CF (2002). *A study of caprock hydromechanical changes associated with CO2 injection into a brine Reservoir*. Environmental Geology, Vol. 42(2), 296–305.

[57] Rutqvist J, Wu YS, Tsang CF, Bodvarsson G (2002). *A modeling approach for analysis of coupled multiphase fluid flow, heat transfer, and deformation in fractured porous rock*. International Journal of Rock Mechanics and Mining Sciences, Vol. 39(4), 429–442.

[58] Rutqvist J, Liu HH, Vasco DW, Pan L, Kappler K, Majer E (2011). *Coupled non-isothermal, multiphase fluid flow, and geomechanical modeling of ground surface deformations and potential for induced micro-seismicity at the In Salah CO2 storage operation*. Energy Procedia, Vol. 4, 3542–3549.

[59] Pogacnik J, O’Sullivan M, O’Sullivan J (2014). *A Damage Mechanics Approach to Modeling Permeability Enhancement in Thermo-Hydro-Mechanical Simulations*. In: Proceeding of 39th Workshop on Geothermal Reservoir Engineering Stanford University, Stanford, California, 24-26 February.

[60] Pogacnik J, O’Sullivan M, O’Sullivan J (2015). *Linking TOUGH2 and ABAQUS to model Permeability Enhancement Using a Damage Mechanics Approach*. In: Proceeding of World Geothermal Congress 2015, Melbourne, Australia, 19-25 April.

[61] Aki K, Richards PG (2002). Quantitative Seimology 2nd Edition, University Science Books, 2002, the USA, ISBN: 978-1891389634.

[62] Shearer PM (2009). Introduction to seismology 2nd Edition, Cambridge University Press, 2009, the UK, ISBN: 978-0521708425.

[63] Kanamori H, Anderson DL (1975). *Theoretical basis of some empirical relations in seismology*. Bulletin of the Seismological Society of America, Vol. 65(5), 1073-1095.

[64] Hanks TC, Kanamori H (1979). *A moment magnitude scale*. Journal of Geophysical Research, Vol. 85(B5), 2348-2350.

[65] Feng WT, Were P, Li M, Hou ZM, Zhou L (2016). *Numerical study on hydraulic fracturing in tight gas formation in consideration of thermal effects and THM coupled processes*. Journal of Petroleum Science and Engineering, Vol. 146, 241-254.

[66] Morris A, Ferrill DA, Henderson DB (1996). *Slip-tendency analysis and fault reactivation*. Geology, Vol. 24, 275–278.

[67] Sima LQ, Wang C, Wang L, Wu F; Ma L, Wang ZJ (2017). *Effect of pore structure on the seepage characteristics of tight sandstone reservoirs: A case study of Upper Jurassic Penglaizhen Fm reservoirs in the western Sichuan Basin*. Natural Gas Industry, Vol. B4, 17-24.

[68] Bunger A P, Detournay E, Garagash, D I (2005). *Toughness-dominated hydraulic fracture with leak-off*. International Journal of fracture, Vol. 134, 175-190.

Appendix A Fracture width and volumetric concentration of proppant at the end of stimulation and at the compacted status

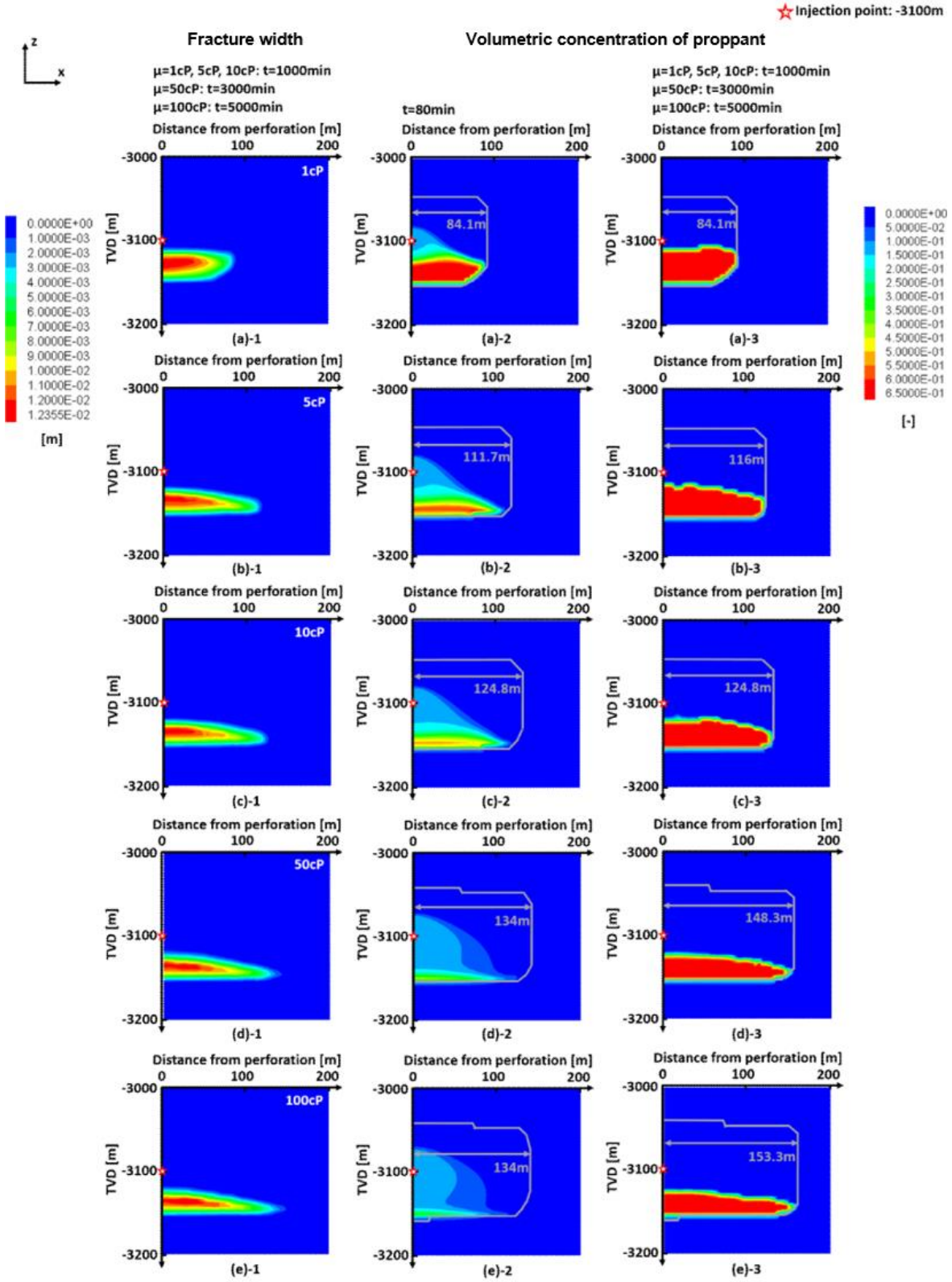

Appendix B Mechanical and hydraulic properties of the rock formations in Leer

TVD at sole	Rock group	Density ρ	Young's modulus E	Poisson ratio μ	Permeability k	Porosity φ
[m]		[kg/m^3]	[MPa]	[-]	[μD]	[%]
-4,290.00	/	/	/	/	/	/
-4,309.61	overburden	2,573.25	20,631.93	0.20	66.87	0.1
-4,315.16	BA/Silt_1	2,573.25	20,631.93	0.20	66.87	7.4
-4,320.25	BA/Sand_6	2,552.00	23,445.84	0.19	106.7	8.7
-4,321.52	BA/Shale_4	2,589.36	22,249.28	0.16	91.62	8.4
-4,324.07	BA/Sand_5	2,569.14	20,620.94	0.18	75.77	7.8
-4,327.19	BA/Shale_3	2,581.63	19,698.41	0.26	75.97	7.8
-4,329.62	BA/Sand_4	2,631.00	21,118.74	0.23	5.22	0.1
-4,336.35	BA/Sand_3	2,577.10	24,452.58	0.20	76.73	7.7
-4,336.70	BA/Shale_2	2,594.33	29,427.65	0.24	87.42	8.2
-4,338.20	BA/Sand_2	2,538.62	29,469.20	0.19	151.6	9.8
-4,339.36	BA/Shale_1	2,515.20	29,251.89	0.24	105.3	8.8
-4,342.62	BA/Sand_1	2,539.68	25,580.99	0.26	314.8	11.3
-4,345.88	WU/Shale_2	2,632.32	23,570.89	0.26	48.41	7.8
-4,351.83	WU/Sand_6	2,538.24	27,687.11	0.21	7233.0	9.8
-4,360.93	WU/Sand_5	2,513.78	28,965.69	0.20	9720.0	11.1
-4,366.39	WU/Silt_1	2,566.96	27,967.81	0.19	48.11	7.8

-4,382.37	BA/Chan-nel_Sand_1	2,505.54	28,951.79	0.19	12360.0	11.1
-4,393.83	WU/Sand_2	2,529.59	29,079.88	0.22	3265.0	9.3
-4,394.29	WU/Shale_1	2,622.50	26,212.79	0.28	66.07	8.3
-4,398.58	WU/Sand_1	2,508.32	27,595.61	0.25	7572.0	10.7
-4,405.41	EB/Shale_2	2,602.52	20,806.48	0.22	77.75	7.9
-4,408.91	Ebstorf_Silt_1	2,614.48	30,366.26	0.22	67.85	7.4
-4,430.86	Vulcanite_8	2,695.85	30,372.57	0.22	5.107	0.1
-4,505.00	basement	2,695.85	30,571.94	0.22	5.107	0.1

Appendix C Thermal properties of the rock formations in Leer

Rock group	Thermal conductivity λ	Thermal expansion coefficient α_T	Specific heat capacity c
	[W/(m·°C)]	[°C^{-1}]	[J/(kg·°C)]
All formations	2.0	8×10^{-6}	1200